

GEOLOGICA ULTRAIECTINA

Mededelingen van de  
Faculteit Aardwetenschappen der  
Rijksuniversiteit te Utrecht

No. 67

**TOMOGRAPHY WITH P, PP AND pP DELAY-TIME DATA  
AND  
THE THREE-DIMENSIONAL MANTLE STRUCTURE  
BELOW THE CARIBBEAN REGION**

**ROB VAN DER HILST**

# **TOMOGRAPHY WITH P, PP AND pP DELAY-TIME DATA AND THE THREE-DIMENSIONAL MANTLE STRUCTURE BELOW THE CARIBBEAN REGION**

**SEISMISCHE TOMOGRAFIE MET P, PP EN pP REISTIJD GEGEVENS  
EN DE DRIE DIMENSIONALE MANTEL STRUKTUUR  
ONDER HET CARAIBISCHE GEBIED**  
(met een samenvatting in het Nederlands)

**PROEFSCHRIFT**

**TER VERKRIJGING VAN DE GRAAD VAN DOCTOR AAN DE  
RIJKSUNIVERSITEIT TE UTRECHT OP GEZAG VAN DE  
RECTOR MAGNIFICUS PROF. DR. J.A. VAN GINKEL  
INGEVOLGE HET BESLUIT VAN HET COLLEGE VAN DEKANEN  
IN HET OPENBAAR TE VERDEDIGEN OP DONDERDAG  
3 MEI 1990 DES NAMIDDAGS TE 12.45 UUR**

**DOOR**

**ROBERT DIRK VAN DER HILST**

**GEBOREN OP 12 JANUARI 1961, TE OOSTZAAN**

PROMOTOR:            PROF. DR N. J. VLAAR  
CO-PROMOTOR:       DR W. SPAKMAN

The research described in this thesis was carried out at the

Department of Theoretical Geophysics  
Institute for Earth Sciences  
University of Utrecht  
P.O. Box 80.021, 3508 TA Utrecht  
The Netherlands

3 May 1990

CIP-DATA, KONINKLIJKE BIBLIOTHEEK, DEN HAAG

Hilst, Robert Dirk van der

Tomography with P, PP, and pP delay-time data and the three-dimensional mantle structure below the Caribbean region / Robert Dirk van der Hilst. - [Utrecht : Instituut voor Aardwetenschappen der Rijksuniversiteit Utrecht]. - (Geologica Ultraiectina . ISSN 0072-1026 ; no. 67)

Thesis Utrecht. - With ref. - With summary in Dutch.

ISBN 90-71577-20-1

SISO am-west 565 UDC 550.34.038(729)(043.3)

Subject headings: seismic tomography / 3D Caribbean mantle structure.

## *Contents*

### Chapter 1

#### Caribbean tectonics and seismic delay-time tomography: An introduction

1.1 The Caribbean region .....	1
1.2 Complications in the investigation of the tectonic evolution of the Caribbean region .....	2
1.3 The contribution of seismic tomography to the study of the tectonic history of the Caribbean region. ....	4
1.4 The concept of seismic delay-time tomography .....	5
1.4.1 The tomographic system of equations .....	5
1.5 The ray geometry .....	8
1.5.1 Distribution of earthquake hypocenters and seismological stations .....	8
1.5.2 The reference model of seismic velocities .....	10
1.5.3 The seismic waves considered in this tomographic investigation .....	11
1.5.4 Discretization of the investigated Earth volume: the cell model .....	11
1.6 The data set .....	13
1.6.1 Data selection .....	13
1.6.2 Hypocenter relocation and corrections to the delay time data .....	14
1.7 Formulation of scientific problems and organization of this thesis .....	16

### Chapter 2

#### Importance of the reference model in linearized tomography

2.1 Introduction .....	19
2.2 Linearization and reference model: assumptions and implications .....	20
2.3 Derivation of a new reference model .....	22
2.4 Application to the mantle below the Caribbean region .....	26
2.5 A continuous high velocity anomaly down to lower mantle depths .....	29
2.6 Discussion and concluding remarks .....	31
Appendix 2A: .....	33

### Chapter 3

#### On the use of PP and pP data in delay time tomography

3.1 Introduction .....	37
3.2 Limitations imposed on the spatial resolution if only direct P phases are used .....	41



## *Contents*

3.3	Illumination of structure by seismic rays of the pP and PP phases .....	43
3.3.1	Illumination by PP waves .....	43
3.3.2	Illumination by pP waves .....	45
3.4	The data .....	45
3.4.1	PP delay times .....	51
3.4.2	pP delay times .....	54
3.5	Residual differential times .....	58
3.6	Tomographic inversion of PP and pP delay times .....	61
3.6.1	The tomographic system of equations .....	62
3.6.2	Hitcount .....	62
3.6.3	Effects on spatial resolution of the addition of PP and pP phases .....	64
3.6.4	Implications for the velocity structure .....	69
3.7	Conclusions .....	72
	Appendix 3.A: The tomographic system of equations .....	76
	Appendix 3.B: Figure 3B .....	79

## Chapter 4

### Tectonic framework of the Caribbean region

4.1	Introduction .....	91
4.2	The tectonic framework of the Caribbean region .....	91
4.3	Tectonic problems that can be investigated by seismic tomography .....	96

## Chapter 5

### Tomographic images of variations of the P velocities in the mantle beneath the Caribbean region

5.1	Introduction .....	107
5.2	Presentation of the results of the tomographic inversions .....	108
5.2.1	Results of the inversion of P, PP and pP delay-time data .....	108
5.2.2	The sampling of Earth structure by P, PP and pP rays .....	108
5.2.3	The harmonic sensitivity test .....	109
5.2.4	The cell-spike sensitivity test .....	111
5.2.5	The harmonic model fit .....	111
5.2.6	Shortcomings of the sensitivity tests .....	112
5.2.7	The inversion of randomly permuted data .....	113
5.2.8	The presentation of the results .....	115
5.3	Inversion results for the upper mantle .....	115
5.3.1	Layer 1: 0 - 33 kilometer .....	116

## *Contents*

5.3.2 Layer 2: 33 - 85 kilometer .....	118
5.3.3 Layers 3 and 4: 85 - 185 kilometer .....	119
5.3.4 Layers 5, 6 and 7: 185 - 390 kilometer .....	121
5.3.5 Layers 8, 9 and 10: 390 - 660 kilometer .....	122
5.3.6 Summary of results for upper mantle structures .....	123
5.4 Inversion results for the lower mantle .....	185
5.4.1 Layers 11, 12 and 13: 660 - 1000 kilometer .....	185
5.4.2 Layers 14 and 15: 1000 - 1325 kilometer .....	186
5.4.3 Summary of results for lower mantle .....	186
5.5 Comparison with results of other investigations .....	187
5.6 Conclusions .....	191

## Chapter 6

### Mantle structures below the convergent margins of Middle America, The Lesser Antilles, and northwestern South America

6.1 Introduction .....	193
6.2 The Middle America subduction zone .....	194
6.2.1 Subduction of the Cocos Plate: a brief review of its complexity .....	195
6.2.2 The shallow mantle structure: results of other investigations .....	195
6.2.3 The shallow mantle structure: results of tomographic inversions .....	197
6.2.4 Tomographic images of the deep mantle structure below Middle America .....	213
6.2.5 Summary and discussion of mantle P-velocity structure below Middle America .....	214
6.3 Subduction of Atlantic lithosphere below the Greater and Lesser Antilles .....	216
6.3.1 Seismotectonic setting: other investigations .....	216
6.3.2 Spatial resolution in tomographic images of mantle below the eastern Caribbean .....	218
6.3.3 The aspherical mantle structure below the eastern part of the Caribbean Plate .....	218
6.3.4 Discussion of tomographic images and some tectonic implications .....	227
6.4 Evidence for underthrusting of the Caribbean below South America .....	230
6.5 Conclusions .....	231

## *Contents*

References .....	236
Summary and conclusions .....	242
Samenvatting (Summary in dutch) .....	246
Dankbetuiging (Acknowledgements) .....	248
Curriculum Vitae .....	250

## *Chapter 1*

### **Caribbean tectonics and seismic delay-time tomography: an introduction**

The research which is described in this thesis has as principal objectives: (1), the further development of the method of seismic  $P$  delay-time tomography of Spakman and Nolet [Nolet, 1985; Spakman and Nolet, 1988; Spakman, 1988]; and (2), the application of the improved tomographic method to investigate the aspherical mantle structure below the Caribbean region.

Several topics are addressed in this introduction. In sections 1.1, 1.2, and 1.3, I describe the geographic region below which we investigate the mantle structure, I briefly outline current problems in the investigation of the tectonics of the Caribbean region, and explain the possible contributions of seismic tomography to this investigation. Subsequently, the concept of seismic delay-time tomography is explained qualitatively in section 1.4, and in sections 1.5 and 1.6 I address the principal aspects of this method in relation to its application to the Caribbean region. In section 1.7, I formulate the questions to which answers are sought in this study, and describe the organization of this thesis.

#### **1.1 The Caribbean region**

The Caribbean region encompasses the geographical area of the Gulf of Mexico, Central America, the Caribbean Sea region, and the northwestern part of South America (Figure 1.1). As shown in Figure 1.1, the area covered in the tomographic computations is much larger and also includes a major part of South America. Tomographic images of the mantle structure below the latter area are not discussed in this thesis but will be published

elsewhere.

## **1.2 Complications in the investigation of the tectonic evolution of the Caribbean region**

The Caribbean region is one of the most intensively studied areas on Earth. In the past decades, many investigators acquired and analyzed a wealth of geological and geophysical data to investigate the complex tectonic history of this region. The plate tectonic evolution of the Caribbean region has been controlled by the interaction of 6 major lithospheric plates: the North and South American Plates, the Pacific Plate, the Cocos and the Nazca Plates and the Caribbean Plate (Figure 1.2). Since the Late Paleocene [Ross and Scotese, 1988], the Caribbean Plate has not been connected to large segments of spreading ridges, or to subduction zones. Major plate-driving forces, like ridge-push and slab-pull, are small or absent, and Caribbean Plate motion has been determined by relative movements of the surrounding plates. Unresolved tectonic problems remain about the origin and nature of the Caribbean Plate, and about almost all portions of present boundaries between the tectonic units in this region.

Many investigators concur with an allochthonous origin of the present-day Caribbean Plate [e.g., Pindell et al., 1988]. These investigators postulate that the Caribbean Plate moved from a Pacific origin into the "gap" created by rifting between North and South America at the expense of the young proto-Caribbean lithosphere [Pindell and Dewey, 1982; Pindell et al., 1988; Ross and Scotese, 1988]. Because of the young age of the proto-Caribbean lithosphere, underplating and lithospheric doubling [Vlaar, 1983] may have occurred below the overriding Caribbean Plate resulting in a complex, highly heterogeneous and relatively buoyant Caribbean crust [Burke et al., 1978; Mann and Burke, 1984].

In spite of the general agreement on the origin of the Caribbean Plate, Caribbean Plate motion of the order of several thousands of kilometers relative to the North and South American Plates is still subject to controversy. Evidence exists for large amounts of left lateral slip along the boundary zone between the Caribbean Plate and the North American Plate [Holcombe and Sharman, 1983; Mann and Burke, 1984; Rosencrantz and Sclater, 1986], but the amount of slip along the boundary between the Caribbean Plate and the South American Plate is uncertain [Mann and Burke, 1984]. The deformation in this plate boundary zone is extremely complex and occurs along a diversity of faults of different types and within a number of micro plates [Mann and Burke, 1984; Bonini et al., 1984]. The deformation along the western and eastern boundaries of the Caribbean Plate has been determined by subduction of respectively the Cocos Plate at the Middle America trench and the subduction of Atlantic lithosphere at the Lesser Antilles trench. Whether or not the downgoing Atlantic lithosphere is part of the North American Plate or part of the South American Plate, or both, is not clear [Stein et al., 1982]. The subduction of the Cocos Plate has been complex due to large variations along the trench of lithospheric age, the subduction of bathymetric features, and the collision of ridge segments with the trench.



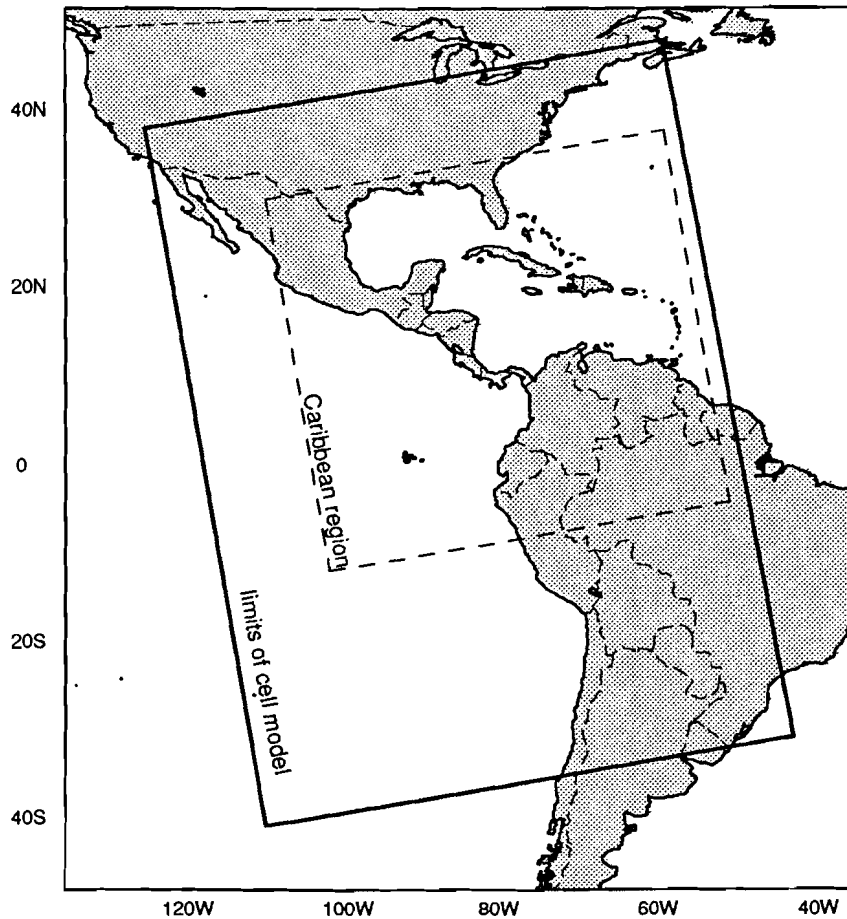


*Figure 1.1.* Geographic map of South America and the southern part of North America. The rotated frames outline the limits of the cell model used in this investigation (Figure 1.6), and the boundary of the geographic area that will be referred to as the Caribbean region.

Pertinent information about the present-day tectonics of the area is obtained from studies of the seismicity of the region. As will be discussed below, these investigations are complicated by the particular spatial distribution of earthquake hypocenters and seismological stations in relatively narrow zones along the plate boundaries. In addition, the seismicity in the region is restricted in depth to the upper 250 km. Another complication is the geographical distribution of land and sea. The larger part of the Caribbean region is covered by sea, and the area which is easily accessible to direct observations, or for the installation of instruments (e.g., seismometers), is relatively small.

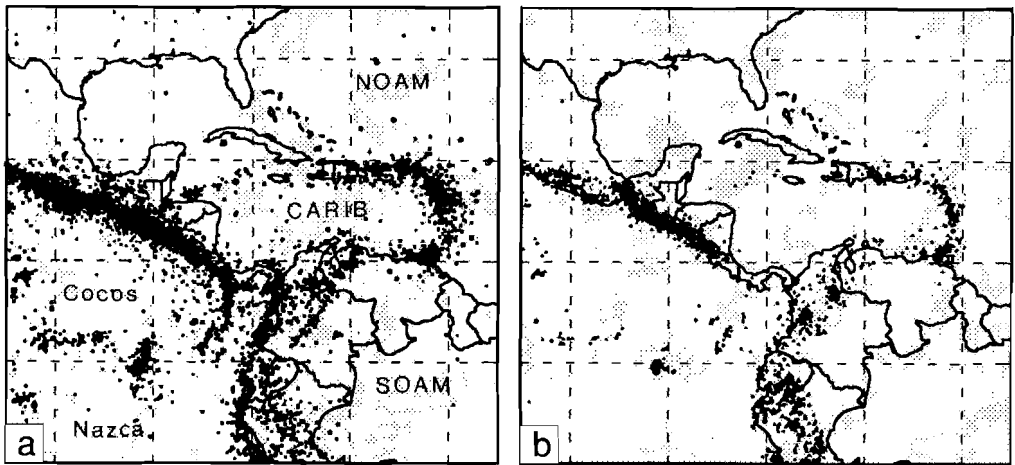


*Figure 1.2.* The locations of the earthquakes that contributed to the data set used in this study. (a) Epicenters of earthquakes with focal depths < 70 km (b) Epicenters of earthquakes with focal depths > 70 km

*CARIB* Caribbean Plate, *Cocos* Cocos Plate, *Nazca* Nazca Plate, *NOAM* North American Plate, *Pacif* Pacific Plate, *SOAM* South American Plate.

In spite of these complications, recent publications of plate kinematical reconstructions demonstrate the high level of actual knowledge about the tectonic history of the region [Ross and Scotese, 1988; Pindell et al., 1988]. Additional references are; Molnar and Sykes [1969], Pennington [1981], Stein et al. [1982], Burbach et al. [1984], and Dewey and Suárez [1990], for an overview of the seismicity of the region; and Bowin [1976] and Bonini [1978], for studies on the gravity field of the Caribbean region.

### 1.3 The contribution of seismic tomography to the study of the tectonic history of the Caribbean region.

Knowledge about the structures in the mantle below the Caribbean region is of crucial importance to assess and complement existing plate-kinematic models, and to understand the geodynamics of the region. To obtain information about mantle structure, methods are commonly used that reveal information about either short-wavelength structures in the upper part of the upper mantle, or about long-wavelength structures in the deeper part of the upper mantle and in the lower mantle.

Small-scale structures in the upper mantle can be studied by the investigation of the seismicity in the area. For example, detailed information can be obtained about the three-dimensional morphology of the seismogenic part of subduction zones. However, the seismic active part of a subduction zone often describes only the shallowest part of the down going lithosphere [Wortel, 1982] and the morphology of the aseismic part is not revealed by analyses of seismicity. Similarly, in the case of aseismic subduction or ceased subduction, the presence of subducted lithosphere in the mantle may not be indicated by

seismicity. In the case of the Caribbean region two additional draw-backs exist. Firstly, the seismicity in the Caribbean area is restricted to relative shallow depths: approximately 250 km in the Middle America and Lesser Antilles subduction zones (Figure 1.2). Below the northern and southern plate boundary zones, where strike slip faults prevail, the seismicity is shallower than 70 km (Figure 1.2). Secondly, the seismicity in the Caribbean region is mainly concentrated along the plate boundaries (interplate seismicity), and the seismicity in central parts of the plates (intraplate seismicity) is low. Information about shallow mantle structures can also be obtained from regional studies of the magnetization in subduction zones [Counil and Achache, 1987; Counil et al., 1989].

Large-scale structures in the lower mantle below the Caribbean region were discovered by, e.g., Jordan and Lynn [1974] who used information about travel times of seismic body waves. Gravity anomalies [e.g., Bowin, 1976] and the shape of the geoid may also provide information about long-wavelength density perturbations at large depths in the mantle. Neither of these studies could establish the relationship between the lower mantle structures and the upper mantle, or the relevance of the lower mantle structures for present-day dynamic processes and for plate kinematics.

Detailed information about both upper and lower mantle structures can be obtained with seismic tomography. In the past decade, many successful applications have been reported of seismic tomography in which data of body waves were used [e.g., Hirahara and Mikumo, 1980; Grand, 1987; Spakman, 1988]. This method provides a powerful tool to investigate relatively small-scale velocity structures (of the order of 100 - 500 km) even at large depths in the mantle.

## **1.4 The concept of seismic delay-time tomography**

In this study, I apply the tomographic method developed by Spakman and Nolet [1988]. This method, which was used to investigate the upper mantle structure below the Mediterranean [Spakman, 1988; Spakman et al., 1988], is here improved in order to obtain high resolution images of the variations in the propagation velocity of compressional body waves in the mantle below the Caribbean region.

The theory of linearized delay-time tomography, which underlies the present study, has been intensively studied and reviewed [Nolet, 1985; Spakman and Nolet, 1987; Spakman, 1988]. In this introductory chapter, this theory is not discussed in detail. I rather want to explain the concept of seismic delay-time tomography, and introduce the algebraic description of the tomographic problem in a qualitative manner.

### **1.4.1 The tomographic system of equations**

The Earth's structure is sampled by seismic waves. These are waves that originate at the source of an earthquake (the hypocenter), travel through the Earth, and are recorded at seismological stations. The record (the seismogram) of an earthquake contains information about the physical properties of the Earth's interior, sampled along the ray path from source to receiver. The physical property of importance for the present study is the propagation velocity of compressional waves, which can be computed from the travel times of the

waves from source to receiver. The travel time can be determined if we know the location of the hypocenter, the time the earthquake occurs (origin time), and the times at which the compressional waves arrive in the seismogram. In order to judge whether or not the thus determined travel times are indicative of unknown variations in propagation velocity in the Earth, one can compare the observed travel times with theoretical travel times computed in an assumed reference Earth model of seismic velocities. We have a fairly good understanding of the average radially-symmetric distribution of seismic velocities in the Earth. Two examples of one-dimensional reference models that are often used in seismology are the Jeffreys-Bullen (JB) velocity model [Jeffreys-Bullen, 1940], and the Parametrically Reference Earth Model [PREM, Dziewonski et al., 1975]. If the travel time observed at a particular station deviates from the travel time predicted from the reference model, the actual Earth is different from the considered one-dimensional model. In the diagram of Figure 1.3 ray traces are shown of direct waves that originate at a surface source and which are recorded at seismological stations. The travel times of the waves that sample structure B will deviate from the travel times computed in the spherical velocity model outside the structure. The objective in seismic tomography is to explain the difference between the observed and predicted travel times by updates of our perception of the actual Earth structure. The aspherical structure that causes the mismatch can be investigated by examining seismograms of waves that sample approximately the same Earth's volume and are recorded at different stations or of waves that originate at other hypocenters. The more homogeneous the sampling of the Earth's interior by different waves, and the more accurate the arrival times are picked in the seismograms, the better the physical nature (location, shape, size, seismic properties) of anomalous structures can be determined.

In its simplest form, the relation between the rays of waves that propagate through the Earth's interior, the aspherical Earth's structure, and the observed travel times, is mathematically represented by a system of linear equations, which is expressed by the matrix equation

$$A \mathbf{x} = \mathbf{d} \quad (1.1)$$

In (1.1) the matrix  $A$  contains information about how the seismic waves sample the Earth's volume under study, e.g., information about the length of the rays, the vector  $\mathbf{x}$  provides information about the variation of the velocity of wave propagation relative to the reference model velocities, and the data vector  $\mathbf{d}$  contains the delay times, which are the differences between the observed travel times and the travel times computed from the reference model.

Both  $A$  and  $\mathbf{d}$  are known within limits which will be discussed below. The model vector  $\mathbf{x}$ , the aspherical part of the Earth structure, is to be determined from (1.1). In seismic delay-time tomography the elements of  $\mathbf{x}$  can be determined by the tomographic inversion of the delay time data. Usually,  $\mathbf{x}$  can not be determined uniquely because of errors in the data, and additional criteria are needed to choose a solution. In this investigation a least squares criterion is used, and the tomographic system represented by (1.1) is solved by the LSQR inversion algorithm of Paige and Saunders [1982]. For more information about the

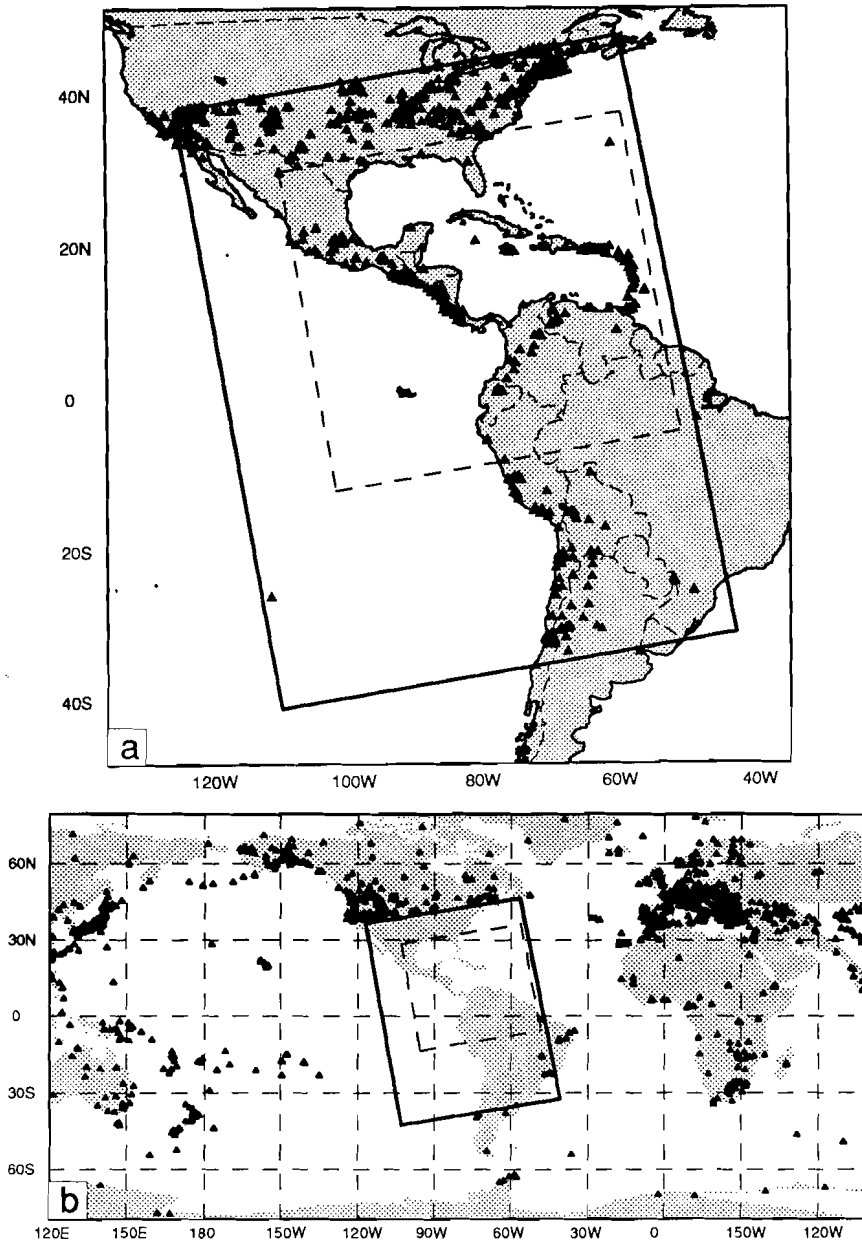


*Figure 1.3.* The distribution of stations that reported the  $P$ -wave travel time residuals used in this study. (a) Stations located within the limits of the cell model ( $n=936$ ,  $nreg=313,285$ ), (b) Stations for which station corrections were computed in the tomographic inversion ( $n=1566$ ,  $nreg=353,559$ ). These include the stations for which the station corrections of Dziewonski and Anderson [1983] are available ( $n=706$ ,  $nreg=324,263$ ).



matrix  $A$  and the solution of (1.1) I refer to Nolet [1985], Van der Sluis and Van der Vorst [1987], and Nolet and Spakman [1988].

In the next section, I discuss particulars of the sampling of the mantle structure by seismic waves, which relate to the construction of the matrix  $A$  in (1.1). Subsequently, the data set that is used to construct  $d$  is described. In sections 1.5 and 1.6, I restrict myself to aspects specific for the application of the method to investigate the mantle structure below the Caribbean region. For more elaborate discussions I refer to Spakman [1988] (his chapter 1).

## 1.5 The ray geometry

With the ray geometry employed in this study I mean the spatial distribution of ray traces of the waves that sample effectively the mantle structure below the region under investigation. In the ideal case, the seismic waves sample the Earth's interior homogeneously from different directions. However, in large-scale seismic tomography this situation is utopic. Different than in, e.g., medical tomography and bore hole tomography in exploration geophysics, in global seismic tomography no man-made sources are used and we do not have much control about the ray geometry. The ray geometry necessary to construct matrix  $A$  in (1.1) critically depends on: (1), the distribution of earthquake hypocenters and seismological stations; (2), the three-dimensional velocity model of the Earth; (3), the type of seismic waves considered in the tomographic study; and (4), the discretization of the Earth's volume under study. For information about the actual computation of the ray paths I refer to Spakman [1988].

### 1.5.1 Distribution of earthquake hypocenters and seismological stations

Figure 1.2 shows the distribution of epicenters of the earthquakes in Central and South America used in this investigation. The earthquakes occurred between January 1964 and July 1987, and were recorded at the seismological stations shown in Figure 1.4a. Operators at these stations reported their observations to the International Seismological Centre (ISC) in the U.K, or to the National Earthquake Information Center (NEIC) of the U.S. Geological Survey.

The geographical distribution of epicenters is obviously highly heterogeneous on this large scale: both intraplate and interplate earthquakes occur predominantly in relatively narrow zones along the major plate boundaries. Figure 1.4a shows the stations used in this study that are located within the geographical limits of the cell model. I want to stress that the locations of most stations coincide with the narrow zones along the plate boundaries. This geographical coincidence of the epicenters and the locations of the stations has two important consequences. Firstly, the mantle structure below the region will be unevenly sampled by the seismic waves. Consequently, some mantle regions may not be sampled by the waves considered in this study, and aspherical structure will not be discernible by seismic tomography. An example is given by structure A in Figure 1.3. In other mantle regions, many waves may sample structure in a limited range of directions, which causes that in that predominant direction no distinction can be made between separate structures.

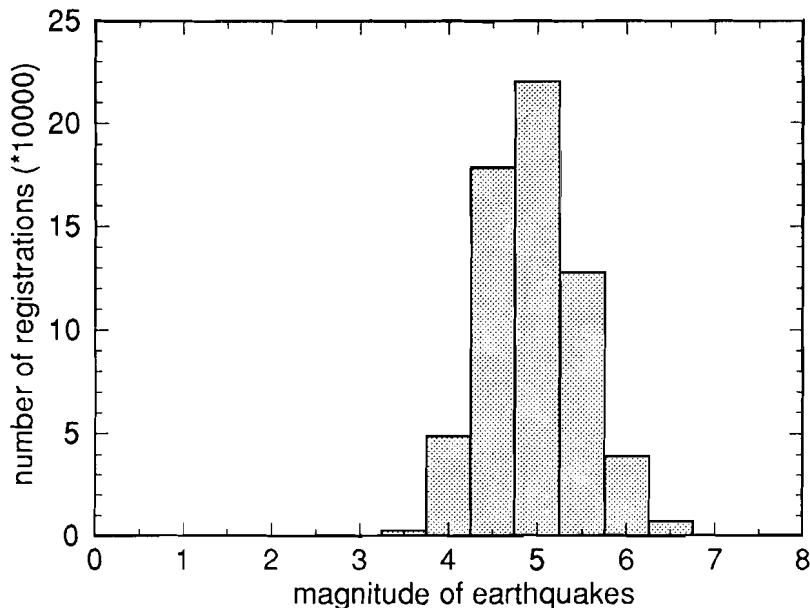


*Figure 1.4.* The distribution of the magnitudes of the earthquakes used in this study versus the number of registrations. The magnitude cut-off resulted from the requirement that an events should be recorded at least at ten different stations.

Secondly, the exact locations of earthquake hypocenters may be poorly determined because many earthquakes are recorded at stations within a narrow range of azimuths and /or distances [e.g., Molnar and Sykes, 1969; Dewey and Algermissen, 1972].

Typically some tens of thousands of earthquakes are considered in large-scale tomographic investigations. Therefore, it is not feasible to investigate individual earthquakes and general selection criteria are needed to assure the reliability of the source parameters. A principal selection criterion used in this investigation is that a minimum of 10 stations should have recorded a particular earthquake. For the investigated region, the minimum of 10 recording stations implicitly results in the rejection of earthquakes with magnitudes lower than approximately 3.5 (Figure 1.5). Additional criteria for the acceptance of earthquakes are discussed in section 1.6. I realize that better criteria are available to select earthquakes with reliable hypocentral parameters, for example those that take into account information about the azimuth and/or the epicentral distance. However, in order to assure a sufficient number of data to investigate the mantle below the Caribbean region, I could not be too strict in selecting the earthquakes.

Whereas the earthquakes considered in this study occurred within the region under investigation, I used stations that are located both inside and outside the geographical area outlined by the solid frame in Figure 1.4. This is necessary because the mantle structure below the hypocenter is only sampled by waves that travel initially downward from the

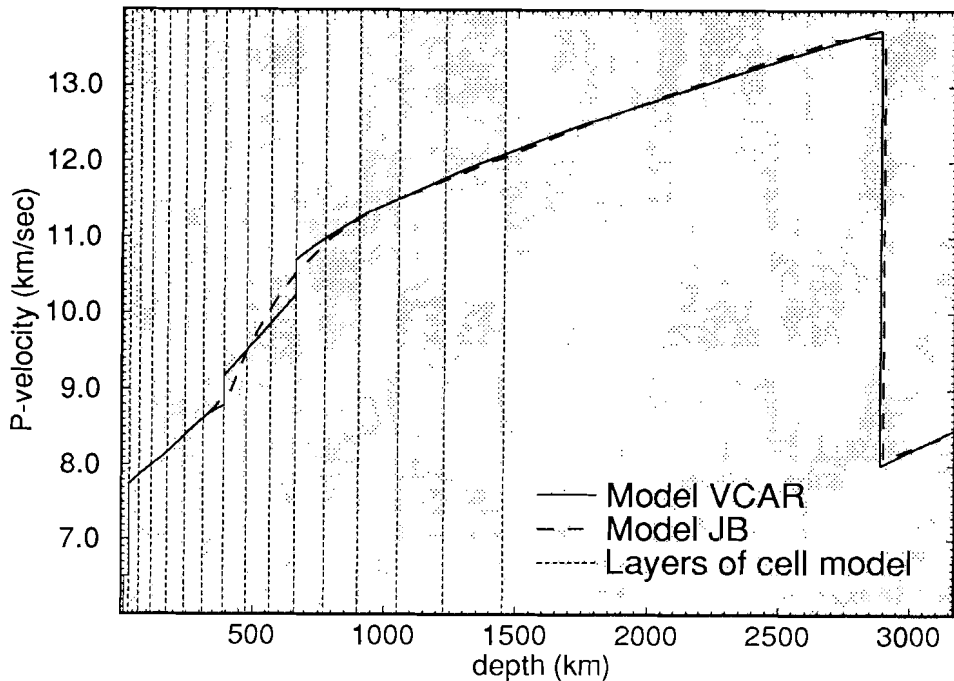


Figure 1.5. Reference models of seismic velocities and outlines of the layer boundaries of the cell model.

source and are received at distant stations. For example, if information is to be obtained about the lower mantle structure from data of compressional waves that travel directly from hypocenter to seismological stations, a minimum distance between epicenter and station of approximately 3,000 km is required. In this study, more than 2,500 stations contributed to the data set: 939 stations are located inside the investigated area (Figure 1.4a), and 1566 outside the area (Figures 1.4b and 1.4c). See section 1.6 for information about the number of observations at these stations.

### 1.5.2 The reference model of seismic velocities

The actual trace of a ray between the earthquake hypocenter and a seismological station is determined by the three-dimensional distribution of seismic velocities in the Earth. However, the true propagation velocity of compressional waves in the mantle is not known: the determination of the variations in seismic velocities in the mantle is the very purpose of the tomographic investigation. In fact, the need to know the solution of the tomographic problem in terms of seismic velocities in order to compute the ray geometry necessary to carry out the tomographic investigation, makes the problem non-linear and difficult to solve. Fortunately, the non-linearity can be removed and the tomographic problem can be represented by a system of linear equations (1.1) which can be solved by relatively simple algebraic techniques.

For the computation of both the ray geometry and the theoretical travel times, the actual aspherical Earth can be approximated with a one-dimensional reference model of seismic velocities. Mathematically, the tomographic problem is then linearized around the reference model. The choice of an appropriate one-dimensional reference model to replace the true velocity model of the Earth is very important in seismic tomography, because the reference model controls all three elements  $A$ ,  $x$  and  $d$  of the basic equation (1.1): it determines the geometry of the rays between sources and receivers, it is used to compute the theoretical travel times which are subtracted from the observed travel times to give the delay times ( $d$ ), and it serves as a reference velocity model relative to which a solution  $x$  is sought. In Figure 1.6 two examples of one-dimensional models of seismic  $P$  velocities are given. The dashed line denotes the global JB velocity model. The solid line represents a regional model of compressional velocities, which is assumed to better describe the one-dimensionally averaged seismic velocities in the mantle below the Caribbean area and South America. This model of the Velocities below the CARibbean, hereafter referred to as model VCAR, is a result of the study presented in this thesis. I used VCAR as a reference model in this tomographic investigation. The most important differences between the JB model and VCAR occur at depths near 400 and 670 km: JB velocities vary rather smoothly with depth, whereas VCAR is characterized by first order discontinuities at depths of 390 and 660 km.

### 1.5.3 The seismic waves considered in this tomographic investigation

For a given spatial distribution of earthquakes and seismological stations, the effective sampling of mantle regions depends on the type of the seismic waves considered in the tomographic investigation. In most recent tomographic investigations with body waves, only the direct  $P$  waves have been considered. Using data of direct  $P$  waves, which are compressional waves that travel directly from the earthquake hypocenter to the seismological station, has the advantage that a large number of data is available, and that reading errors in the arrival times are small compared the reading errors of compressional waves that arrive later at the station. The disadvantage of the direct  $P$  wave in sampling of mantle structure is that shallow velocity structures between source and receiver do not contribute to the seismogram observed in a station.

In the absence of stations or earthquakes in a particular area, information about shallow structures can be obtained from analyses of travel times of seismic phases that are reflected at the Earth's surface in such an area. Examples of such waves include the later arriving depth phase  $pP$ , which travels initially upward from the hypocenter and is reflected at the Earth's surface near the epicenter, and the  $PP$  phase, which travels initially downward from the source and is reflected at the Earth's surface approximately half way between the epicenter and the recording station.

### 1.5.4 Discretization of the investigated Earth volume: the cell model

The relation between the ray geometry, the elements of matrix  $A$ , and the solution vector  $x$ , depends on the parameterization of the tomographic problem. Here, I have subdivided the

Table 1.1. Layers of reference model VCAR

layer number	depth range [km]	mean velocity VCAR [km/sec]
1	0 - 33	6.064
2	33 - 85	7.827
3	85 - 130	7.973
4	130 - 185	8.124
5	185 - 245	8.305
6	245 - 312.5	8.512
7	312.5 - 390	8.710
8	390 - 475	9.336
9	475 - 565	9.680
10	565 - 660	10.044
11	660 - 760	10.826
12	760 - 875	11.080
13	875 - 1000	11.322
14	1000 - 1150	11.542
15	1150 - 1325	11.792

mantle under investigation in a large number of blocks (Figure 1.7). For every ray between hypocenter and seismological station the transection of the ray trace through the block model is computed. The lengths of the ray segments in particular blocks of the model form the principal elements of the matrix  $A$ . In each block a velocity perturbation relative to the reference model is sought by solving the linear system of equations (1.1) [see Spakman and Nolet, 1988; Spakman, 1988]. The structure of the velocity perturbations in the mantle below the Caribbean is presented by horizontal and vertical cross sections through the block model.

The geographical reference frame of the block model is rotated anti-clockwise over  $10^\circ$  to include the largest possible seismic region within given horizontal dimensions of the cell model. The model consists of 15 layers covering the entire upper mantle, as well as the lower mantle down to 1325 km. The thickness of the layers increases with depth: from 33 km of the top layer to 175 km of the bottom one. The layer boundaries are given in Table 1.1 together with the mean velocity of reference model VCAR relative to which a solution is sought. The layer boundaries are described by the dotted lines in Figure 1.6. The horizontal dimensions of  $1.25^\circ \times 1.25^\circ$  correspond to approximately  $140 \times 140$  km at the surface, and to approximately  $100 \times 100$  km at the bottom of the cell model. Every layer is subdivided in 50 cells in the rotated latitudinal direction, and 65 cells in the rotated longitudinal direction. The total number of blocks for which a solution is sought is 47,850. Within a single block the velocity is considered constant.



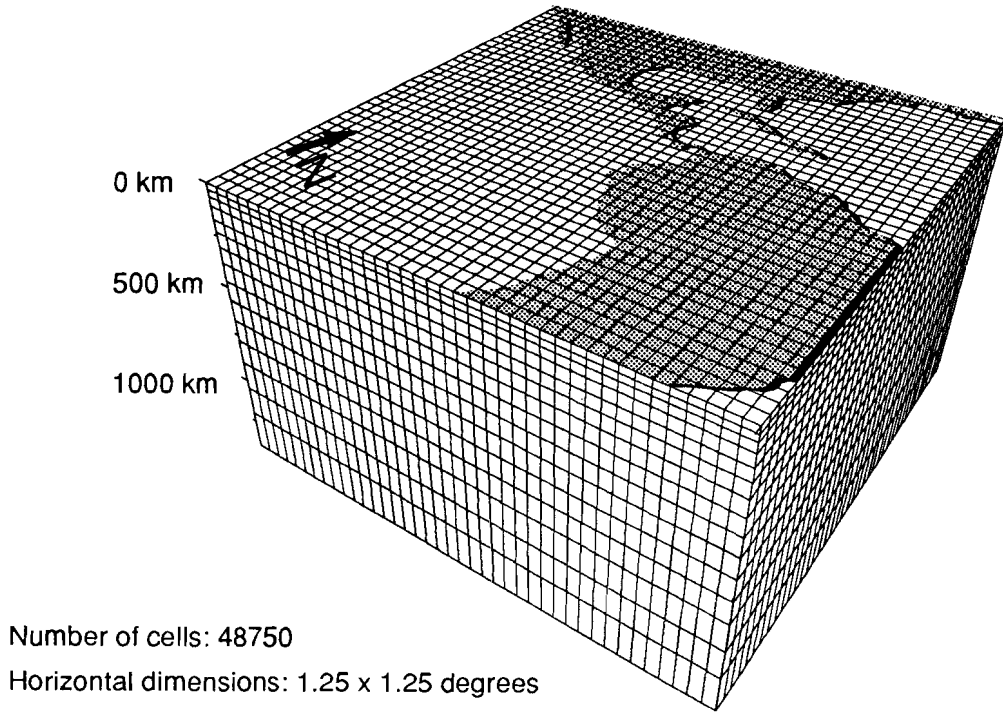


*Figure 1.6.* The block model used to discretize the mantle below the Caribbean region and a large part of South America. The model consists of 15 layers of 3,250 blocks each (50 in longitudinal direction, 65 in latitudinal direction).

## 1.6 The data set

The largest source for the  $P$ ,  $PP$ , and  $pP$  delay-time data used in this tomographic investigation are the Bulletin tapes (Jan 1964 - Jun 1985) of the International Seismological Centre (ISC). This data set was enlarged by the addition of  $P$  phase data obtained from the National Earthquake Information Center (NEIC) of the U. S. Geological Survey in Golden (CO, U.S.A.) (Jul 1985 - Jul 1987). Analog WWSSN and Canadian Station Network records were used for the implementation of  $PP$  waves in this investigation.

### 1.6.1 Data selection

In this section, I address the principal selection criteria for the  $P$  delay times. The incorporation of  $PP$  and  $pP$  waves in the tomographic investigations is one of the subjects of this thesis and the data of these phases are not discussed here.

During an initial stage of the computations  $P$  waves were kept with delay times with absolute values below 7 sec. However, for all the results presented in this thesis,  $P$  delay

times in the time interval  $[-5, +5]$  sec were considered. As discussed previously, an other important selection criterion for the selection of  $P$  data is, that delay times from at least 10 different stations should be available for each earthquake. Earthquakes with less registrations are rejected early on in the data processing. With this selection criterion a data set results with nearly 800,000 delay times. Three additional criteria were used to refine this data set further. Firstly, data of an earthquake were discarded when the absolute value of the mean travel-time residual for that particular event exceeded 1.6 sec, or if the rms of delay times reported for that earthquake was larger than 4.5 sec. Secondly, data associated with rays that did not transect the cell model between the hypocenter and the station were discarded. Thirdly, some data were rejected because of the failure to compute the correct ray path from source to receiver. With these criteria, the final canonical data set consists of approximately 650,000  $P$  delay times. These data were obtained from 2505 stations: 936 inside the cell model (with over 310,000 registrations) and 1566 outside the cell model (which reported more than 350,000 delay times).

Similar to Spakman [1988] and Spakman and Nolet [1988], I considered composite rays and averaged up to five ray paths and corresponding data from small clusters of earthquakes to small clusters of stations. An important effect of this procedure is the reduction of random noise relative to signal in the data [also Spakman and Nolet, 1988]. This "clustering" operation reduced the number of rays and corresponding delay times from approximately 650,000 to 331,273. The total number of 331,273 data used to solve the tomographic problem (1.1) represents some tens of thousands of earthquakes (the exact number is lost during data processing) occurring in 8506 hypocenter clusters. I show the distribution of the delay times that were used in this investigation in Figure 1.7. These delay times are determined relative to the reference model VCAR.

### 1.6.2 Hypocenter relocation and corrections to the delay time data

With regard to the time corrections to be applied to the delay times a distinction can be made between general corrections applied prior to the computations necessary to solve the tomographic problem, and corrections which form part of the solution of the problem.

At an early stage of the data processing, I corrected the delay times for the elevation of the stations. For the region under investigation this is important, because many stations are located at high elevations. For example, the station LPB (La Paz Bolivia) with nearly 12,000 registrations has an elevation of over 3200 meter. I also corrected the delay times for the Earth's ellipticity according to the formulae of Dziewonski and Gilbert [1976]. In contrast to the ellipticity correction applied by the ISC [Jeffreys-Bullen, 1967], the correction of Dziewonski and Gilbert allows for non-zero focal depths.

The locations of hypocenters and origin times of the earthquakes used in this study are determined at the ISC with the JB reference model of seismic velocities. Errors in earthquake location and origin time and the effects of aspherical structure on the four hypocentral parameters may contaminate the seismic velocity part of the solution. Therefore, a small trade-off between seismic velocities and changes in hypocentral parameters is allowed [Spakman and Nolet, 1988]. To do this, relocation coefficients are

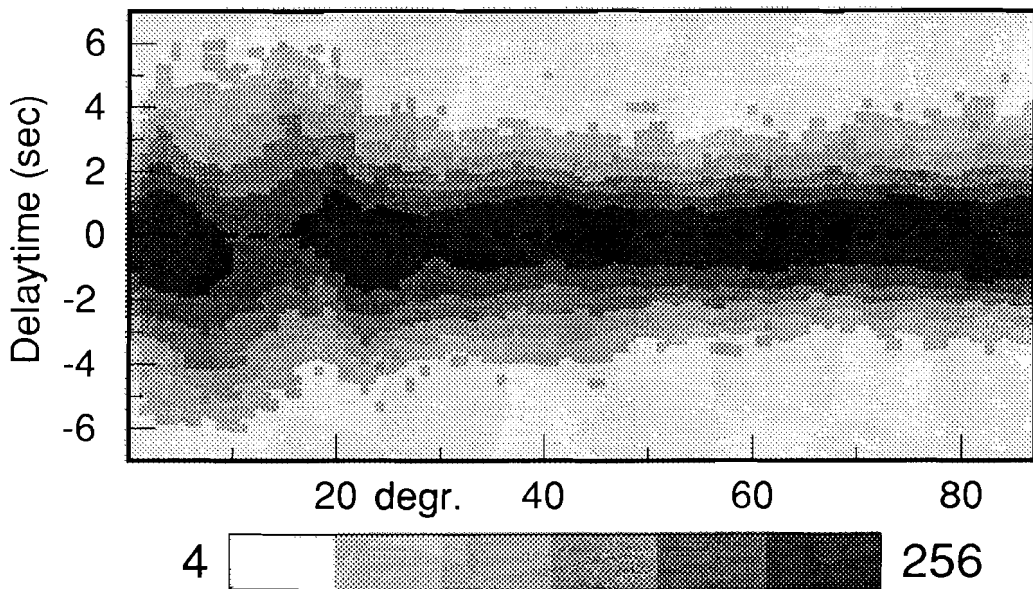


Figure 1.7. The distribution of travel time residuals relative to reference model VCAR versus epicentral distance from source to receiver. The number of delay times that contributed to this distribution is 331,273.

computed prior to solving (1.1). With these coefficients, which form part of the matrix  $A$ , the computation of the effects on the delay times of changes in hypocentral parameters is carried out during the tomographic inversion. The relocation vector is part of the solution vector  $x$ . I remark that the physical location of the hypocenter is not changed, and the ray path is not adjusted to the "relocated" source. Every relocation involves four unknowns to adjust for three spatial and one time parameter. To reduce the number of unknowns, the relocation parameters are not computed for individual earthquakes, but the same relocation parameters are assumed for all earthquakes within a particular cluster. With 8506 clusters of earthquakes, this adds over 34,000 unknowns to the tomographic system (1.1).

Another problem is, that part of the delay time may have been acquired along ray segments outside the cell model. Therefore, a correction has to be made for stations that are located outside the employed cell model. All hypocenters considered in this study are located within the cell model. For 706 stations outside the model I corrected the delay times (324,263 in total) with the known station corrections of Dziewonski and Anderson [1983]. This correction is assumed to absorb the effects on the delay times of the aspherical upper mantle structure outside the cell model. To adjust for effects of lower mantle structure outside the model, and for stations for which no Dziewonski and Anderson correction is available, an additional correction is computed during inversion for all stations outside the cell model [see Spakman, 1988]. This adds 1566 unknowns to the system of (1.1).

In conclusion, in this tomographic investigation a solution is sought for over 84,300 unknowns (48,700 velocity perturbations, 34,000 earthquake relocation parameters, and 1566 station corrections), using information of approximately 650,000 observed travel times, which are condensed to over 331,000 equations. The matrix  $A$  of (1.1) thus consists of 331,000 rows, and approximately 84,300 columns.

## 1.7 Formulation of scientific problems and organization of this thesis

The principal question to be answered in this thesis is whether or not high resolution images can be obtained of the aspherical mantle structure below the Caribbean region with the method of seismic delay-time tomography. Closely related to this question is whether the tomographic method that employs  $P$  delay-time data as published by the ISC can be improved with the objective to increase the reliability of the tomographic images.

Results of preliminary investigations suggested that important features in the tomographic images are influenced significantly by shortcomings of the used reference model. In chapter 2, I therefore investigate the importance of the choice of a reference model of seismic velocities. I show that the use of a model that inadequately describes the average spherical Earth model of seismic velocities below the region under study gives rise to serious artifacts in the tomographic images. In particular, these artifacts effect the images of structure near the transition from upper to lower mantle and may result in erroneous interpretations. In chapter 2, I derive a new reference model for the mantle below the Caribbean and show how the ISC delay times can be corrected relative to the new model, and how the reference model artifacts are reduced.

If only direct  $P$  waves are considered in tomographic investigations, shallow mantle structures below intraplate regions are often poorly resolved. These structures may be sampled more adequately by  $PP$  and/or  $pP$  waves. In chapter 3, I investigate whether the ray paths and travel time residuals of the later arriving  $PP$  and  $pP$  waves can be incorporated in the tomographic method. I address the presumably larger errors in the delay times of these phases, discuss the benefits and the disadvantages of conventional differential travel-time studies, and show that the incorporation of the  $PP$  and  $pP$  phases improves the quality of tomographic images.

A brief outline of the geological and tectonical setting of the Caribbean region is given in Chapter 4. In chapters 5 and 6, I present results of the tomographic investigation of the aspherical mantle structure below the Caribbean region. The aspherical structure is presented by variations in the propagation velocity of compressional waves in the Earth's mantle. For the results presented in these chapters we used  $P$ ,  $PP$ , and  $pP$  delay time data, and assumed the  $P$  velocity model VCAR as a reference model.

In chapter 5, I focus on the description of velocity anomalies which are relevant for the tectonics of the region, and address the reliability of the images resulting from the tomographic investigation. I show that at shallow depths the aspherical structures is well resolved only below plate boundary zones, that the resolution of structure between approximately 390 and 660 km low, and that lower mantle structures are very well resolved.

In chapter 6, I discuss the mantle structures below Middle America, the Lesser and Greater Antilles, and the northwestern part of South America in more detail. By means of cross sections through the three-dimensional mantle structure of variations in seismic velocities below the Caribbean region, I demonstrate the existence of velocity anomalies that can be associated with subduction at the Middle America trench and below the Lesser Antilles arc. The tomographic images show that the imaged aspherical structure below the Caribbean region is not restricted to the upper mantle. I discuss the aspherical lower-mantle structure, and emphasize the relations between the images of upper mantle and lower mantle anomalies. Evidence from the tomographic images for underplating of the Caribbean Plate below the northwest South America is provided.





## *Chapter 2*

# **Importance of the reference model in linearized tomography**

### **2.1 Introduction**

In the past decade, tomographic studies have provided us with images of the three-dimensional structure of the Earth's interior [e.g., Nolet, 1987]. Body wave data have been used in regional [e.g., Hirahara, 1981; Grand, 1987; Spakman et al., 1988; Zhou, 1988] and global (lower mantle) studies [e.g., Dziewonski, 1984]. In these investigations the non-linear problem of travel time inversion is linearized using Fermat's Principle (FP), leading to a description of the tomographic problem relative to a reference model of seismic velocities. The reference velocity model determines the source locations, delay times and, together with the distribution of earthquakes and seismological stations, the ray geometry, and thus the system of equations representing the tomographic problem. The assumptions underlying the application of FP impose restrictions on the reference model and may cause the inversion results to be biased towards this reference model.

Notwithstanding the obvious importance of the reference model, usually little attention is paid to the choice of a proper model. In this chapter we emphasize the influence of the reference model on images resulting from linearized tomographic inversions and introduce a proper reference model for the investigation of Caribbean mantle  $P$ -velocity structure.

Parts of this chapter are published as:

Van der Hilst, R. D., and W. Spakman, Importance of the reference model in linearized tomography, *Geophys. Res. Lett.*, 10, 1093-1096, 1989.

With data errors, poor ray coverage, model discretization, and numerical approximations [Spakman and Nolet, 1988; Spakman et al., 1989] choice of an inappropriate reference model may lead to artifacts in the image and it is important to distinguish between these and the "true" velocity perturbations. Reference model artifacts are illustrated by new results from a tomographic investigation of the  $P$  velocity structure of the mantle beneath the Caribbean region.

## 2.2 Linearization and reference model: assumptions and implications

In delay time tomography we invert delay times for estimates of the slowness deviations  $\Delta s(\mathbf{r})$  of the actual Earth's slowness field  $s(\mathbf{r})$  with respect to a reference slowness model  $s_o(\mathbf{r})$ . The delay time can be defined as the difference between the observed travel time  $T$  and the reference travel time  $T_o$ , which is computed from the reference model  $s_o$ . Representing travel time by a ray integral we can write for delay time  $d$ :

$$d = T - T_o = \int_{L(s)} s(\mathbf{r}) d\mathbf{l} - \int_{L_o(s_o)} s_o(\mathbf{r}) d\mathbf{l}_o \approx \int_{L_o(s_o)} \Delta s(\mathbf{r}) d\mathbf{l}_o \quad (2.1)$$

where  $L$  is the actual (unknown) ray path and  $L_o$  the ray path in the reference model. In linearized delay-time tomography Fermat's Principle (FP) is applied to the first integral of (2.1). FP states that small perturbations in ray path  $L$  lead to a second-order error in  $T$ . In linearized tomography this second-order error is neglected and  $L(s)$  can be replaced by  $L_o(s_o)$ . The delay time  $d$  is now linearly related to the unknown slowness anomaly field  $\Delta s(\mathbf{r})$ . Note that we implicitly assumed that the true source and station locations are known. In a more subtle derivation of (2.1) additional source mislocation and station correction terms appear on the right hand side [e.g., Spakman, 1988]. In our tomographic inversions these extra terms are included. For a discussion about algorithms commonly used to solve the linear system of equations we refer to Nolet [1985] and Spakman and Nolet [1988].

In the present chapter, we qualitatively discuss the choice of the reference model and whether second-order effects due to ray bending can be neglected. If published residual times are used, we are not free in our choice of a reference model but have to adopt the velocity structure used for the computation of the data. ISC delay times (published in monthly Bulletins of the International Seismological Centre), which are widely used in tomographic studies, are computed relative to the Jeffreys-Bullen travel-time tables [Jeffreys and Bullen, 1940]. The JB velocity structure (dashed curve in Figure 2.1a) is therefore often used as a reference model in tomographic inversions. It is a global model, averaging velocity structures of continental and oceanic, and tectonically active and stable areas. The JB model lacks a low velocity layer and first order discontinuities in the upper mantle. Using ISC delay times we compute the ray geometry in the JB model. Some JB ray paths are plotted in Figure 2.1b. For comparison, also PREM-model ray paths are plotted.

When we apply FP to linearize the inversion problem, we implicitly assume that the reference ray paths are close to the ray paths in the true Earth. From Figure 2.1b we infer that in the lower mantle, JB and PREM ray paths are close to each other. In the upper

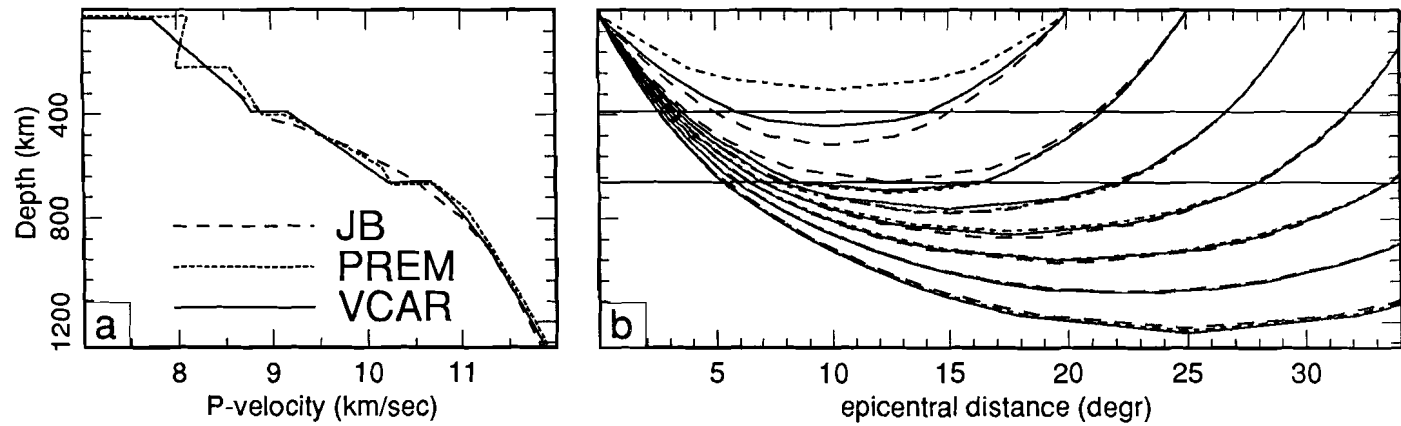


Figure 2.1. Differences between the global JB, PREM models, and the regional VCAR velocity structure. b: Geometry of rays in JB, VCAR and PREM arriving at epicentral distances of 20° to 50°, with 5° intervals.

mantle, however, distances between JB and PREM ray paths may be as large as 100 km, mainly due to the presence of seismic discontinuities in the latter model [also Zielhuis et al., 1989]. Note that in regional tomographic studies, cell dimensions are typically of the order of 100 km [Hirahara, 1981; Spakman 1988; Zhou, 1988]. Differences between JB and, e.g., PREM can be considered indicative of differences between velocity structures in different parts of the Earth mantle. Therefore, for a particular tomographic problem, the choice of a model that appropriately describes the average Earth is important, because usage of an inadequate model may lead to

- substantial differences between true and reference rays, resulting (1), in non-linear effects which may be too strong to justify the neglect of second order terms in the derivation of (2.1), and (2), in mapping of anomalies at incorrect locations
- mapping of velocity anomalies relative to incorrect reference velocities.

### 2.3 Derivation of a new reference model

Can the global JB model adequately be used as a reference model for the mantle below the Central American region? An important indication that JB may not be the most appropriate model for this study is given by the data set itself. In our tomographic study we use ISC data (1964 - June 1985) and an additional set of NEIC data (July 1985 - July 1987). The distribution of delay times versus epicentral distance is given in Figure 2.2a. We note that if the JB model were an adequate description of the average mantle structure of the area under investigation, we would expect the data to be evenly distributed around the line  $delay = 0$ , marked by the horizontal dashed line. From Figure 2.2a we infer, however, systematic deviations with epicentral distance. The observation that, at particular distance intervals, body waves arrive systematically before or after the computed JB travel time, indicates that the JB velocity structure deviates from the average one-dimensional velocity profile in the true Earth [Fukao, 1977 (Figure 15); Zielhuis et al., 1989]. This suggests that, for our regional tomographic study, we can improve on JB as reference model. Instead of using another global model, like PREM, we modified existing  $P$ -velocity models [Jeffreys-Bullen, 1940; Burdick, 1981; Dziewonski et al., 1975] with the objective of removing the mentioned trends in the data. We remark that, in contrast to Grand [1987], we use one reference model although the investigated region comprises both tectonic stable and active areas. We maintained JB for shallow depths and, consequently, we did not consider a low velocity zone. We computed travel times from updated models, reduced these times relative to the Jeffrey-Bullen tables, and matched the trends in the data with the resulting reduced travel-time curves [Zielhuis et al., 1989]. By trial and error we arrived at model VCAR (Figure 2.1a), the reduced travel-time curve of which is given in Figure 2.2a. The VCAR  $P$ -velocities as function of depth are given in Table 2.1. In the reduced travel-time curve we recognize triplication branches, between  $14^\circ$  and  $28^\circ$  epicentral distance, due to large gradients or discontinuities in the upper-mantle velocity structure (Figure 2.1a and Table 2.1). Part of the spreading in ISC data in this distance range is due to picking (later) arrivals, associated with these triplications, which may have larger amplitudes than first arrivals. As a consequence, reading errors are not random. The trends for distances

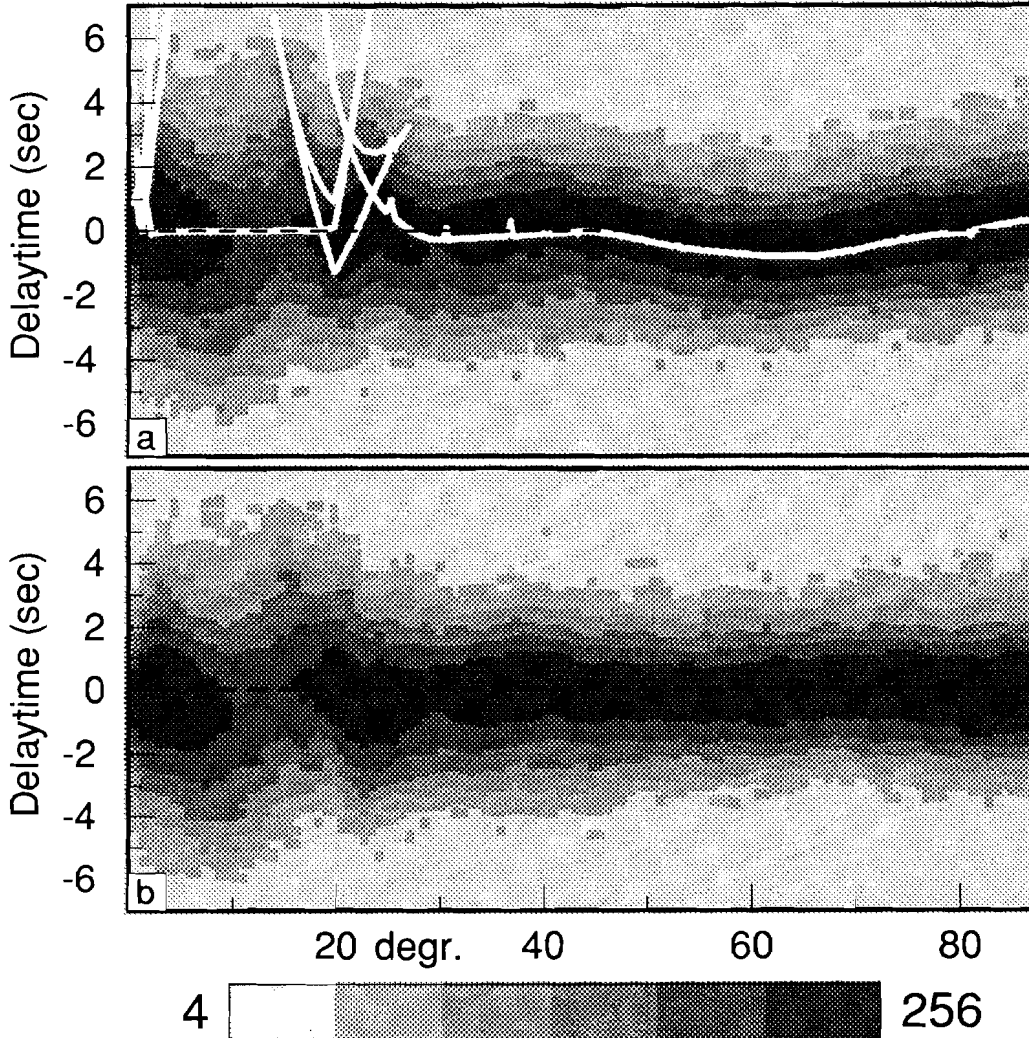


Figure 2.2. a: Distribution of original ISC/NEIC (1964-1987) vs. epicentral distance. The white curve marks the difference between JB and VCAR travel time. b: Distribution of delay times corrected relative to model VCAR. The scale is logarithmic. Note the effect at distances beyond  $30^\circ$ , while the difference between JB and VCAR is small for the mantle below 800 km (Figure 1a).

beyond  $30^\circ$  are well fitted by the reduced travel-time curve of VCAR.

Subsequently, with the ray geometry computed in the new model, the ISC/NEIC delay times (Figure 2.2a) were corrected relative to the new reference model VCAR (see Appendix 2A). These corrections are of the same order of magnitude as the values of delay times used in the inversion. The distribution of the delay times relative to VCAR is shown in Figure 2.2b. Evidently, for epicentral distances exceeding  $30^\circ$ , a substantial part of the

Table 2.1:  $P$  velocity structure: model VCAR

radius [km]	depth [km]	$v_P$ [km/sec]	radius [km]	depth [km]	$v_P$ [km/sec]
6371.0	0.0	5.570	4500.0	1871.0	12.632
6356.0	15.0	5.570	4400.0	1971.0	12.747
6356.0	15.0	6.500	4100.0	2271.0	13.093
6338.0	33.0	6.500	4000.0	2371.0	13.203
6338.0	33.0	7.750	3900.0	2471.0	13.314
6300.0	71.0	7.863	3700.0	2671.0	13.529
6274.6	96.4	7.940	3600.0	2771.0	13.635
6240.0	131.0	8.044	3500.0	2871.0	13.726
6211.2	159.8	8.130	3485.7	2885.3	13.726
6180.0	191.0	8.228	3485.7	2885.3	8.002
6147.9	223.1	8.330	3400.0	2971.0	8.150
6084.5	286.5	8.540	3300.0	3071.0	8.317
6040.0	331.0	8.670	3200.0	3171.0	8.477
5981.0	390.0	8.790	3100.0	3271.0	8.630
5981.0	390.0	9.170	3000.0	3371.0	8.777
5950.0	421.0	9.290	2900.0	3471.0	8.917
5900.0	471.0	9.490	2800.0	3571.0	9.050
5875.0	496.0	9.586	2600.0	3771.0	9.295
5750.0	621.0	10.078	2400.0	3971.0	9.514
5711.0	660.0	10.230	2200.0	4171.0	9.706
5711.0	660.0	10.690	2000.0	4371.0	9.871
5650.0	721.0	10.860	1800.0	4571.0	10.009
5577.4	793.6	11.030	1600.0	4771.0	10.120
5450.7	920.3	11.300	1400.0	4971.0	10.204
5323.9	1047.1	11.499	1300.0	5071.0	10.236
5197.2	1173.8	11.696	1217.1	5153.9	10.258
5100.0	1271.0	11.844	1217.1	5153.9	11.091
5000.0	1371.0	11.989	1200.0	5171.0	11.096
4900.0	1471.0	12.123	1000.0	5371.0	11.140
4800.0	1571.0	12.257	600.0	5771.0	11.205
4700.0	1671.0	12.384	300.0	6071.0	11.232
4600.0	1771.0	12.513	0.0	6371.0	11.241

ISC/NEIC delay-time values is explained by the difference between the JB and VCAR lower-mantle structures and need thus not be explained in terms of lateral heterogeneities.

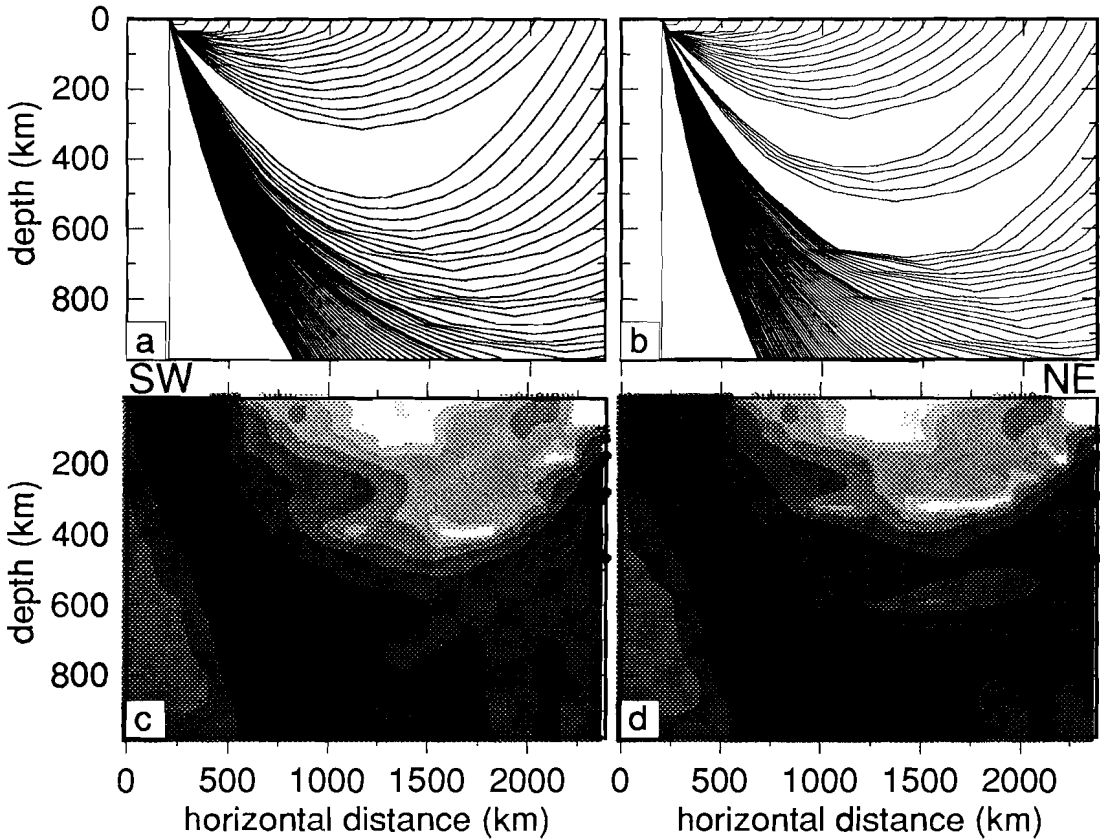


*Figure 2.3.* Inhomogeneity in ray distribution due to presence of strong velocity gradients, or discontinuities, in the upper mantle velocity structure of reference models JB and VCAR. a: Geometry of rays in the JB model. b: Geometry of rays in the VCAR model. c: Vertical section through 3D model of cell hit count (section 4.3.2) across the Gulf of Mexico. For location of the section, see Figure 2.4. The scale used for contouring of the hit count values is 10-logarithmic, with power increments of 0.5. d: Same, for model VCAR. Note the resemblance between features of low cell hit-count in Figures c and d, and the "gap" in Figures a and b.

Although the data between  $14^\circ$  and  $28^\circ$  are corrected, the previously mentioned triplication branches are not removed, because in the correction procedure we could not distinguish between first arrivals and later arrivals associated with triplications. The correction of ISC data relative to VCAR reduced the data variance, prior to inversion, with 10%. We note that, in the present study, ISC-reported hypocentral parameters are used, which are determined in the JB velocity structure. Ideally, the hypocenter should be relocated in the new reference model. This will be done in future investigations [personal communication, E.R. Engdahl, USGS, 1990]. In Appendix 2A, we derive an expression for the relocation part of the tomographic inversion. The error in the delay time due to taking the ISC



hypocenter instead of the hypocenter in the new reference model, is of second order.

VCAR ray paths are shown in Figure 2.1b. Note that differences between JB and VCAR ray paths are of the order of 100 km. We assume that VCAR ray paths are closer to the true ray paths than the JB rays and that the non-linearity of the inverse problem is smaller than in the case of the JB model. However, we have to realize that, with the presumably more realistic ray geometry of model VCAR, Earth structure within the cell model is sampled more irregularly than is the case when JB is used. This is illustrated by Figure 2.3. Figure 2.3a shows schematically the geometry of seismic rays in the JB model, computed for a surface focus. The strong gradient in the JB velocity structure near 400 km (Figure 2.1a) causes the absence of ray paths, associated with first arrivals, with turning points just above that depth. *P* phases corresponding to the receding branch of the triplications have turning points in this "gap", but these phases are not considered in our study. Consequently, depth resolution will be low in upper mantle regions just above discontinuities. The ray paths computed in model VCAR show sparsely-sampled mantle regions just above the 400 and 660 km discontinuities (Figure 2.3b). The effects of strong gradients in the reference velocity structure are reflected in the cell hit count (the number of rays crossing a particular cell of the model of Figure 1.6 (see also section 4.3.2)). In Figures 2.3c and 2.3d this is demonstrated, both for the JB and the VCAR model, with a cross section through the mantle below the Gulf of Mexico. Because of the absence of intraplate earthquakes and seismological stations in the Gulf of Mexico, cell hit count is low at shallow depths below this region, just above 400 km in the JB image (Figure 2.3c), and above 400 and 670 km in the VCAR image (Figure 2.3d). The low hit count in the mentioned upper mantle regions indicate inadequate sampling of structure by direct *P* waves, which is important in discussions of the spatial resolution.

## 2.4 Application to the mantle below the Caribbean region

In our tomographic study, the mantle below Central and South America is discretized into 48,750 cells with constant horizontal dimensions of  $1.25^\circ$  by  $1.25^\circ$  and vertical dimensions increasing from 33 km (top) to 225 km (bottom). Together with relocation parameters and station corrections, we solved for nearly 80,000 unknowns. We only considered earthquakes ( $m_b > 2$ ) which were recorded at at least ten stations (see chapter 1). This resulted in a data set of 700,000 ISC/NEIC delay times. All tomographic images to be discussed in this chapter are obtained after 20 iterations. The inversions are slightly damped and the solutions smoothed (for details about the inversion scheme, see Spakman and Nolet [1988]). To investigate the effect of the reference model on tomographic images we performed two computations: in one, we used the original ISC/NEIC data (Figure 2.2a) and the JB ray geometry; in the other, the corrected data (Figure 2.2b) and VCAR ray geometry were used. Hereafter, the two inversions are referred to as JB and VCAR inversions, respectively. We illustrate the influence of the reference model with two mantle cross sections through the 3D velocity structure, the locations of which are given in Figure 2.4.

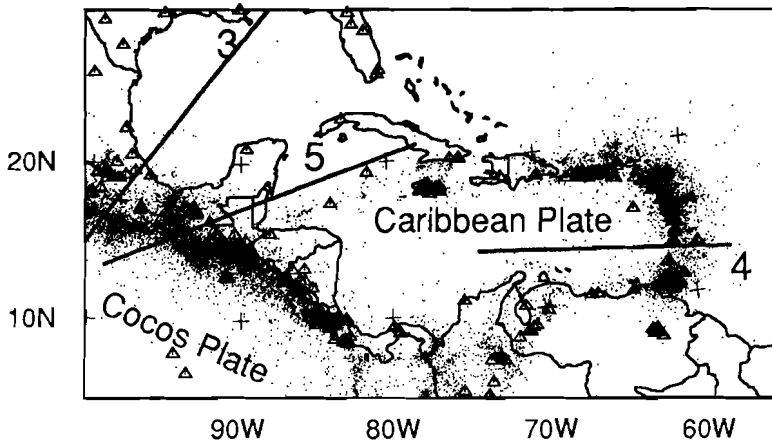
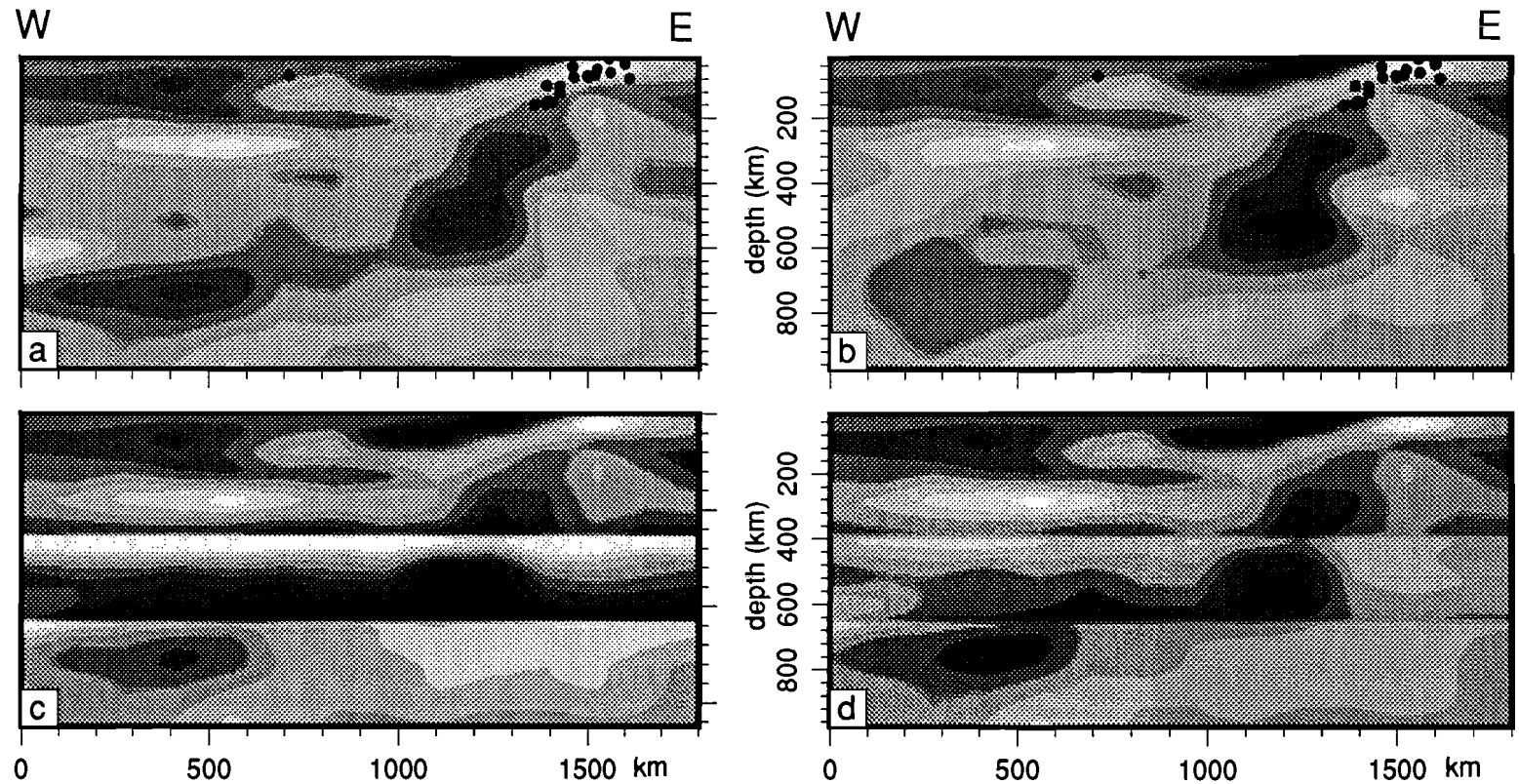


Figure 2.4. Location of the cross sections as discussed in the text. The numbers 3, 5 and 6 relate to corresponding Figures.

Figure 2.5a represents the result of the JB inversion for a section across the Lesser Antilles arc. The most striking feature in this image is the high velocity structure dipping steeply from the top of the model to a depth of about 600 km, although the seismic zone is restricted to the upper 200 km. This structure may be interpreted as the (blurred) image of the subduction of the Atlantic Plate below the eastern part of the Caribbean Plate. Near the transition between upper and lower mantle, the dip decreases and the high velocity anomaly changes to a subhorizontal position. The apparent continuation and flattening of the velocity structure in this image may give rise to erroneous interpretations with regard to mantle dynamics. Figure 2.5b shows the result of the VCAR inversion for the same section. This result does not show the continuation and flattening of the high velocity structure associated with the subduction zone as was suggested by the JB image.

The left hand side of the JB image (Figure 2.5a) suggests an alternation of layers with velocities lower and higher than the JB reference model at a depths of about 670 km. Just above this depth level low velocities are visible whereas just below this interface high velocities (relative to JB) can be seen. Similar features are present in tomographic images of Zhou [1988, e.g. Figure 2.5b] and Spakman et al. [1989]. The alternation can be understood by studying the differences between the velocity structures given in Figure 2.1a. Compared with model VCAR, JB velocities are higher just above the discontinuity and lower just below. The suggested stratification of the upper mantle are images of these discontinuities. Using the updated reference model, we were able to remove features in the images that can be attributed to the inadequacy of the JB model as a one-dimensional starting model for this particular area. Below the Caribbean Plate the 400 km discontinuity is not recovered. Due to poor ray coverage this part of the model is hardly illuminated by seismic rays, resulting in poor resolution. Recall that not only the velocity perturbations are displayed relative to model VCAR, but the data set and ray geometry, used in the inversions, differ as well.



*Figure 2.5.* Vertical mantle cross section across the Lesser Antilles arc. For the scale key used in this graph see Figure 6. The dots in the upper right corner represent earthquake hypocentra. a: Result of JB inversion. b: result of VCAR inversion. c: Image resulting after addition of differences between JB and VCAR velocities to the JB solution (Figure a). d: Same, but difference between JB and VCAR is multiplied with the model fit (see chapter 5).

If the non-linear effects of ray geometry and mapping of anomalies at incorrect locations were negligible, we should be able to obtain the image in Figure 2.5b from Figure 2.5a by simply computing the JB solution relative to the VCAR velocity model. Adding the JB model velocity values to the JB perturbations, and subtracting the VCAR velocities (see Appendix 2A), results in the image of Figure 2.5c. The image of Figure 2.5c is predominated by the upper mantle discontinuities. This predominance, and absence of images of upper mantle discontinuities in large parts of Figure 2.5a, can be explained in terms of amplitude recovery and spatial resolution in the tomographic images. To obtain Figure 2.5c, we considered 100% of the velocity differences between JB and VCAR. In contrast, the tomographic inversion only recovers part of the amplitudes of the velocity structure, because of damping, smoothing, event relocation [Spakman, 1988] and because of poor resolution of shallow structures below the Caribbean Plate (chapter 5). Resolution aspects can be taken into account by scaling the JB and VCAR velocities with the synthetic model fit, and adding the difference between the scaled velocity values to the JB solution. The synthetic model fit is the correlation between a known input model and the inversion response to this model [Spakman and Nolet, 1988], see also chapter 5 of this thesis. The result of this scaling is given in Figure 2.5d. It is interesting to note that in several parts of Figure 2.5d, the image shows resemblance with the result of the VCAR inversion. For example, the amplitude of the high velocity structure between 1000 and 1500 km at a depth of 500-600 km (increased relative to the JB solution), and the amplitude of the structure at a depth of 800 km and at a horizontal distance of 400 km (decreased relative to JB). Important differences still exist near the 660 km discontinuity, between 500 and 1000 km horizontal distance. Thus, we were not able to reproduce the image of Figure 2.5b by a simple linear superposition of the JB solution (Figure 2.5a) and the (scaled) velocity differences between JB and VCAR. We conclude that the effects of the corrections discussed above are not restricted to the linear domain.

The absence of the 670 km discontinuity in the JB model also affects the structures in the section across the Middle America trench (Figure 2.6). In the JB image (Figure 2.6a) the arrow points to a gap in the rather continuous zone of high velocities which extends from the surface to the bottom of the model (at a depth of over 1300 km). The low velocities we expect to image (relative to JB) just above the discontinuities (as discussed above) are superimposed on the positively valued perturbations that may be associated with a cold slab. In Figure 2.6b the VCAR image shows the velocity anomaly being almost continuous across the discontinuity, suggesting that the gap in Figure 2.6a may be regarded as an artifact of using JB to compute data and ray paths (assuming that artifacts of smoothing and resolution are the same for both sections).

## 2.5 A continuous high velocity anomaly down to lower mantle depths

The presence of anomalously high velocities in the lower mantle below the western part of the Caribbean Plate has been reported by several authors. Analyzing  $S-S_cS$  and  $P-P_cP$  differential times, Jordan and Lynn [1974] discovered strong lateral velocity gradients in the lower mantle below this region. This conclusion was confirmed by Lay [1983], Vidale

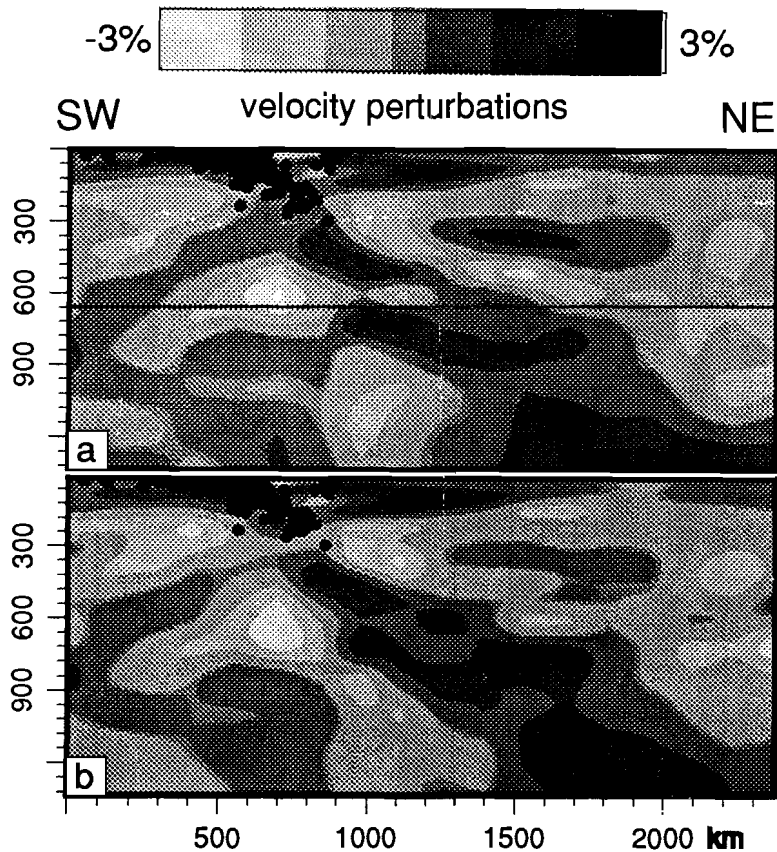


*Figure 2.6.* Vertical mantle cross section across the Middle America subduction zone. a: JB inversion. The arrow points to a gap in the velocity structure at the transition between upper and lower mantle. b: result of VCAR inversion. See text for uncertainties about resolution in the transition zone.

and Garcia-Gonzalez [1988] and Grand [1987]. Grand's tomographic inversion of S and SS delay times revealed a dipping high-velocity anomaly, continuous from the Caribbean area to the southern border of Canada, ranging from 700 to 1700 km in depth. Grand found little heterogeneity in the shear-wave velocity structure of the upper mantle.

The question whether or not the reported high velocity anomaly in the lower mantle exists, and can be continued across the transition zone (between 400 and 670 km) to the surface as suggested by Figure 2.6b, cannot be answered without analyzing the spatial resolution in the image. We inverted data derived from known velocity anomalies in order to obtain upper estimates for the resolution. Gaussian noise was added to the synthetic data. A discussion about this method is beyond the scope of this chapter and we refer to Spakman and Nolet [1988] and to chapter 5 of this thesis. The subject of resolution will be

addressed to in a separate paper about the three-dimensional structure of the Middle America subduction zone (see also chapters 5 and 6). Here we suffice with giving some conclusions. Comparison of the inversion response to synthetic velocity models with the exact model, revealed that smoothly varying anomalies are well resolved in the lower mantle part of the image and at shallow levels just below the seismic active area. Between the discontinuities, resolution is worse. With respect to the reference model we recall that: (1), the geometry of rays bottoming in the transition zone strongly depends on the velocity structure; (2), structure just above the discontinuities is poorly sampled by rays of the direct phase; and, (3), corresponding ISC data are contaminated due to misidentification of later arriving triplication phases. It is important to realize, that the resolving power of the data is assessed with a fixed reference geometry and with Gaussian noise added to the data. Thus, (1) and (3) are not taken into account in the performed synthetic tests. Moreover, due to effects of mantle discontinuities on ray geometry, results of sensitivity tests suggests lower resolution of upper mantle structures for model VCAR, than for the JB model. Obviously, from the apparently more satisfying results of sensitivity tests with JB, one can not conclude that JB would be a better reference model for our purposes. The non-linear step of computing a new ray geometry and correcting the data, prior to the final inversions, is not considered in sensitivity tests. Consequently, inversion of synthetic data does not provide additional information about possible inadequacies of the reference model, and gives upper estimates of the true resolution, in particular, for structure in the transition zone.

From Figure 2.6b it is evident that the slab-like velocity anomaly is broader in the lower mantle than in the upper mantle. This may partly be due to the use of larger cells to discretize the lower mantle. Both in the upper and lower mantle the images are blurred due to data errors, image distortion by the inversion algorithm and smoothing [Spakman and Nolet, 1988]. Also, the use of a ray geometry derived from shooting in a 1D reference model, neglecting 3D ray bending effects, may overestimate the width of the anomaly [Engdahl and Gubbins, 1987]. Consequently the width of the actual anomaly is difficult to determine and the structure may be narrower than imaged in Figures 2.5 and 2.6. We remark that absolute values of the imaged amplitudes are systematically underestimated due to smoothing, damping and event relocation [Spakman, 1988].

## **2.6 Discussion and concluding remarks**

We showed that in linearized tomographic inversions the 1D reference model plays a very important role. A substantial part of the values of ISC delay times can be explained by the use of a one-dimensional reference model different than JB. Some important features in the tomographic images can be attributed to the inadequacy of the JB model for the mantle region under study. In particular, images of structure near the transition from upper to lower mantle are sensitive to whether or not the reference model contains upper mantle discontinuities. This becomes especially important when tomographic images are used for the study of the subduction process. The change in dip of a high velocity anomaly at the base of the upper mantle, as imaged in Figure 2.5, does not necessarily mean that the

subducting slab behaves in a similar way and one should be very careful in interpreting such an observation. The flattening of the anomaly in Figure 2.5 appeared to be an artifact of the JB reference model. The effect may be enhanced if lack of resolution occurs in directions of predominant ray illumination, which causes velocity perturbations to be "smeared out" in this direction [Spakman et al., 1989]. Reference model artifacts and lack of resolution may provide alternative explanations for the feature of slab fingering in the transition zone. We remark that sensitivity tests, as described by Nolet and Spakman [1988] and Humphreys and Clayton [1990], do not give valuable information about the choice between alternative reference models.

In both examples shown, the high velocity structures extend well below the seismic zones. The occurrence of a-seismic subduction [e.g. Wortel, 1982] may have important implications for the reconstruction of the Neotectonic history of the Caribbean area.

The image across the Middle America trench confirms earlier observations of lower mantle velocity anomalies below the western Caribbean Plate [e.g., Jordan and Lynn, 1974]. However, from resolution analyses it can not unambiguously be concluded that the high velocity feature is continuous across the transition zone to the site where presently the Cocos Plate subducts beneath Middle America. The lower mantle structure may tentatively be interpreted as the image of the subducted Farallon Plate [e.g., Jordan and Lynn, 1974; Grand, 1987]. If so, the broadening of the slab below the transition zone may also be explained by advective thickening due to the increase in viscosity [Fischer and Jordan, 1988]. We have to realize, however, that tomographic images provide us with velocity perturbations and that continuity of velocity structure does not automatically mean continuity of tectonic structures. The phenomenon of thermal coupling [Nataf, 1987] may also result in a continuous high-velocity anomaly across the 670 km discontinuity and can not be excluded on basis of tomographic images only.

*Acknowledgments:* Rob van der Hilst thanks the USGS in Colorado for their hospitality and for providing NEIC data. Discussions with Roel Snieder and Alet Zielhuis, and comments by an anonymous reviewer improved the manuscript. Visiting the USGS was supported by NATO (grant 0910/87). This investigation was financially supported by the Netherlands Organization for Advancement of Pure Research (NWO). Supercomputer (C205) calculations were supported by SURF (NFS).

---

## Appendix 2A:

In this Appendix, we show that the delay time  $\delta t_1$ , corresponding to reference model VCAR can be directly obtained from the reported ISC delay time  $\delta t_o$ , which corresponds to the Jeffreys Bullen (JB) reference model. We also show that, even if we do not know the location of the earthquake in reference model VCAR, an expression can be derived in which  $\delta t_1$  is linearly related to the unknown slowness anomaly field  $s_1(\mathbf{r})$ .

With  $\mathbf{x}$  the source location,  $s(\mathbf{r})$  the slowness field, and  $L(\mathbf{x};s)$  the ray geometry, we can write for the travel times

$$\begin{aligned} T(\mathbf{x};s) &= \int_{L(\mathbf{x};s)} s \, dl, \\ T_o(\mathbf{x}_o;s_o) &= \int_{L(\mathbf{x}_o;s_o)} s_o \, dl_o, \\ T_1(\mathbf{x}_1;s_1) &= \int_{L(\mathbf{x}_1;s_1)} s_1 \, dl_1 \end{aligned} \quad (2A.1)$$

where subscripts (o) denote the hypocenter, slowness field, and ray geometry for the Jeffreys-Bullen model, and subscripts (1) refer to the new reference model VCAR. We also define the travel time computed in the new reference model, but with the source located in the JB model, as

$$T_1'(\mathbf{x}_o;s_1) = \int_{L(\mathbf{x}_o;s_1)} s_1 \, dl_1 \quad (2A.1b)$$

Given the ISC delay time  $\delta t_o$ , and the travel times in both reference models, the travel time residual for the new reference model VCAR,  $\delta t_1$  can be written as

$$\delta t_1 = T - T_1 = (T - T_o) + (T_o - T_1) = \delta t_o + (T_o - T_1) \quad (2A.2)$$

In equation (2.1) we showed how a delay time  $\delta t$  can be linearly related to the true Earth's slowness field. In (2.1) we did not consider the relocation terms, that result from the linearization and are necessary to compute the relocation vector during the tomographic inversion, and the station correction. If we include these terms in (2.1), we can formally write for the delay time in the new model,  $\delta t_1$ ,

$$\begin{aligned} \delta t_1 &= T(\mathbf{x};s) - T_1(\mathbf{x}_1;s_1) = \int_{L(\mathbf{x};s)} s \, dl - \int_{L(\mathbf{x}_1;s_1)} s_1 \, dl_1 \\ &= \int_{L(\mathbf{x}_1;s_1)} \Delta s_1 \, dl_1 + (\mathbf{x} - \mathbf{x}_1) \cdot \nabla_{\mathbf{x}_1} T_1(\mathbf{x}_1;s_1) + \Delta t + h(\mathbf{x}_1;s_1;\mathbf{x}_s) + \varepsilon_o \end{aligned} \quad (2A.3)$$

where  $\nabla_{\mathbf{x}_1} = (\delta/\delta x_1, \delta/\delta y_1, \delta/\delta z_1)$ , the gradient operator containing partial derivatives with respect to the cartesian focal coordinates of  $\mathbf{x}_1$ ,  $\Delta t$  the error in origin time, and, with  $\mathbf{x}_s$  the station location,  $h(\mathbf{x}_1;s_1;\mathbf{x}_s)$  the station correction [Spakman, 1988]. The error term  $\varepsilon_o$



contains, e.g., reading errors and second and higher order terms of approximations (Fermat's Principle, and Taylor expansion) [Spakman, 1988]. Note that in (2A.3) no assumption on the reference model is made, and the derivation by Spakman [1988] holds for any reference model (as long as conditions to apply Fermat's Principle are satisfied). The problem now arises that we do not know  $\mathbf{x}_1$ , because we only have available  $\mathbf{x}_0$ , the ISC-reported hypocenter, located in the JB model. In the derivation below we show that (2A.3) can be approximated by

$$\begin{aligned}\delta t_1 &= T(\mathbf{x};s) - T_1(\mathbf{x}_1;s_1) = \int_{L(\mathbf{x};s)} s \, dl - \int_{L(\mathbf{x}_1;s_1)} s_1 \, dl_1 \\ &= \int_{L(\mathbf{x}_0;s_1)} \Delta s_1 \, dl_1 + (\mathbf{x}-\mathbf{x}_0) \cdot \nabla_{\mathbf{x}} T_1'(\mathbf{x}_0;s_1) + \Delta t + h(\mathbf{x}_0;s_1;\mathbf{x}_s) + \epsilon_1\end{aligned}\quad (2A.4)$$

Following Spakman [1988, his equation 3], we formally write

$$\delta t_o = \int_{L(\mathbf{x};s;\mathbf{x}_s)} s \, dl - \int_{L(\mathbf{x}_0;s_o;\mathbf{x}_s)} s_o \, dl_o + \Delta t + h(\mathbf{x}_0;s_o;\mathbf{x}_s) + \epsilon \quad (2A.5)$$

where  $\epsilon$  is an error term (e.g., reading errors).

In this expression, we can incorporate the new reference model of slowness  $s_1(\mathbf{r})$  by rewriting (2A.5) as

$$\begin{aligned}\delta t_o &= \int_{L(\mathbf{x};s)} s \, dl - \int_{L(\mathbf{x};s_1)} s_1 \, dl_1 + \int_{L(\mathbf{x};s_1)} s_1 \, dl_1 \\ &\quad - \int_{L(\mathbf{x}_0;s_o)} s_o \, dl_o + \Delta t + h(\mathbf{x}_0;s_o;\mathbf{x}_s) + \epsilon\end{aligned}\quad (2A.6)$$

where the second and third ray integrals are computed in slowness field  $s_1(\mathbf{r})$  of model VCAR, but with the (unknown) true hypocenter. Following Spakman [1988], we can apply Fermat's Principle to the first integral, combine the first and second integral, and subsequently make a Taylor expansion of the combined first and second integral and of the third integral in (2A.6), around the source location  $\mathbf{x}_0$  in the Jeffreys Bullen model. If we combine  $\epsilon$  (2A.6) and the second order (and higher) terms of the Taylor expansion in  $\epsilon'$ , we rewrite (2A.6) as

$$\begin{aligned}\delta t_o &= \int_{L(\mathbf{x}_0;s_1)} (s-s_1) \, dl_1 + (\mathbf{x}-\mathbf{x}_0) \cdot \nabla_{\mathbf{x}} \left[ \int_{L(\mathbf{x}_0;s_1)} (s-s_1) \, dl_1 \right] + \int_{L(\mathbf{x}_0;s_1)} s_1 \, dl_1 \\ &\quad + (\mathbf{x}-\mathbf{x}_0) \cdot \nabla_{\mathbf{x}} \left[ \int_{L(\mathbf{x}_0;s_1)} s_1 \, dl_1 \right] - \int_{L(\mathbf{x}_0;s_o)} s_o \, dl_o + \Delta t + h(\mathbf{x}_0;s_o;\mathbf{x}_s) + \epsilon'\end{aligned}\quad (2A.7)$$

In (2A.7) we neglect the second term containing the cross multiplication of perturbations.

With (2A.1b) and (2A.2) we arrive at

$$\delta t_1 = \int_{L(\mathbf{x}_0; s_1)} \Delta s_1 dl_1 + \Delta \mathbf{x}_0 \cdot \nabla_{\mathbf{x}_0} T_1'(\mathbf{x}_0; s_1) + \Delta t + h(\mathbf{x}_0; s_0; \mathbf{x}_s) + \varepsilon_1 \quad (2A.8)$$

In (2A.7) we related  $\delta t_1$  linearly to  $\Delta s_1(\mathbf{r})$ , the slowness perturbation for the new reference model, and showed that the JB source  $\mathbf{x}_0$  can be used for the computation of the ray geometry and for the construction of the gradient operator necessary for the relocation. The station correction does not depend non-linearly on  $s_0$  and will be computed explicitly during the inversion. The same holds for  $\Delta t$ . We can thus replace  $s_0$  by  $s_1$  in the corresponding term of (2A.8). We finally write

$$\delta t_1 = \int_{L(\mathbf{x}_0; s_1)} \Delta s_1 dl_1 + \Delta \mathbf{x}_0 \cdot \nabla_{\mathbf{x}_0} T_1'(\mathbf{x}_0; s_1) + \Delta t + h(\mathbf{x}_0; s_1; \mathbf{x}_s) + \varepsilon_1 \quad (2A.9)$$

which equals equation (2A.4).



## Chapter 3

# On the use of PP and pP data in delay time tomography

### 3.1 Introduction

In recent years, many successful applications of seismic body-wave tomography have been reported. Body waves, travelling from earthquake hypocenters to seismological stations, illuminate Earth structure along their ray paths (or ray tubes). The quality of this illumination is determined by observational errors in, e.g., travel time and by the azimuthal coverage and number of rays sampling a particular region. [Spakman and Nolet, 1988; Humphreys and Clayton, 1990]. The sampling of any Earth volume by seismic rays is determined by: (1) the distribution of earthquake hypocenters and seismological stations; (2), the type of body-wave phases used in the inversions; and (3), the three-dimensional velocity structure through which these phases travel. In linearized delay-time tomography, the application of Fermat's Principle allows us to approximate the true (unknown) three-dimensional velocity structure by a (known) one-dimensional reference model of seismic velocities for computation of the ray geometry [e.g., Spakman, 1988]. In this paper, we assume a one-dimensional velocity model that is an appropriate representation of the average velocity structure of the volume under scrutiny [Van der Hilst and Spakman, 1989], and address the dependence of the ray geometry on (1) and (2).

Parts of this chapter are submitted for publication as:

Van der Hilst, R. D., and E. R. Engdahl, On the use of PP and pP data in delay time tomography, *Geophys. J. Int.*, 1990.

On a global scale, the distribution of earthquakes and seismological stations is very heterogeneous. High seismicity is mainly confined to interplate regions and seismological stations are mostly located in continental areas and on some islands in oceanic regions. This imposes major limitations on the applicability and resolving power of seismic body-wave tomography. If only the direct ( $P$  or  $S$ ) waves are used, shallow structures beneath many intraplate regions (oceanic areas in particular) are poorly illuminated and not adequately resolved. In that case, anomalous velocity structures can only be detected at larger depths [e.g., Dziewonski et al., 1977; Dziewonski, 1984]. On the other hand, in areas with high seismicity and/or with good station coverage, regional tomographic studies with resolution in the order of 100 km have been successful in imaging upper mantle structures. For example, because of the velocity contrast between the cold slab relative to the ambient mantle, the morphology of some subducting slabs has been revealed by tomographic methods, [Hirahara, 1981; Spakman et al., 1988; Zhou, 1988].

Because interplate tectonics is often accompanied by high seismicity, interplate regions provide targets for the successful application of seismic body-wave tomography. However, this seismotectonic setting is typically poorly illuminated by seismic rays. For example, on the scale of the areas typically covered in large-scale tomographic investigations, convergence between oceanic plates often leads to an essentially two-dimensional geometry of seismicity, with a nearly linear distribution of recording stations at regional distances along the island arc. Consequently, sampling by seismic rays will be confined to a limited range of directions. A well-studied example is the Aleutian subduction zone [Engdahl and Gubbins, 1987]. Implications for the spatial resolution in tomographic images of the Mariana and Izo Bonin subduction zones are discussed by Hirahara [1977, 1981], Spakman et al. [1989] and Zhou and Clayton [1989]. Ocean - continent collision may result in the evolution of back-arc seas, with relatively low intraplate seismicity. In the absence of seismological stations within the back-arc areas, shallow structures in the upper mantle below, e.g., the Sea of Japan are not sampled by  $P$  or  $S$  waves and, as a consequence, not resolved by tomographic experiments in which only direct waves are used [Hirahara and Mikumo, 1980; Spakman et al., 1989; Zhou, 1988]. Other examples of tectonic provinces below which the upper mantle structure is typically not sampled by direct waves are basins like the Gulf of Mexico and cratonic areas without seismological stations (e.g., the Pre-Cambrian Guyana shield in northern South America). In Figure 3.1 we illustrate the heterogeneous sampling of shallow mantle structures by seismic rays in a schematic way. A structure (in white) is located in the mantle below an area characterized by the absence of both sources and receivers. Only the mantle region below and on either side of the anomaly is illuminated by direct  $P$  waves. Consequently, this structure will not be detected by direct  $P$ -wave delay-time tomography.

Important sources of information about mantle regions, not ordinarily sampled by direct  $P$  or  $S$  waves, are provided by the later-arriving multiple  $P$  or  $S$  phases (Figure 3.1) [e.g., Stewart 1976; Woodward, 1987, 1989; Grand, 1987] and by depth phases ( $pP$  and  $sP$ ) [Engdahl and Billington, 1986; Engdahl and Gubbins, 1987]. In this paper, we examine the applicability of ISC  $PP$  and  $pP$  data, used in addition to data for the direct  $P$  phase, to

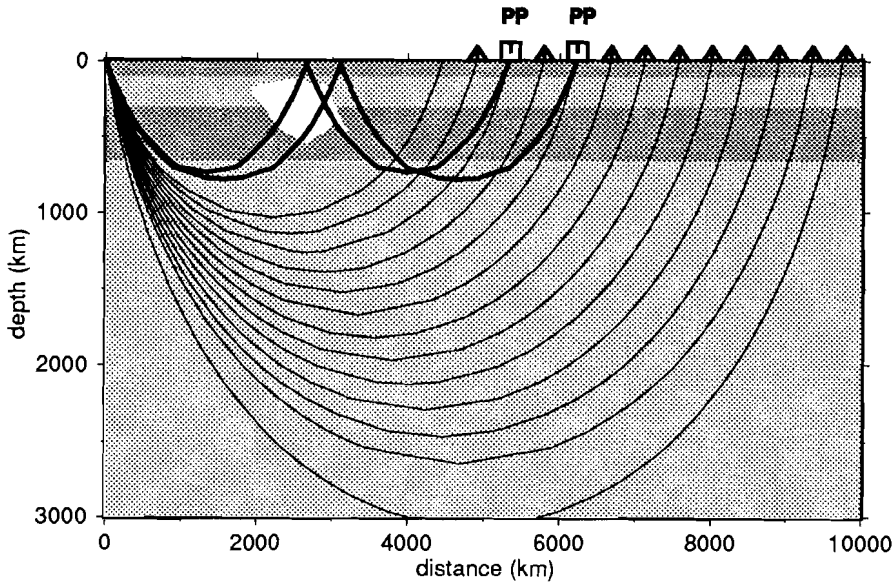


Figure 3.1. Schematic representation of the differences in sampling of Earth structure by  $P$  waves and by  $PP$  waves. The white spot marks an anomaly in a laterally homogeneous velocity structure. This anomaly is not sampled by direct  $P$  waves and, as a consequence, will not be detected by  $P$ -wave delay-time tomography. Information can, however, be obtained by the incorporation of surface-reflected  $PP$  waves.

tomographic investigations [Van der Hilst and Engdahl, 1989]. We illustrate results of this study with examples from a tomographic investigation of the three-dimensional velocity structure of the mantle below the Caribbean region. Within Caribbean region we encompass the geographical area comprised of the Gulf of Mexico, Central America, the Caribbean Sea region, and the northwestern part of South America (Figure 3.2). In the present paper, we do not emphasize the interpretation of the tomographic images with regard to the tectonic evolution of the Caribbean. Rather, we focus on the following questions: Do  $PP$  and  $pP$  waves contribute positively to the ray geometry? What are the sources of error in the ISC  $PP$  and  $pP$  delay-time data? How do we incorporate these phases in the tomographic scheme? What are the differences between results of the inversion of  $P$  phase data only and images obtained from the combined inversion of  $P$ ,  $PP$  and  $pP$  data? Does the addition of these phases improve the spatial resolution in the images?

These topics determine the organization of this paper. In section 3.2 we address some specific problems that complicate the interpretation of tomographic images of the mantle beneath the Caribbean region, arising from the, tectonically related, spatial distribution of earthquake hypocenters and stations. In the third section we show how the sampling of Earth structure by seismic waves can potentially be improved by the incorporation of  $pP$  and  $PP$  phases. Of special consideration in this study is the quality of  $PP$  and  $pP$  delay

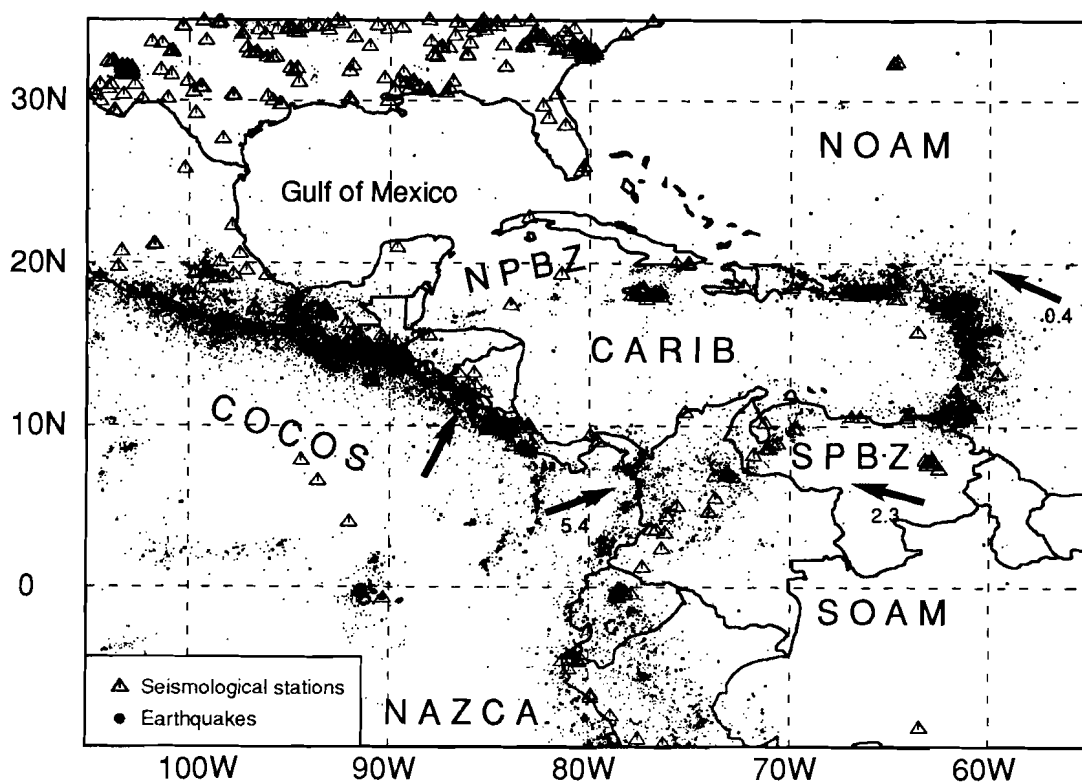


Figure 3.2. Seismotectonic map of the Caribbean region and distribution of earthquake epicenters and seismological stations. Relative plate motion vectors of the five major plates in this region are taken from Minster and Jordan [1978].

times as reported by the International Seismological Centre (ISC). This problem will be addressed in section 3.4. In studies using reflected phases, usually the spatial distribution of residual differential times  $PP-P$  or  $SS-S$  is investigated [e.g., Stewart, 1976; Dorbath and Dorbath, 1983; Girardin, 1980; Woodward, 1987]. In the fifth section of this paper we consider this approach and present the spatial distribution of  $PP-P$  differential travel-time residuals for the Caribbean region. Subsequently, the sixth section deals with the implementation of  $pP$  and  $PP$  delay times in the tomographic computations. We call attention to the differences in the resolving power of inversions using either  $P$  delay-time data alone or using  $P$ ,  $pP$  and  $PP$  residual times together. The results of the inversion of  $P$ ,  $pP$  and  $PP$  delay times are compared with images of  $P$  delay-time inversions and with the information obtained from the differential travel-time study.

### 3.2 Limitations imposed on the spatial resolution if only direct P phases are used

The plate-tectonic evolution of the Caribbean area is very complicated. To better understand and complement existing plate kinematic models (for reviews see Mann and Burke [1984], Pindell et al. [1988], Ross and Scotese [1988]), it is important to learn more about upper mantle processes in the region. Seismic delay-time tomography provides us with a powerful method to obtain a detailed high-resolution image of three-dimensional velocity structures in the mantle. However, the application of body-wave tomography in the Caribbean area is complicated by several problems. In Figure 3.2, the present geography of the Caribbean area is shown together with earthquake epicenters and seismological stations. The seismicity of the area is mainly confined to seismic zones produced by the subduction of the Atlantic Plate in the east and the Cocos Plate in the west, and along the complex northern and southern Plate Boundary Zones (PBZs, [Mann and Burke, 1984]). The tectonic evolution of this region has resulted in a morphology of island arcs (e.g., The Lesser and Greater Antilles, and Middle America), that strongly limits the locations of seismological stations to narrow zones. This heterogeneous, strongly tectonics-related distribution of sources and receivers imposes limitations on the resolution of structure by tomographic methods.

In the central parts of the Gulf of Mexico seismicity is low. In the Caribbean Plate intraplate earthquakes do occur [Molnar and Sykes, 1969], but their number is relatively low. Both in the Gulf area and in the Caribbean Sea region seismological stations are sparsely distributed along the edges. As a consequence, shallow structures in the upper mantle below these areas will be poorly illuminated by direct *P* waves. For the depth range between 0 and 33 km, this "under exposure" is illustrated by Figure 3.3. Figure 3.3 results from the tomographic investigation of the *P* velocity structure of the mantle beneath the Caribbean region using only *P*-wave delay times. In this study, the mantle was subdivided into 48,750 cells and velocity perturbations in each cell were determined by the inversion of over 700,000 *P* delay times as reported to ISC/NEIC between 1964 and July 1987. In Figures 3.3 and 3.4, the sampling of the upper mantle beneath the Caribbean region is expressed by the hit count: the number of rays crossing a particular block in the cell model. Figure 3.4a is a vertical cross section striking nearly west to east across the Caribbean Plate, showing high hit count below the Middle America and Lesser Antilles trenches and, at shallow depth levels, the low hit count below the Caribbean Plate. The large variations in hit count below the Gulf area, the Caribbean Plate and the Guyana shield area, separated by high-seismicity PBZs, are further illustrated by Figure 3.4b. Spakman and Nolet [1988] showed that the hit count is important in the interpretation of tomographic images. In mantle areas with low hit count, existing velocity anomalies can be overlooked if the LSQR inversion algorithm [Paige and Saunders, 1982] is used, because velocity perturbations will be "zero-biased" [Spakman and Nolet, 1988].

The vertical sections through the three-dimensional model of hit count (Figure 3.4) reveal that ray illumination by *P* waves is strongly biased. Because of the location of the majority of seismic stations and earthquake epicenters parallel to the Middle America



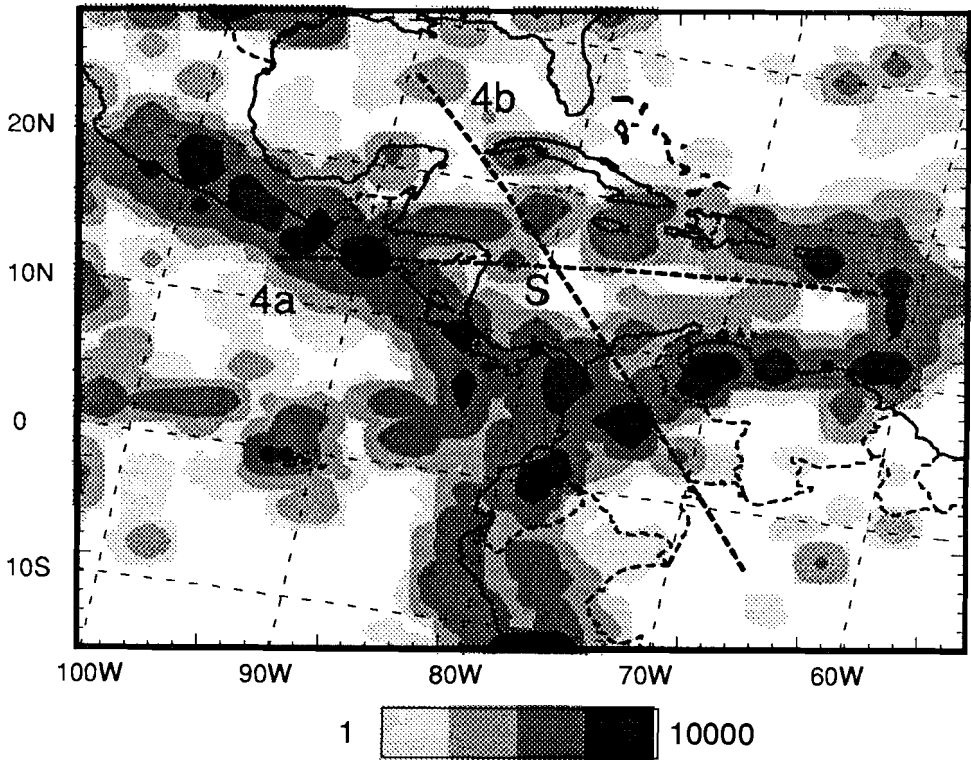


Figure 3.3. Map view of the hit count, illustrating the sampling of the top layer of the cell model (0 - 33km) by direct  $P$  waves. The scale is logarithmic. The dashed lines mark the surface intersections of the vertical cross sections shown in Figures 3.4a and 3.4b. Where they intersect the hit count is close to zero (the white area).

Trench (MAT) and the Lesser Antilles Trench (LAT), the waves travelling east to west, from the MAT to the LAT, outnumber  $P$  waves from other directions (Figure 3.4a). The ray geometry, employed in the tomographic computations, is predominated by  $P$  waves travelling over an epicentral distance of ca.  $25^\circ$  and bottoming at a depth of ca. 750 km. The steep, (apparently) northwest-dipping, high hit-count features in Figure 3.4b indicate that the earthquakes near the northern and southern PBZs are predominantly recorded at stations in North America. This predominance of rays in one particular direction causes many equations of the linear tomographic system to be dependent. The lack of information in the model space orthogonal to the high hit-count features may cause any existing velocity perturbations to be "smeared out" in that direction [Spakman et al., 1989; Van der Hilst and Spakman, 1989]. These results are very relevant to the interpretation of velocity anomalies in tomographic images.

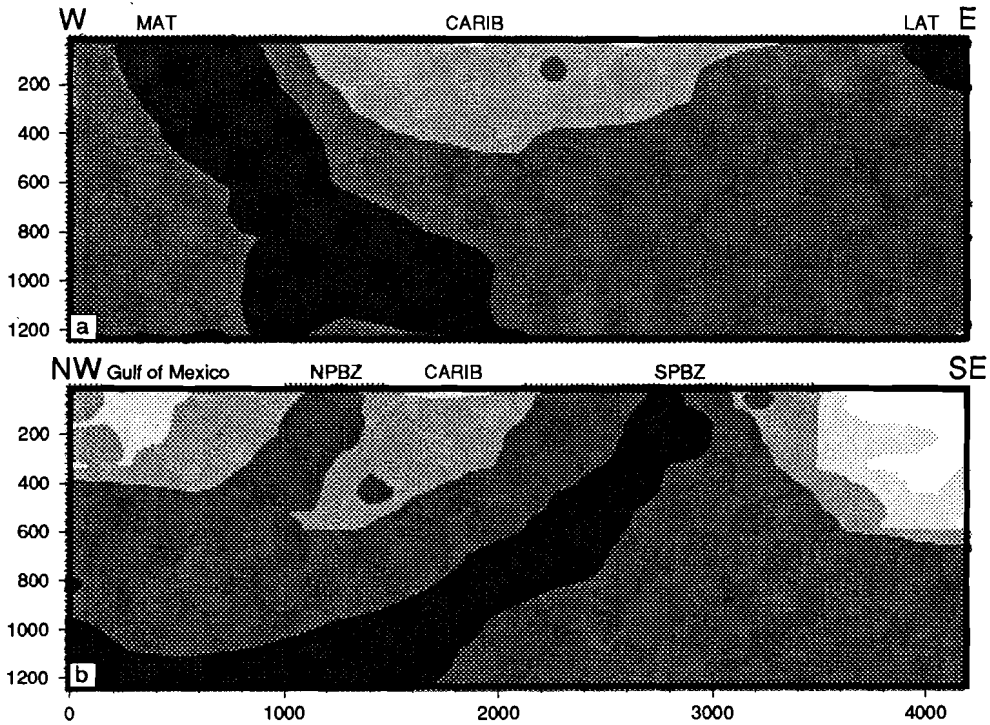


Figure 3.4: Vertical mantle cross-sections through the three-dimensional model of  $P$  hit count. (a) West to east section across the Middle America and Lesser Antilles subduction zones. This section indicates the predominance of ray illumination between the seismic zones of these subduction zones. (b) Northwest to southeast section across the Caribbean Plate showing the predominance of rays traveling from the northern and southern Plate Boundary Zones to seismological stations in North America.

### 3.3 Illumination of structure by seismic rays of the pP and PP phases

To sample shallow Earth structure below the Caribbean region, which is not adequately illuminated by direct  $P$  waves,  $pP$  and  $PP$  waves with reflection points in this region should be used. In this section we discuss geometrical considerations. Criteria used for the selection of the data, data processing, and statistics, as well as problems involved in the determination of the bounce point locations, are discussed in section 4.

#### 3.3.1 Illumination by $PP$ waves

Most  $PP$  waves suitable for this study travel from sources in South America to receivers in North America (Figure 3.5); only a few ray paths from events in North America to stations in South America and from events in the Pacific to stations in Europe are used. The geographical distribution of sources and receivers (Figure 3.5) resulted in a spreading of  $PP$  reflection points in the Caribbean region as shown in Figure 3.6. In Figure 3.6 (and

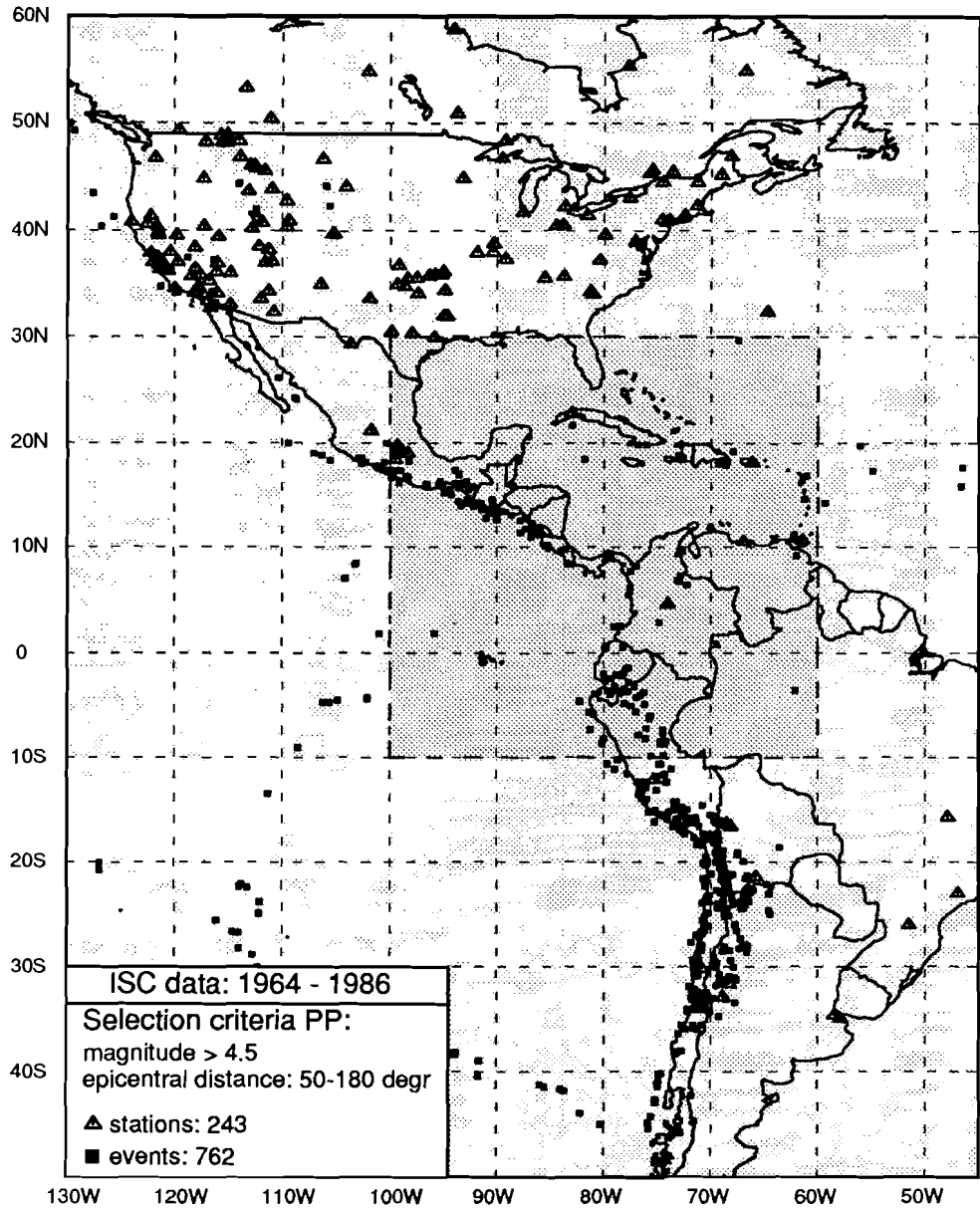


*Figure 3.5:* Geographic map of the Americas showing the distribution of earthquakes and stations used in the selection of *PP* data. Because of the large epicentral distances and the requirement that *PP* waves should reflect in the Caribbean region, earthquake epicenters suitable for this study are mainly located in Peru, Bolivia and Chile, with recording stations mainly confined to the USA and Canada. Stations in Greenland and in Europe that recorded *PP* waves reflected in the Caribbean region are not shown on this map.

3.8) the symbols are plotted at the theoretical locations of the reflection points of the *PP* (and *pP*) waves. In calculating reflection point coordinates we made allowance for the focal depth of the source. If simply the mid points between sources and receivers are taken [e.g., Darragh, 1985] errors in the location of reflection points may be as large as  $2.5^\circ$  [also Dorbath and Dorbath, 1981].

Schematically, the ray geometry of both *P* waves and *PP* waves are plotted in Figure 3.1: every bounce point of *PP* (or *pP*) can be considered both as an additional receiver and source [Engdahl and Gubbins, 1987]. If, in addition to the *PP* phase, the direct *P* is available, the travel time residuals can be used in differential travel-time investigations. For epicentral distances beyond  $95^\circ$  no direct waves are recorded, but *PP* waves arriving at these distances are used to illuminate the shallow structures between epicenter and station.

Figure 3.1 demonstrates another important benefit of using the *PP* phase together with *P* waves. *PP* waves may improve the quality of ray coverage where the *P* hit count is high, but where illumination by *P* rays is predominant in one direction. In Figure 3.1 it is shown that, in the mantle regions between the velocity structure and the recording stations, usage of *PP* adds rays orthogonal to the *P* rays. Thus, incorporation of *PP* waves may enhance the resolution and reduce the "smearing" of anomalies in the direction of predominant ray illumination. The quality of reported *PP* travel-time data is discussed in section 4.

### 3.3.2 Illumination by *pP* waves

Figure 3.7 gives the distribution of sources and receivers used for the selection of *pP* data, resulting in *pP* reflection point locations as presented in Figure 3.8. Due to the shallow seismicity in the area, *pP* reflection points (Figure 3.8) are generally close to the earthquake epicenters (see Figure 3.2). Consequently, for events in the Caribbean region *pP* ray paths remain close to *P* ray paths and their contribution to illuminating mantle structures not sampled by the direct *P* phase is small compared to the contribution of *PP* waves. However, as Engdahl and Gubbins [1987] pointed out in their study of the Aleutian subduction zone, incorporation of depth phases better constrains the focal depths and stabilizes the inversion for the velocity structure. Moreover, for shallow structures above seismic zones, *pP* waves give a much better illumination than direct waves if no stations are located in the vicinity of the epicenter. A better constraint on structures at shallow depths in the seismically active area, results in better resolution at deeper levels as well, because it acts against the "smearing" of velocity anomalies along predominant ray paths.

## 3.4 The data

Ideally, to determine arrival times of the *PP* phase, the attenuated and Hilbert transformed *P*-wavelet should be correlated with the part of the seismogram containing the reflected phase [Girardin, 1980; Woodward, 1989]. In this study, the objective is to incorporate *pP* and *PP* phase data in the tomographic inversions, together with some hundreds of thousands of *P* phases. Hence, instead of relying on a few high-quality data, as many published data as possible are used, assuming that the overall effect of larger reading errors

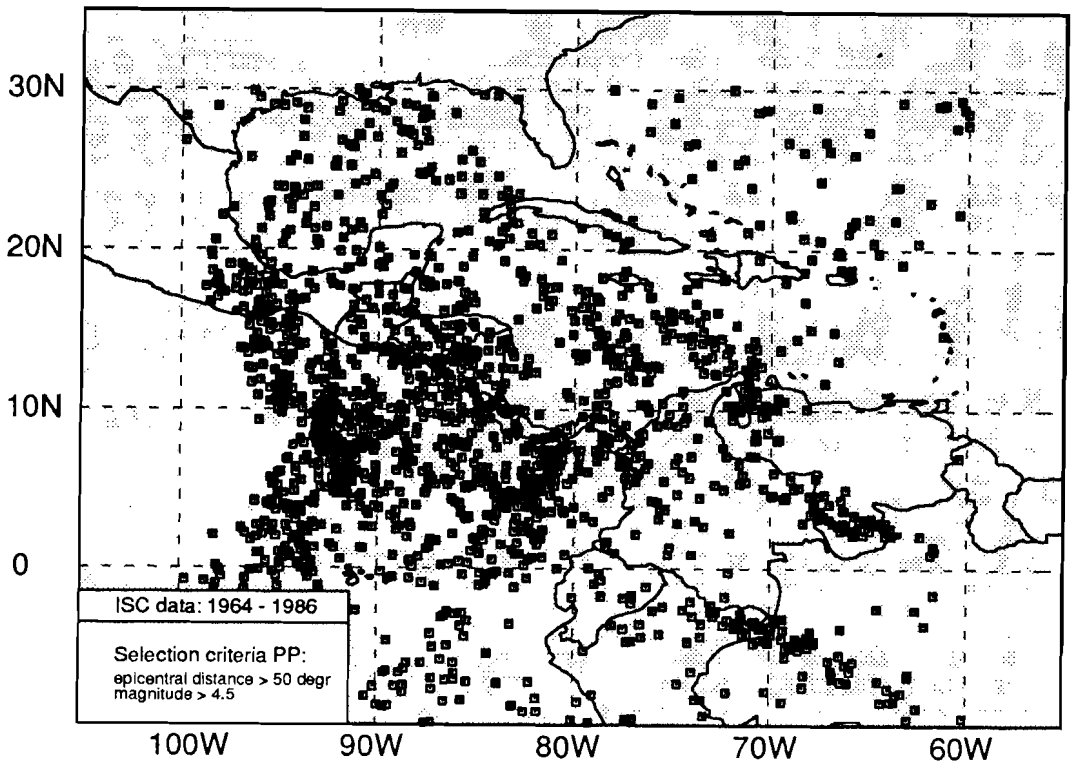


Figure 3.6. Geographic distribution of *PP* reflection points in the Caribbean region.

in individual data will be averaged out (see also Stewart [1976] and Darragh [1985]). In this study, delay time data are obtained from two sources: the ISC bulletin tapes and analog WWSSN and Canadian Network records. We believe that the data reported by ISC were primarily read from short-period seismograms. However, it is difficult to trace whether at a particular station *PP* was read from LPZ or from SPZ seismograms. The phase may have been read from either pass band, depending on the quality of the seismograms. With WWSSN and Canadian Network analog records, we examined *PP* arrivals primarily from the LPZ records, because it is often difficult to recognize *PP* on SPZ traces, even though the picks may be more accurate. We also examined the GDSN digital data set (CD-ROM, 1980-1984), but only a small number of event-station pairs with *PP* reflection points in the Caribbean region were found. The small number of data that can be derived from digital seismograms is not considered in the present study, and we emphasize the use of reported ISC phase data. In future studies [also Woodward, IGPP, personal communication, 1989] we will use the statistics of the digital data to quantitatively estimate the effect of *PP* pulse deformation due to a phase shift [Hill, 1974; Choy and Richards, 1975].

In Table 3.1 information is given about the data sets and about the selection criteria used in this investigation. Lower limits in epicentral distance are adopted for both the *PP*

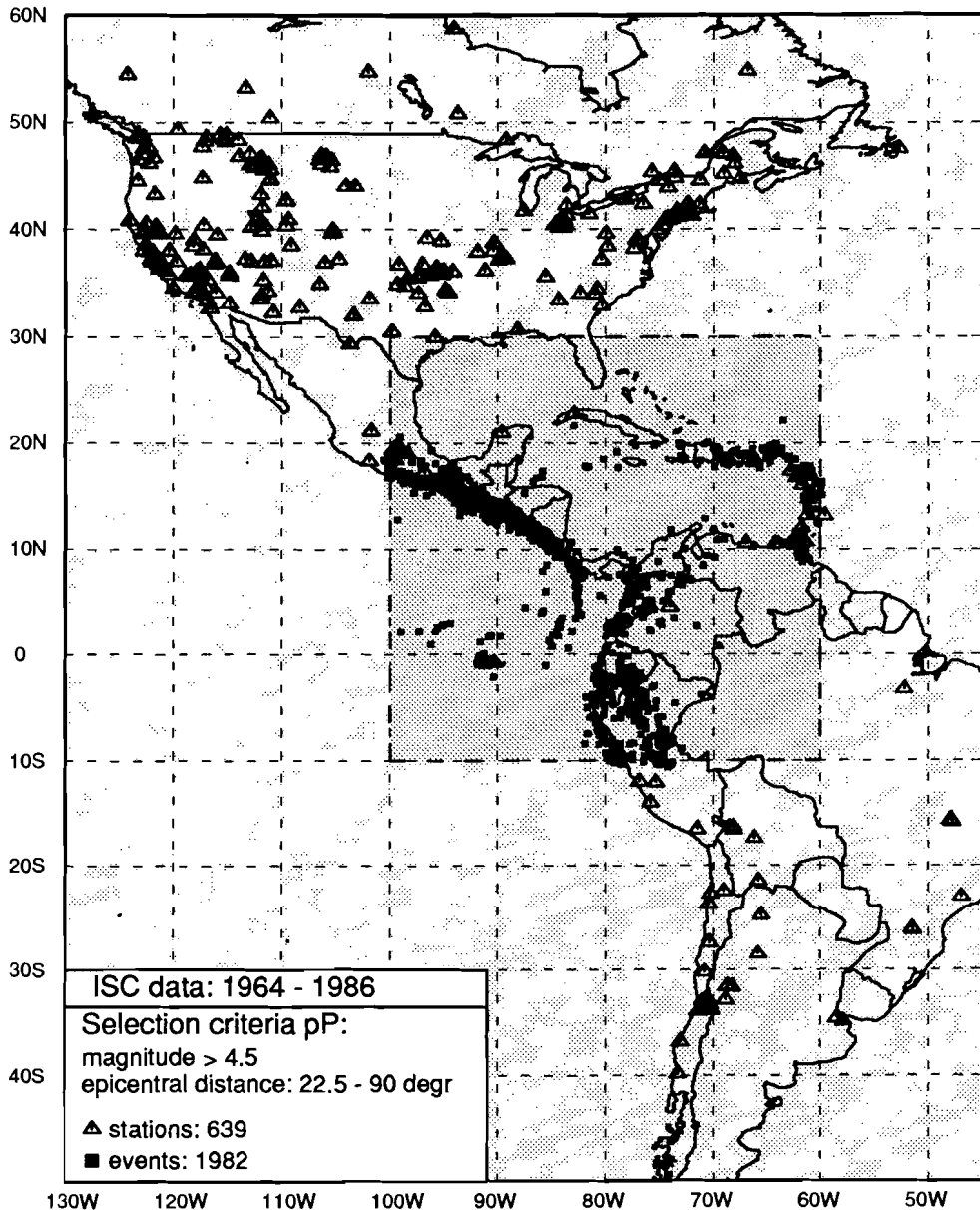


Figure 3.7. Geographic map of the Americas showing the distribution of events and stations, the combination of which give *pP* bounce points in the Caribbean region (Figure 3.8). Earthquake locations are mainly confined to the Caribbean region, whereas the recording stations are located in both North and South America.

and *pP* phases, to avoid complications of triplications due to upper mantle discontinuities. Following the data selection criteria outlined in Table 3.1, the distribution of 762

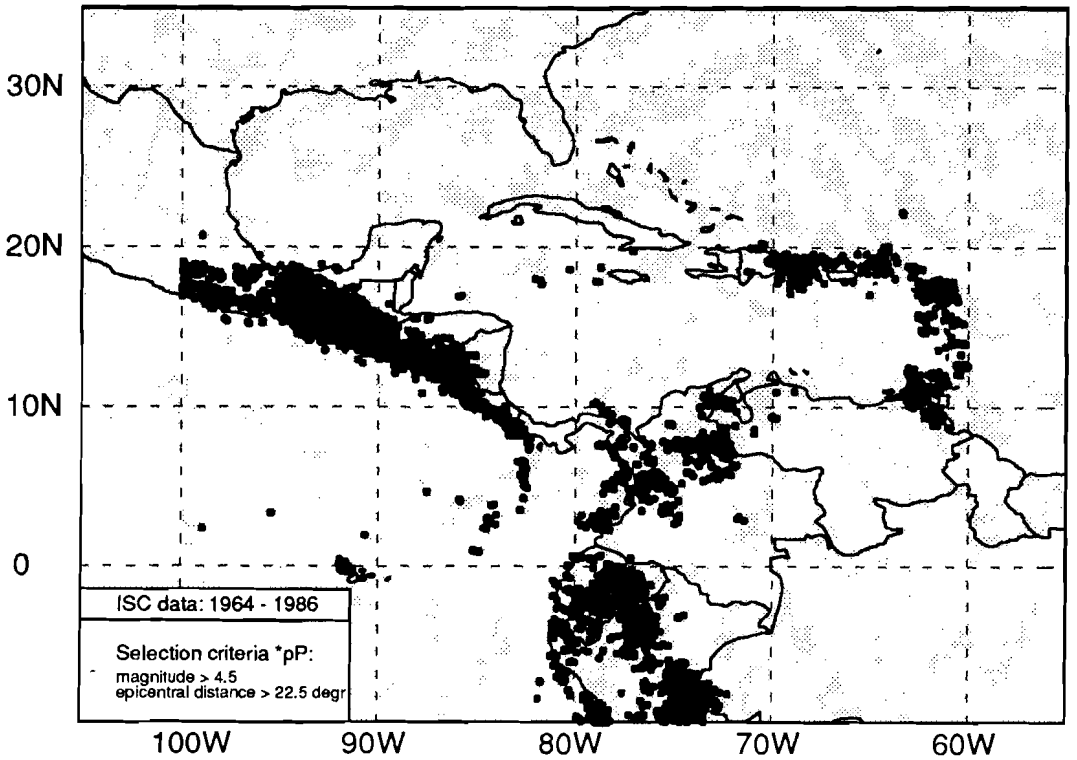


Figure 3.8. Geographic distribution of *pP* reflection points in the Caribbean region.

earthquakes and 243 stations resulted in a data set of 1928 *PP* delay times. Nearly 12,000 *pP* travel-time residuals resulted from the registration of 1982 events at one or more of 639 stations involved in this investigation. The majority of *pP* phases used in this study have reflection points on land. In future investigations the upper and lower limits for the *pP* delay times of -7.5 and +7.5 sec, as adopted by the ISC, will be reexamined.

It is assumed that the *PP* and *pP* phase data as reported by the ISC are corrected for ellipticity according to a modified formula for the direct *P* wave, given by the JB tables [1967]. Note that the ISC uses no allowance for focal depth in this correction. For surface-reflected waves the JB ellipticity correction  $\delta t_{ell, PP}$  can be written as

$$\delta t_{ell, PP} = f\left(\frac{\Delta}{2}\right) * [h_1 + 2h_2 + h_3] \quad (3.1)$$

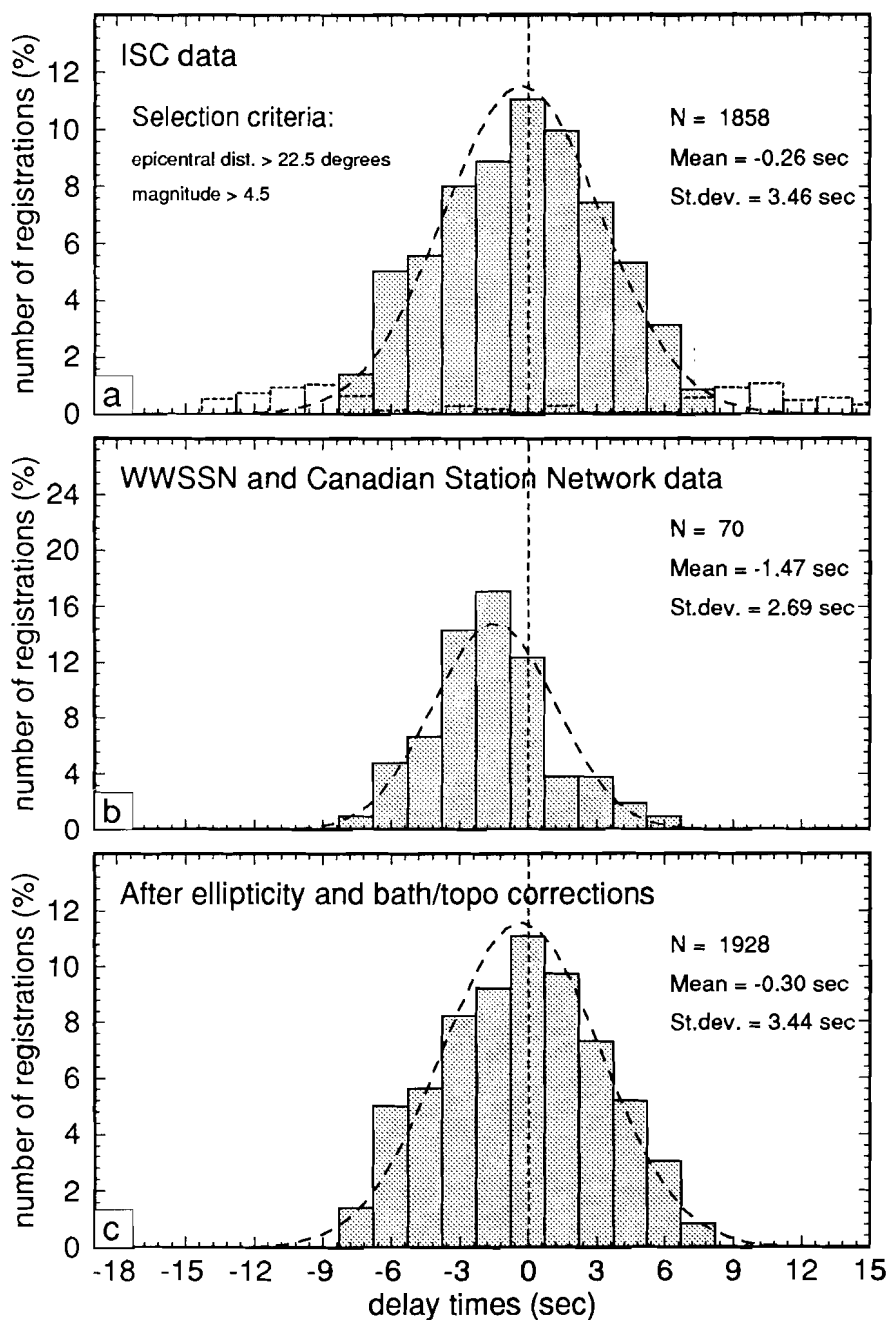
where  $\Delta$  is the distance from epicenter to station,  $h_1$ ,  $h_2$  and  $h_3$  are the reference ellipsoid heights of the epicenter, reflection point and station above the mean sphere, respectively, and  $f(\Delta/2)$  is the function tabulated on page 50 of the 1967 edition of the Seismological Tables. To allow for the effect of non-zero focal depth we replaced the JB ellipticity correction (3.1) with an ellipticity correction formulated by Dziewonski and Gilbert [1976].

	<i>PP</i>	<i>pP</i>
number of earthquakes	762	1982
number of stations	243	639
minimum distance (degr)	50.0	22.5
maximum distance (degr)	180	90
minimum magnitude	4.5	4.5
minimum focal depth (km)	0	33
delay time window (sec)	$\pm 7.5$	$\pm 7.5$
number of rays	1928	11696

Table 3.1: Number of earthquakes and stations involved in the investigation of *PP* and *pP* data, the criteria adopted to select the data, and the final number of *PP* and *pP* rays. For frequency distributions of the residuals, see Figure 3.9 (*PP* data) and Figure 3.11 (*pP* delay times). Note that these numbers refer to the data selection before the incorporation in the tomographic investigation. In the subsequent computation of tomographic system of equations (3A.5) additional data may have been discarded, e.g., because we failed to find the correct ray paths.

*Figure 3.9.* Frequency distributions of the ISC *PP* delay times and data derived from analog WWSSN and Canadian Network records. These data are input to the programs that construct and solve the tomographic system of equations. (a) Histograms of the original ISC data which are catalogued as *ISC identifications* (shaded distribution) and as *operator identifications* not confirmed by the ISC (dashed lines). (b) Frequency distributions of *PP* delay times from WWSSN and Canadian Network seismograms, determined relative to JB times in the delay time window  $[-7.5, +7.5]$  sec. These data are read primarily from LPZ records, because it is often difficult to recognize *PP* on short-period seismograms. (c) Frequency distribution of the combination of ISC identified data and data read from analog records, after ellipticity and bathymetry/topography corrections.





### 3.4.1 PP delay times

Only lower mantle *PP* phases are considered (Table 3.1) to avoid complications associated with the triplication branches of the *PP* phase. The frequency distribution of the original ISC *PP* travel-time residuals is given in Figure 3.9a. The shaded histogram is defined as ISC data that are confirmed as *PP* (or *pP* in Figure 3.11) by the ISC identification program. Operator identifications that are not confirmed by the ISC program, are represented in a histogram (Figure 3.9a, dashed line) which shows few small residuals and has maxima near -10 and +10 seconds. ISC used upper and lower limits of +7.5 and -7.5 sec as selection criteria (see any January issue of the *Bulletin of the International Seismological Centre*). These limits are also maintained for the ISC data used in this study (Table 3.1). By adopting these bounds, possibly many of the *PP* delay times corresponding to reflection at the continental Moho are rejected [Stewart, 1976]. Precursors to *PP* that are reflected at the oceanic Moho will not be filtered out from the data set, because the difference in arrival time will be too small.

The ISC-confirmed travel-time residuals are approximately normally distributed about a mean of -0.26 seconds with a standard error of 3.46 seconds. The values for the mean and the standard deviation of the distribution are comparable to the figures published by Zhou and Clayton [1985], although they report more scatter which is due to the acceptance of delay times that are not confirmed by the ISC [Zhou, 1989]. In Figure 3.9b the frequency distribution of the delay times read from analog WWSSN and Canadian Network records (primarily long period) is given. For a direct comparison with the ISC confirmed data, we discarded residuals with absolute values larger than 7.5 sec. The distribution has a standard deviation of 2.68 sec and a mean of -1.47 sec. The significantly larger spread of ISC confirmed residuals (3.46 sec) may reflect larger reading errors. It may, however, also result from the ISC phase identification process: the distribution of ISC confirmed residuals (Figure 3.9a, shaded) includes many phases that were not identified as *PP* by station operators, but are labeled as *PP* by the ISC identification program. Note that neither of the distributions shown in Figures 3.9a and 3.9b are corrected for topography or bathymetry.

In the computation of travel time residuals the ISC assumes surface reflections. Figure 3.10a shows a bathymetric and topographic map of the Caribbean region. Comparison of the distribution of reflection points (Figure 3.6) with the bathymetric map shows that many *PP* reflect at the sea bottom. If a wave reflects at the sea bottom, the true ray path will have a smaller travel time than the ray path of the wave reflecting at the earth's surface. Even in a homogeneous earth, neglect of this difference will introduce a negative time residual for the *PP* phase, suggesting faster wave propagation below these areas. By the same argument topography would produce ray paths with larger travel times. Therefore, it is necessary to apply a correction for topography and bathymetry to the delay times of reflected phases. This correction is given by

$$\delta t_{topo/bath} = \frac{2H}{v_{crust}} * [1 - ((v_{crust} * p)/R_o)^2]^{1/2} \quad (3.2)$$

where  $H$  is the height above or below mean sea level,  $v_{crust}$  the crustal  $P$  velocity of the reference velocity model,  $p$  the ray parameter and  $R_o$  the earth's radius. This correction is equivalent to the topographic correction applied by Grand [1987, equation 7]. Corrections for crustal thickness are not employed (as by Grand [1987]), since only highly schematic maps of crustal thicknesses and velocities are available for the Caribbean region [e.g., Case et al., 1984]. The height  $H$  in (3.2) is determined from Figure 3.10a. Replacement of the ellipticity correction and application of (3.2) lead to the frequency distribution given in Figure 3.9c. The difference between the mean value of the  $PP$  delay-time distributions before and after these corrections is 0.44 sec. However, the effect of both the improved ellipticity correction and the bathymetry/topography correction does not significantly affect the standard deviation.

The frequency distribution given in Figure 3.9c suggests that the  $PP$  onset may be read systematically early. However, in view of the value of the standard deviation (3.44 sec) and the number of error sources, this negative bias (0.30 sec) should not be considered significant. Apart from the presence of lateral velocity heterogeneities, several other factors can contaminate the  $PP$  data or contribute to systematic deviations from the theoretical  $PP$  arrival times:

- a) the dependence of the  $PP$  delay time values on the reference model used for the computation of the theoretical travel times [Buchbinder, 1982; Van der Hilst and Spakman, 1989 (for  $P$  waves)].
- b) the asymmetry of reflections within the diametrical plane, due to reflections at dipping surfaces, lead to precursors to the arrival time of the maximum-time  $PP$  phase [Wright, 1972, King et al., 1975].
- c) the departure from the assumption that  $PP$  paths are confined to the diametrical plane: the problem of reflection at dipping surfaces [Wright, 1972] is essentially three-dimensional. Paths, diverging from the diametrical plane should be more strictly called non-minimum time paths [Jeffreys and Lapwood, 1957].
- d) reflections at surfaces other than the free surface or the sea bottom (e.g., at the sediment-basement interface or at the Moho), may give rise to a bias towards negative delay times, suggesting wave propagation faster than in the average Earth (see Wright [1972] for references; also Engdahl and Billington [1986] for depth phases).
- e) the (often) emergent character of the onset of the  $PP$  phase. This may either be caused by the long source time functions typical for the larger earthquakes in South America [H. Paulssen, personal communication, 1989] or by
- f) the distortion of the wave form, due to phase shifts, along the non-minimum time  $PP$  ray path. This phase shift transforms an impulsive  $P$  pulse into an emergent  $PP$  wave form [Jeffreys and Lapwood, 1957; Hill, 1974; Choy and Richards, 1975].
- g) (in exceptional cases) misidentification of phases because of focal mechanism effects on their amplitudes.

In addition, wavefront-healing effects [Wielandt, 1987] may cause slow mantle regions to remain undetected, in particular, when *PP* data are used to investigate the aspherical mantle structure.

Without analyzing many original seismograms, it is not possible to discuss quantitatively the distinct contribution to published data of each of the effects mentioned above. Therefore, we will qualitatively discuss the most important effects and assess their contributions to *PP* delay times.

Buchbinder [1982] demonstrated that the values of *PP* delay times are strongly dependent on the adopted reference velocity model. This dependency affects the travel times both in a linear as well as in a non-linear way. Travel time residuals depend on theoretical travel times computed in some reference velocity model and consequently the derived velocity anomalies should be regarded as relative to this reference model. However, a non-linear effect arises from the dependency of ray geometry on the reference velocity model. Van der Hilst and Spakman [1989], discussed this problem for *P* waves and advocated the use of a reference model that is as close as possible to the average one-dimensional velocity structure of the mantle region under scrutiny. They showed that the ray geometry of waves bottoming in the lower mantle is not very sensitive to velocity heterogeneities in the upper mantle. In this study, only lower mantle *PP* phases that are recorded at distances beyond  $50^\circ$  are used. Hence, we assume that the dependence of *PP* delay times on the reference velocity model is linear.

Jeffreys and Lapwood [1957] showed that, if ray paths are confined to the diametrical plane (i.e., it passes through hypocenter, bottoming points, the reflection point and the seismological station), *PP* is a stationary maximum-time phase for epicentral distances up to  $180^\circ$ . In this two-dimensional geometry, asymmetric reflections due to reflections at dipping surfaces [Wright, 1972], or scattering near the reflection point [King et al., 1975], result in  $P_{A\pm}P$  waves with  $A \neq \Delta/2$ , that have arrival times smaller than *PP* (or  $P_{\Delta/2}P$ ). Here, we adopt the notation of Wright:  $\Delta$  is the epicentral distance and the  $\pm$  sign refers to one of the two possible asymmetries. We remark that *PP* waves do not reflect at a single ray-theoretical point and that asymmetric reflections can only be observed if signals are coherent over the dimensions of the reflection zone, which may be hundreds of kilometers wide (see section 4.2. about *pP* delay times). *PP* arrives later if the wave is reflected at a dipping surface outside the diametrical plane and is subsequently focussed to the recording station. The *PP* paths are then not true maximum-time [Jeffreys and Lapwood, 1957]. King et al. [1975] showed that the *PP* travel time, as a function of ray parameter and azimuthal deviation in the direction of scattered waves, is a complex saddle back. The effects on travel time are of the same order of magnitude as calculated by Wright [1972] for asymmetric reflections in the diametrical plane [King et al., 1975]. Note that asymmetrically reflected *PP* waves precede the theoretical arrival time by typically, tens of seconds [Wright, 1972; King et al., 1975]. These precursors are either not recognized as *PP* by station operators or are beyond the selection criteria applied by the ISC. Only reflections with small asymmetry, having reflection points (or scattering zones [King et al., 1975]) near those computed theoretically, may contaminate the data set.

If precursors frequently occur, the distributions (Figure 3.9) would show an asymmetry to more negative values. Excess of later arrivals would result in the distributions being asymmetric to positive values. The absence of either kind of asymmetry in the frequency distributions shown in Figure 3.9 suggests that either both effects average out or that the effect of asymmetric reflections due to dipping reflectors or scattering is small, for the region being studied. Figure 3.10b shows the slope of surface reflectors in the Caribbean region. This map is derived from the bathymetry map (Figure 3.10a). Large dips of reflection zones ( $> 1$  degree) may occur in the vicinity of plate boundaries and the location of bounce points in these zones may be in error. Fortunately, near plate boundaries, seismicity is high and the occurrence of reflection points and the amount of associated *PP* phase data will be outnumbered by *P* phase data. Hence, in any simultaneous inversion of *P* and *PP* phase data, the effect of asymmetric reflections will be suppressed. Figure 3.10 shows that in the central parts of the Gulf of Mexico and the Caribbean Plate gradients in bathymetry are small and errors due to asymmetric reflections will be well within the level of reading errors. The contaminating effect of asymmetric reflections is therefore smallest in areas where the contribution of *PP* data to resolve Earth structure is the most important.

More difficult to assess is the influence to the *PP* time residuals of the distortion of the *PP* pulse due to a phase shift in each frequency component [G. Choy, (USGS, Golden) personal communication, 1988]. For sufficiently high frequencies the phase shift is  $\pi/2$  and the *PP* pulse is the Hilbert transform (allied function) of the *pP* (or inversed *P*) wavelet [Jeffreys and Lapwood, 1957; Hill, 1974; Choy and Richards, 1975; Woodward, 1987, 1989]. Impulsive *P* onsets transform to emergent *PP* pulses. The *PP* pulse is acausal and the emergent leader is precursory to the ray geometrical travel time [Jeffreys and Lapwood, 1957; Hill, 1974; Choy and Richards, 1975]. Consequently, if mispicked due to ignorance of this pulse deformation, the *PP* phase may also be read before the time predicted by geometrical ray theory. WKBJ modelling shows that this effect can be several seconds. For short-period data the effect is smaller. From the investigation of (long period) synthetic wave forms, Zhou [1989] also concluded that the effect may be of the order of several seconds, but that the (neglected) phase shift contaminates the ISC *PP* picks in a random manner.

Wave-front healing effects due to diffraction of seismic waves near velocity anomalies result in a bias towards early arrivals, and consequently to higher average velocities in the Earth volume under study [Wielandt, 1987]. This effect is described by Wielandt for the minimum travel-time direct phase, but will more seriously effect non-minimum travel-time phases, like the *PP*. However, unless the diffracted waves are identified as such and the corresponding ray paths are known, this problem cannot be circumvented.

### 3.4.2 *pP* delay times

In this study, *pP* data are used only for earthquakes with ISC-reported focal depths deeper than 33 km (1) to assure substantial difference between *P* and *pP* paths; (2), to avoid the complexities of crustal events; and (3) to improve the reliability of depth phase identification because of increased separation in phase arrival times. Figure 3.11a shows

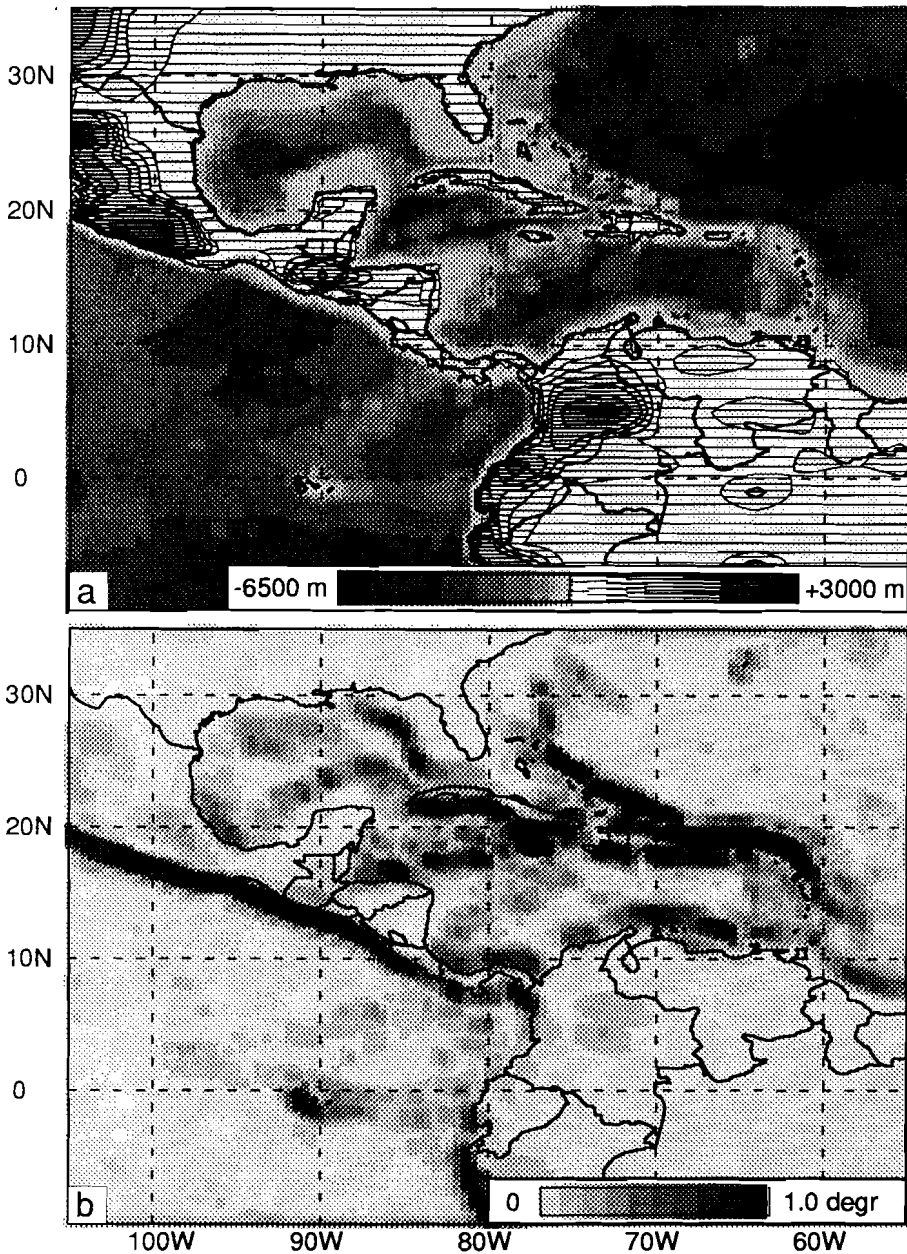


Figure 3.10. (a) Map of the Caribbean region showing the bathymetry and topography. This map is used for the correction of  $pP$  and  $PP$  travel-time residuals. In the bathymetry file, depths below sea level are given at grids of  $5' \times 5'$ . The topographic map is less accurate:  $1.5^\circ \times 1.5^\circ$ . (b) Map showing values of surface slopes. This map is obtained from Figure 3.10a. In intraplate regions, the slope of surface reflectors does not exceed  $0.3^\circ$ .

frequency distributions of  $pP$  delay times that are confirmed by the ISC and include operator identifications between  $22.5^\circ$  and  $25^\circ$  (shaded histogram), and of data that are cataloged as operator  $pP$  identifications beyond  $25^\circ$  and not confirmed by the ISC (dashed lines). In this study, operator  $pP$  identifications beyond  $25^\circ$  and not confirmed by the ISC, are rejected. The exception is made for data with epicentral distances below  $25^\circ$ , because at those distances ISC does not confirm phases like  $pP$ , regardless of quality. Figure 3.11b gives the distribution after correction of the ISC data (Figure 3.11a) for ellipticity [Dziewonski and Gilbert, 1976] and for bathymetry and topography.

A mean of -1.6 seconds for the distribution shown in Figure 3.11b suggests that  $pP$  phases systematically arrive before the theoretical travel time. Thus, ISC focal depths (based solely on  $P$  arrival times) are not consistent with the arrival times of depth phases computed for the Jeffreys-Bullen velocity model. Although we suspect that this inconsistency is the result of hypocenter location and velocity model errors, these sources of errors cannot be assessed until we actually perform the tomographic inversions. However, there are other possible explanations for this negative bias, which include the effects of asymmetry in the propagation path and phase misidentifications caused by near-source structure.

Comparison of the distribution of  $pP$  reflection points (Figure 3.8) and estimates of the gradients in bathymetry (Figure 3.10b) shows that many depth phases reflect in the vicinity of plate boundaries, where slopes of surface reflectors are large ( $> 1^\circ$ ). Both for  $pP$  and  $PP$  phases, it is important to realize that reflection does not take place at one single point but rather at a reflection zone, the width of which is determined by the Fresnel zone of the wave. Nolet [1987a] estimates the maximum half width of a ray with a wave length of 10 km and length of 1,000 km, to be 36 km (and 112 km for a ray length of 10,000 km). Thus, for shallow earthquakes the dimension of the reflecting zone of the depth phase may be rather small. Reflections at a dipping reflection zone may lead to small asymmetries of reflections of  $pP$  waves [Wiens, 1987]. In contrast to asymmetrically reflected  $PP$  waves, the small asymmetry in  $pP$  reflections will not lead to precursors to the theoretical travel times, because  $pP$  is a minimum travel-time phase [e.g., Jeffreys and Lapwood, 1975]. However, Wiens [1987] argues that small changes in delay times due to sea floor dips may result from modifications of the relative amplitudes of, e.g., the  $pwP$  phases. Wiens concluded that on long-period records this effect is not apparent (see also below). We note that  $pP$  residuals reported by the ISC are primarily read from short-period seismograms.

Jeffreys and Lapwood [1957] and Hill [1974] showed that  $pP$  waves propagate along minimum-time ray paths and arrive as inverted, but undistorted,  $P$  pulses. Thus, pulse distortions due to phase shifts (see previous section about the  $PP$  phase) do not complicate the reading of  $pP$  onsets. Similar to the  $P$  phase, a small bias towards negative  $pP$  delay times may result from diffraction effects [Wielandt, 1987].

Another problem is the likely contamination of the  $pP$  data set with misidentifications of the  $pP$  phase. For discussions on this topic, the reader is referred to Yoshii [1979], Forsyth [1979], Engdahl and Billington [1986], Engdahl and Gubbins [1987], and Schenk et al. [1989]. For sub-oceanic regions, they distinguish the  $pP$  proper, reflecting at the sea

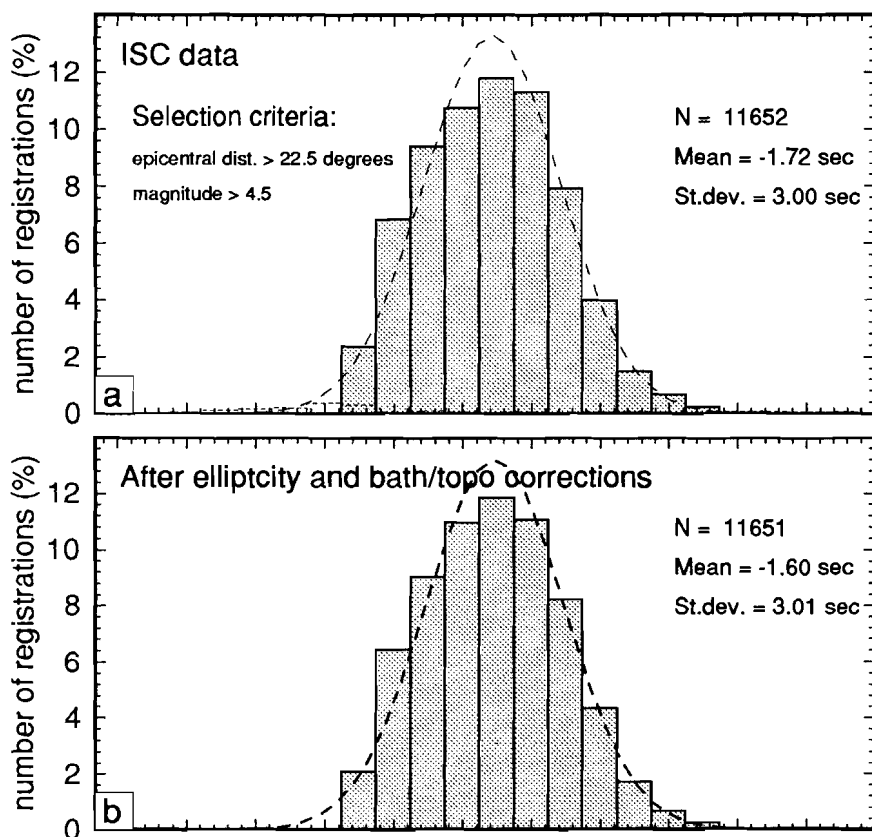


Figure 3.11. Frequency distributions of  $pP$  travel-time residuals. (a) Original ISC data, without any corrections. Shaded distribution: *ISC identifications* (beyond 25° epicentral distance) and *operator identifications* between 22.5 and 25°. Dashed histogram: *Operator identifications* beyond 25° not confirmed by the ISC program. (b) Frequency distribution of ISC confirmed data corrected for ellipticity [Dziewonski and Gilbert, 1976] and for bathymetry/topography.

bottom, the  $[pP]$  [Engdahl and Billington, 1986], reflecting at the sediment-basement interface, the  $pwP$  (and  $swP$ ), transmitted at the sea bottom and reflected at the water surface, and the precursory, Moho-reflected,  $pMP$ .

Forsyth [1982] and Engdahl and Billington [1986] demonstrate that relative amplitudes of the direct  $P$  and the depth phases  $[pP]$ ,  $pP$  and  $pwP$  depend on the frequency dependent reflection coefficients, source mechanism and radiation pattern. Wiens [1989] reported observational evidence for bathymetry effects on the relative amplitudes of these phases. Water-sediment interfaces may have small short-period impedance contrasts. Consequently, on short-period (WWSSN) seismograms  $pwP$  may have an amplitude comparable to or larger than the  $pP$  phase reflecting at the sea bottom, and  $pwP$  may easily



be misidentified as  $pP$ . The danger of misidentifications will be enhanced in case of reflection at dipping surfaces [Wiens, 1989], because  $pwP$  may have larger amplitudes. On long-period seismograms, 70-80% of the long-period, long-wavelength  $P$ -wave energy will be reflected at the crust-water interface and  $pwP$  and  $swP$  can be ignored [Forsyth, 1982]. With a water  $P$  velocity of 1.5 km/sec, and water depths of 3 to 6 km,  $pwP$  typically arrives 4 to 8 seconds after the  $pP$  phase. If, as Yoshii [1979] suggests, many ISC  $pP$  are actually  $pwP$ , we would expect the frequency distribution of ISC  $pP$  delay times to be biased towards positive values. An explanation for the absence of this positive bias in Figure 3.11b, is the mapping of the time error into the focal depth, which would thus be overestimated [Yoshii, 1979; Forsyth, 1982; Engdahl and Billington, 1986]. This would happen if the focal depth is determined from  $pP$  arrival times and if misidentification of depth phases were systematic in the seismic records (SPZ) from a single event. Commonly, however, ISC focal depth determinations are not based on  $pP$  times but on  $P$  arrival times. Identification of  $pwP$  as  $pP$ , on SPZ, would then result in positive delay times, which may, however, be too large to be confirmed by the ISC and may be excluded from the catalog, because ISC only identifies phases close to the JB arrival time.

If the long-period impedance contrast at the sea bottom is small and the contrast at the sediment-basement interface large, then for thick sedimentary layers [ $pP$ ] may be the predominant phase on LPZ records. These picks would result in negative delays. The maximum in Figure 3.11a (operator identifications) near -9 sec may be due to reflection at the continental Moho. Schenk et al. [1989] show that reflections at the continental Moho can be sharp, but reflections at the oceanic Moho are less clear. In the latter case,  $pMP$  reflections may result in a smooth transition to  $pP$ , and the true  $pP$  onset may only be discerned by a change of slope and/or thinning of the seismogram trace [Schenk et al., 1989, their figures 4 and 9]. The  $pMP$  with an oceanic reflection point precedes the true  $pP$  by several seconds.

The contamination of the  $pP$  data set with [ $pP$ ],  $pwP$ ,  $swP$  and  $pMP$  and the use of routinely determined, frequently unreliable, focal depths can hardly be avoided if one relies on published phase data alone. Accurate determination of focal depth and  $pP$  time residuals is only possible if original seismograms are studied and the frequency dependence - SPZ or LPZ - is acknowledged [Forsyth, 1982; Engdahl and Billington, 1986]. For these analyses, Engdahl and Kind [1986] demonstrated, with data from the broad-band Graefenberg array, the particular advantages and promising value of digital broad-band data. The further development of worldwide networks of digital (particularly broad-band) seismographs is therefore essential.

### 3.5 Residual differential times

In many investigations  $PP$  (or  $SS$ ) and  $pP$  data have been used in combination with other phases. The major advantages of taking the difference in travel time between the direct  $P$  phase and the later arriving  $PP$  or  $pP$  phase, are (1) the significant reduction of the effects of errors in the locations of station and hypocenter, in origin time and from near station heterogeneities, and (2) the possibility to confine the cause of the residual differential times

to the vicinity of the bounce point of the reflected wave. In this section we define parameters and derive the necessary relationships to analyze residual differential times. We also briefly discuss the conventional approach and its drawbacks.

In 1976 Stewart summarized a method to determine differential travel-time residuals ( $\delta t_{PP-P}$ ), described its advantages and discussed the underlying assumptions. Because of the simplicity and strength of the method, the derivation of Stewart has been used by many investigators [e.g., Girardin, 1980; Dorbath and Dorbath, 1981; Buchbinder, 1982; Darragh, 1985]. In this paragraph we follow a similar approach. Note, that - in contrast to the investigators cited- we combine the contribution of errors in origin time and event mislocation into one single relocation term and we treat the reflection point residual differently. We can write the  $P$ -wave travel-time residual as

$$\delta t_P = \delta t_{v,P} + R_{h,P} + R_{t,P}(\Delta) + R_{st,P} + \varepsilon_P \quad (3.3)$$

where  $\delta t_{v,P}$  is the travel time residual due to heterogeneous velocity structures along the  $P$  ray path.  $R_{h,P} = R_{h,P}(t, z, x, y)$  represents the contribution of errors in the hypocentral parameters, and  $R_{t,P}(\Delta)$  is the error in reference travel-time tables, which is due to the difference between the reference velocity model (Jeffreys-Bullen model in the case of ISC data) and the true one-dimensional average velocity structure.  $R_{st,P}$  is the station correction and  $\varepsilon_P$  is the reading error. Similarly, for  $PP$  residuals we write

$$\delta t_{PP} = \delta t_{v,PP} + R_{h,PP} + R_{t,PP}(\Delta) + R_{st,PP} + \varepsilon_{PP} \quad (3.4a)$$

where  $\delta t_{v,PP}$  is the effect of velocity structures along the  $PP$  ray path and  $R_{t,PP}(\Delta)$  is the error in reference travel-time tables for  $PP$  waves. For  $pP$  delay times:

$$\delta t_{pP} = \delta t_{v,pP} + R_{h,pP} + R_{t,pP}(\Delta) + R_{st,pP} + \varepsilon_{pP} \quad (3.4b)$$

Then the differential travel-time residual  $\delta t_{PP-P}$  should formally be written as

$$\begin{aligned} \delta t_{PP-P} &= \delta t_{PP} - \delta t_P \\ &= (\delta t_{v,PP} - \delta t_{v,P}) + (R_{h,PP} - R_{h,P}) + (R_{t,PP} - R_{t,P})(\Delta) \\ &\quad + R_{ST} + \varepsilon \end{aligned} \quad (3.5a)$$

where  $R_{ST} = R_{st,PP} - R_{st,P}$  and  $\varepsilon = \varepsilon_{PP} - \varepsilon_P$ .

Replacing all  $PP$  subscripts by  $pP$  gives the expression for the  $\delta t_{pP-P}$  differential travel-time residual.

In the conventional use of  $PP-P$  residuals [e.g., Stewart, 1976], approximations to equation (3.5a) are made. For lower mantle phases, the angle of incidence at the station will be almost the same for the  $P$  wave and the  $PP$  wave. It is usually assumed that the difference between the station corrections for  $P$  and  $PP$  is negligible, and thus  $R_{ST} \approx 0$ . By the same argument the contributions of  $R_{h,PP}$  and  $R_{h,P}$  will cancel in the case of shallow events [Stewart, 1976; Buchbinder, 1982]. The difference between contributions of velocity structures along the ray paths can be thought to be predominated by velocity anomalies in the vicinity of the reflection point. By taking  $R_{refl} \approx \delta t_{v,pP} - \delta t_{v,P}$ , equation (3.5a)

transforms to

$$\delta t_{PP-P} \approx R_{t,PP}(\Delta) - R_{t,P}(\Delta) + R_{refl} + \varepsilon \quad (3.5b)$$

[Buchbinder, 1982]. Stewart [1976] argues that for earthquakes within a limited source region, recorded at a restricted network of seismological stations, the difference between  $R_{t,P}(\Delta)$  and  $R_{t,PP}(\Delta)$  can be considered constant and be set to zero if one is interested only in relative values of  $R_{refl}$ . If it is also assumed that  $\varepsilon_P \approx \varepsilon_{PP}$  [Stewart, 1976; Girardin, 1980; Dorbath and Dorbath, 1981; Darragh, 1985], the expression for the residual differential-time further reduces to

$$\delta t_{PP-P} \approx R_{refl} \quad (3.5c)$$

[Stewart, 1976]. In Figure 3.12 we present the distribution of reflection point residuals, computed according to Stewart's approximation. We argue, however, that the approximations leading to (3.5b) and especially (3.5c) are not very accurate.

The assumption  $\varepsilon_P \approx \varepsilon_{PP}$  is only valid for clock errors, but not for reading errors [Buchbinder, 1982]. This is obvious if one acknowledges the problems in picking the *PP* onset and the existence of various sources of errors (see previous sections).

Buchbinder [in his Figure 3.1] not only showed that the value of the differential time residual strongly depends on the assumed reference model, but also that the difference  $R_{t,PP}(\Delta) - R_{t,P}(\Delta) = 2R_{t,P}(\Delta/2) - R_{t,P}(\Delta)$  cannot be considered constant. A similar result was found by Van der Hilst and Spakman [1989], who investigated the influence of the reference model on tomographic images [their figure 2].

Neither (3.5b) nor (3.5c) are valid for deep earthquakes, because *P* and *PP* waves sample different near-source regions and the difference between  $R_{h,P}$  and  $R_{h,PP}$  will not reduce to zero. Moreover, it can no longer be assumed that  $R_{refl} \approx \delta t_{v,PP} - \delta t_{v,P}$  and, in any case, this approximation is problematic because the extent of the velocity structures, at depth and laterally, contributing to  $\delta t_{PP-P}$  are not known. For example, if only lower mantle *PP* (and *P*) phases are considered, the "vicinity of the reflection point" comprises the whole upper mantle below the reflection point (Figure 3.1). Moreover, if one maintains this approximation, *P* delays will be mapped into  $R_{refl}$ . The argument that the lower mantle velocity structure is sufficiently homogeneous [e.g., Stewart, 1976] is not valid. Many investigators have demonstrated the existence of large-scale velocity structures in the lower mantle [e.g., Jordan and Lynn, 1974; Dziewonski et al., 1977; Grand, 1987; Van der Hilst and Spakman, 1989], although the amplitudes of the perturbations may be smaller than typical of the upper mantle. In this context, the inferences by Gudmundsson et al. [1989] from a stochastic analysis of ISC *P* delay times are relevant. They argue that, at least in mantle regions below subduction zones, a relatively high level of heterogeneity extends from ca. 300 km to ca. 1000 km in depth. (They report, however, lack of vertical resolution and we remark that the figure of 300 km, the lower limit of the strongly heterogeneous part of the upper mantle, may primarily reflect characteristics of the depth distribution of earthquakes). Besides, it can be inferred that even for large epicentral distances (e.g.,  $70^\circ$ ), the lateral distance between the *P* and the *PP* rays at the base of the upper mantle is still of

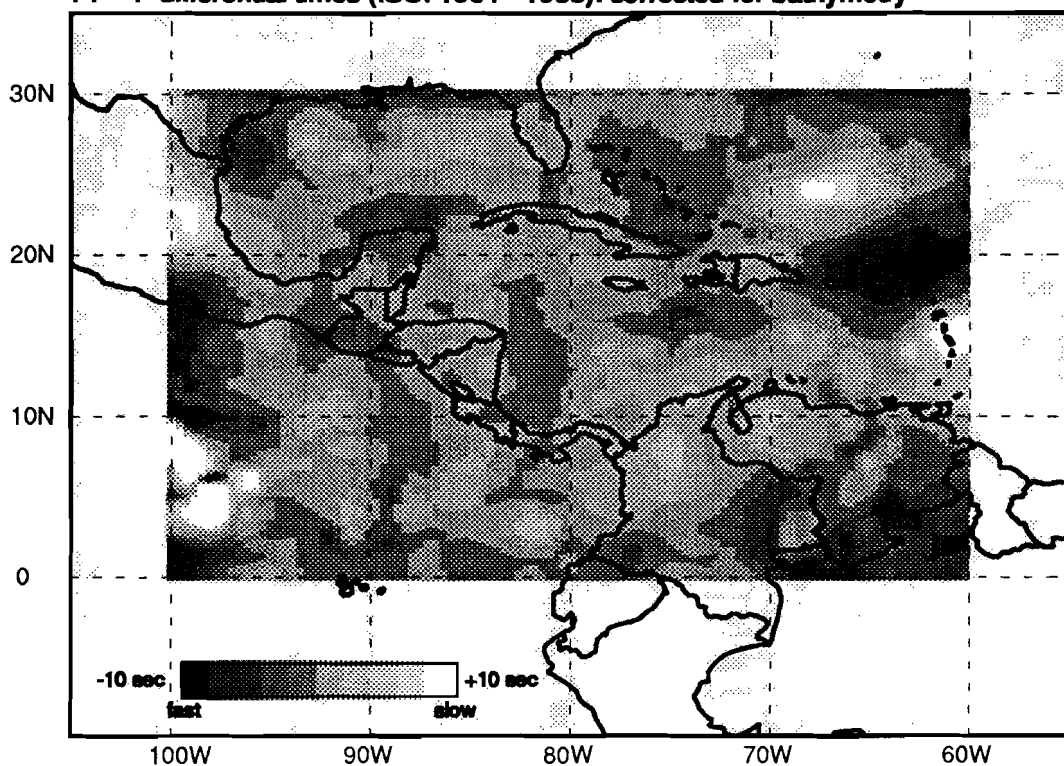
**PP - P differential times (ISC: 1964 - 1985): corrected for bathymetry**

Figure 3.12. Geographical distribution of  $\delta t_{pp-p}$  differential times plotted at the  $PP$  reflection point. The 1795 residuals used in this distribution were computed according to the approximations of Stewart [1976].

the order of  $3^\circ$ . Thus, also upper mantle structure sampled by  $P$  waves may be mapped into bounce point residuals, which is not desirable.

These objections and the restriction to shallow focii can be overcome by employing equation (3.5a) directly, in which case the  $PP$  and  $P$  ray paths and associated residuals are treated separately. As we will see below, this approach has the additional advantage that the calculation of  $\delta t_{pp-p}$  is straightforward. Equation (3.5a) is difficult to deal with in the conventional approach of differential travel times, but can be solved by inversion.

### 3.6 Tomographic inversion of PP and pP delay times

In our tomographic investigation of the mantle  $P$ -velocity structure below the Caribbean region with  $P$ ,  $PP$  and  $pP$  phases, we will take advantage of the conventional differential travel-time approach wherever possible. We determine the velocity structure by solving the system of equations formed by (3.3) for the direct  $P$  phases only, by (3.4a) and (3.4b), in case only the  $PP$  or  $pP$  residual is known, and by (3.5a), if the corresponding  $P$  delay times are also present in the data set and differential travel-time residuals can be formed.

We expect that the incorporation of differential travel-time residuals is beneficial for the convergence of the iterative inversion. In this section we present results of our investigation and compare the solutions obtained from inversion of  $P$  data only with the solutions obtained by inverting the combination of  $\delta t_{PP}$ ,  $\delta t_{pP}$ ,  $\delta t_{PP-P}$  and  $\delta t_{pP-P}$  delay times. We also show results of a tomographic inversion in which all ( $P$ ,  $PP$  and  $pP$ ) data are used. A geodynamic discussion of the tomographic images presented in this section will be published elsewhere. Our present objective is to focus on the justification and effects of incorporating  $PP$  and  $pP$  phases in the inversion scheme.

### 3.6.1 The tomographic system of equations

The three-dimensional velocity structure of the mantle region under study was subdivided into rectangular blocks with horizontal dimensions of  $1.25^\circ$  by  $1.25^\circ$  and vertical dimensions ranging from 33 km for the top layer to 150 km for the bottom layer, centered at a depth of 1235 km. The ray geometry of the  $P$ ,  $PP$  and  $pP$  waves in this 3D cell model, was determined by ray tracing in a one-dimensional reference model of seismic velocities. In this study, we linearized the inversion problem using reference model VCAR, derived in a study by Van der Hilst and Spakman [1989]. We refer to chapter 1 for more details. The system of linear equations to be solved by tomographic inversion, consists of the linearized, discrete, equivalents of (3.3), (3.4a,b) and (3.5a). This system can be represented by a simple matrix equation (see Appendix A).

We followed Van der Hilst and Spakman [1989] and corrected the  $PP$  and  $pP$  delays relative to the regional 1-D velocity model VCAR. By doing this, the terms  $R_{t,P}$ ,  $R_{t,PP}$  and  $R_{t,pP}$  in equation (3.5a), are removed from the tomographic equations (3A.5) prior to inversion. After this correction we discarded the residuals outside the  $[-7.5, +7.5$  sec] delay time window. The resulting frequency distributions are presented in Figure 3.13b and 3.13c for  $PP$  and  $pP$  data, respectively. Figures 3.13a-c give the frequency distributions of the travel time residuals for the different seismic phases prior to inversion and after all the corrections mentioned above.

The tomographic system of equations is solved by least squares, using the conjugate gradient algorithm LSQR of Paige and Saunders [1982]. For all results shown below, 30 iterations were used. The variance reduction during inversion is 33% for the combined data set (Table 3.2). For the separate seismic phases the reductions during the combined inversion are given in Table 3.2, and are illustrated by the frequency distributions of the travel time residuals of the  $P$ ,  $PP$  and  $pP$  phases, before and after the inversion (Figure 3.13).

For details and theory of the tomographic inversion we refer to Paige and Saunders [1982], Nolet [1985], Spakman and Nolet [1988] and Spakman [1988].

### 3.6.2 Hitcount

In section 3.2 we used the hit count as one of the indicators of the quality of the illumination with seismic waves, showing regions of "under exposure" in the Caribbean region. In Figure 3.14a we show the illumination by  $PP$  and  $pP$  rays of the cells in the top

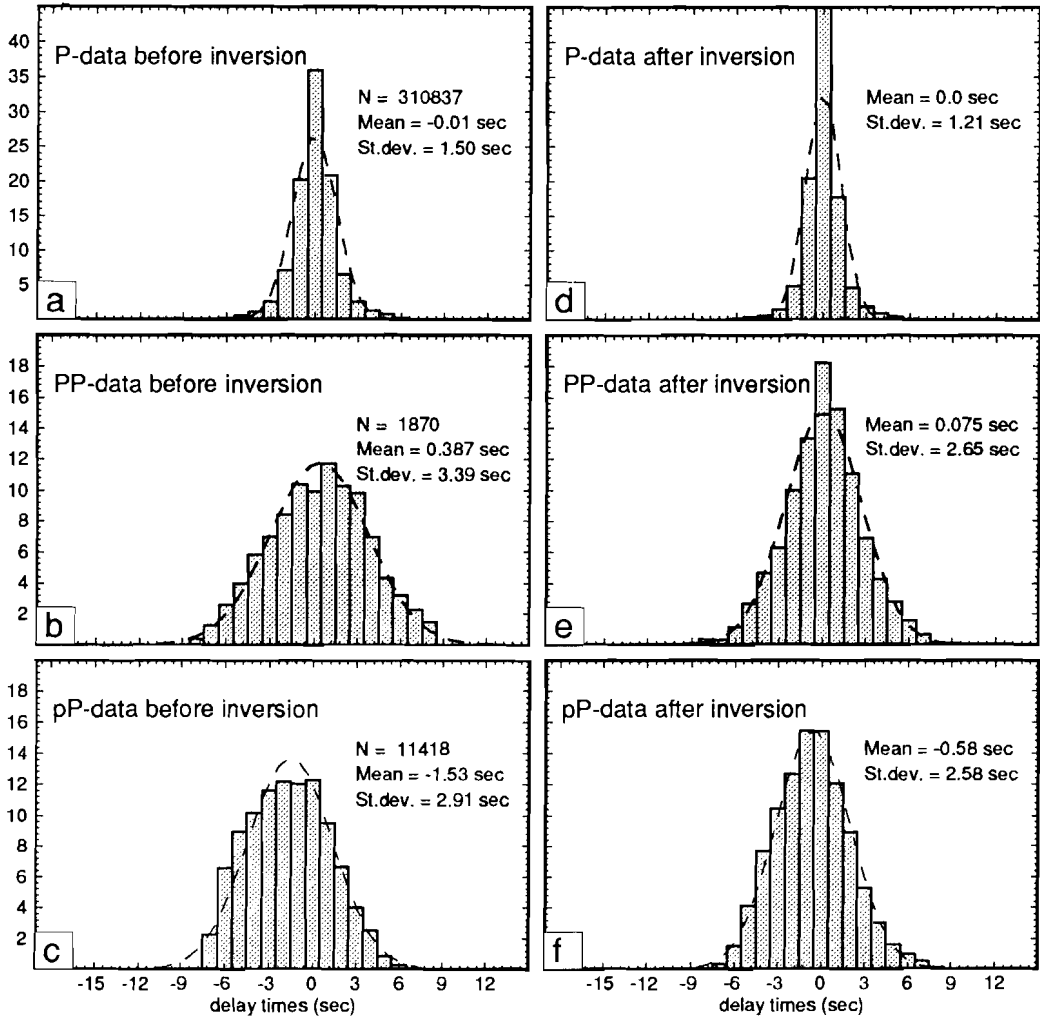


Figure 3.13. Frequency distributions of  $P$ ,  $PP$  and  $pP$  data before and after inversion. During the computation of matrix  $A$  in equation (6), the delay times were corrected relative to a reference model different from the Jeffreys-Bullen model [see Van der Hilst and Spakman, 1989]. (a,d)  $P$  delay times, (b,e)  $PP$  delay times  $\delta t_{PP}$  combined with residual travel-time differences. (c,f)  $pP$  delay times  $\delta t_{pP}$  combined with  $\delta t_{pP-P}$ .

layer of the model. To better illustrate the quantitative improvement of the sampling of Earth structure due to incorporation of  $PP$  and  $pP$  data, we present with Figure 3.14b a map in which the shaded areas show where the combined hit count of  $PP$  and  $pP$  phases equals or exceeds the  $P$  hit count. We observe that, in particular, intraplate regions at this depth level benefited from the addition of  $PP$  and  $pP$  phases. Similar figures constructed for deeper layers (Appendix 3B) demonstrate that the excessive  $PP + pP$  hit count below the

	$P$	$PP$	$pP$	All
number of iterations	30	30	30	30
weighting factors	1.0 (1.4)	2.2	2.2	-
mean (before inversion)	-0.0131	0.387	-1.53	-
$\sigma$ (before inversion)	1.50	3.39	2.91	-
mean (after inversion)	0.00323	0.075	-0.582	-
$\sigma$ (after inversion)	1.21	2.65	2.58	-
variance reduction	35.0%	38.9%	21.4%	33.0%

Table 3.2: Numerical information about the delay time inversions. In all inversions the same parameters for damping, smoothing, station corrections and relocation are applied.

Caribbean Plate decreases rapidly with depth, whereas the depth extent of the differential hit count in the Gulf area, below the Guyana shield and, in particular, near the Bahama's and the Galapagos Islands, is much larger. As mentioned in the third section, it is important to recognize that, although the  $PP$  and  $pP$  hit count may be lower than the  $P$  hit count in many parts of the model, cells are illuminated from different directions by the reflected waves, thereby improving the quality of the ray geometry. We will show below that the independent information supplied by  $PP$  and, particularly,  $pP$  data produces significant changes in the tomographic images of upper mantle layers (e.g., Figure 3.16). Figure 3.14c is a composite map of Figures 3.3 and 3.14a and displays the hit count for the top layer in the case where all phases are used.

### 3.6.3 Effects on spatial resolution of the addition of $PP$ and $pP$ phases

The assessment of spatial resolution in tomographic images is still a problem in large-scale seismic delay-time tomography. To obtain estimates of resolution, one approach is to compute the inversion response to a known 3D input model of seismic velocities [Spakman and Nolet, 1988, Humphreys and Clayton, 1990]. In this paragraph we discuss the differences in performance between the  $P$  inversion and the  $P + PP + pP$  inversion in response to a harmonic sensitivity model [Spakman and Nolet, 1988 (page 175)].

The velocity structure in every layer of the input model consists of two superposed sine functions, with an amplitude of 5% velocity perturbation relative to the reference model. A set of synthetic delay times is calculated, by adopting the ray geometry computed for the real data experiment. To mimic the statistical properties of the true delay times, randomly distributed noise is to the synthetic data. The ability of the tomographic inversion algorithm to recover the input model by inversion of the synthetic (and noisy) data, can then be used to assess the resolution in the tomographic image derived from the true travel-time residuals.

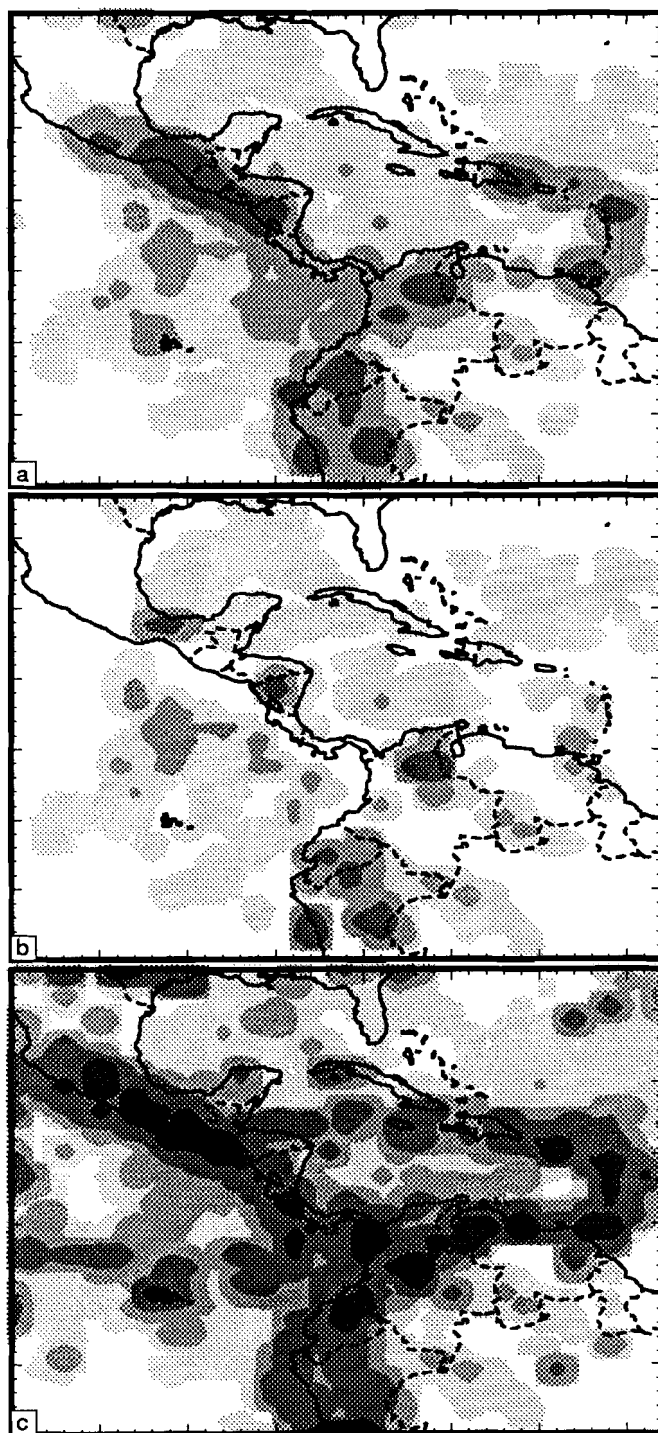


*Figure 3.14.* Effect on hit count of the addition of *PP* and *pP* data for the top layer of the cell model: (a) *PP* + *pP* hit count, (b) map of the areas where the *PP* + *pP* hit count equals or exceeds the *P* hit count. (c) hit count if all phases are considered.



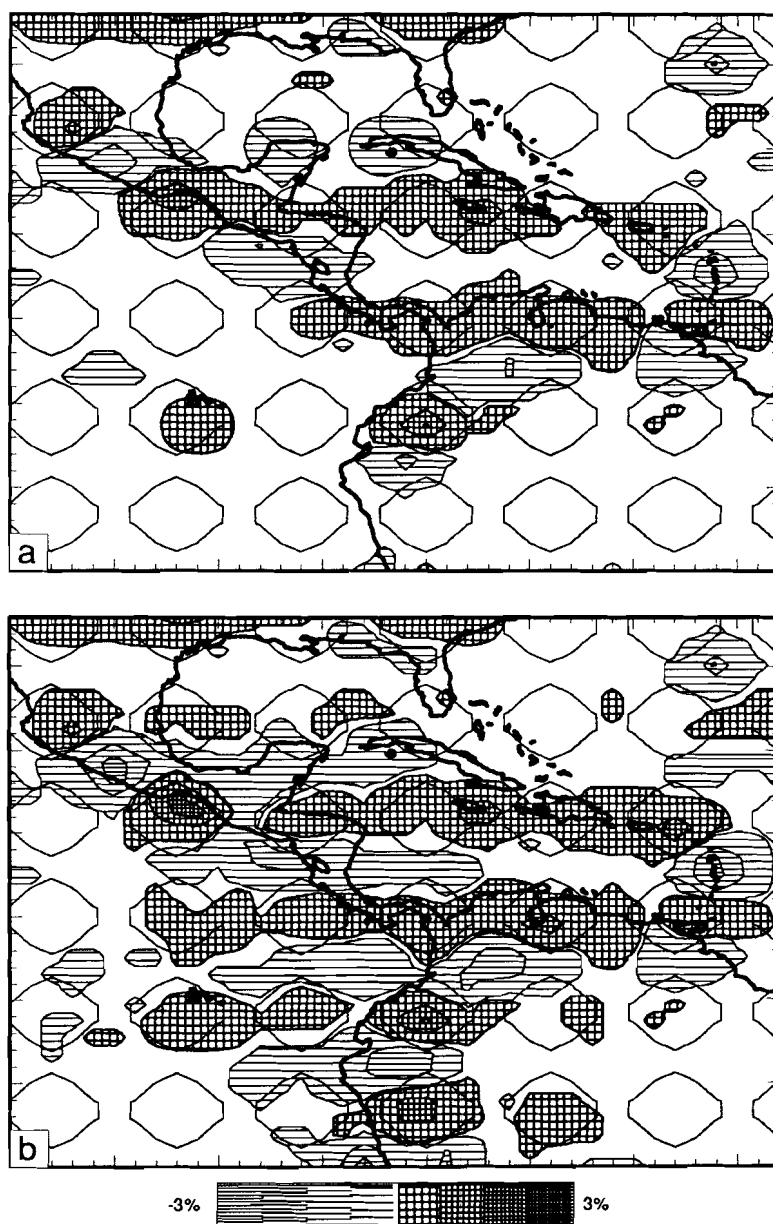


*Figure 3.15.* Results of harmonic sensitivity tests for the top layer of the cell model. Random noise was added to the synthetic travel-time residuals, with standard deviations depending on the type of seismic phases (see text). (a) Response to the ray geometry determined by the *P* phase, and (b) after inclusion of *P*, *PP* and *pP* phases.

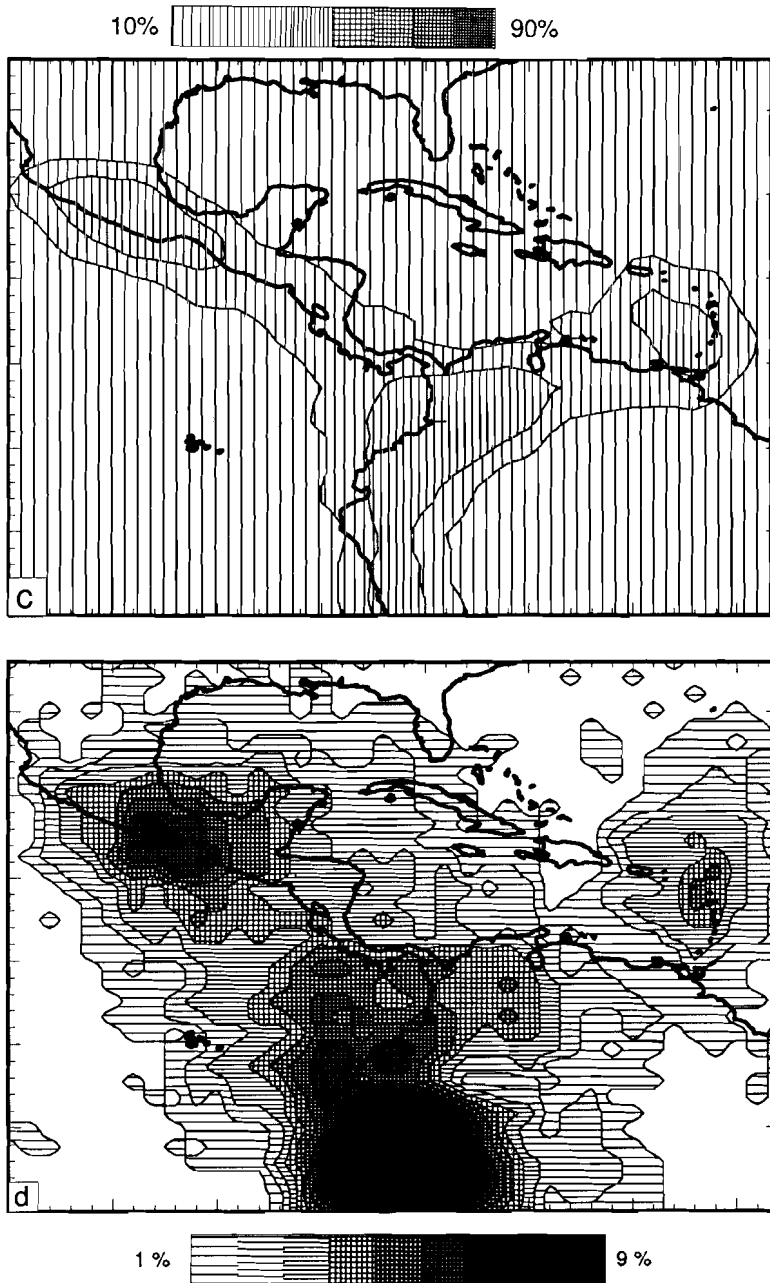


(Figure 3.15 continued) (c) laterally smoothed harmonic fit for top layer of the model (d) regions where the harmonic fit benefited by the inclusion of *PP* and *pP* data.

With the harmonic sensitivity test, results of which are presented in this paragraph, we investigate the resolution of smoothly varying, lateral velocity perturbations with scale

lengths of some hundreds of kilometers, typical for the velocity structures in the upper mantle. We remark that this kind of test only yields information about the performance of a particular inversion algorithm (here LSQR) in combination with a fixed, reference ray geometry. Neither the uncertainties in the ray geometry, nor the possible non-randomness of the travel time residuals (e.g., in the triplication range), are taken into account in the test [Van der Hilst and Spakman, 1989]. Of importance for this study is that the noise level of the constituent phases differ, and that, as we have seen in the above section about the data, many sources of systematic sources of errors exist for  $PP$  and  $pP$  travel-time residuals. Moreover, possible inconsistencies between hypocentral parameters and travel time residuals, e.g., as we discussed for the  $pP$  phase, are not modelled by synthetic tests.

To model the larger errors in  $PP$  and  $pP$  data relative to  $P$  data, we added more noise to the synthetic data corresponding to  $PP$  and  $pP$  rays. As scaling factors, we adopted the reciprocals of the figures we used to weigh the matrix rows: we added Gaussian noise with  $\sigma = \sqrt{\gamma} \times 0.8$  sec to the data, with  $\gamma$  as defined in Appendix A. Note that we attributed greater variance to the  $P$  residuals obtained from readings between 15 and 25°. The distribution of the delay times, used in this study, versus epicentral distance [Van der Hilst and Spakman, 1989] and the statistical investigation of Gudmundsson et al. [1989] demonstrate a greater scatter of delay times in this distance range. As in the real data inversion, we also performed row weighting in the inversion of synthetic data by effectively left-multiplying matrix  $A$  in equation (3A.5) and (3A.7) with weight matrix  $W_{ph}$  and left-multiplying the data vector  $d$  with  $W_{ph}^{-1}W_{ph} = I$ .

In Figure 3.15 we present the results of the harmonic sensitivity tests for the top layer of the model: Figure 3.15a gives the result of the  $P$  experiment, and Figure 3.15b the response if all seismic phases are incorporated. For this depth level we observe a rather poor recovery of the input amplitudes, both for the  $P$  as well as for the  $P + PP + pP$  case. However, from similar figures constructed for deeper levels (Figures of Appendix 3B) and from Figure 3.16, we demonstrate that with depth the match of both the input pattern and the amplitudes strongly improves. For the  $P$  inversion, large areas in the top layer do not indicate the presence of anomalies. Although in many regions the amplitude recovery may be low, when all phases are considered the sign of the velocity perturbation is more often mapped correctly than in the  $P$  experiment. In Figure 3.15c we display the harmonic response in a different way, because straight comparison of the output model with the input model may be difficult and gives mainly local information. The harmonic model fit represents the quality of the image recovery in every cell, smoothed both laterally and with depth with a moving-average window [Spakman and Nolet [1988]. We infer from Figure 3.15c, that for this crustal layer, reasonable (> 30%) recovery of the input model occurs in a rather narrow zone along the Middle America trench, the northern Plate Boundary Zone, and along the Colombia-Peru convergent boundary. Because we emphasize the effect of incorporating  $PP$  and  $pP$  phases in the  $P$  delay-time inversion, we are not as much interested in the overall harmonic fit but in the differences between the fit of the  $P$  inversion and the result if all phases are included. Figure 3.15d displays only those areas where the  $P + PP + pP$  harmonic fit is better than the harmonic fit with  $P$  phases only.

(Note the difference in scale). As expected, nowhere in the model is the  $P+PP+pP$  fit worse than the  $P$  fit. Figure 3.15d demonstrates that over a large area (slightly exaggerated due to the lateral smoothing) the model fit benefited from the inclusion of later arrivals. In particular near the Middle America trench and in the northwestern part of South America the improvement in the harmonic model fit is substantial. For example near central Mexico, the  $P+PP+pP$  fit exceeds the  $P$  fit with over 6% (Figure 3.15d). With an absolute fit in the order of 40-50% (Figure 3.15c), the relative gain due to the incorporation of  $PP$  and  $pP$  data is in the order of 15%. Although the model fit with all data is better than the  $P$  fit, the difference decreases rapidly with depth (also Figure 3.17). For the entire model, including all cells- including poorly illuminated cells - the fit increased from 17.9% to 18.5%, a gain of nearly 3%.

### 3.6.4 Implications for the velocity structure

The solution of the tomographic system of equations in terms of velocity perturbations relative to the reference model (VCAR), is given in Figure 3.16. Figures 3.16a-d show the solution for the top layer of the model (0 to 33 km depth) from the  $P$  inversion, the  $PP$  inversion, the  $PP + pP$  inversion, and the inversion which incorporates all phases. Although the amplitudes of the velocity perturbations in this layer are not well resolved (see previous paragraph), we present this result because it illustrates the effect of the implementation of the  $PP$  and  $pP$  phases in the tomographic inversion.

First, we draw attention to the resemblance between the images of the  $P$  inversion (Figure 3.16a) and features in the images of the  $PP$  and  $PP + pP$  inversions (Figures 3.16b and 3.16c). From the consistency between these images (and the solutions at larger depths), we conclude that, in spite of the many sources of (substantial) errors,  $PP$  and  $pP$  residual-time data can yield useful information in tomographic studies.

The result of the  $P$  inversion (Figure 3.16a) suggests rather strong lateral heterogeneity in the velocity structure along the Middle America trench and the northwest coast of South America. In contrast to this image, the velocity structure in the same geographical zone is smoothly resolved by the inversion of  $PP$  and  $pP$  delay times (Figure 3.16c). Despite the higher  $P$  hit count (Figure 3.16b), the densely and rather homogeneously distributed  $pP$  rays (Figures 3.8 and 3.14a) contributed significantly to the image (Figure 3.16d). We remark that the large shift in mean value of the  $pP$  delay-time distribution (from -1.5 sec to -0.5 sec, Figure 13) is accommodated by high velocities near the reflection points and by relocation of the earthquakes to shallower depths.

To further demonstrate the influence of the  $PP$  and  $pP$  phases on the results of tomographic inversions, we present an upper mantle section across the Middle America trench near the boundary between the cratonic Chortis block and southern Central America (Figure 3.17). For this northeast-southwest trending section, the velocity perturbations are given for the  $P$  solution in Figure 3.17a. At larger depths below Middle America, part of a high-velocity feature is visible that is continuous in a northwest to southeast direction and

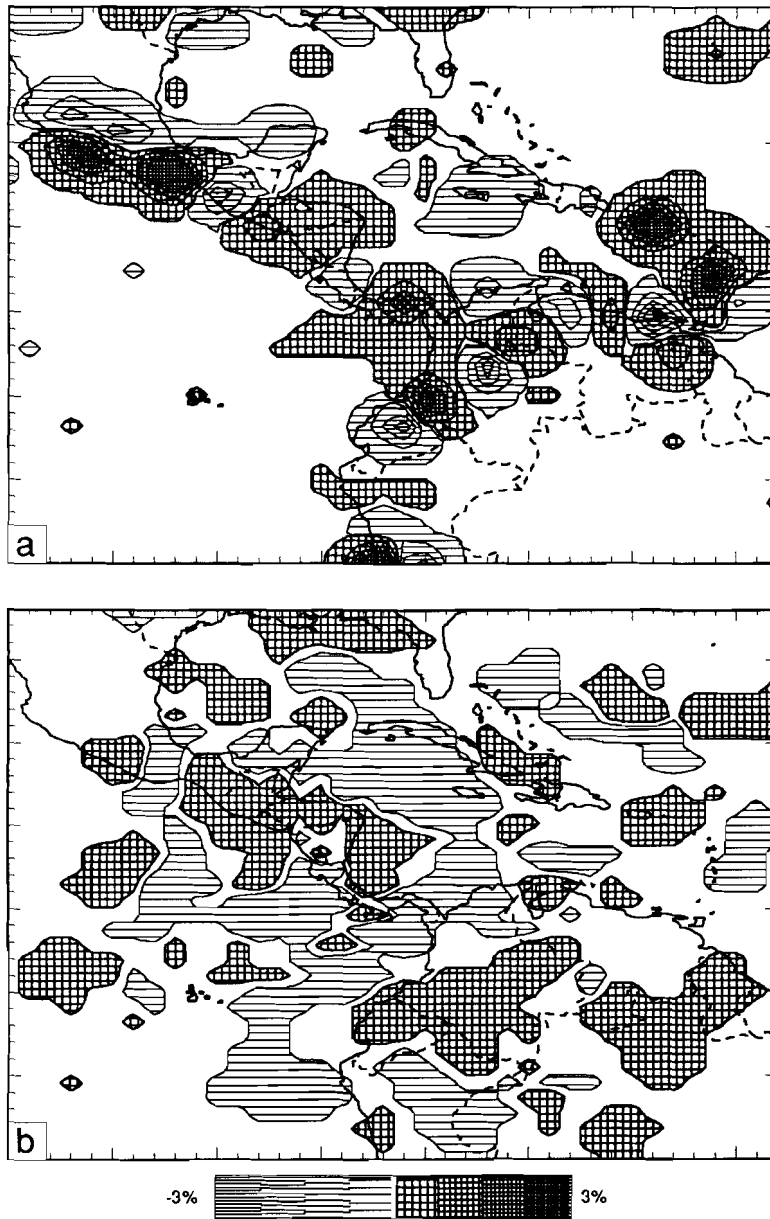
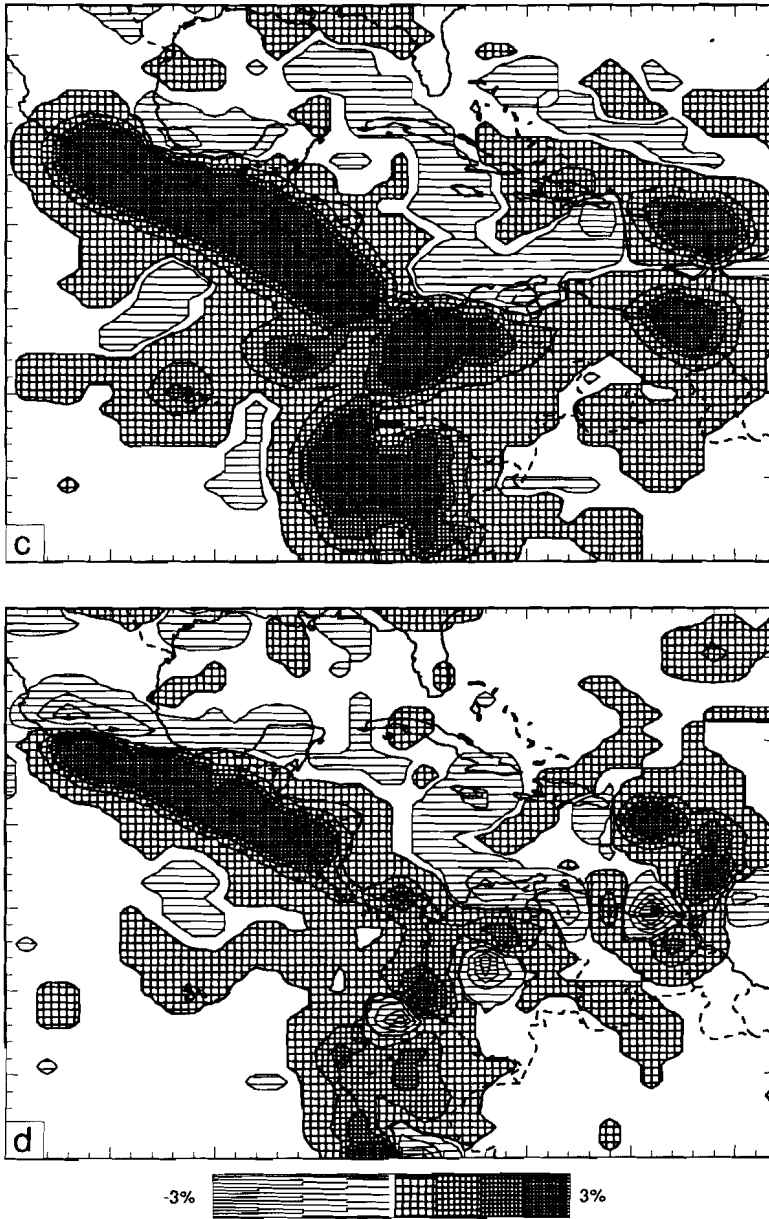


Figure 3.16. Velocity perturbations relative to a 1-D reference model. Results of the inversion of respectively (a)  $P$  delay times ( $\delta t_P$ ), (b)  $\delta t_{PP}$  and  $\delta t_{PP-P}$ .



(Figure 3.16 continued) (c)  $\delta t_{PP}$ ,  $\delta t_{PP-P}$ ,  $\delta t_{pP}$  and  $\delta t_{pP-P}$ , (d) all phase data:  $\delta t_P$ ,  $\delta t_{PP}$ ,  $\delta t_{pP}$ ,  $\delta t_{PP-P}$  and  $\delta t_{pP-P}$ .

apparently extends into the lower mantle [also Van der Hilst, 1989; Van der Hilst and Spakman, 1989]. The presence of this high-velocity structure in tomographic images is consistent with and confirms results of earlier investigations [Jordan and Lynn, 1974; Lay, 1983; Grand, 1987; Vidale and Garcia-Gonzales, 1988]. The morphology of this feature is very much comparable in the results of both the  $P$  inversion and the  $P + PP + pP$  image. The velocity structure in the mantle below Central America is discussed in more detail in chapters 5 and 6. At shallower depths (down to 400km) the two experiments yield, however, entirely different images. In Figure 3.17a the seismicity apparently bears no clear relation with the velocity structures shown. Earthquake hypocenters in Figure 3.17b appear to occur within a slab-like high-velocity structure. In this depth interval the  $PP$  and particularly the  $pP$  phases contribute significantly to illumination of the structure. By comparison of the harmonic model fits of the  $P$  case and the  $P + PP + pP$  inversion (previous section), we can demonstrate that the resolution in the section of Figure 3.17b is better than that of Figure 3.17a. Figure 3.17c represents the differences in harmonic fit for the same cross section (for explanation see section 3.6.3). From Figure 3.17c it can again be inferred that the shallow levels of the image gained most from the inclusion of later arrivals. Near the 390 km discontinuity the  $P + PP + pP$  fit is equals the  $P$  fit. At this depth level we observed a drop in image recovery (Figures B.7b and B.8b of Appendix 3B).

The location of the section of Figure 3.17 is near the sections discussed by Burbach et al. [1984] (sections B and C) and Burbach and Fröhlich [1986], sections MA2 and MA3. They investigated the geometry and possible segmentation of the Cocos Plate subducted below Middle America by examining reliable ISC locations of hypocenters of some hundreds of well-chosen earthquakes. The result presented in Figure 3.17 demonstrates, however, that the locations of earthquakes outline only (the shallow) part of the high-velocity structure, which can be tentatively be interpreted as the blurred image of the subducted Cocos Plate. The difference (and relationship) between the seismic (Wadati-Benioff) zone and structures that can be associated with subduction, is also observed in other convergent plate boundaries: the Aleutian subduction zone [Engdahl and Gubbins, 1987], the subduction of the African Plate below the Aegean Plate [Spakman et al., 1988], and the Lesser Antilles subduction zone [Van der Hilst, 1989; Van der Hilst and Spakman, 1989]. We argue that the imaging of the aseismic parts of subducted lithosphere complements valuable studies on seismicity [e.g., Burbach et al., 1984], and is crucial to tectonophysical and geodynamical interpretations.

### 3.7 Conclusions

In this paper we investigated the value of published  $PP$  and  $pP$  phase data in tomographic delay-time inversions. Incorporation of  $PP$  and  $pP$  phases in this tomographic study can potentially improve the quality of the images because: (1), these phases sample Earth structure not ordinarily sampled by direct  $P$  phases; (2), these phases add rays that are oblique to rays of direct phases, which is especially important where the latter sample mantle structure in selected directions; and (3),  $pP$  data better constrain the earthquake focal depths. We demonstrated, from the distribution of reflection points and the cell hit

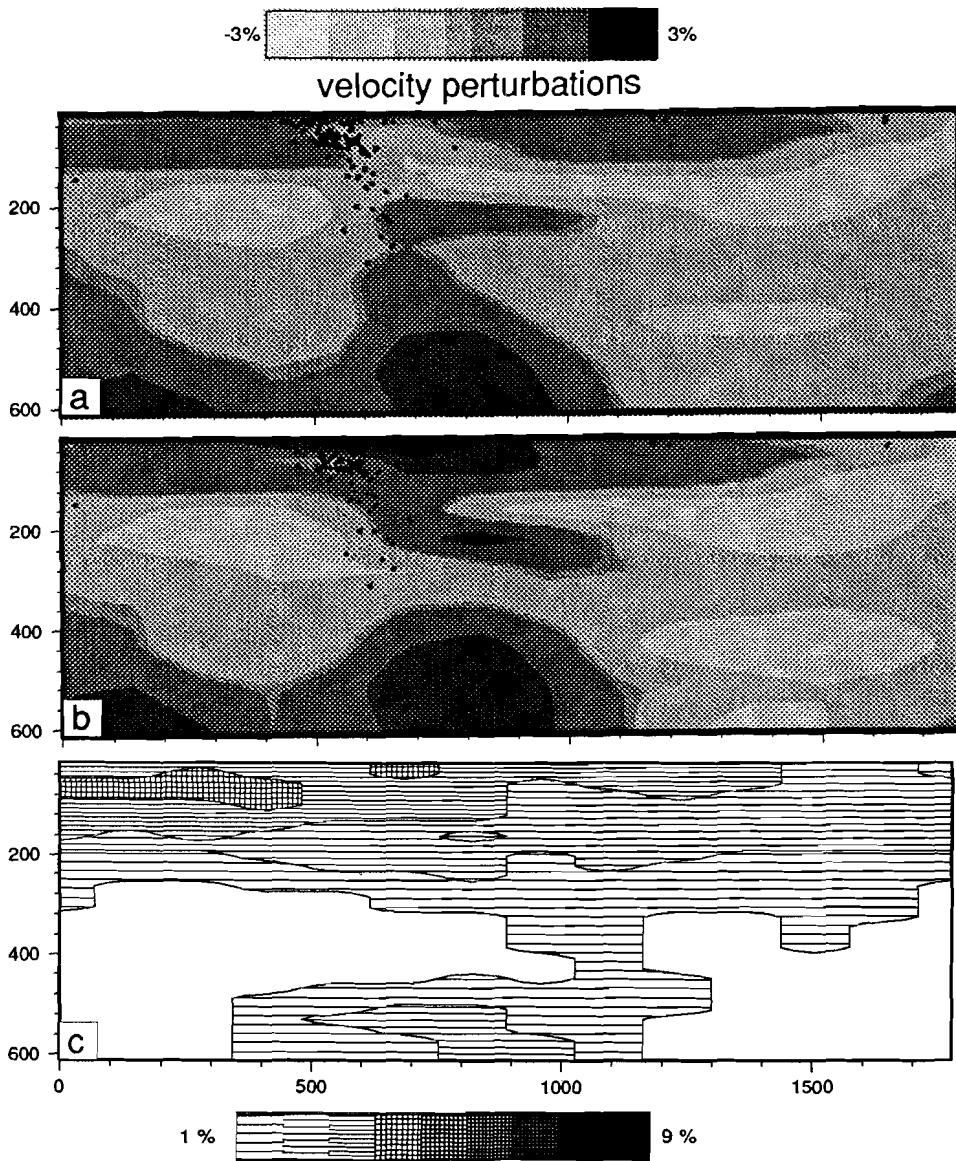


*Figure 3.17. Vertical upper mantle cross sections illustrating the differences between the  $P$  and the  $P + PP + pP$  solution. The cross section is constructed across the Middle America subduction zone near the Lake of Managua (Nicaragua). (a) Result of  $P$  inversion, (b) Result of  $P + PP + pP$  inversion. (c) Mantle regions where  $P + PP + pP$  harmonic fit is better than the  $P$  fit.*

count, that  $PP$  and  $pP$  waves contributed positively to ray geometry in the cell model employed in the tomographic investigation and thus to the sampling by seismic waves of



mantle structure below the Caribbean region. We note, however, that because of the relatively shallow seismicity in the area, the difference between ray paths of  $pP$  waves and the direct  $P$  wave is small.

We investigated the possibility that large errors (as compared to  $P$ ) in reported  $PP$  and  $pP$  travel-time residuals may decrease the quality of the tomographic images. We did not attempt to improve the quality of the data set by the addition of high-quality digital data. Rather we summarized the different sources of errors in ISC phase data and assessed the contributions of these errors to the  $PP$  and  $pP$  delay times. We did not discern systematic biases in the reported  $PP$  data, which may be due to the random character of the errors or due to the properties of the ISC identification program. No evidence is found for the predominance of  $pwP$  phases, misidentified as  $pP$ , in the  $pP$  data set for the Caribbean region. The ISC reported focal depths are determined from direct  $P$  arrival times. We conclude that the  $pP$  delay times reported by the ISC are inconsistent with these depths. In the inversion, the large negative mean value of the  $pP$  delay-time distribution was accommodated by shallower foci and high velocity images in the top layer of the cell model. The larger errors in  $PP$  and  $pP$  data relative to  $P$  data are recognized in the weighting scheme used in the inversion.

We showed that, despite the many sources of (large) errors in  $PP$  and  $pP$  data and the difficulty to assess their individual contributions, simultaneous inversion of ISC  $PP$  and  $pP$  data provide tomographic images consistent with  $P$  images. From this observation we conclude that the ISC delay times of later arriving phases such as  $PP$  and  $pP$  do contain valuable information about velocity structures in Earth's mantle.

In contrast, the correlation between the results of the tomographic inversion of  $P$ ,  $PP$  and  $pP$  data and the image resulting from differential travel-time or reflection point residuals is not significant. We argued that one of the major drawbacks of the conventional approach to differential travel-time studies [e.g., Stewart, 1976] is that the residual is assumed to be caused primarily by velocity structures in the vicinity of the reflection point. The depth extent of the velocity anomalies contributing to the travel time residuals is, however, not known and may comprise the whole upper mantle in the case where only teleseismic data are considered.

We demonstrated the improved spatial resolution when  $PP$  and  $pP$  phases are included in this tomographic study. Below large areas we still have to cope with lack of spatial resolution, either due either to serious underexposure by the particular seismic waves incorporated in the study or the low quality and high noise level of the data. These provide arguments for a further expansion and improvement of global networks of digital recorders, both on land and sea(bottom). We realize that, for the mantle below the Caribbean region, improvements due to the inclusion of  $PP$  and  $pP$  data on image resolution and changes in velocity structure are small. This is not surprising because (1) the number of  $pP$  and particularly  $PP$  data is very low with respect to the number of  $P$  data, (2) we had to decrease the influence of  $PP$  and  $pP$  data even further because of the higher level of data errors, and (3), the difference in ray geometry between  $pP$  waves and the direct  $P$  waves is small due to lack of seismicity at greater depths.

With these arguments in mind, we conclude that the incorporation of *PP* and *pP* phases in the *P* delay time tomographic study of the velocity structures in the Caribbean mantle has been successful. Much care should be taken in correcting for bathymetry and topography and in the proper choice of a reference model. The modification and extension of software, necessary to incorporate the surface reflected *PP* and depth phase *pP* (together with *PP-P* and *pP-P* differential times) in tomographic investigations, is straightforward. We argue that with relatively small efforts tomographic images can be obtained with higher spatial resolution.

In some respects this study can be considered preliminary. With regard to the data errors, much work remains to be done. In particular, the effect of waveform distortions due to phase shifts (Hilbert transforms) in each frequency component of the *PP* phase [Choy and Richards, 1975] and the contamination of the *pP* delay times with reflections at surfaces other than those assumed [Engdahl and Billington, 1986; Schenk et al. 1989] need further attention. The examination of high-quality digital data, preferably broad-band [Engdahl and Kind, 1986] may be essential for this purpose. Finally, the inconsistency between ISC focal depths and the reported *pP* delay times needs to be examined by those responsible for the routine processing of data at the ISC.

By virtue of the improvements realized in the Caribbean region, application of the method to areas with a greater depth distribution of earthquake foci is promising. We are presently working on a simultaneous tomographic inversion of *P*, *PP* and *pP* delay time data (together with the differential residual times), to further investigate northwestern Pacific subduction zones [Van der Hilst et al., 1990b]. Because of the deep seismicity in that area, differences between *pP* and *P* ray paths are large and, consequently, shallow mantle structures below back-arc (Sea of Japan) and intraplate areas (Philippine Plate) within this region will be better illuminated by *pP* waves. Better constraints on the shallow structures and on the focal depths also improve resolution of the subducted Pacific Plate in the down-dip direction. This improvement is important to the investigation of the morphology of the subducted slab near the 670 km discontinuity.

#### *Acknowledgments:*

RvdH thanks the USGS in Colorado for their hospitality during his visits. The help of Jim Taggart in selecting the WWSSN analog data from the USGS microfilm library was appreciated. Bob Woodward kindly provided RvdH with some useful software. Discussions with Guust Nolet and Bob Woodward improved the manuscript. The visits of RvdH to the USGS were supported by NATO (grant 0910/87). This investigation was financially supported by the Netherlands Organization for Advancement of Pure Research (NWO).

### Appendix 3.A: The tomographic system of equations

Following for example the derivations by Spakman and Nolet [Spakman, 1988; Spakman and Nolet, 1988], we can rewrite equation (3) to

$$d_i = (\delta t_P - R_{t,P}(\Delta))_i \approx \delta t_{v,P} + R_{h,P} + R_{st,P} \quad (3A.1)$$

$$\approx \int_{L_o} \Delta s \, dl_o + \Delta \mathbf{x} \cdot \nabla_{\mathbf{x}} T_o + \Delta t + R_{st,P} \quad (3A.2)$$

$$\Rightarrow \sum_{l=1}^{nbloc} L_{il} s_l + \sum_{m=1}^4 G_{ij}^m g_j^m + H_{ik} h_k, \quad i=1, \dots, ndata \quad (3A.3)$$

To obtain (3A.2) we linearized the travel time residual and replaced  $\delta t_{v,P}$  by the ray integral of the slowness deviation  $\Delta s(\mathbf{r})$ , the difference between the actual earth's slowness field  $s(\mathbf{r})$  and the reference slowness model  $s_o(\mathbf{r})$ .  $L_o$  is the ray path in the reference model. The relocation part  $R_{h,P}$  is expressed in terms of the change in total travel time  $T_o$  due to a small change in  $\Delta \mathbf{x}$  in the source vector and the origin time error  $\Delta t$  (as shown in Appendix 2,  $\nabla_{\mathbf{x}}$  is an operator of partial derivatives with respect to cartesian focal coordinates). In (3A.3) *nbloc* is the total number of cells used in the investigation, and *ndata* is the number of data (per seismic phase) used in the investigation.  $L_{il}$  is the path length of the  $i$ -th reference ray in cell  $l$ ,  $G_{ij}^m$  is the  $m$ -th relocation component of  $\nabla_{\mathbf{x}} T_{ij}$ , where  $\nabla_{\mathbf{x}}$  contains derivatives with respect to the components of source vector  $\mathbf{x}_s = (z_s, x_s, y_s)$ ,  $T_{ij}$  is the total travel time of the  $i$ -th ray from the  $j$ -th event, and  $H_{ik}$  is a segment of ray  $i$  in station cell  $k$  with slowness anomaly  $h_k$ .

Equation (3A.3) can be computed for the  $P$ ,  $PP$  and  $pP$  parts of the problem. In case of differential times two sequential matrix rows corresponding to the reflected phase and the direct phase can simply be subtracted. With regard to the relocation part we have the following remarks:

- \* For the  $PP$  and  $pP$  phases, the coefficients of  $G_{ij}^m$  ( $m = 1, 2, 3, 4$ ) are calculated in the same way as for  $P$  waves.  $m = 1, 2, 3, 4$  correspond to the respective contributions of the origin time, focal depth, and latitude and longitude.
- \* In case of differential times subtraction of matrix rows leads to  $(G_{ij}^m)_{PP \text{ (or } pP)} - (G_{ij}^m)_P$  for  $m=1, 2, 3, 4$ .
  - For  $PP-P$  this difference becomes (very) small for all  $m$ 's, and the effect of origin time errors and hypocenter mislocation will indeed be decreased.
  - for  $pP-P$  the differences between the coefficients vanish for  $m=1, 3, 4$  but doubles for  $m=2$ . Consequently, effects of errors in origin time and latitude-longitude, will be reduced, while the focal depths will be stronger constrained.

- \* We avoided to add 4 unknowns to every  $PP$  or  $pP$  ray. For every  $PP$  and  $pP$  record we checked the event against previous event(-cluster) numbers. When the earthquake was already encountered in the computation of the  $P$  part of the

problem, the 4 relocation coefficients were stored in the same matrix column to better constrain the corresponding relocation parameters. Only in case of new events, extra relocation parameters are added to the system.

For the three phases, the linear system (3A.3) can be represented by a matrix equation. With

$$\mathbf{d} = \begin{bmatrix} \delta t_P - \mathbf{R}_{t,P} \\ \delta t_{PP} - \mathbf{R}_{t,PP} \\ \delta t_{pP} - \mathbf{R}_{t,pP} \end{bmatrix}, \quad \hat{\mathbf{L}}_{PP} = \begin{bmatrix} \mathbf{L}_{PP} \\ \mathbf{L}_{PP-P} \end{bmatrix}, \quad \hat{\mathbf{L}}_{pP} = \begin{bmatrix} \mathbf{L}_{pP} \\ \mathbf{L}_{pP-P} \end{bmatrix},$$

$$\mathbf{L} = \begin{bmatrix} \mathbf{L}_P \\ \hat{\mathbf{L}}_{PP} \\ \hat{\mathbf{L}}_{pP} \end{bmatrix} \quad (3A.4)$$

(where - for the subsequent seismic phases -  $\delta t_{P, (PP \text{ or } pP)}$  and  $\mathbf{R}_{t, P, (PP \text{ or } pP)}$  are respectively the data vectors containing the delay times (after the corrections mentioned in the section about the data), and the vectors containing the time differences between the Jeffreys-Bullen velocity model and the adopted reference model VCAR), and

$$\mathbf{A} = (\mathbf{L} \mid \mathbf{G} \mid \mathbf{H})$$

$$\mathbf{W}_{ph}^{-1/2} \mathbf{A} = \hat{\mathbf{A}}$$

$$\mathbf{W}_{ph}^{-1/2} \mathbf{d} = \hat{\mathbf{d}}$$

we write for (3A.3):

$$\hat{\mathbf{A}} \mathbf{x} = \hat{\mathbf{d}}, \quad \mathbf{x} = \begin{bmatrix} \mathbf{s} \\ \mathbf{g} \\ \mathbf{h} \end{bmatrix} \quad (3A.5)$$

where matrix  $\mathbf{L}$  contains all information about (reference) ray geometry in the cell model,  $\mathbf{G}$  is the matrix of earthquake relocation coefficients, and  $\mathbf{H}$  the matrix of station correction coefficients.  $(\mathbf{s} \mid \mathbf{g} \mid \mathbf{h})^T$  is the solution vector (slowness perturbations, relocation parameters and station corrections) and  $\hat{\mathbf{d}}$  is the delay time vector.

To take into account the fact that the uncertainty in  $PP$  and  $pP$  data is larger than in  $P$  data, we have to perform a weighting procedure. We therefore left-multiplied both sides of (3A.5) with a  $ndata \times ndata$  diagonal matrix  $\mathbf{W}_{ph}^{-1/2}$ , where  $\mathbf{W}_{ph}$  is

$$\mathbf{W}_{ph} = \begin{bmatrix} \mathbf{C}_P & \mathbf{C}_{PP} & \mathbf{0} \\ \mathbf{0} & \mathbf{C}_{PP} & \mathbf{C}_{pP} \end{bmatrix} \quad (3A.6)$$

where, e.g.,  $\mathbf{C}_P = \text{diag}(\gamma_P)$ . Formally, the system (3A.5) should have been weighted with the non-diagonal covariance matrix of the data, which is - due to lack of information about the correlation between individual data - generally approximated by the diagonal variance

matrix [Nolet, 1987a]. Using ISC data it is difficult to assess the standard deviation of each individual delay time. We therefore attribute the same variance to all data corresponding to a particular seismic phase [also Spakman and Nolet, 1988]. By taking different estimates of the variance we weight the different seismic phases constituting the tomographic system. In absence of reliable uncertainty estimates of data errors, the determination of the weights  $\gamma_{P, PP, \text{ or } pP}$ , the elements of  $\mathbf{W}_{ph}$ , is due to subjective considerations. It is important to realize that the distribution of the delay times as discussed in section 3.4 results from both errors and lateral heterogeneity. Consequently, the variance of the data prior to the inversions is not a proper measure of the noise in the data. The larger variance in  $PP$  and  $pP$  data distributions relative to  $P$  data, does not necessarily reflect a higher noise level, but could also be due to differences in sensitivity to lateral heterogeneities in the velocity structure. Hence, we discarded the variances of the frequency distributions of the  $P$ ,  $PP$  and  $pP$  phases prior to inversion as suitable weighting factors. Rather, we want to use the variance  $\hat{\sigma}^2$  of the  $P$ ,  $PP$  and  $pP$  travel time residuals after the inversion, because we feel that these numbers reflect more properly that part of the data that cannot be explained by the velocity structure, and can thus be regarded the variance of noise. Of course these values are unknown a priori. To obtain estimates of the variance reduction, we performed a test inversion with  $\mathbf{W}_{ph} = \mathbf{I}$  and computed the variances  $\hat{\sigma}_{P, PP \text{ or } pP}^2$  of the residual  $P$ ,  $PP$  and  $pP$  times after 30 iterations. Thus, for the diagonal elements of  $\mathbf{W}_{ph}$ , we have

$$\gamma_P = \hat{\sigma}_P^2, \quad \gamma_{PP} = \hat{\sigma}_{PP}^2, \quad \gamma_{pP} = \hat{\sigma}_{pP}^2 \quad (3A.7)$$

After the preliminary inversion without row weighting, we determined  $\hat{\sigma}_P$ ,  $\hat{\sigma}_{PP}$ , and  $\hat{\sigma}_{pP}$  to be 1.0 sec (1.4 sec for the triplication range data), 2.2 and 2.2 sec respectively.

Matrix  $\mathbf{W}_{ph}$  can thus be regarded as an approximated variance matrix. The least squares solution then involves the minimization of

$$\text{Min} (\mathbf{A} \mathbf{x} - \mathbf{d})^T \mathbf{W}_{ph}^{-1} (\mathbf{A} \mathbf{x} - \mathbf{d}) \quad (3A.8)$$

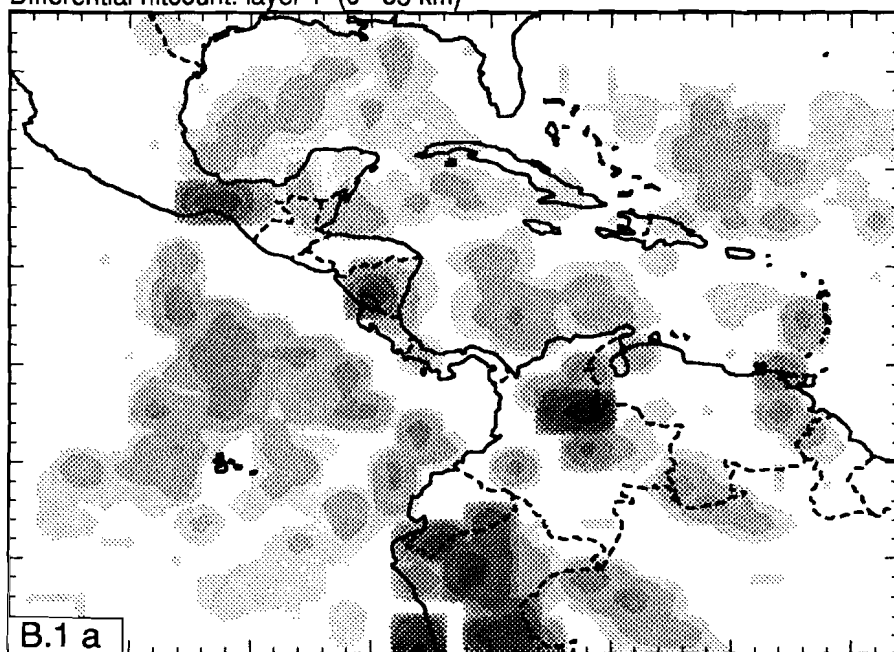
[Nolet, 1987a (eqn. 44 )].

### Appendix 3.B:

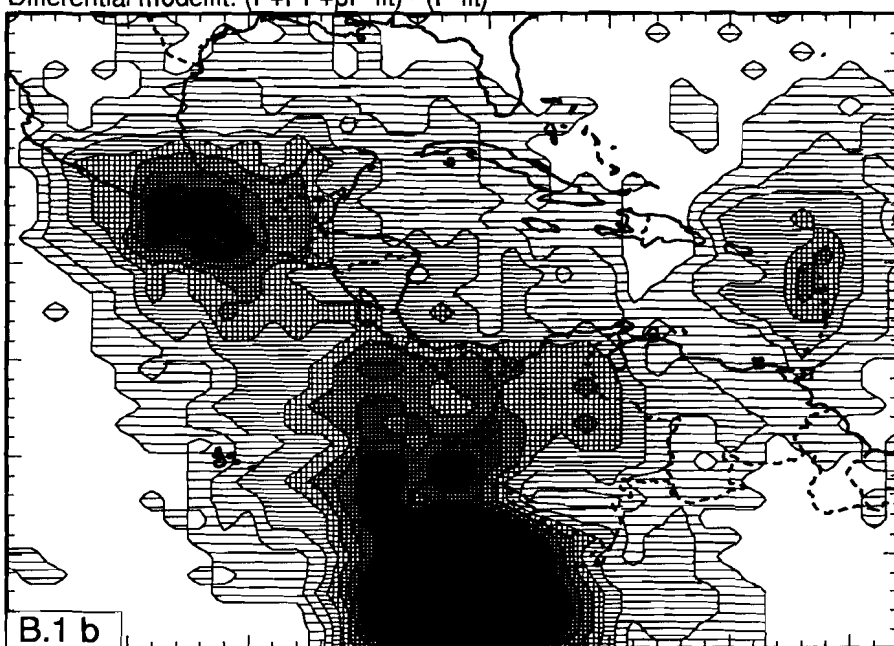
;

*Figure 3B.* Differences between cell hit count and harmonic model fit of the investigation with  $P$  data only, and the investigation with  $P$ ,  $PP$ , and  $pP$  data. The differences are presented for the (10) upper mantle layers. (a) Mantle regions where the combined hit count of  $PP$  and  $pP$  phases exceeds the cell hit count of the  $P$  phase only. (b) Mantle regions where the harmonic model fit has improved from the incorporation of  $PP$  and  $pP$  delay-time data.

Differential hitcount: layer 1 (0 - 33 km)

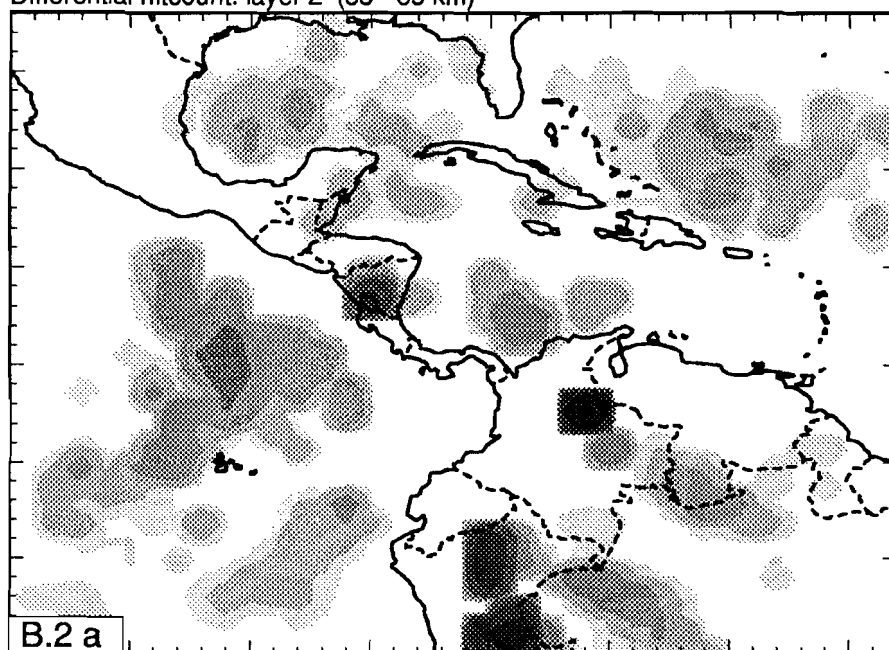


1 3000

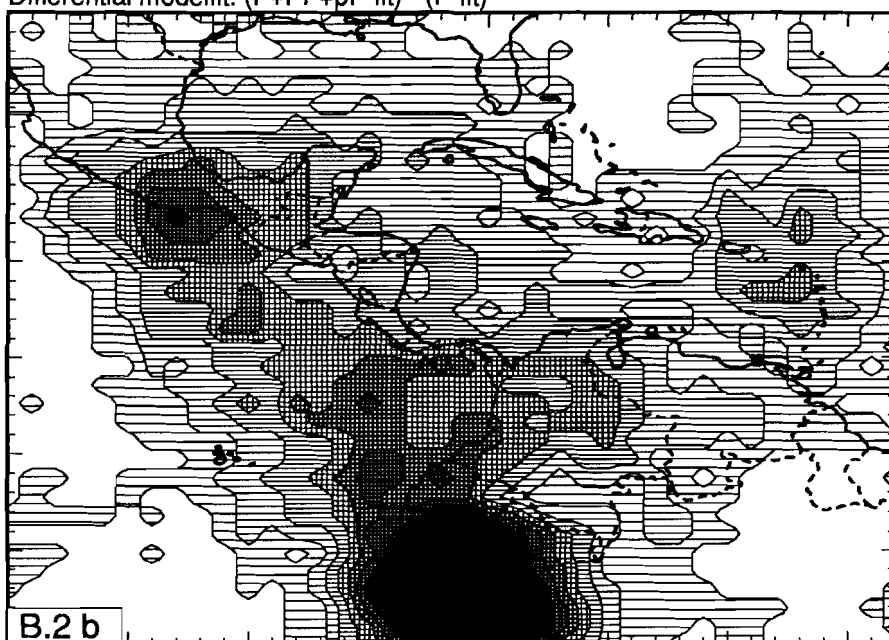
Differential modelfit:  $(P+PP+pP\text{-fit}) - (P\text{-fit})$ 

1 % 9 %

Differential hitcount: layer 2 (33 - 85 km)

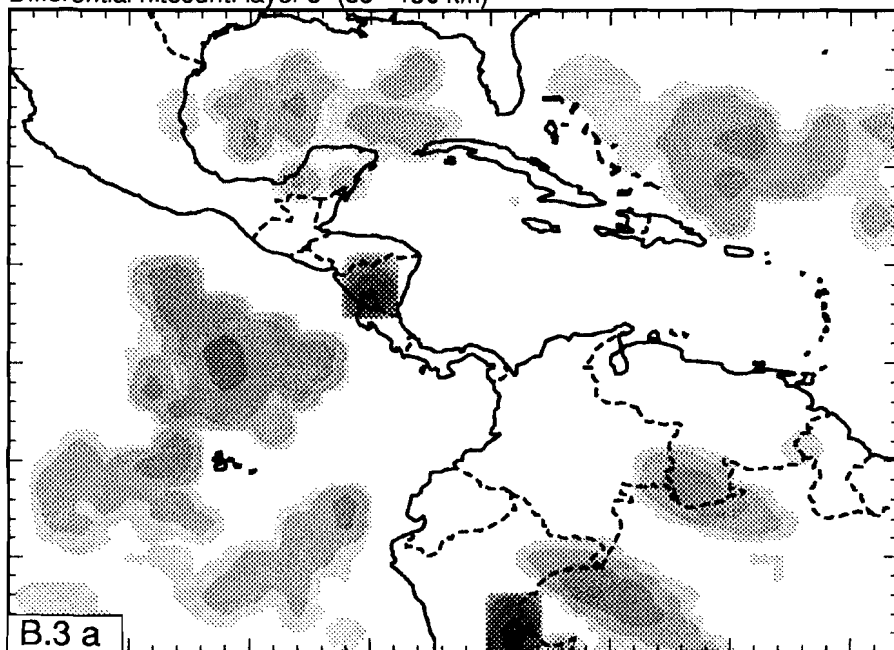
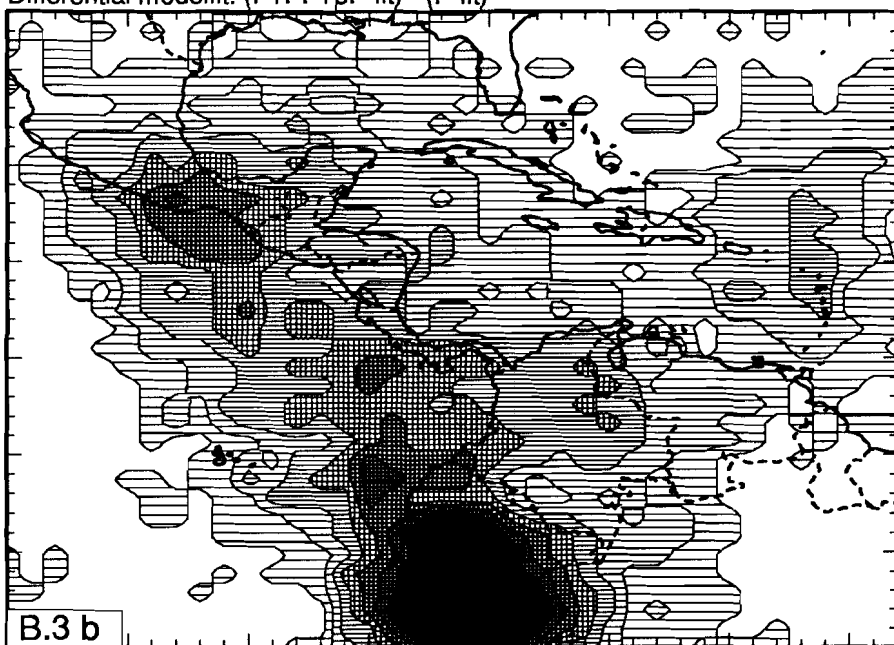


Differential modelfit:  $(P+PP+pP\text{-fit}) - (P\text{-fit})$

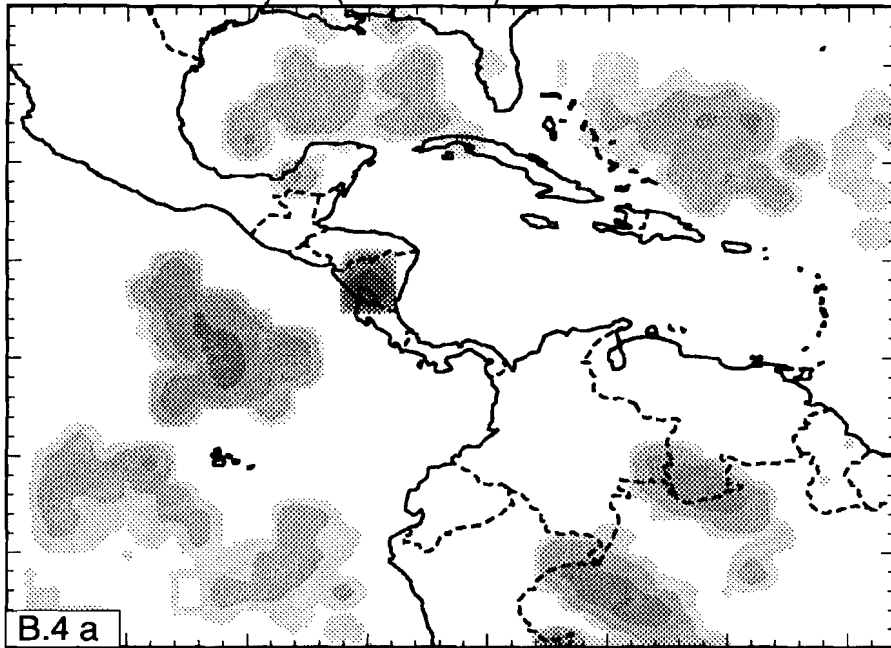




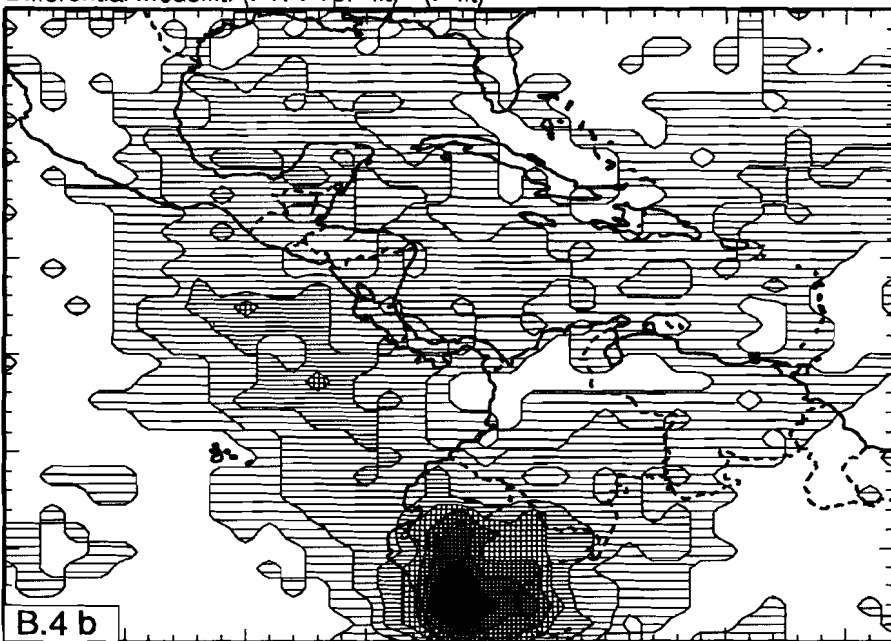
Differential hitcount: layer 3 (85 - 130 km)

Differential modelfit:  $(P+PP+pP\text{-fit}) - (P\text{-fit})$ 

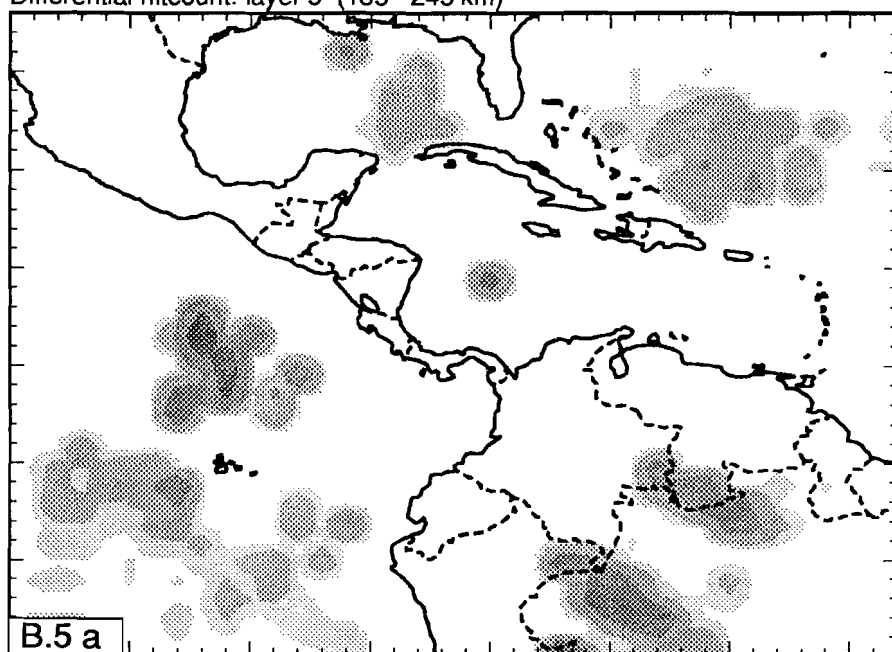
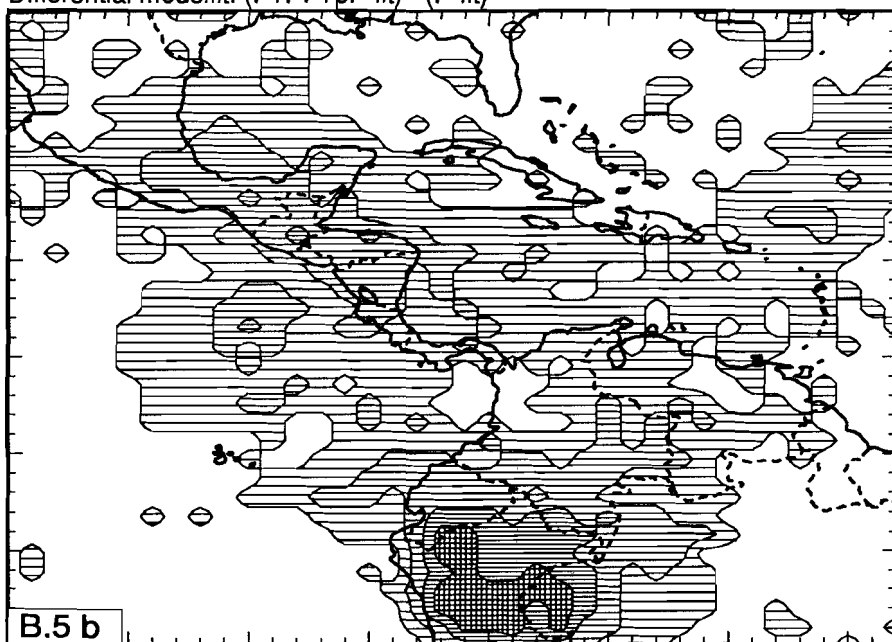
Differential hitcount: layer 4 (130 - 185 km)



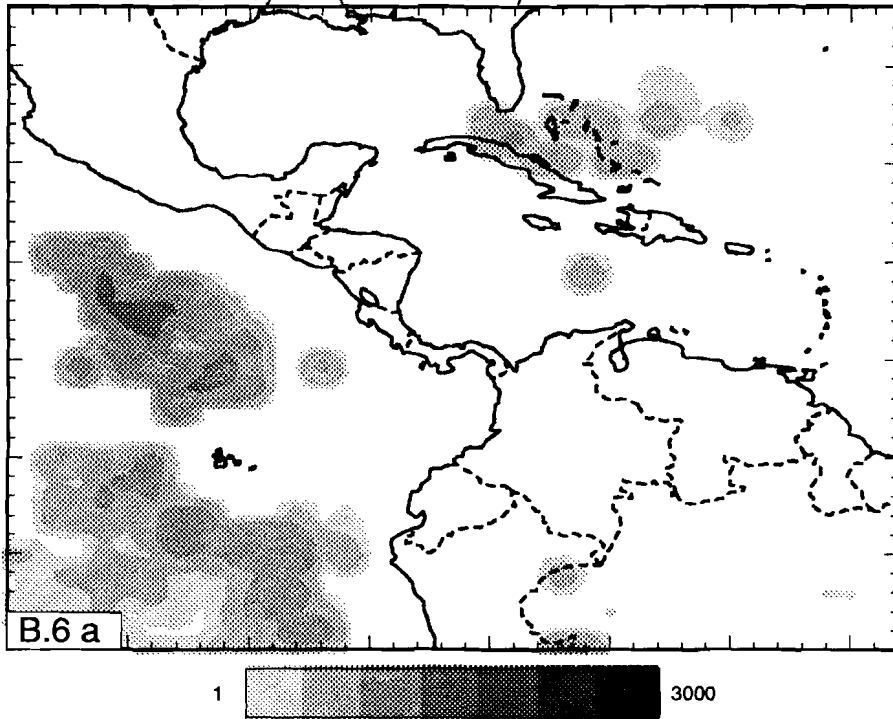
Differential modelfit:  $(P+PP+pP\text{-fit}) - (P\text{-fit})$



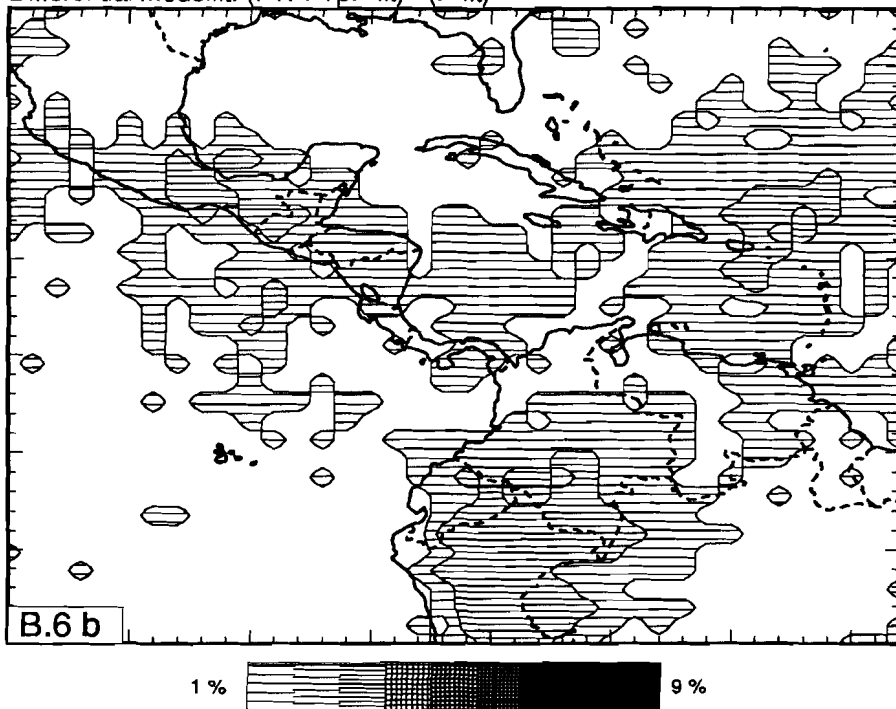
Differential hitcount: layer 5 (185 - 245 km)

Differential modelfit:  $(P+PP+pP\text{-fit}) - (P\text{-fit})$ 

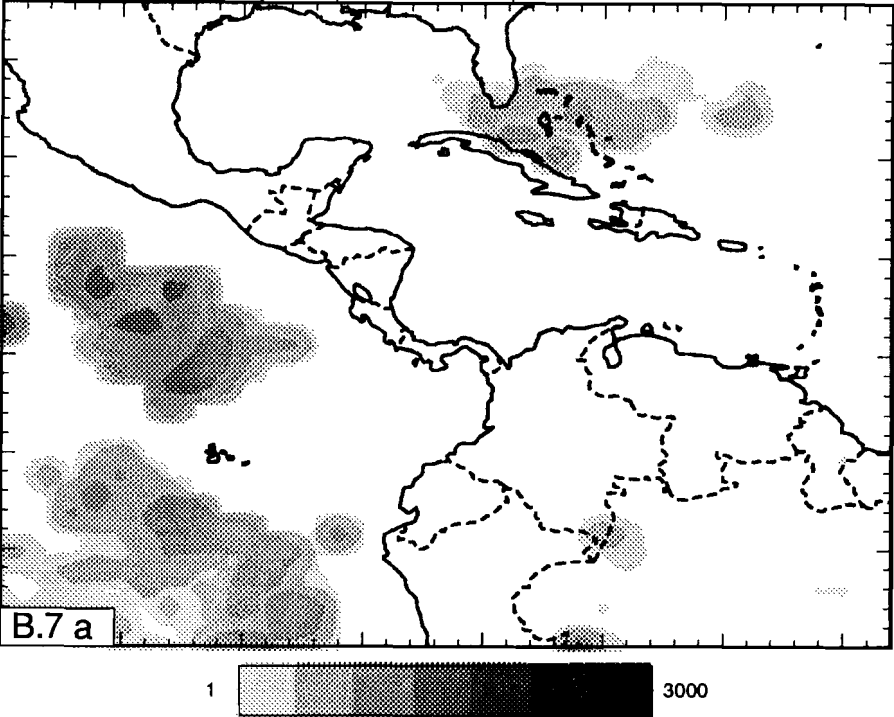
Differential hitcount: layer 6 (245 - 312.5 km)



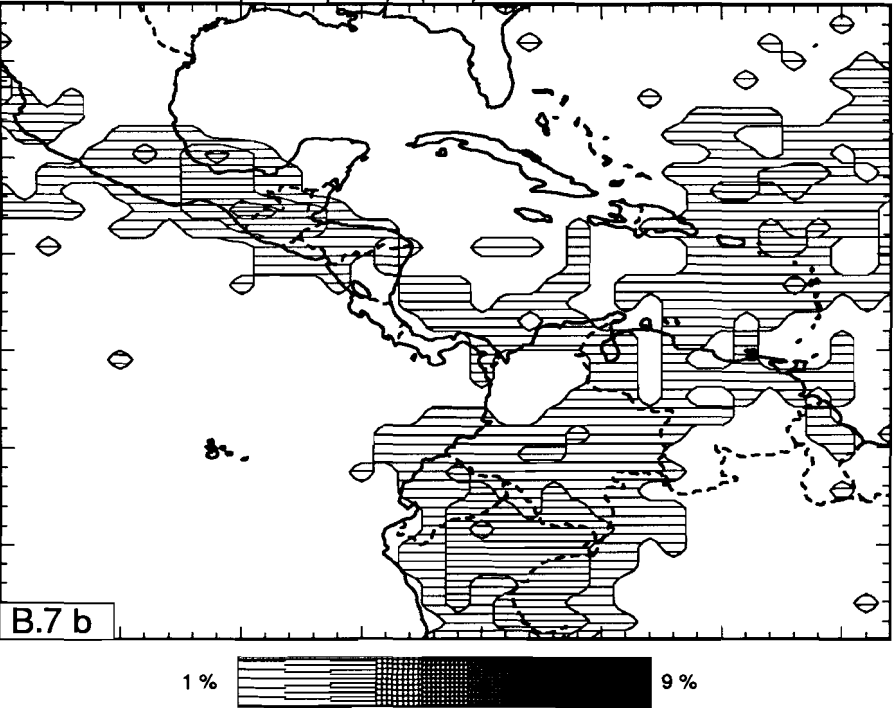
Differential modelfit:  $(P+PP+pP\text{-fit}) - (P\text{-fit})$



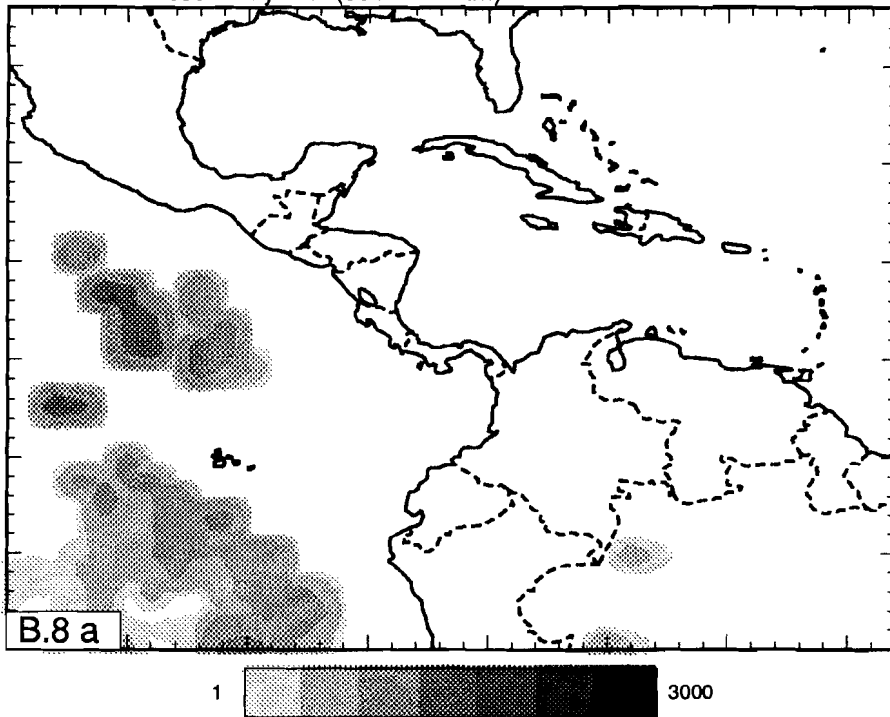
Differential hitcount: layer 7 (312.5 - 390 km)



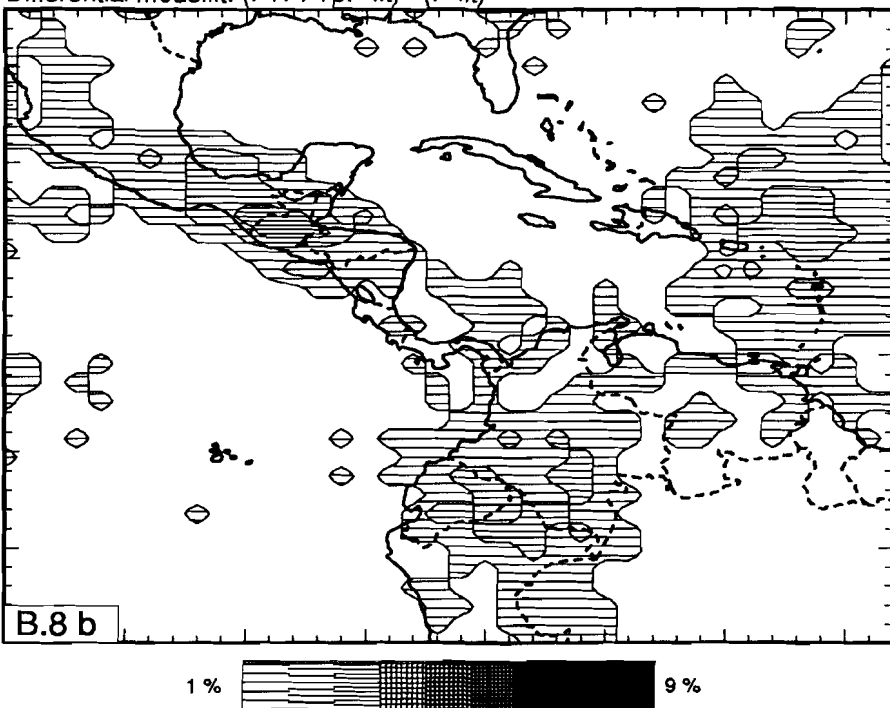
Differential modelfit:  $(P+PP+pP\text{-fit}) - (P\text{-fit})$



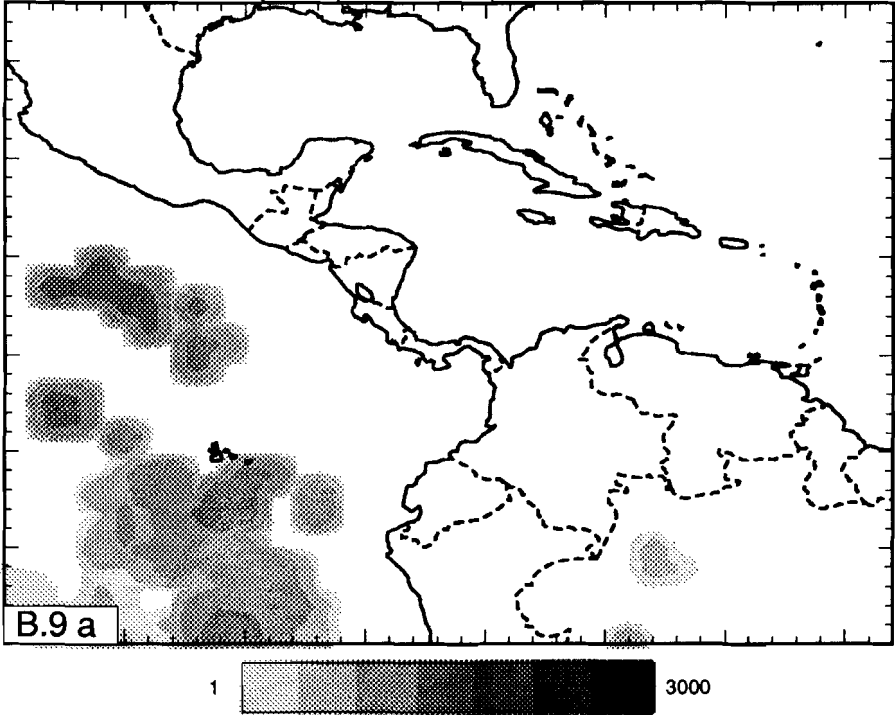
Differential hitcount: layer 8 (390 - 475 km)



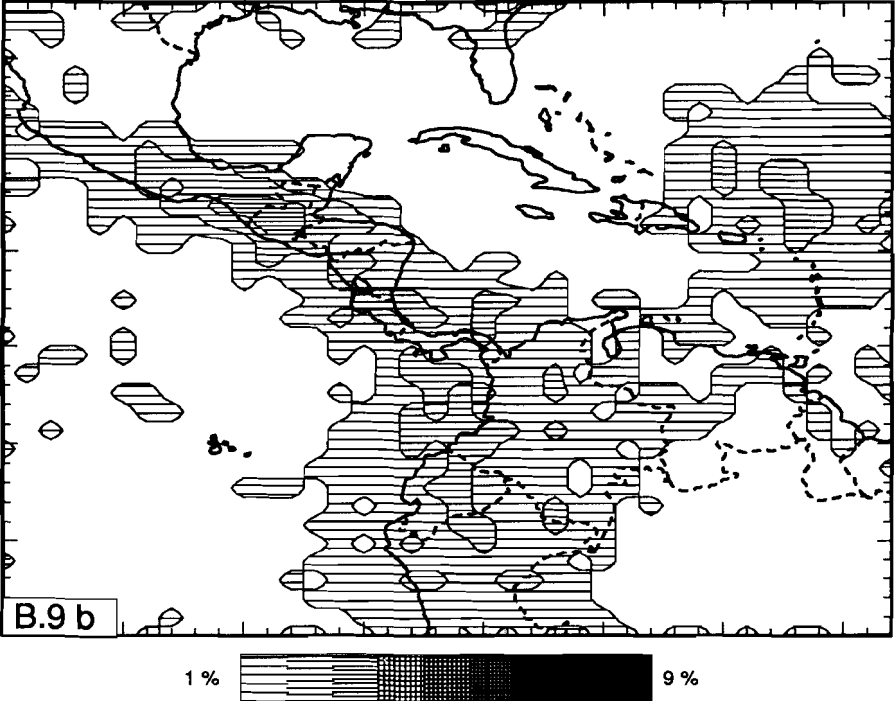
Differential modelfit:  $(P+PP+pP\text{-fit}) - (P\text{-fit})$



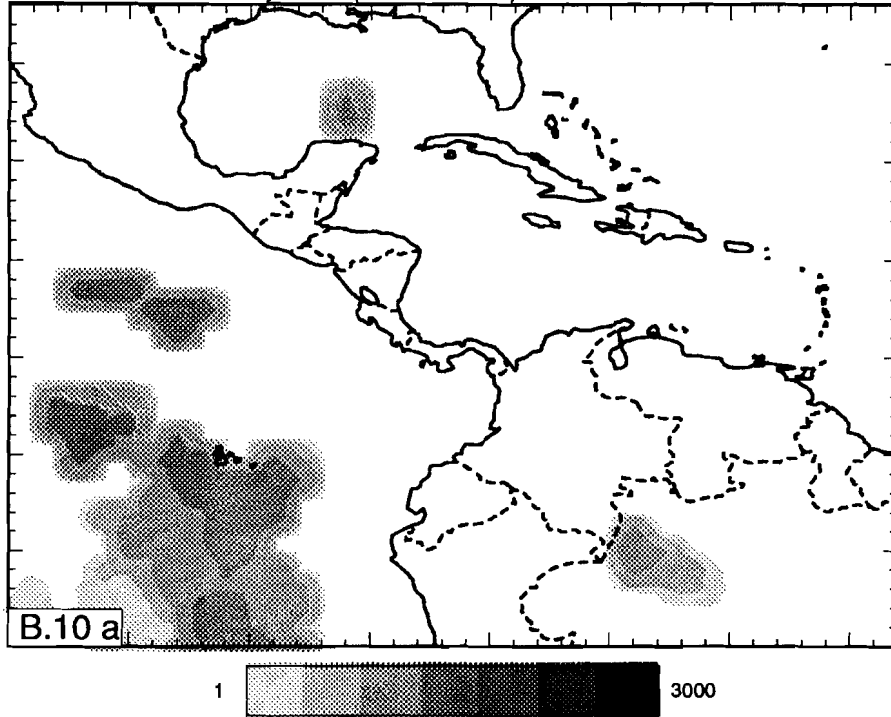
Differential hitcount: layer 9 (475 - 565 km)



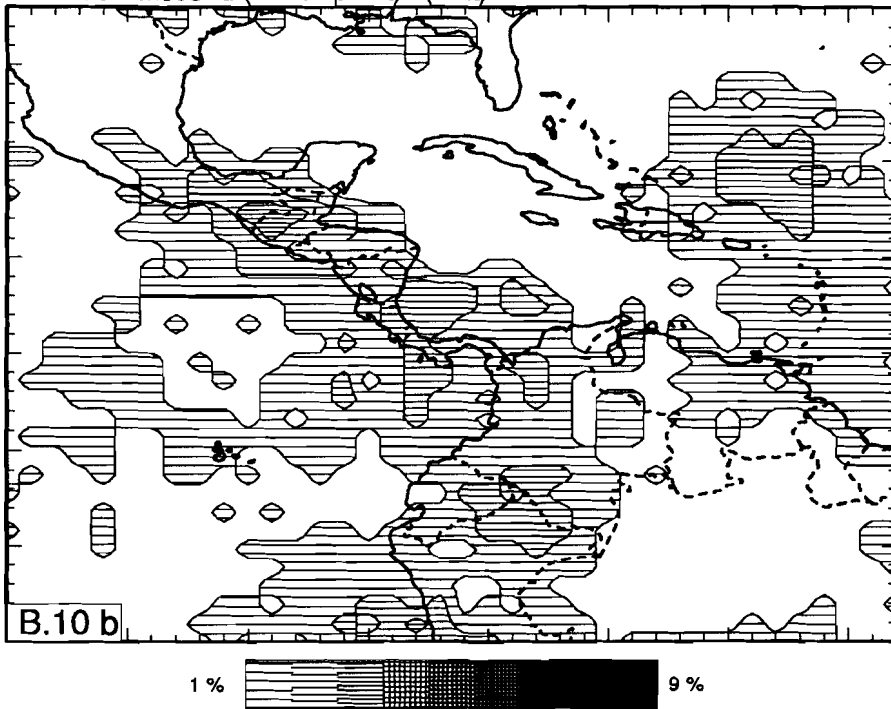
Differential modelfit:  $(P+PP+pP\text{-fit}) - (P\text{-fit})$



Differential hitcount: layer 10 (565 - 660 km)



Differential modelfit:  $(P+PP+pP\text{-fit}) - (P\text{-fit})$







## *Chapter 4*

### **Tectonic framework of the Caribbean region**

#### **4.1 Introduction**

In the previous chapters, I discussed improvements on the method of seismic delay-time tomography. In chapters 5 and 6, I shall focus on the aspherical variations of  $P$  wave velocities in the mantle below the Caribbean region, and their relation to the tectonic history of this region. To provide a reference for the discussions in these chapters, I briefly outline the tectonic framework of the Caribbean region in section 4.2 below. In section 4.3, I formulate the principal tectonic problems that will be investigated in chapters 5 and 6 by means of the tomographic images.

#### **4.2 The tectonic framework of the Caribbean region**

The definitions of many boundaries of tectonic elements within the Caribbean region are still subjected to controversy. Therefore, the outlines on the maps of Figure 4.1 serve the single purpose of a (seismo)tectonic and geographic reference for our discussions of tomographic images in chapters 5 and 6. The most important sources for the definitions (locations and nomenclature) of tectonic elements and geological provinces referred to in this chapter, are the geological and tectonic maps of Case and Holcombe [1980], and the description of individual tectonic elements by [Case et al., 1984]. Appropriate references to recent literature are given. The abbreviations used in this thesis are listed in Table 4.1.

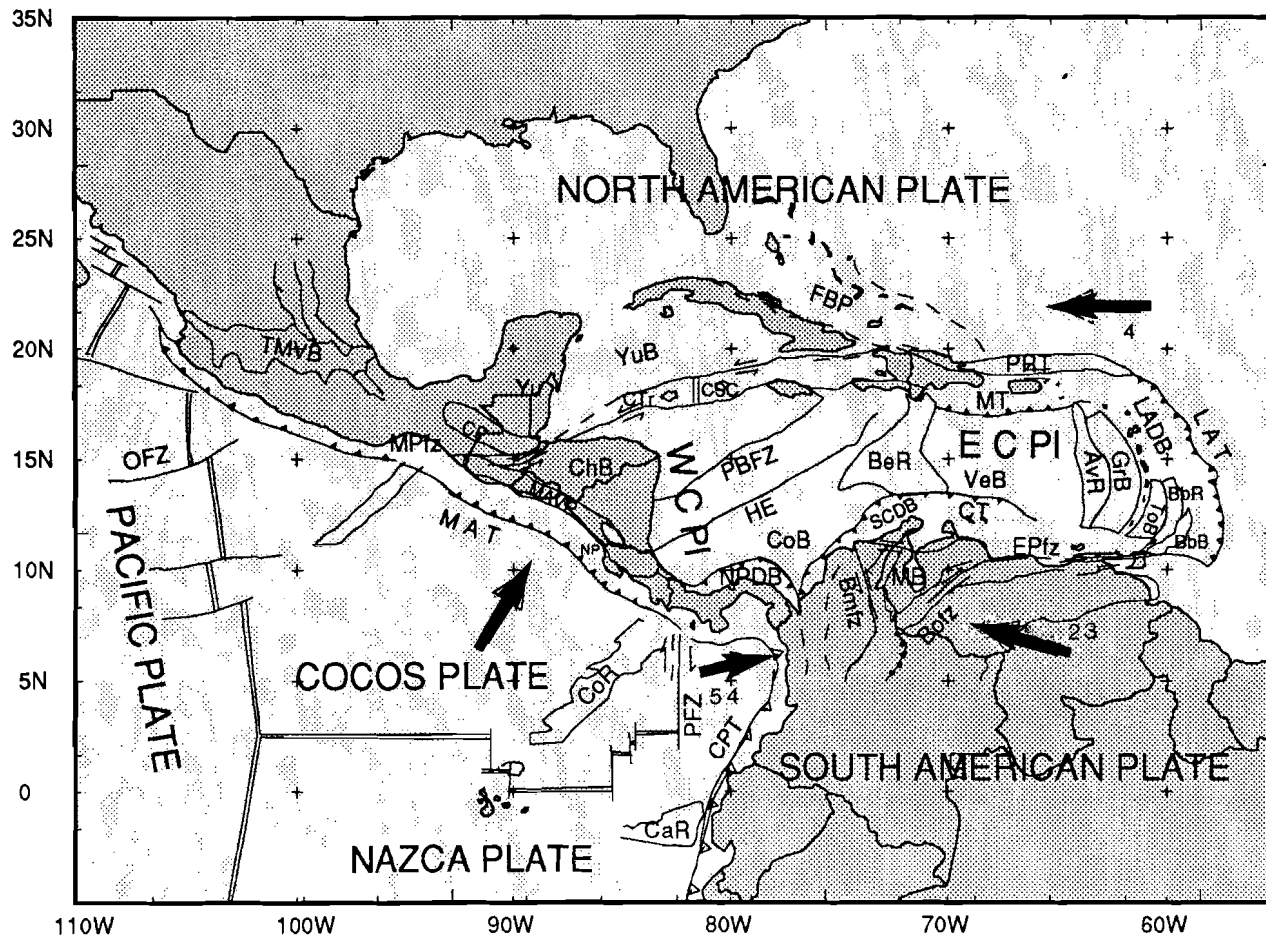


*Figure 4.1.* Tectonic map of the Caribbean region. Directions and rates (in mm/year) of relative plate motions are after Minster and Jordan [1978]. Boundaries and names of tectonic units are from Case and Holcombe [1980]. Meaning of the abbreviations: *AvR* Aves ridge, *BbB* Barbados basin, *BbR* Barbados ridge, *BeR* Beate ridge, *Bmfz* Bucaramanga-Santa Martha fault zone, *Bofz* Bocono fault zone, *CaR* Carnegie ridge, *ChB* Chortis block, *CoB* Colombia basin, *CoR* Cocos ridge, *CP* Chiapas-Peten massif, *CPT* Colombia-Peru trench, *CSC* Cayman spreading center, *CT* Curacao trench, *CTr* Cayman trough, *EPfz* El Pilar fault zone, *FBP* Florida-Bahama platform, *GFr* Gulf of Fronseca, *GrB* Grenada basin, *HE* Hess Escarpment, *LADB* Lesser Antilles deformed belt, *LAT* Lesser Antilles trench, *MAT* Middle America trench, *MAVP* Middle America volcanic province, *MB* Maracaibo block, *MPfz* Motagua-Polochic fault zone, *MT* Muertos trench, *NP* Nicoya peninsula, *NPDB* Northern Panama deformed belt, *OFZ* Orozco fracture zone, *PBFZ* Pedro Bank fracture zone, *PFZ* Panama fracture zone, *PRT* Puerto Rico trench, *SCDB* Southern Caribbean deformed belt, *Swfz* Swan fracture zone, *ToB* Tobago basin, *TMVB* Trans Mexican volcanic belt, *Yu* Yucatan, *YuB* Yucatan basin, *VeB* Venezuela basin.

The tectonic evolution of the Caribbean region is controlled by the interaction of five distinct plates: the North American Plate, the South American Plate, the Cocos Plate, the Nazca Plate, and the Caribbean Plate. On a smaller scale, micro plates and tectonic blocks are important. In Figure 4.1 tectonic and geologic units are shown together with some relevant bathymetric features. In Figure 4.2, I present some incremental stages of the tectonic model that was recently published by Ross and Scotese [1988].

In the north, the interaction between the North American and the Caribbean Plates resulted in deformation dominated by (left lateral) wrench tectonics along the Northern Plate Boundary Zone (NPBZ) [Mann and Burke, 1984]. The western part of the NPBZ is determined by the Cayman Through (CTr in Figure 4.1), flanked by large throughgoing sinistral strike-slip faults. Extension occurs in the Cayman Spreading Centre (CSC, Figure 4.1) [Rosencrantz and Sclater, 1986]. Further west, the landward continuation of the NPBZ forms the Motagua-Polochic-Jocatan fault zones (MPfz, Figure 4.1) [Burkhart, 1983]. Eastward, the deformation is controlled by a complex system of local "push-ups", "restrained bends" and "pull-apart basins" [for an extensive review and further references, see Mann and Burke, 1984; Mann et al. 1985]. The deformation within the eastern part of the NPBZ is mainly limited between the Muertos Trench (MT, Figure 4.1), in the south, and the Puerto Rico Trench (PRT) in the north [McCann and Sykes, 1984].

In the eastern part of the Caribbean Plate, the style of deformation, due to the interaction with both the North and South American Plates, is controlled by subduction of old (80-100 Ma) oceanic lithosphere of the Atlantic Plate (Figure 4.2) - and of bathymetric features on this plate - below the Lesser Antilles Arc [e.g., Molnar and Sykes, 1969; Stein et al., 1982, 1983, 1986; McCann and Sykes, 1986]. A well developed accretionary wedge (Lesser Antilles Deformed Belt, LADB) [Masclé et al., 1986], a Neogene Lesser Antilles Volcanic Arc (LAVA) and back-arc extension basins (Grenada Basin, GrB) [Bouysse, 1988] are prominent tectonic and structural features. Down to about 200 km depth a well defined Wadati-Benioff zone exists, in particular below the northern part of the arc [Stein et al., 1982; Sykes et al., 1982; McCann and Sykes, 1984].

The tectonics of the western part of the Caribbean has been determined by the convergence between the Cocos Plate and the North American and Caribbean Plates (Figure 4.2). Subduction related seismicity occurs in seismic zones down to 250 km [Dewey and Algermissen, 1974; Burbach et al., 1984]. Neogene calc-alkalic volcanism occurs in the Middle America Volcanic Province (MAVP) [Stoiber and Carr, 1973; Case and Holcombe, 1984]. Important for tectonics and seismicity is the subduction of bathymetric features in the Cocos Plate (Cocos Ridge, CoR, and Tehuantepec Ridge, ThR) at the Middle America trench (MAT) [LeFevre and McNally, 1985; Wolters, 1986], and the subduction of young oceanic lithosphere. The Panama Fracture Zone (PFZ) and the Galapagos spreading system separate the Cocos Plate from the Nazca Plate.

The tectonic interaction between the Caribbean Plate, the Nazca Plate, and the South American Plates is very complicated. Deformation in this western part of the Southern Plate Boundary Zone (SPBZ) is determined by (predominantly right lateral) transpression and the presence of small tectonic blocks like the Panama, Maracaibo (MB) and Andean

Table 4.2. Approximate geographical locations of regions and tectonic features

Abbreviation	Name	latitude	longitude	Figure
<i>AvR</i>	Aves Ridge	15° N	-62° W	4.1
<i>BbB</i>	Barbados Basin	11° N	-60° W	4.1
<i>BbR</i>	Barbados Ridge	13° N	-60° W	4.1
<i>BeR</i>	Beate Ridge	15° N	-72° W	4.1
<i>Bmfz</i>	Bucaramanga-Santa Martha fault zone	8° N	-72° W	4.1
<i>Bofz</i>	Bocono fault zone	7° N	-70° W	4.1
<i>CaR</i>	Carnegie Ridge	-2° S	-82° W	4.1
<i>CARIB</i>	CARIBbean Plate	15° N	-75° W	3.2
<i>ChB</i>	Chortis Block	14° N	-83° W	4.1
<i>COCOS</i>	COCOS Plate	10° N	-95° W	3.2
<i>CoB</i>	Colombia Basin	11° N	-79° W	4.1
<i>CoR</i>	Cocos Ridge	5° N	-83° W	4.1
<i>CP</i>	Chiapas-Peten massif	17° N	-91° W	4.1
<i>CPT</i>	Colombia-Peru Trench	7° N	-80° W	4.1
<i>CSC</i>	Cayman Spreading Center	18° N	-80° W	4.1
<i>CT</i>	Curacao Trench	13° N	-69° W	4.1
<i>CTr</i>	Cayman Trough	18° N	-82° W	4.1
<i>EPfz</i>	El Pilar fault zone	11° N	-63° W	4.1
<i>FBP</i>	Florida-Bahama Platform	22° N	-73° W	4.1
<i>GFr</i>	Gulf of Fronseca	13° N	-87° W	6.2
<i>GrB</i>	Grenada Basin	15° N	-66° W	4.1
<i>HE</i>	Hess Escarpment	12° N	-79° W	4.1
<i>LADB</i>	Lesser Antilles Deformed Belt	16° N	-61° W	4.1
<i>LAT</i>	Lesser Antilles Trench	16° N	-59° W	4.1

blocks [Pennington, 1981; Mann and Burke, 1984; Bonini et al., 1984]. Convergence between the Caribbean and South American Plates resulted in the Northern Panama and Southern Caribbean Deformed Belts (NPDB and SCDB, Figure 4.1). The seismicity of this complex Plate Boundary Zone is investigated by, among others, Dewey [1972], Pennington [1981] and Kellogg and Bonini [1982]. Deformation in the eastern part of the SPBZ occurs along throughgoing dextral strike slip faults (e.g., the El Pilar fault zone (EPfz) Figure 4.1). In the central parts of the Caribbean Plate, the oceanic Colombia and Venezuela Basins (CoB and VeB in Figure 4.1) are bordered by the Hess Escarpment (HE), the Beate Ridge (BeR), and the Aves Ridge (AvR).

(Table 4.2. continued)

<i>MAT</i>	Middle America Trench	12° N	−91° W	4.1
<i>MAVP</i>	Middle America volcanic province	13° N	−89° W	4.1
<i>MB</i>	Maracaibo block	10° N	−71° W	4.1
<i>MPfz</i>	Motagua-Polochic fault zone	15° N	−91° W	4.1
<i>MT</i>	Muertos Trench	18° N	−69° W	4.1
<i>NPBZ</i>	Northern Plate Boundary Zone	20° N	−85° W	3.2
<i>NP</i>	Nicoya Peninsula	11° N	−83° W	4.1
<i>NPDB</i>	Northern Panama Deformed Belt	10° N	−80° W	4.1
<i>NOAM</i>	NORTH AMERICA Plate	28° N	−65° W	3.2
<i>OFZ</i>	Orozco Fracture Zone	15° N	−107° W	6.2
<i>PBFZ</i>	Pedro Bank Fracture Zone	14° N	−80° W	4.1
<i>PFZ</i>	Panama Fracture Zone	8° N	−81° W	4.1
<i>PRT</i>	Puerto Rico Trench	19° N	−63° W	4.1
<i>RFZ</i>	Rivera Fracture Zone	19° N	−108° W	6.2
<i>RP</i>	Rivera Plate	21° N	−107° W	6.2
<i>SCDB</i>	Southern Caribbean Deformed Belt	13° N	−71° W	4.1
<i>SPBZ</i>	Southern Plate Boundary Zone	8° N	−66° W	3.2
<i>SOAM</i>	SOUTH AMERICA Plate	8° N	−66° W	3.2
<i>SwFZ</i>	Swan Fracture Zone	16° N	−89° W	4.1
<i>TeR</i>	Tehuantepec Ridge	13° N	−97° W	6.2
<i>ToB</i>	Tobago Basin	12° N	−61° W	4.1
<i>TMVB</i>	Trans Mexican Volcanic Belt	20° N	−100° W	4.1
<i>Yu</i>	Yucatan	18° N	−90° W	4.1
<i>YuB</i>	Yucatan Basin	20° N	−82° W	4.1
<i>VeB</i>	Venezuela Basin	14° N	−69° W	4.1

### 4.3 Tectonic problems that can be investigated by seismic tomography

Of course not all problems in our understanding of the tectonic evolution of the Caribbean region can be solved by the analyses of tomographic images. Structures with spatial dimensions smaller than approximately 150 km can not be resolved with the tomographic method applied here. Moreover, relative motions between plates or other tectonic units do not necessarily result in detectable variations of the *P* wave velocities. For example, strike slip motions do not perturb the spherical symmetry and will thus not be discerned by seismic tomography, unless aspherical structures are off set. In the following I describe the tectonic or geodynamic phenomena that can be investigated with the tomographic method applied in this study.

**A controversy in global geodynamics: the mode of mantle convection:**

The recently published tectonic models, e.g., that of Ross and Scotese [1988] shown in Figure 4.2, indicate that subduction processes have been active in the Middle America realm at least since the Middle Cretaceous (Fig 4.2a), and below the Greater and Lesser Antilles since Late Cretaceous times (Figure 4.2c,d). If the principal aspects of the outlines of these tectonic models are correct, some thousands of kilometers of lithosphere of the Farallon Plate, and of the Proto-Caribbean and the Atlantic Plate, must have been consumed below the Middle America and Antilles arcs respectively. With respect to the latter region, I remark that the reconstruction of Ross and Scotese [1988] reveals a maximum age of the Proto-Caribbean lithosphere of approximately 40 Ma, although most of the Proto-Caribbean lithosphere must have been much younger when it was overridden by the Caribbean Plate. The Mesozoic and earliest Paleogene motions of the Caribbean Plate probably resulted in underplating and lithospheric doubling [Vlaar, 1983] rather than in the down going of subducted Proto-Caribbean lithosphere. Old oceanic lithosphere of the Atlantic Plate (of the order of 100 Ma) was encountered first in Late Paleocene - Early Eocene times (Figure 4.2f,g). This event may have triggered the down going subduction below the Caribbean Plate. With hypothetical rates of convergence between the Caribbean Plate and the Atlantic Plate of the order of 0 to 2 cm/yr, several hundreds of kilometers of Atlantic lithosphere must have disappeared in the deeper mantle below the Caribbean Plate.

With regard to these processes an important question arises. What happened to the enormous amounts of subducted lithosphere? The definitive answer to this question will have crucial implications for our perception of mantle convection: is the subduction process restricted to the upper mantle, or is the lower mantle involved as well? Jordan and Lynn [1974] "discovered" aspherical variations of the propagation velocities of seismic body waves in the lower mantle below the western part of the Caribbean region. These investigators tentatively related the anomalously high *P* and *S*-wave velocities in the lower mantle to the past subduction of the Farallon Plate below Middle America. Although, they could not establish a relationship between upper and lower mantle structures, Jordan and Lynn [1974] postulated the penetration of the subducted slab into the lower mantle and advocated the possibility of whole mantle convection. This scenario contradicts the hypothesis of layered mantle convection, according to which large-scale upper-mantle flow processes are separated from convection in the lower mantle. The results of Jordan and Lynn [1974] were confirmed by other investigators [Lay, 1983; Grand, 1987; Vidale and Garcia-Gonzalez, 1988].

The principal questions to be answered in chapters 5 and 6 are: firstly, whether or not tomographic images can be obtained that confirm the observations of, e.g., Jordan and Lynn [1974]; and, secondly, whether or not the relationship between upper and lower mantle structures can be investigated from the tomographic images.



### **Tectonic problems specific for the Caribbean region:**

Tectonic problems specific for the Caribbean region can also be investigated if tomographic images of the aspherical variations of the *P*-wave velocity below the Caribbean region can be obtained that show resolvable structure of the order of some hundreds of kilometers.

- *The Neogene plate reorganizations in the Middle America realm:*

The imaged slab morphology can be used to update regional tectonic models. For example, the left lateral motion of the Chortis Block relative to the present-day central Mexico and Yucatan (Figures 4.2i,j,k) can be expected to have influenced the process of subduction of the Farallon and Cocos Plates and thus the resulting morphology of the subducted slab. Also the effects of attempted subduction of young oceanic lithosphere near Mid Oceanic Ridges (e.g., the arrival of the East Pacific Rise at the Middle America trench) may be discernible from the tomographic images.

- *The role of the Hess Escarpment in the tectonic evolution of the region:*

In the plate model of Ross and Scotese [1988], the Hess Escarpment plays an important role in the tectonic history of the Caribbean Plate: The Hess Escarpment is modelled as the surface expression of an arc-arc transform fault that had been the plate boundary along which the Caribbean Plate moved towards the east with respect to North America in Late Cretaceous to Middle Eocene times (Figures 4.2i,j,k). No Neogene activity of the Hess Escarpment is modelled by Ross and Scotese. Because the Hess Escarpment cuts off subduction zones, which are usually well imaged by seismic tomographic methods, this phenomenon can be investigated from the tomographic images. Of particular interest is the depth extent of a structure such as the Hess Escarpment, and of plate boundaries in general.

- *The opening of the Grenada Basin in the southeastern part of the Caribbean Plate:*

Ross and Scotese [1988], and other investigators [e.g., Bouysse, 1988], postulated a Middle Eocene east-to-west opening of the Grenada Basin as being due to the retrograde motion of the Lesser Antilles subduction zone. Others have proposed a north-to-south opening of the Grenada Basin [cf. Ross and Scotese, 1988] that resulted from the relative motion between the Caribbean Plate and the (continental) South American Plate. If the Grenada Basin is a back-arc extension basin that opened due to the "roll back" of the subduction zone, the retrograde motion of the slab must have been more efficient in the southern part of the Lesser Antilles than in the north. The resulting lateral difference in slab morphology should then be discernible from the tomographic images.

- *The boundary between the North and South American Plates:*

The location of the boundary between the North and South American Plates is controversial. Different investigators advocate different intersections of this boundary with the Lesser Antilles trench. For a review of possible locations I refer to Harper [1990]. The tomographic investigation of the morphology of the subduction zone below the northern and southern Lesser Antilles, may reveal differences that are indicative for the presence of a plate boundary or for a gradual transition from the North American to the South American Plate.

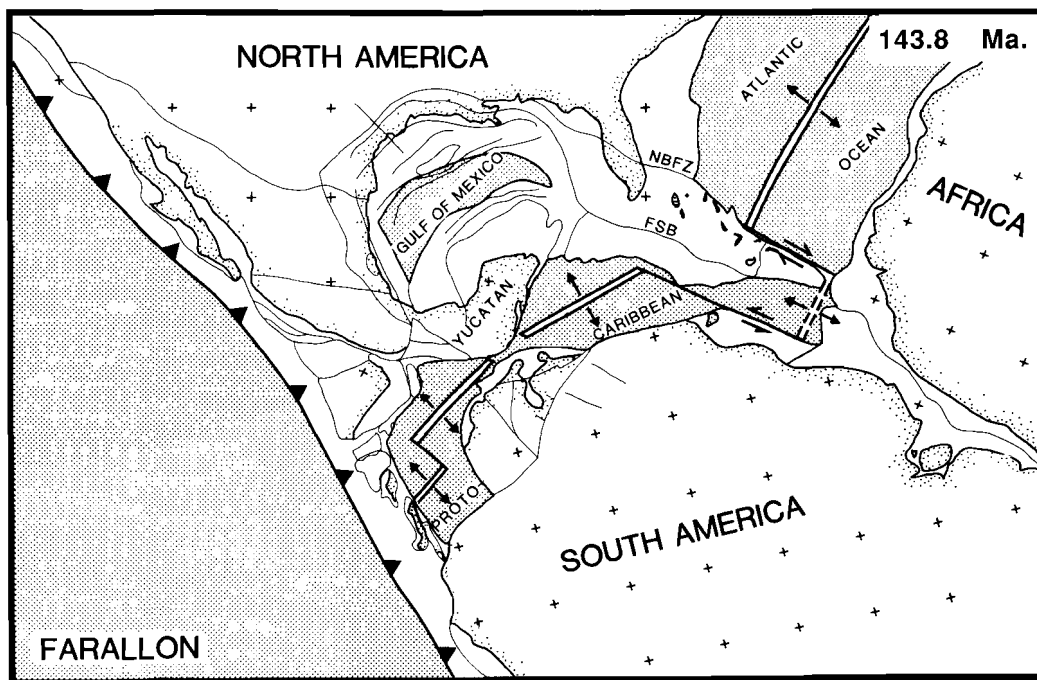
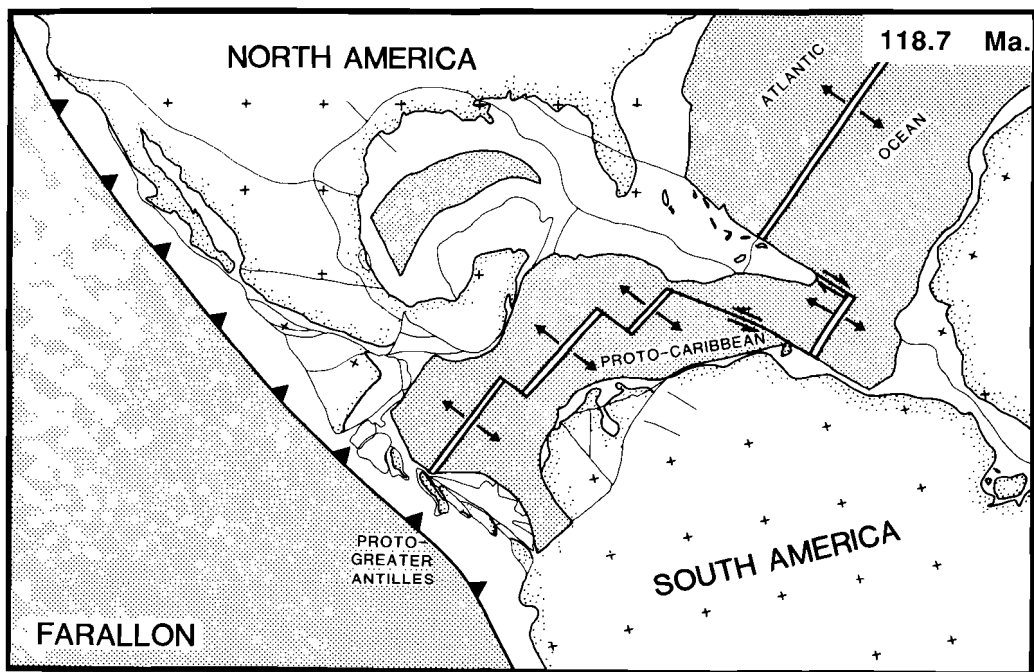
If a boundary is suggested from the images, the differences between the subduction of the

atlantic part of the North American Plate, and that of the South American Plate, may explain the differences in seismicity along the Lesser Antilles trench. The possible boundary between the two American Plates may also be related to the problem of the opening of Grenada Basin as described above.

- *The boundary between the Caribbean and the South American Plate:*

Even with the sophisticated technique used by Ross and Scotese [1988], the boundary between the Caribbean and the South American Plates is difficult to model, because the deformation occurs along faults of different types and in several micro plates. The aspherical structures in the upper mantle below the southern plate boundary can be investigated with the objective to establish the nature of the plate contact between the Caribbean Plate and the South American Plate.

*Figure 4.2.* An example of a plate tectonic reconstruction of the Caribbean region. Figure are taken from: Ross and Scotese [1988]

*Figure 4.2a. Tithonian (Late Jurassic)**Figure 4.2b. Early Aptian (Early Cretaceous)*

*Figure 4.2c. Late Albian (Early Cretaceous)*

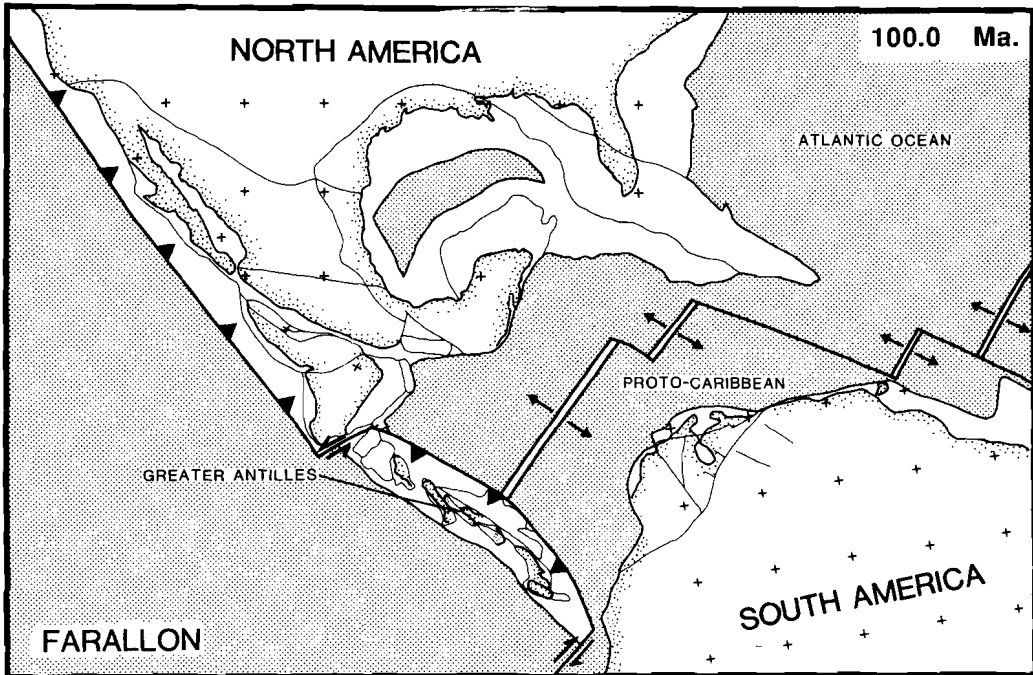


*Figure 4.2d. Middle Campanian (Late Cretaceous)*

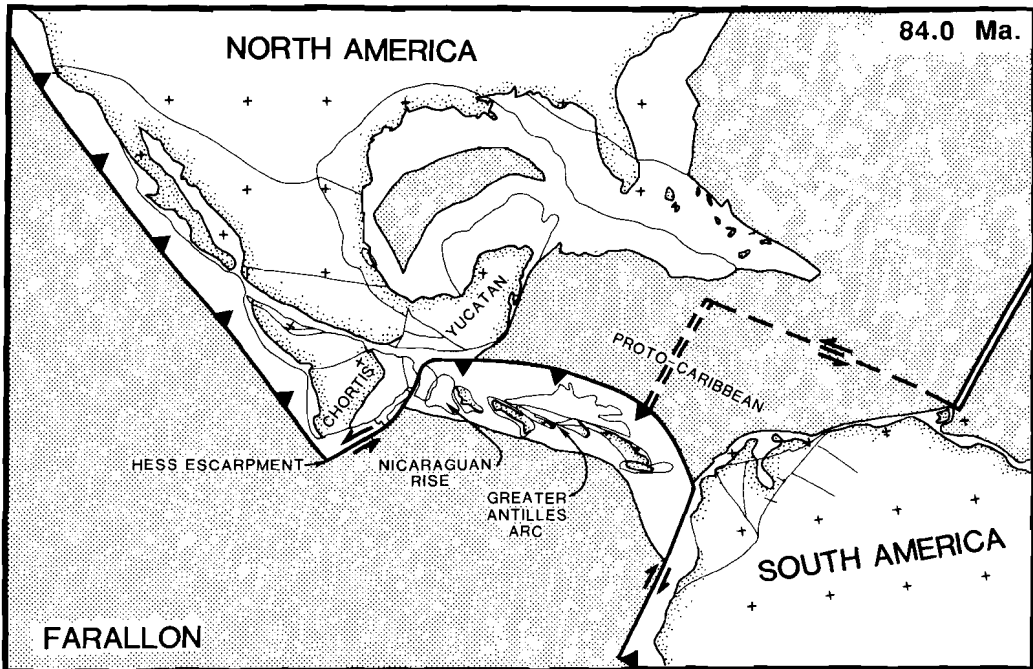


Figure 4.2e. Late Campanian (Latest Cretaceous)

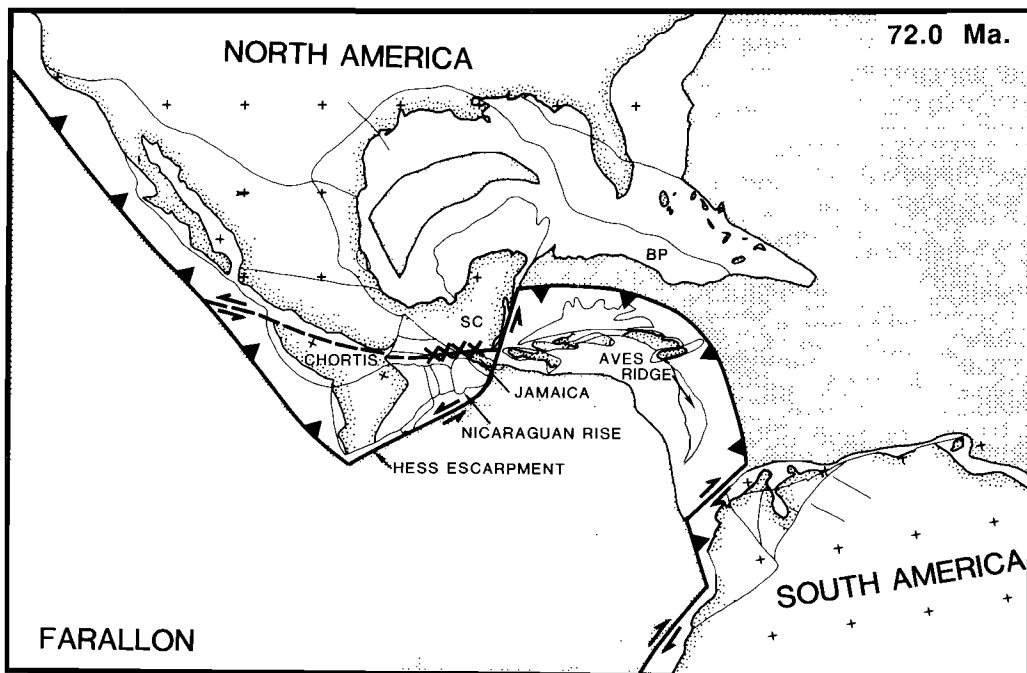


Figure 4.2f. Late Paleocene

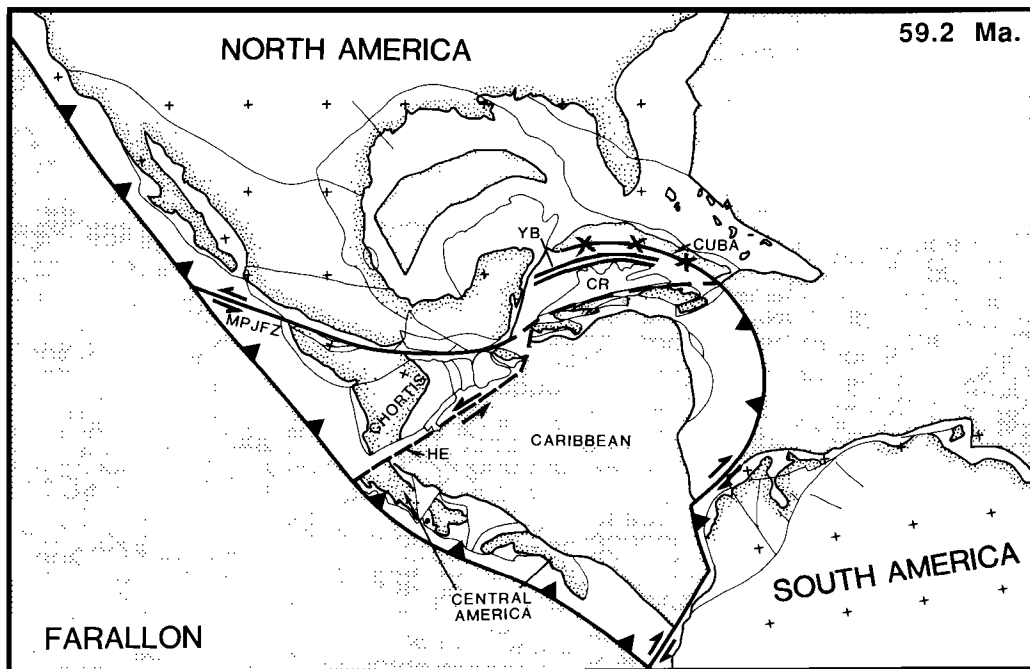


Figure 4.2g. Middle Eocene

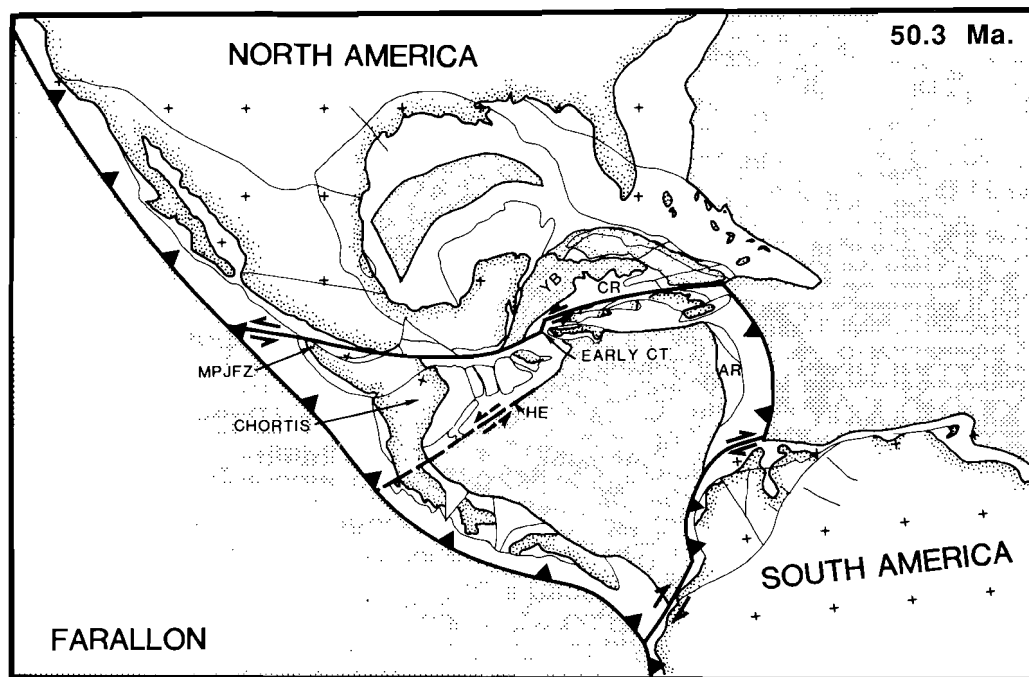


Figure 4.2h. Late Eocene

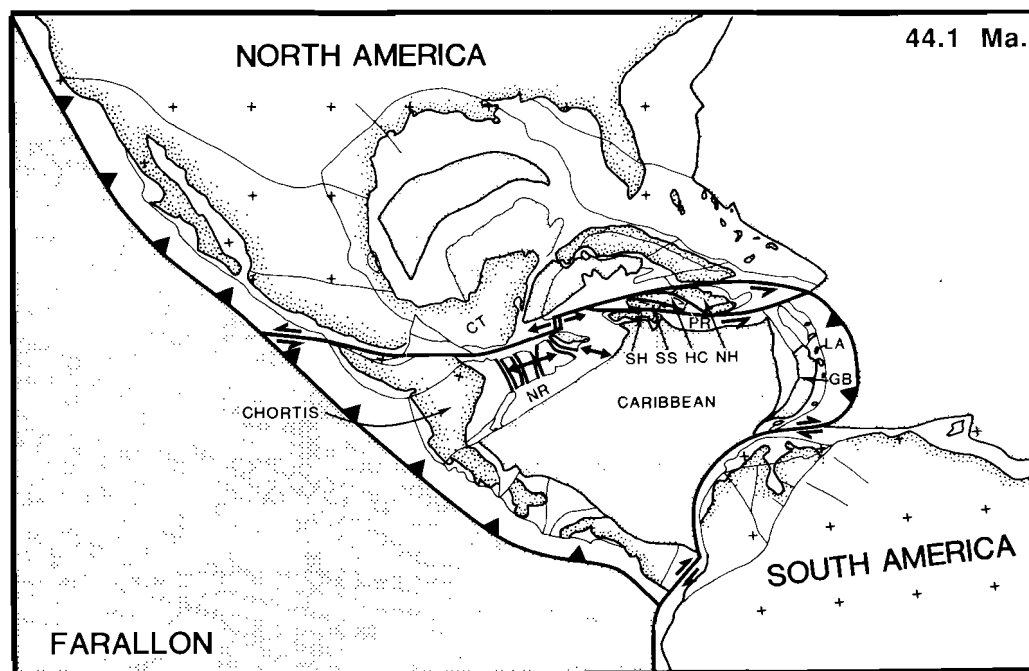


Figure 4.2i. Early Oligocene

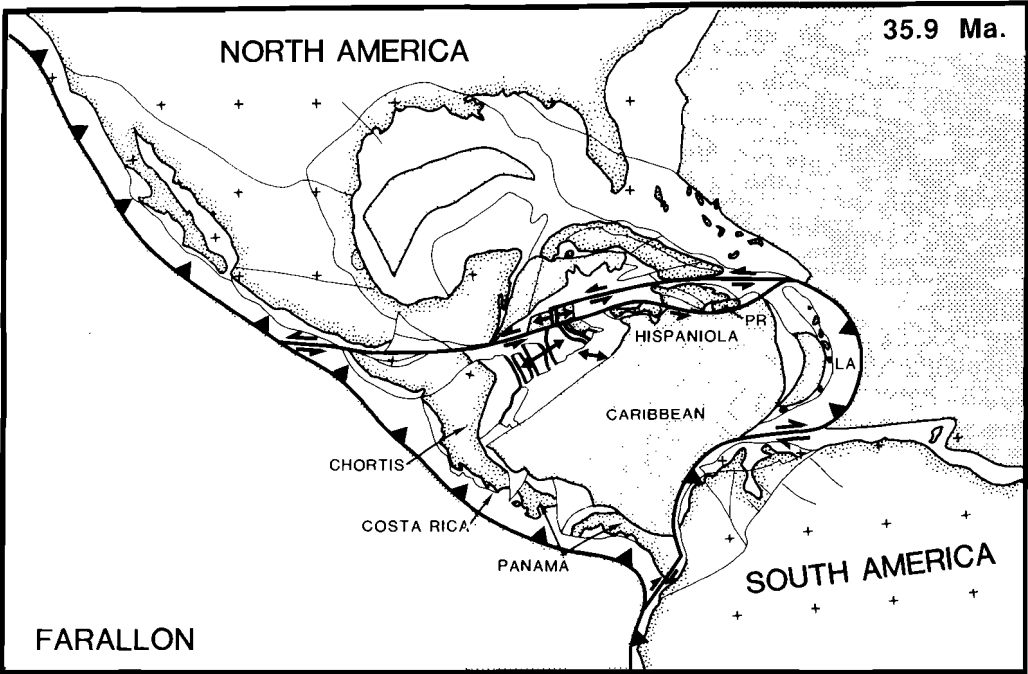


Figure 4.2j. Early Miocene

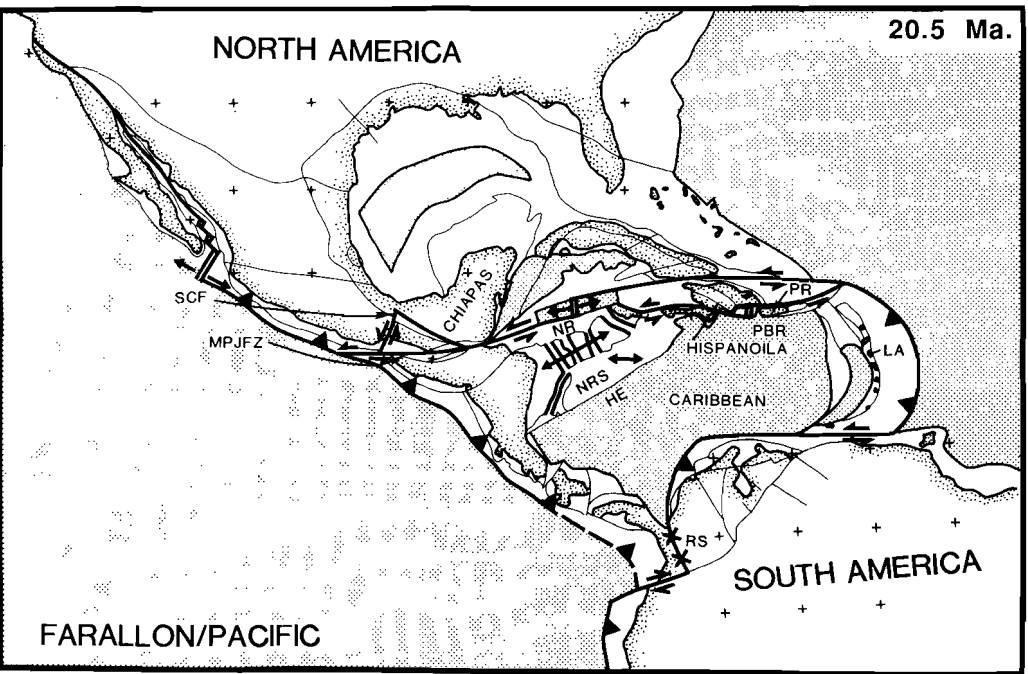


Figure 4.2k. Late Miocene

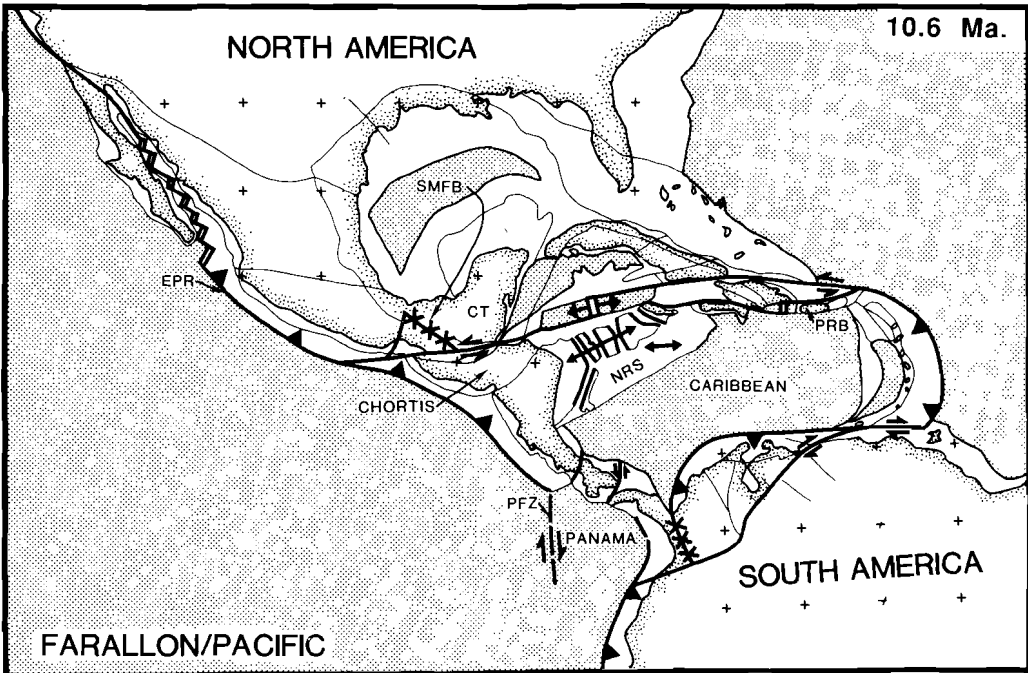
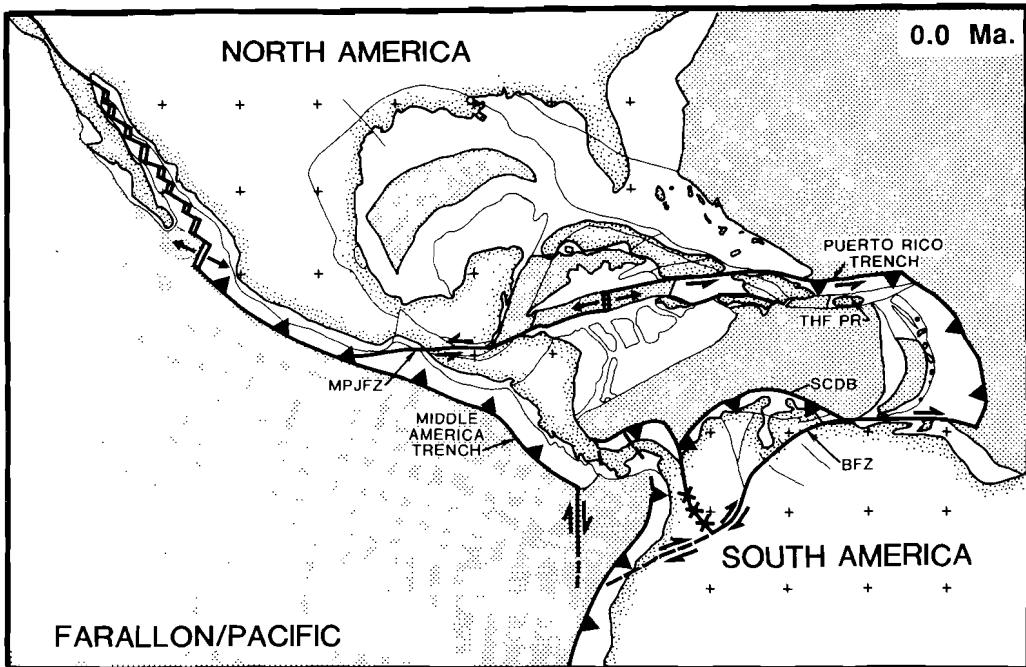


Figure 4.2l. Active plate boundaries, present day







## *Chapter 5*

### **Tomographic images of variations of the $P$ velocities in the mantle beneath the Caribbean region**

#### **5.1 Introduction**

In chapters 2 and 3, I discussed improvements on the method of  $P$  delay-time tomography. In chapter 2, I showed how reference model artifacts can be reduced by using reference model VCAR, which describes the 1D velocity structure of the mantle below the Caribbean more adequately than the Jeffreys-Bullen  $P$  structure [Van der Hilst and Spakman, 1989]. In chapter 3, I demonstrated the improvement on  $P$  delay-time tomography with the incorporation of later arriving  $PP$  and  $pP$  phases. Tomographic investigations, in particular of upper mantle structures on (sub-) global scales, are hampered by the uneven distribution of earthquakes and seismological stations, and the resulting inhomogeneous sampling by seismic rays. I showed that incorporation of  $PP$  and  $pP$  phases improved the sampling of the shallow mantle structure, and concluded that in spite of the larger errors in  $PP$  and  $pP$  data these phases enhanced the spatial resolution in regions of the mantle which are not adequately sampled by the direct  $P$  phase [Van der Hilst and Engdahl, 1989, 1990a].

Although illustrated by examples from the Caribbean region and motivated by complexities specific for this area, these investigations served the general purpose of improving the technique of body wave tomography. The modifications to the method of  $P$ -delay time tomography, extensively described by Spakman and Nolet [1988] and Spakman [1988], are generally applicable to other geographical areas.

In the remaining two chapters, I present and discuss results of the tomographic investigation of the aspherical variations of  $P$ -velocities in the mantle below the Caribbean Area. Unless explicitly stated otherwise, I address neither results of inversions in which the Jefreys-Bullen model was used as a reference, nor results of inversions of data sets restricted to  $P$  delay times. The discussion is restricted to solutions of the tomographic inversions, linearized around reference model VCAR, of  $P$ ,  $PP$ ,  $pP$  delay times and  $PP-P$  and  $pP-P$  differential travel-time residuals. In this chapter, I present the results of the inversions by means of horizontal sections through the 15 layers of the cell model. I describe and discuss in a systematic manner: (1), the velocity anomalies; (2), the sampling of mantle structure by seismic waves, expressed by the cell hit count; (3), results of two sensitivity tests, performed to assess the spatial resolution in the images; and (4), the result of an inversion of randomly permuted data. Here, the results are not interpreted in terms of geodynamics or the tectonical evolution of the area. However, wherever relevant I refer to the outlines of the tectonical and geological setting in chapter 4.

## 5.2 Presentation of the results of the tomographic inversions

As shown previously, the geographical region considered in this investigation includes the southern part of North America, Middle America and a major part of South America (chapter 1). It is not convenient to present results of this tomographic investigation by horizontal sections that encompass the entire area. I only present the results for the Caribbean region, in order to obtain comprehensible displays of the tomographic images without loss of detail. The images of the South American region, which are not considered here will be published elsewhere. As mentioned in section 5.1 of this chapter, I consider several aspects in the discussion of the results of the tomographic investigation. These aspects are discussed in sections 5.2.1 to 5.2.7.

### 5.2.1 Results of the inversion of $P$ , $PP$ and $pP$ delay-time data

I have noted previously (e.g., in Appendix 3A) that besides slowness anomalies the solution vector also contains relocation parameters and station correction terms. Here, I focus on the velocity part of the solution vector. When the solution is obtained with actually reported data, I denote this part of the solution with  $\mathbf{x}_{data}$  throughout this chapter. Positive (negative) values of the velocity anomalies indicate faster (slower) propagation of compressional body waves with respect to reference model VCAR. The velocity anomalies are discussed in combination with results of various inversions that are used to assess the reliability of the structures in the tomographic images. Only the most relevant observations are discussed.

### 5.2.2 The sampling of Earth structure by $P$ , $PP$ and $pP$ rays

Information about the distribution of the seismic rays employed in the tomographic investigation can be obtained by investigating the cell hit count. The hit count of a particular cell of the model is the total number of rays crossing that cell. The irregular and strongly inhomogeneous sampling by seismic rays is caused by the uneven distribution of

earthquakes and stations. Strong gradients in the velocity structure of the reference model, e.g., near upper mantle discontinuities, also cause inhomogeneities in ray distribution. This effect, illustrated in Figure 2.3, explains in part the low vertical resolution of structures in layers of the cell model immediately above the upper mantle discontinuities.

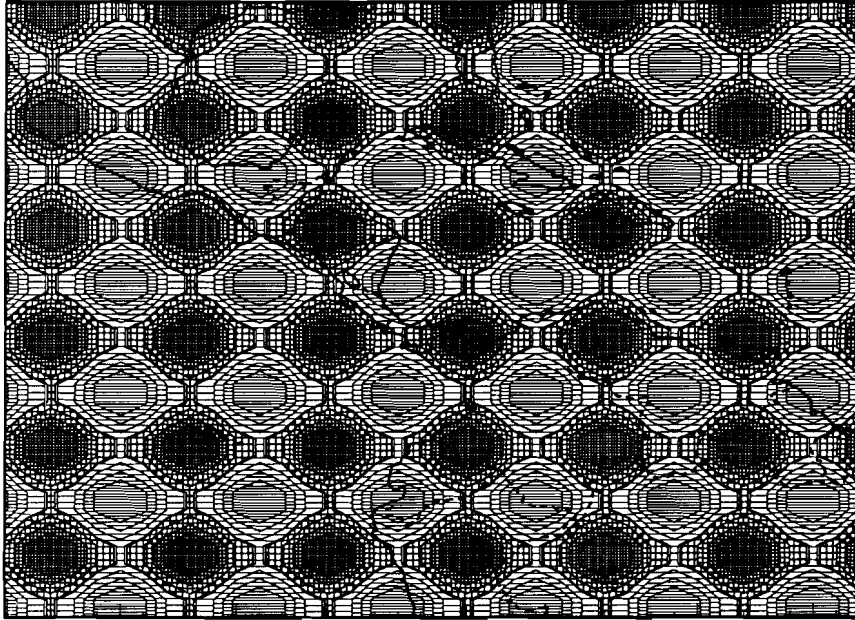
As discussed by Spakman and Nolet [1988], in the results of the data inversion there is an important relationship between the hit count and the amplitude of the imaged anomalies (see also section 5.2.6). Regions within the cell model that are characterized by high cell hit count show faster convergence than model regions with low cell hit count [Spakman and Nolet, 1988]. Consequently, velocity anomalies may be biased to zero, or not recovered at all, in mantle regions where the hit count is low [Spakman and Nolet, 1988]. It is important to realize that the cell hit count is a scalar number, which does not contain information about the directions of ray illumination. In mantle regions with high hit count, the resolution of structure can be poor if the structure is predominantly sampled from a limited range of directions. This is often the case near subduction zones, thus hampering the tomographic interpretation of these important structures [Spakman et al., 1989; and chapter 3 of this thesis]. Here, I only display the total hit count, hereafter referred to as  $N_{hit}$ , which is determined by the  $P$ ,  $PP$ , and  $pP$  phases. Information about the contribution of the  $PP$  and  $pP$  phases to the cell hit count can be obtained by comparing the figures in this chapter with the Figures of Appendix 3B.

### 5.2.3 The harmonic sensitivity test

In general, the interpretation of tomographic images of velocity perturbations is complicated by the presence of artifacts [Spakman and Nolet, 1988; Van der Hilst and Spakman, 1989; Spakman et al., 1989]. Therefore, it is important to have information about the spatial resolution in the images. In large-scale tomographic studies it is not possible to compute the resolution matrix. However, upper estimates of resolution can be obtained with sensitivity tests [Spakman, 1988; Spakman and Nolet, 1988; Humphreys and Clayton, 1990]. In this chapter, two tests are considered to investigate the reliability of structures of different length scales: the harmonic and the spike sensitivity test.

The input velocity model I use in the harmonic sensitivity test consists of two superimposed sine functions (Figure 5.1). The amplitude of both sine functions is 5% of the layer-average of model VCAR (Table 1.1, Figure 1.5). In horizontal direction, the pattern of the synthetic velocity model has a predominant wavelength of 6 cells ( $\approx 900\text{km}$ ). To investigate vertical resolution, the synthetic structure of odd layers is shifted by half a wavelength relative to the pattern of the even layers (Figure 5.1). From this model, a set of synthetic data is obtained by solving the forward problem using the same ray geometry as employed in the real data case [Spakman and Nolet, 1988]. Analyses of the correlation between the input model and the inversion response to this model are used to assess the reliability of the imaged velocity structures. With the harmonic sensitivity test the image resolution is tested of smoothly varying velocity structures in the Earth mantle [Spakman, 1988]. The inversion response to the exact harmonic input model will hereafter be referred to as  $x_{harmonic}$ .

Harmonic model in odd layers



Harmonic model in even layers

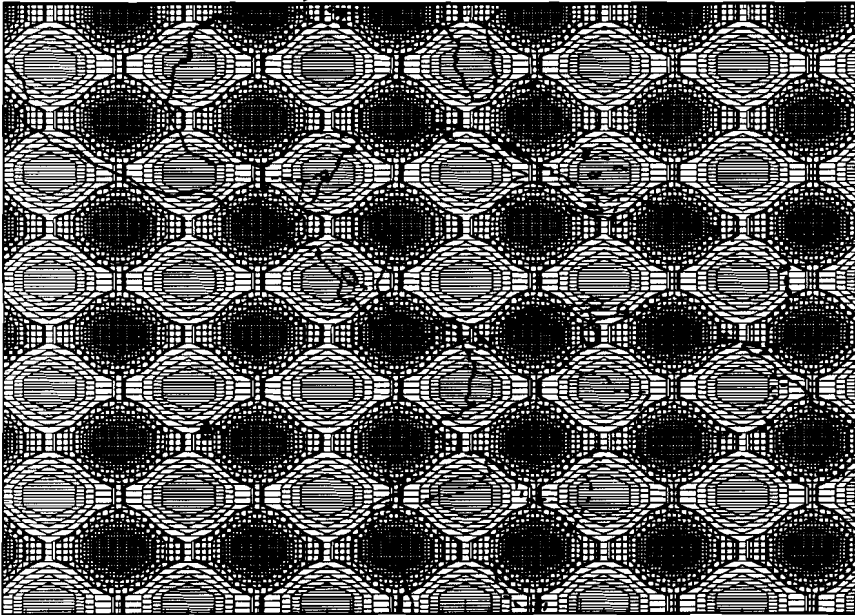


*Figure 5.1.* The exact harmonic input model for odd and even layer numbers respectively. Contoured according to scale bar of Figure 5.3c.

To model the large errors in ISC delay times, synthetic data errors are added to the synthetic delay times prior to the inversion. As discussed in chapter 3 (section 3.6.3 and Appendix 3A), I added Gaussian noise with a standard deviation of  $\sqrt{\gamma} \times 0.8$  sec, where  $\sqrt{\gamma}$  depends on the type of seismic phase (section 3.6.3 and Appendix 3A, [Van der Hilst and Engdahl, 1990a]. In addition, the value of  $\sqrt{\gamma}$  for *P* phases depends on whether or not the phases are recorded in the triplication range where the data can be expected to be contaminated by mispicks (Appendix 3A).

#### 5.2.4 The cell-spike sensitivity test

The second test carried out to investigate the resolution in tomographic images is called the cell-spike sensitivity test [Spakman, 1988]. With this test, the resolution can be assessed of structure at a shorter length scale than with the harmonic sensitivity test. The input model for this test (Figure 5.2) is characterized by zero slowness in all but a few equidistantly spaced blocks of the model depicted in Figure 1.6. The inversion response to a slowness anomaly in a single cell of the model can formally be regarded to be a row, or column, of the resolution matrix [Spakman and Nolet, 1988; Humphreys and Clayton, 1989]. Because the model used in this study consists of nearly 50,000 cells, it is not feasible to compute the spike responses for all cells. However, if the separation between the spikes is sufficiently large, the response to this input model provides in one inversion an indication of the resolution for many cells of the model [Spakman and Nolet, 1988]. Careful examination of the response to the spike input model provides information about the performance of the inversion algorithm in combination with a fixed reference ray geometry.

In the spike test, the anomalies have amplitudes of 5% relative to the layer average of VCAR and are separated by at least two cells in lateral direction and by one cell in vertical direction (Figure 5.2). The response to the synthetic spike model will hereafter be referred to as  $\mathbf{x}_{spike}$ .

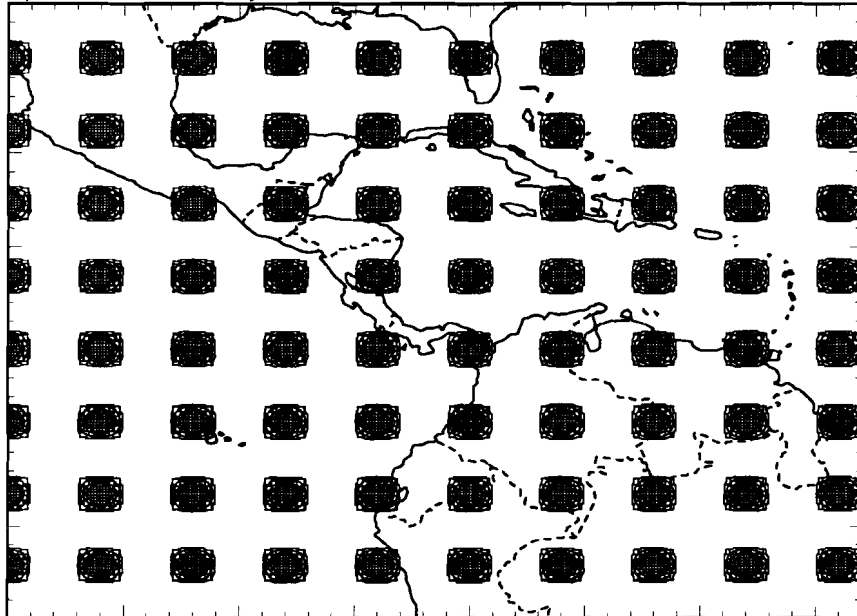
#### 5.2.5 The harmonic model fit

Detailed examination of the correlations between the sensitivity test results and the exact synthetic models is important, but inconvenient if one wants to get a quick impression about the average amplitude recovery, or compare the individual layer solutions with each other. To obtain a convenient image of the spatial resolution and amplitude response, I follow Spakman [1988] and Spakman and Nolet [1988] and compute the fit  $f_j$  in the vicinity of cell  $i$ , between the harmonic input model  $\hat{\mathbf{x}}$  and the inversion response  $\mathbf{x}$  ( $= \mathbf{x}_{harmonic}$ ) to that model. The fit  $f_j$  can be defined as

$$f_j = 1 - \frac{((\hat{\mathbf{x}} - \mathbf{x})^T \mathbf{W}_j (\hat{\mathbf{x}} - \mathbf{x}))^{1/2}}{(\hat{\mathbf{x}}^T \mathbf{W}_j \hat{\mathbf{x}})^{1/2}} \quad (4.1)$$

[Spakman and Nolet, 1988 (eqn. 18)], where  $\mathbf{W}_j$  is a three-dimensional smoothing window centered at cell  $j$ , that rapidly tapers to the sides with  $0.5^k$ , with  $k$  the number of cells separating a cell from cell  $j$ . I averaged over three cells horizontally, and one cell vertically.  $\mathbf{W}_j$  serves as a penalty function that weights spatial errors (i.e errors in the

Spike model in odd layers



Spike model in even layers

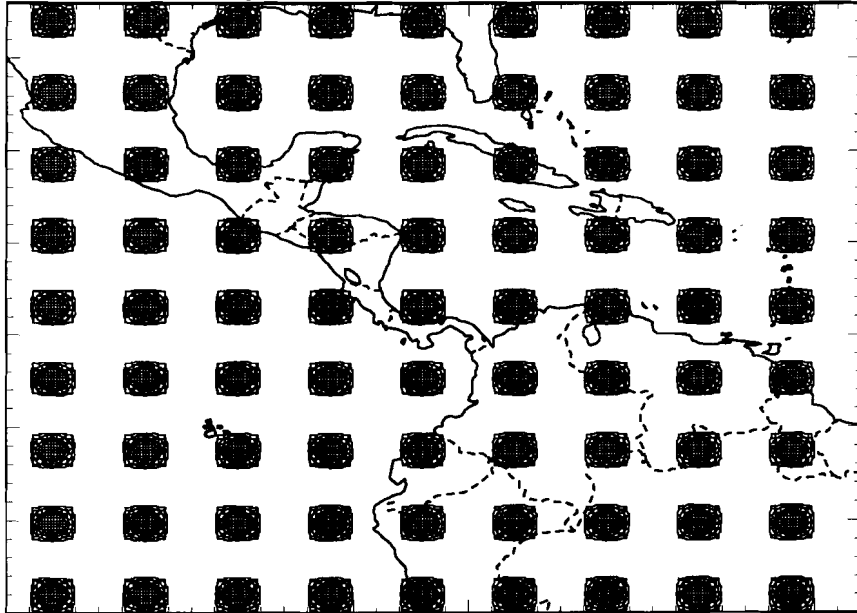


*Figure 5.2.* Exact spike model for odd and even layers. Amplitude: 5% velocity perturbation relative to the reference model.

location of the anomaly). Note that the fit function  $f_j$  equals 1 if  $\mathbf{x}=\hat{\mathbf{x}}$ , and equals 0 for a 100% amplitude misfit. The three-dimensional model fit will hereafter be referred to as  $\text{fit}_{\text{harmonic}}$ .

### 5.2.6 Shortcomings of the sensitivity tests

Several problems limit the diagnostic value of the results of sensitivity tests. (1) For the calculation of synthetic data used in the sensitivity tests, the ray geometry is adopted that is computed for the original problem. Consequently, the synthetic delay times are always consistent with the ray paths. In the original problem, however, the reported delay times correspond to ray paths which are not known exactly: the actual Earth's aspherical structure is not known, and we have to rely on the adequacy of the computed reference ray paths to replace the true ray paths. In chapter 2, it was shown that differences of the order of 100 km can be expected between the actual ray paths in the Earth's upper mantle and the ray paths computed in a spherically symmetric reference model. This uncertainty inheres in the inversion of actually reported data, but does not effect the sensitivity tests. (2) The addition of normally distributed noise to the synthetic delay times does not necessarily mimic the statistical properties of errors in the reported travel-time residuals very well, because many sources of systematic errors exist [Van der Hilst and Spakman, 1989; Van der Hilst and Engdahl, 1989, 1990a]. (3) In sensitivity tests, there are no errors in hypocentral parameters which are thus consistent with synthetic delay times. This is not necessarily true in the case of the reported data. For example, I showed previously that ISC-reported  $pP$  travel-time residuals are not consistent with ISC-reported focal depths [chapter 3, and Van der Hilst et al., 1990b]. This inconsistency results in significant trade-offs between hypocenter relocation and velocity structure, which are not modelled in the synthetic test.

Beside these problems, there is a discrepancy between what can be learned about the reliability of the imaged velocity structures from sensitivity tests, and what can be inferred about these structures from independent investigations (e.g., geological information). As will be discussed later, the imaged velocity structures often correlate very well both with results from independent seismological investigations, as well as with surface tectonical and geological features, even in regions where the harmonic and the spike responses predict low resolution. At present, the sensitivity tests are the only tools available to systematically obtain estimates of spatial resolution for the entire model. Although these tests indicate regions where structure is badly resolved, I argue that the fit between the exact input model and the inversion response to that model should not be considered a definite criterion in judging the reliability of the images.

### 5.2.7 The inversion of randomly permuted data

A general problem in seismic tomography is the relation between the imaged velocity structures and the way these structures are sampled by seismic waves. This tomographic investigation suggests a correlation between the high velocity structures in  $\mathbf{x}_{\text{data}}$  and the mantle regions where the cell hit count ( $N_{\text{hit}}$ ) is high. The question arises, what affects the



		$n$	$\sigma_{noise}$ [sec]	$\sigma_{data}$ [sec]	$mean\ data$ [sec]	$\sigma_{res}$ [sec]	$mean\ res$ [sec]	$red.\ \sigma^2$ [%]
data	$P$	30	-	1.50	-0.01	1.21	0.0	35.9
	$PP$			3.39	0.39	2.65	0.08	38.9
	$pP$			2.91	-1.53	2.58	-0.58	21.4
$x_{harm}$	$P$	30	0.84/0.95	1.24	0.04	0.84	-0.00	51.0
	$PP$		1.2					
	$p$		1.2					
$x_{spike}$	$P$	30	0.84/0.95	1.14	-0.87	0.86	-0.00	64.0
	$PP$		1.2					
	$p$		1.2					
$x_{perm}$	ALL	15	-	1.50	-0.00	1.43	-0.00	6.9

Table 5.1: Information about the different inversions, discussed in section 5.3.

$n$ , number of iterations,  $\sigma_{noise}$ , standard deviation of random noise added to the synthetic data: the different figures for the  $P$  phase refer to data in the entire distance range, but the triplication range (left), and data from within the triplication range (right).  $\sigma_{data}$ , standard deviation of delay times prior to inversion,  $mean\ data$ , mean value of delay times prior to inversion,  $\sigma_{res}$ , standard deviation of delay time residuals after  $n$  iterations,  $mean\ res$ , mean value of residuals after  $n$  iterations,  $red.\ \sigma^2$ , variance reduction obtained after  $n$  iterations.

imaging of velocity heterogeneities more: the data set of delay times, or the way in which the structures are sampled? Grand [1987] and Spakman and Nolet [1988] have tried to answer this question by investigating the performance of the inversion algorithm, after destroying the correspondence between the ray paths and the delay times. In other words, they destroyed the relation between the left-hand side (matrix  $A$ ) and the right-hand side (delay time vector  $d$ ) of the tomographic system of equations (equation 1.1). Whereas Grand [1987] constructed an artificial data vector by generating random delay times in a particular time interval, I followed Spakman and Nolet [1988] and created a new data vector by randomly permuting the delay time vector of the original problem. The sequence of the equations of the tomographic system (the rows of matrix  $A$  in (1.1)) is kept fixed. Next, the result,  $x_{perm}$ , of the inversion of the randomly permuted data is compared to the result of the inversion of the original data,  $x_{data}$ . Note, that the variance and the mean value of the distribution of permuted data are the same as those of the distribution of the original, unperturbed, data. Thus, a non-zero mean value of the distribution, e.g., due to inconsistency of ISC-reported delay times with hypocentral parameters (chapter 3), still maps into the result of the inversion of randomly permuted data [also Spakman and Nolet, 1988].

The comparison between  $x_{perm}$  and  $x_{data}$ , helps us to interpret the tomographic images. In the case which is the most difficult to interpret, the variance reduction upon inversion of

the randomly permuted data is comparable to the variance reduction of the original data; the norm  $|x_{perm}|$  is comparable to  $|x_{data}|$ ; and features in  $x_{perm}$  resemble perturbations in  $x_{data}$ . If we expect to invert for smoothly-varying, or even constant, velocity anomalies, the mentioned correlation does not necessarily mean that the relation between delay times and imaged structure is not meaningful. However, if we invert for smaller scale heterogeneities, as in this study, we may have to conclude that the features in  $x_{data}$  do not necessarily originate from the data, but can be artifacts of ray coverage. On the other hand, if the variance reduction upon inversion of perturbed data is only small compared to the reduction obtained for the unperturbed data, and if we observe in  $x_{perm}$  only low-amplitude perturbations that are not spatially coherent, we may conclude that the structure in  $x_{data}$  is determined by the delay times used in the inversion. In that case, tomographic images provide valuable information about Earth structure.

Thus, interpretation of  $x_{perm}$  is complicated because the true velocity structure is not known. This dilemma can be circumvented if an experiment is carried out in which  $x_{data}$  is considered as a known velocity structure. From the imaged structure,  $x_{data}$ , and with the ray geometry of the original problem, a set of delay times can be computed. Subsequently, these synthetic data are randomly permuted, and the inversion problem solved. The result of this inversion can be compared to  $x_{data}$ . This test is not performed in this study, but can be easily implemented in existing software for future investigations.

### 5.2.8 The presentation of the results

For each layer of the cell model depicted in Figure 1.6, the cell hit count and the results of the inversions that are discussed above are displayed in Figure 5.4. The solutions  $x_{data}$ ,  $x_{harmo}$ ,  $x_{spike}$ , and  $x_{perm}$ , are displayed relative to reference model VCAR. In Figure 5.4, the discrete values in individual blocks of the model are contoured according to the scale keys shown in Figure 5.3. The contouring is based on a linear interpolation between values in individual cells, resulting in a smoothed representation of the discrete function of cell values. Values beyond the scale limits given in Figure 5.3 are indicated in Figure 5.4 by line contours in the hatching of the upper- or lowermost interval. Note that the scales for the displays of  $x_{harmo}$  and of  $x_{spike}$  (Figure 5.3a and 5.3c) reach only 60% of the maximum amplitude of 5% of the input structure.

Relevant quantities concerning the different inversion discussed above are given in Table 5.1. The results that are presented in Figure 5.4a,c,d,e are obtained after 30 iterations. More iterations would lead to only a small additional variance reduction. Although I am aware that even (very) small increases of variance reduction can be significant for parts of the solution I decided to stop after 30 iterations. The values of  $x_{perm}$  that are displayed in Figure 5.4f are given after 15 iterations, because no further reduction of the variance was shown.

## 5.3 Inversion results for the upper mantle

In this section, the results of the inversions are presented and discussed for the individual depth layers. For the top 4 layers, encompassing the depth range between 0 and 185 km, I

discuss the observations for sub-regions within the Caribbean region. I distinguish as sub-regions: (1) Middle America, the adjacent western Caribbean Plate, and western part of the Northern Plate Boundary Zone, (2) the eastern Caribbean Sea and Lesser Antilles realm, together with the eastern part of the northern and southern Plate Boundary Zones (PBZ), and (3) the (western part of the) southern PBZ and north west South America. These sub-regions will be subjected to a more detailed examination in chapter 6. I discuss the entire region for the deeper levels in the mantle. The abbreviations of geographical and tectonical units refer to Figure 4.1, and are listed in Table 4.1.

### 5.3.1 Layer 1: 0 - 33 kilometer

I remarked in section 3.6.3 that velocity structures in the crustal layer are poorly resolved. It can be inferred from Figure 5.4.1e that the harmonic input model is recovered by more than 30% only along the Mexican part of the MAT, along the southern PBZ, and along the convergent plate boundary of northwest South America. Outside these relatively narrow zones the model fit drops rapidly and features in the tomographic images in those regions may not be reliable. The crustal layer is characterized by a very heterogeneous hit count ( $N_{hit}$ ) due to the direct dependence on the locations of recording stations and the uneven distribution of shallow events. In the previous chapter (Figures 3.15 and the Figures of Appendix 3B), I demonstrated that incorporation of  $PP$  and  $pP$  phases in the tomographic inversions improved the illumination of the shallow layers. Because of the particular ray geometry in this layer (few rays bottom in this depth range, hence most rays transect the cells near-vertically) the path lengths of rays are small compared to other layers. It can be assumed that this top layer also absorbs combined effects of station and event errors that could not be explained by the station and relocation corrections during inversion [Spakman, 1988].

#### *Western Caribbean and Middle America*

A broad zone of high velocities extends along the Middle America Trench (MAT), from the Chiapas-Petén massif (CP) in southern Mexico to the Nicoya Peninsula (NP) and the landward continuation of the Hess Escarpment. There, the high velocity structure narrows towards the Isthmus of Panama. Northwest of this high velocity feature, the Trans Mexican Volcanic Belt (TMVB), with neogene volcanism, is marked by low velocities. Figure 5.4.1a does not suggest differences in crustal velocity structure across the Motagua-Polochic fault zone (MPfz). Near the North American-Cocos-Caribbean triple point, the Northern Plate Boundary Zone (NPBZ) is not expressed in the velocity structure at this depth. From the harmonic response  $x_{harmonic}$  (Figure 5.4.1c), I infer that along the MAT the sign of long wavelength variations in velocity structure is reasonably well resolved. However, Figure 5.4.1e shows that only below Mexico the harmonic model fit exceeds 30%, but below the southern part of Middle America the recovery of the input model varies between 20% and 30%. Except for the area near the (mainly Mesozoic) Chiapas-Petén (CP) metamorphic province in south Mexico and Guatemala, velocity perturbations are "smeared out" in longitudinal direction. This suggests either lack of resolution in this

direction, or leaking of anomalies of the second layer into the top layer due to poor vertical resolution. I shall come back to this later.

### *Eastern Caribbean: Lesser Antilles*

The Lesser Antilles convergent boundary is also marked by high velocities. Smoothly varying structures are reasonably well resolved, as is indicated by  $x_{harmonic}$ , in northwest to southeast and north to south directions. West of the Puerto Rico, along the northern PBZ, as well as along the southern PBZ, the harmonic response indicates low resolution. Interesting is the change in velocity structure, along the Lesser Antilles Arc, across the  $15^\circ$  parallel. South of this parallel, the Barbados Ridge (BbR) is flanked by the Tobago and Barbados basins (ToB and BbB). For this region, the resolution at this depth range prohibits direct interpretation of the images.

### *Northern Plate Boundary Zone and northwest South America*

At this depth level, it is difficult to correlate changes in velocity structure along the southern PBZ, and in northwest South America, with geologic or tectonic provinces, because of poor resolution, the coincidence of some abrupt changes in  $x_{data}$  with drops or increases in  $N_{hit}$ , and the probable vertical leaking of (high amplitude) anomalies of the second layer. In this crustal layer, I infer no systematic correlations between the large scale throughgoing strike slip systems in northwest South America and the velocity structure. Sharp velocity contrasts are located in central Colombia and near the border between Colombia and Ecuador. For the latter location, I also observe sharp contrasts in both the cell hit-count image (Figure 5.4.1b) and in  $x_{perm}$  (Figure 5.4.1f), which excludes direct interpretation of the velocity anomalies in terms of geological structure. In contrast, the features in central Colombia do not correlate with abrupt changes in  $N_{hit}$  or  $x_{perm}$ . From Figures 5.4.1c and 5.4.1e, I infer that in this region the harmonic input model is well resolved both in shape as in amplitude. In central Colombia, the features in  $x_{data}$  correlate very well with large-scale tectonic units, as mapped by Martin [1978]. As will be shown below, the variations in velocity structure are rather continuous with depth and may be related to the boundaries between different segments of a subducting plate below the area, which are distinguished by Pennington in his seismicity study [1981, his Figures 6 and 7] Pennington's figure 7 is given in Figure 5.5.

Summarizing, I note that in general the resolution in this layer is poor. Only along the convergent plate boundaries a harmonic fit of over 30% is obtained, which is still low. Whereas the harmonic response indicates reasonable resolution in some regions, e.g., near the South America-Nazca-Caribbean triple junction, the almost absolute failure to recover the input spike model suggests that the small details of the images are not reliable. Some variations in hit count  $N_{hit}$  are reflected in  $x_{data}$ . Note the very small amplitudes in the  $x_{perm}$  display. Although apparently more positive perturbations result from the inversion of randomly permuted data, there is in general no correlation between the pattern and amplitudes of  $x_{data}$  and  $x_{perm}$ .

### 5.3.2 Layer 2: 33 - 85 kilometer

The sampling by seismic waves of structure in this layer is somewhat less inhomogeneous than that of the crustal layer, as can be concluded from the  $N_{hit}$  image (Figure 5.4.2b). In contrast to the top layer of the model, where most rays travel vertically to recording stations, many rays bottom in this sub-crustal layer. These are rays travelling, over ca.  $4^\circ$  epicentral distance (Figure 2.3b), to nearby stations. The more homogeneous sampling by seismic rays (Figure 5.4.2b) results in a significantly better resolution of both the shape and the amplitudes of the exact harmonic and spike models. Recall that the locations of the maxima and minima of the exact harmonic input are shifted by half a wave length with respect to the previously discussed layer, as is shown in Figure 5.1. I infer from Figure 5.4.2d that over most of the area low-amplitude blurring of input spikes occurs, but that many individual spikes are recovered at this depth level. The better amplitude response is significant because no increase in amplitudes is observed in  $x_{perm}$ .

#### *Western Caribbean and Middle America*

Along the MAT, the high  $N_{hit}$  zone is continuous from north of the Trans Mexican Volcanic Belt (TMVB), in central Mexico, to the Panama fracture zone (PFZ). Along the western part of the NPBZ, the cell hit count is also high. The well recovered amplitudes of  $x_{harmonic}$  along the MAT (Figures 5.4.2c and 5.4.2e), and the correct mapping of the input spikes (Figure 5.4.2d), indicate better resolution than in the top layer of the cell model. The velocity structure is not continuous along the MAT, in contrast to both  $N_{hit}$  and  $fit_{harmonic}$ . Similar to the crustal layer, the Neogene TMVB is characterized by velocities about 3% lower than expected from the reference model. In the southeastern direction, the boundary between the metamorphic, mainly Mesozoic, Chiapas-Petén massif (CP) is marked by a transition to higher velocities. The Motagua-Polochic fault zone (MPfz), which marks the westernmost part of the NPBZ, coincides with a drop in the relatively high velocities of the adjacent Chiapas-Petén and the Chortis cratonic block. In Middle America, the correlation between the northern plate boundary and lower velocities is persistent to depths of ca. 200-300 km, as will be shown below. At the 33-85 km depth level, the high velocity structure of the Chortis block is cut off near the landward continuation of the Hess Escarpment (HE). South of the HE, below the southeastern part of the Middle America Volcanic Province (MAVP), with Neogene calc-alkalic components, low velocities extend across the Panama Fracture Zone (PFZ). East of the PFZ, the complex deformation belts surrounding Panama (e.g, the Northern Panama Deformed Belt (NPDB)) are marked by high velocities.

In the Gulf of Mexico region (north of the Cayman trough) a detailed description of the structures is not justified because of poor resolution as inferred from  $x_{harmonic}$ ,  $x_{spike}$ , and  $fit_{harmonic}$ .

#### *Eastern Caribbean: Lesser Antilles*

Apart from northeast of Puerto Rico, the harmonic model is reasonably well recovered. The locations of the spikes are also resolved. However, the amplitude recovery is bad, except

for the spike just west of the Lesser Antilles arc.

Although  $N_{hit}$  varies smoothly in east-west direction,  $x_{data}$  shows a sharp contrast east of Hispaniola. This contrast coincides with the western limit of the Muertos trench. High velocities occur north of the eastern Greater Antilles. The Beate Ridge (BeR) is marked by high velocity features. Below the southern part of the Lesser Antilles, south of the 15<sup>th</sup> parallel, lower velocities prevail than below the northern part. The presence of low velocities below the Barbados ridge and the Barbados and Tobago basins is similar to the observation made for the crustal layer. These low velocities are sharply cut off by the eastern part of the SPBZ strike-slip system, the El Pilar fault zone (EPfz).

#### *Northern Plate Boundary Zone and northwest South America*

The structure below the central part of the Colombia basin is characterized by low velocities comparable to those observed in the crustal layer. In the area south to southeast of the SPBZ, high velocities are observed. This slightly curved, east-to-west trending, high-velocity structure is cut off in the northwest by the Boconó fault zone (Bofz). In central Colombia, the high velocities in the northeast sharply grade to low velocity anomalies in the southwest. This sharp velocity contrast is also visible in the crustal layer (section 5.4.1) and persists to a depth of 130-185 km, as I shall show below. The location of the sharp transition in central Colombia closely coincides with the boundary between the Bucaramanga and the Cauca seismic segments [Pennington, 1981] (see Figure 5.5). Pennington distinguished between three seismic segments in an investigation of seismicity and focal mechanisms in this region, and related them to segments of subducted lithosphere. The drop in velocities across the border between Colombia and Ecuador coincides with Pennington's boundary between the Cauca and Ecuador seismic segments (Figure 5.5). As discussed previously in section 5.3.1, the presence of sharp contrasts in  $N_{hit}$  and  $x_{perm}$ , at approximately the same location, hampers the interpretation of  $x_{data}$  in relation to the seismotectonic setting. Below Ecuador, low velocities prevail where the aseismic bathymetric Carnegie Ridge (CaR, Figures 4.1 and 5.5) is subducted.

#### 5.3.3 Layers 3 and 4: 85 - 185 kilometer

I infer from  $x_{harmo}$ ,  $x_{spike}$ , and  $fit_{harmo}$ , that in the central parts of the images the resolution improves with respect to the previously discussed layers. In particular in the intraplate areas,  $N_{hit}$  has higher values and has become less irregular than in the previously described layers.

The similarities in velocity structures, and the fact that the resolution is not sufficient to justify a detailed description of every individual layer, warrant the discussion of more layers in one text section.

#### *Western Caribbean and Middle America*

In central Mexico, the transition is still visible from the low velocities below the TMVB to the high velocities beneath the CP massif. At this depth level, central Mexico is

characterized by low velocities with a pronounced minimum below the western part of the TMVB. The low velocity saddle-back between the high velocities of the southern CP, north of the MPfz, and the cratonic Chortis block, south of the NPBZ, is also visible between 85 and 130 km, although shifted to the southeast with respect to the shallower layers. This situation changes at larger depths, but the mantle region north of the NPBZ remains marked by high velocities. Towards the northeast, these lower velocities can be followed below the Yucatan Basin (YuB) and the Cayman Trough (CTr). In layer 4 (130 -185km), these low velocities are visible across the entire western Caribbean. The southeastern limit of the high velocity structure below the Chortis block is still located near the landward continuation of the Hess Escarpment. The mantle below the eastern part of the Cocos Plate (hence below the Middle America Volcanic Province (MAVP), below the Cocos Ridge and, across the PFZ, below the northern part of the Nazca Plate) is predominated by low velocities.

Although resolution is poor in the mantle region below the Gulf of Mexico, this area appears to be characterized by higher velocities than the reference model. The transition from relatively low velocities below the YuB, to the higher velocities below the southern edge of the Mexican Gulf is rather sharp, in particular between 130 and 185 km depth (layer 4).

#### *Eastern Caribbean: Lesser Antilles*

The most striking feature of the image of the mantle below the eastern part of the Caribbean Plate is the northeast to southwest trending boundary, separating high velocities on the northwestern side from low velocities to the southeast. High velocities also mark the upper mantle below the Greater Antilles, where oblique convergence between the North American and Caribbean Plates takes place. The propagation velocity of *P* waves is low below the Venezuela basin, Aves ridge, and the Grenada basin, but up to 2.5% higher than the reference model velocity below the Southern Caribbean Deformed Belt (SCDB), along the Curacao Trench, and below the Beate ridge. The harmonic response is good in this area (Figure 5.4.[3,4]c) both for layer 3 as well as for layer 4. In layer 3, the locations, signs, and part of the amplitudes of the spikes are reasonably well resolved in the eastern Caribbean. However, the spike response for the depth range between 130 and 185 km is bad. Further west, long wavelength anomalies are well resolved, but the tomographic inversion fails to recover the input spikes.

#### *Northern Plate Boundary Zone and northwest South America*

The El Pilar fault zone (EPfz, Figure 4.1) forms a sharp cut off between the velocity structures below the eastern Caribbean and below South America. To the west, high velocities are evident beneath the SCDB which can be followed into the very complicated diffuse tectonic boundary between the Panama block and South America. In both layers, but very convincingly in layer 4, correlations are visible between the velocity structures and the Bucaramanga subduction segment [Pennington 1981] (Figure 5.5). The high

velocity structure below the Bucaramanga segment apparently continuous into the high velocity structure of the mantle below the Colombia basin and the southern Caribbean deformed belt (SCDB). Figures 5.4.[3,4]c reveal high resolution along near-coastal regions. The quality of both the spike and the harmonic responses drops rapidly below the Guyana shield. The site of subduction of the Carnegie Ridge (Figures 4.1 and 5.5) is still recognizable by low velocities.

#### 5.3.4 Layers 5, 6 and 7: 185 - 390 kilometer

The results are displayed in Figure 5.4.[5-7]. These layers comprise the 200 km depth interval above the 390 km upper mantle discontinuity. I point to the decrease in both the harmonic and spike responses with increasing depth. This is also evident from the  $fit_{harmonic}$  displays. The harmonic responses suggest lack of lateral resolution. In this context, the following observation in the  $s_{spike}$  displays is relevant: even though the spikes are reasonably well solved at the correct location, "spike-like" anomalies are sometimes also visible at the locations of the input spikes in the adjacent layers. I conclude from this observation, that the apparent lack of horizontal resolution is actually lack of vertical resolution. This lack of vertical resolution can be explained partly by the absence of rays with turning points just above the 390 km discontinuity (chapter 2, Figure 2.3b). Supporting evidence for the characteristic effect of the upper mantle discontinuities comes from Figure 2.3c and from inspection of Figure 5.4.7b, which shows an increased inhomogeneity in the image of the cell hit count relative to adjacent layers.

Low velocities prevail in large regions of layers 5 and 6. The observation that the layers are relatively "slow", is an indication that the reference velocities are too high in this depth interval. Note that no Low Velocity Zone is considered in my reference model (chapters 1 and 2).

In layer 5, the boundary between the Gulf of Mexico region and the northwestern part of the Caribbean Plate is still present, but disappears at greater depths. The location of the Cayman spreading centre is flanked by velocities about 3% lower than the reference model. These low velocities below the Yucatan Trough (YuT) extend westward below the MPfz, where they separate a high velocity structure below south Mexico from an elongated high-velocity feature, below the Chortis block. Note the high-velocity structure which is continuous with depth below central Mexico. Below Yucatan a large east-to-west trending high-velocity lens is visible at depths of ca. 310 to 390 km. With increasing depth, the high velocity feature below the Chortis block almost vanishes and the high velocities below Mexico become highly ruptured. Between ca. 240 and 310 km depth, the mantle below Middle America is predominated by low velocities relative to the reference model.

The Pacific side of the MAT is marked with low velocities, in the 185-390 km depth range. In particular, in layer 5 (185-245 km), very low velocities can be observed below the Cocos Ridge and its northeastern continuation. These low velocities can be continued to the previously described anomalies between 130 and 185 km.

With regard to the aspherical structure below the eastern Caribbean, I focus attention on a high velocity anomaly that is continuous to larger depths. In the mantle beneath the



Greater and Lesser Antilles, a continuous arcuate high-velocity structure exists. This anomaly migrates slightly southwestward with depth. It is difficult to assess the western limit of the high velocity structure, because there is a strong correlation between  $x_{data}$  and  $N_{hit}$ . However, the absence of correlating velocity variations in  $x_{perm}$  suggests that the sharp cut off of the structures in the west is real. This western limit is located near the projected northeastern continuation of the Hess Escarpment, where the Beate ridge and the Muertos trench meet. Whereas in layer 5 the curved structure seems to be cut off below the El Pilar fault system in the south, at deeper levels the high velocities apparently extend across this (imaginary) east-west line.

The  $x_{data}$  displays of the layers 5,6 and 7 show a high velocity structure in the upper mantle below the Southern Caribbean Deformed Belt (SCDB). This structure is continuous at shallower depth levels with the high velocities below the SCDB, as discussed in the section 5.3.4. This structure migrates with increasing depth towards the south or southwest.

### 5.3.5 Layers 8, 9 and 10: 390 - 660 kilometer

The outlines of the plate tectonic framework (Figure 4.1) serve as a geographical reference and bear no direct implication for geodynamical interpretations. Below 390 km depth only large-scale tectonic features are outlined in the velocity panels.

The harmonic fit is worst in the layers just above the 390 km discontinuity, as can be inferred from Figure 5.4.[6-9]e. Below 390 km, the harmonic model fit improves with increasing depth (Figures 5.4.[8-15]e). It is difficult to draw a similar conclusion from  $x_{harmonic}$  and  $x_{spike}$ . The apparent longitudinal leaking in  $x_{harmonic}$ , actually due to lack of vertical resolution (section 5.4.4), decreases in some parts of the images below 390 km, but increases in other regions. In layer 8 just below the 390 km discontinuity  $x_{perm}$  show the highest amplitudes of the upper mantle. In contrast to  $x_{data}$ , the pattern is highly irregular. Nevertheless, we should be cautious in interpreting, e.g., the predominant high velocity structure below the southern part of Middle America (Figure 5.4.8f). The continuity of the imaged velocity anomalies in  $x_{data}$  is continuous with depth, whereas  $x_{perm}$  appears to be random.

In contrast to the discontinuous structures across the NPBZ at depths above 390 km, which I described in previous sections, the images suggest the continuity of structure across the NPBZ below 390 km. This elongated velocity anomaly is cut off below the landward continuation of the Hess Escarpment (compare to Figure 5.3.4a). High velocities extend in northwestern direction at depths between 475 and 660 km below northeastern Mexico and the western Gulf area.

The previously mentioned arcuate high-velocity structure continues to the base of the upper mantle below the eastern part of the Caribbean Plate. This structure migrates further southwest with increasing depth.

In the mantle below northwest South America, a slightly curved, north-to-south trending high-velocity structure can be observed (e.g., Figure 5.4.9a), with velocity perturbations of up to 3% relative to the reference velocity model. In this mantle region resolution is reasonably good, as is inferred from examination of  $x_{harmonic}$ ,  $x_{spike}$  and  $fit_{harmonic}$ .

### 5.3.6 Summary of results for upper mantle structures

I have to conclude from the examination of the synthetic responses that the resolution of small-scale structures is rather poor in large regions of the upper mantle. In general, structure with a wavelength of the order of 300 km is well resolved in most upper mantle regions below interplate realms ( $x_{harmonic}$ , Figures 5.4.[1,10]c). A bad harmonic response is found below the eastern Gulf of Mexico region, and below the Guyana Shield. A minimum in resolution is observed in model layer 7, just above the 390 km discontinuity. This may be attributed to the inhomogeneity in ray geometry in the vicinity of the 390 km velocity discontinuity (chapter 2, Figure 2.3). The tomographic inversion does not recover the input spikes very well. In particular below intraplate areas, spikes are not recovered in the upper 180 km of the cell model (layers 1 to 4). In areas with high cell hit-count, the spike resolution is better, although amplitude recovery is only adequate below the central (and at deeper levels also the northern) part of Middle America. For most layers in the upper mantle, the inversion of randomly permuted data leads to irregular, patchy, patterns of low amplitude anomalies. In general no correlation is observed between  $x_{data}$  and  $x_{perm}$ . However, correlations between  $x_{data}$ ,  $x_{perm}$ , and  $N_{hit}$  exist and velocity anomalies may not be realistic below northwest South America, and at specific depth levels, below the central part of Middle America.

Below the convergent margins of Middle America and the Lesser Antilles, the imaged velocity structures appear to correlate to large depths with large-scale tectonic features outlined on the map of Figure 4.1. These correlations are investigated and discussed in much more detail in chapter 6. Velocity perturbations correlate at shallow depths with, e.g., the Trans Mexican Volcanic Belt in central Mexico, and with the presence of the Cocos Ridge. The transition from the northern part of Middle America to the southern part of Middle America seems to be marked by variations in  $P$  velocity in the upper 250 km. Whereas the imaged structure in the upper 390 km of mantle below Middle America is rather irregular, a coherent pattern of high velocities parallel to the Middle America trench persists below 390 km. The location of the Hess Escarpment coincides with lateral boundaries between large scale velocity anomalies in the upper mantle both below the southern part of Middle America, as well as below the Greater Antilles. Below layer 3, large-scale aspherical variations of the  $P$  wave velocity can be continued across almost the entire upper mantle below the eastern part of the Caribbean Plate.

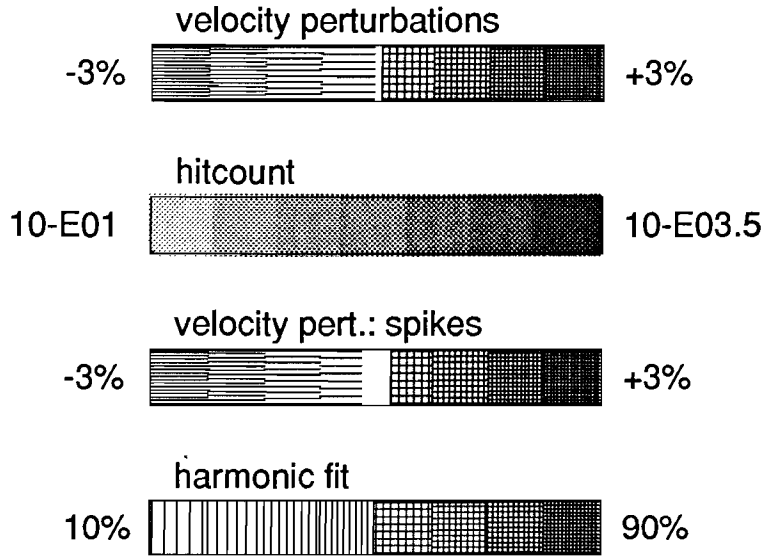
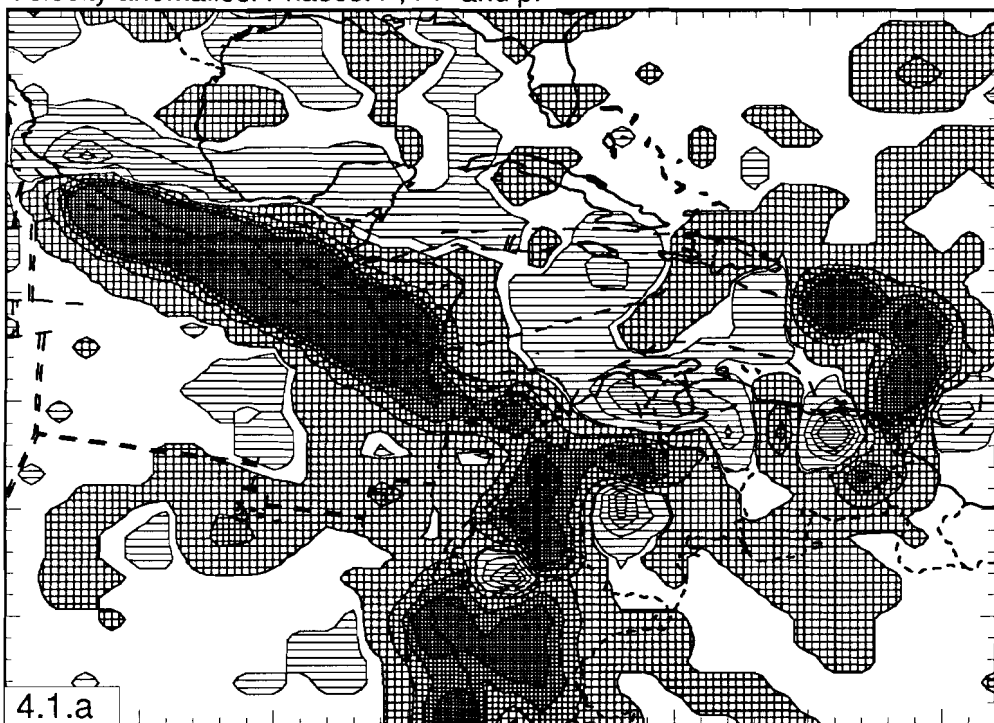


Figure 5.3. Scale bars for the different displays. According to these scale bars the results presented in Figure 5.4 are contoured. The plot key for the permuted data displays is the same as for  $x_{data}$ .

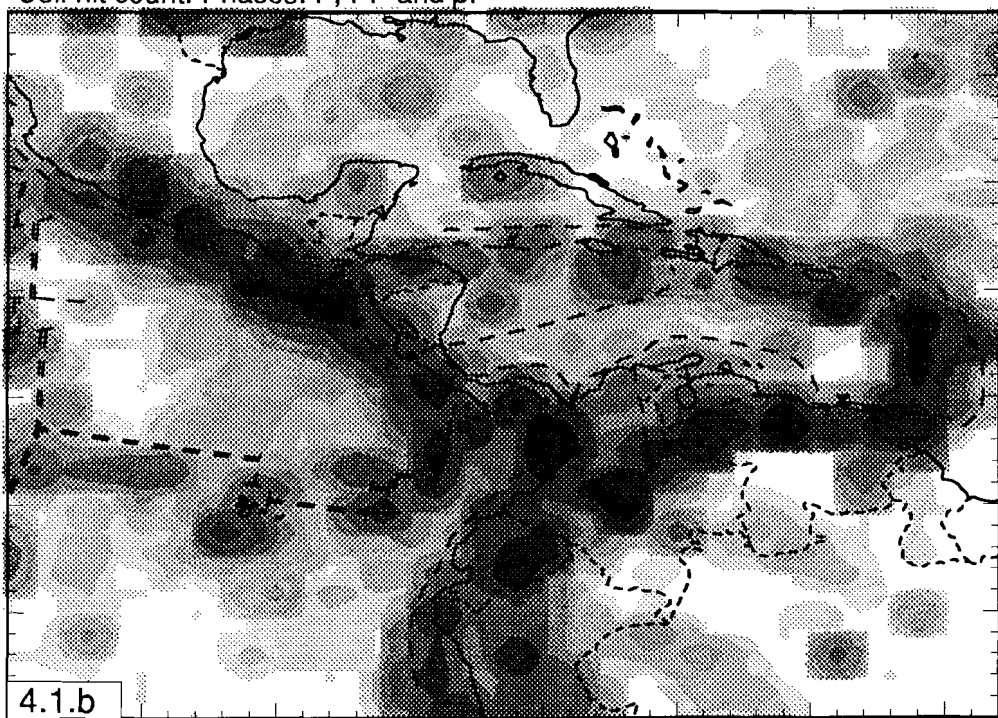
Figure 5.4. For every layer of the cell model: results of the tomographic inversions. For information about some important figures about the inversion see Table 5.1. (a) result of the true data inversion (section 5.2.1). The result is contoured according to the scale bar of Figure 5.3a Cross-hatched features denote regions with  $P$  wave propagation faster than the reference model, horizontally hatched structures mark relatively low velocities. (b) Distribution of cell hit count (section 5.2.2), logarithmically contoured according to Figure 5.3b. (c) Harmonic response (section 5.2.3, contours according to 5.3a). Regular pattern of solid line contours mark exact location of harmonics at +10% contour level. For exact input model see Figure 5.1. (d) Spike response (section 5.2.4). Contour scale is given in Figure 5.3c. Figure 5.2 shows the exact model. (e) The harmonic model fit (section 5.2.5) Contours are according to Figure 5.3d. (f) The result of the inversion of randomly permuted data (section 5.2.7). Contours are according to Figure 5.3a.



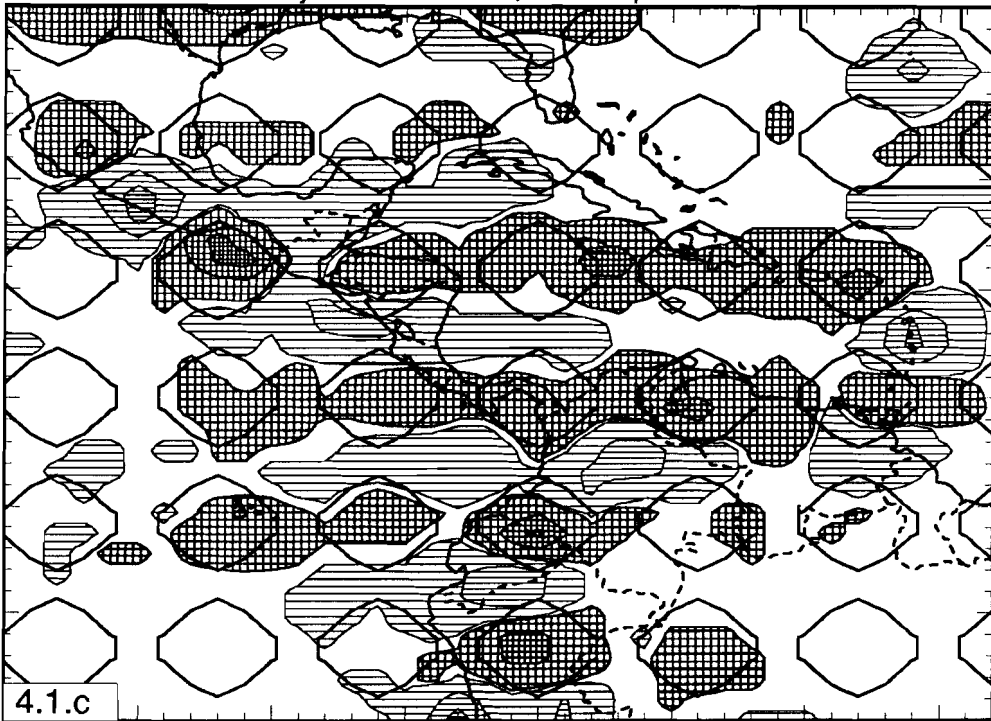
Velocity anomalies. Phases: P, PP and pP



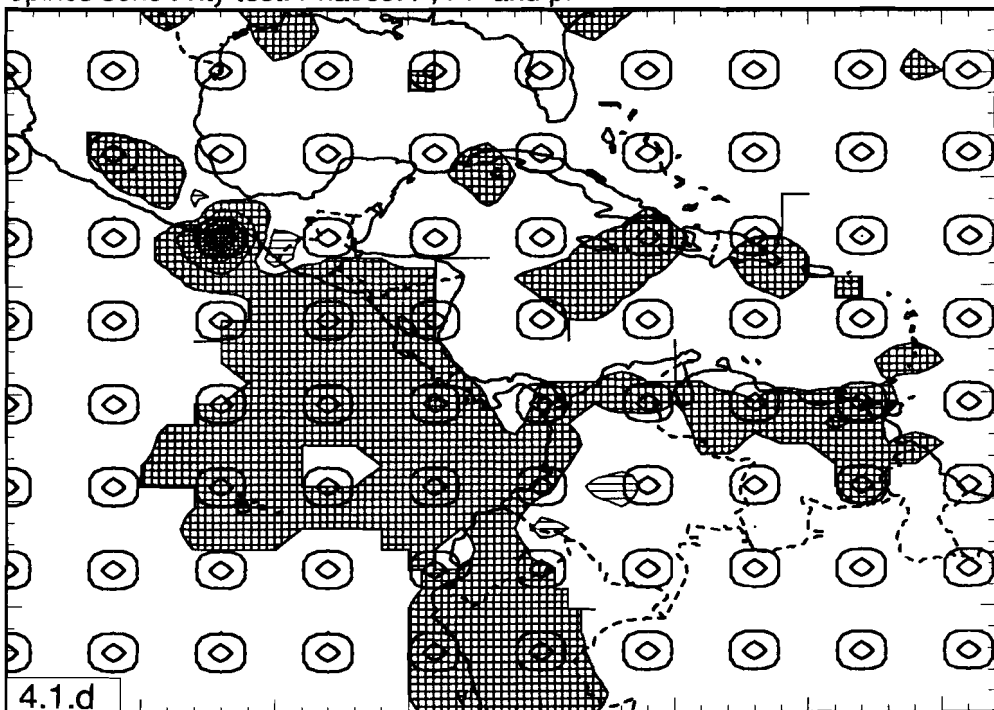
Cell hit count. Phases: P, PP and pP



Harmonic sensitivity test. Phases: P, PP and pP

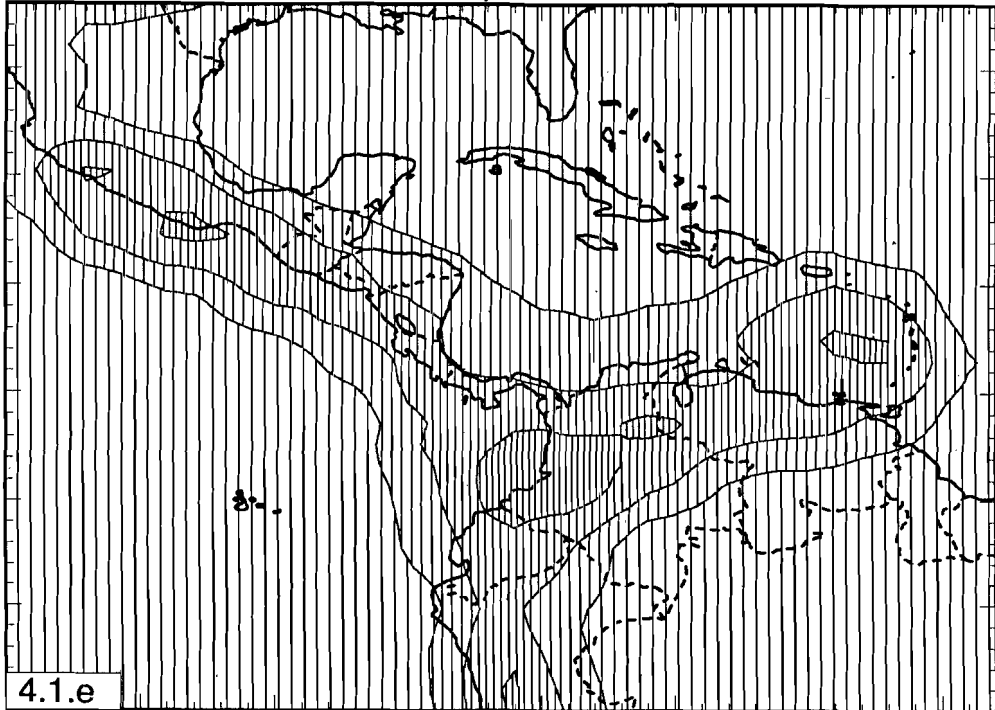


Spikes sensitivity test. Phases: P, PP and pP

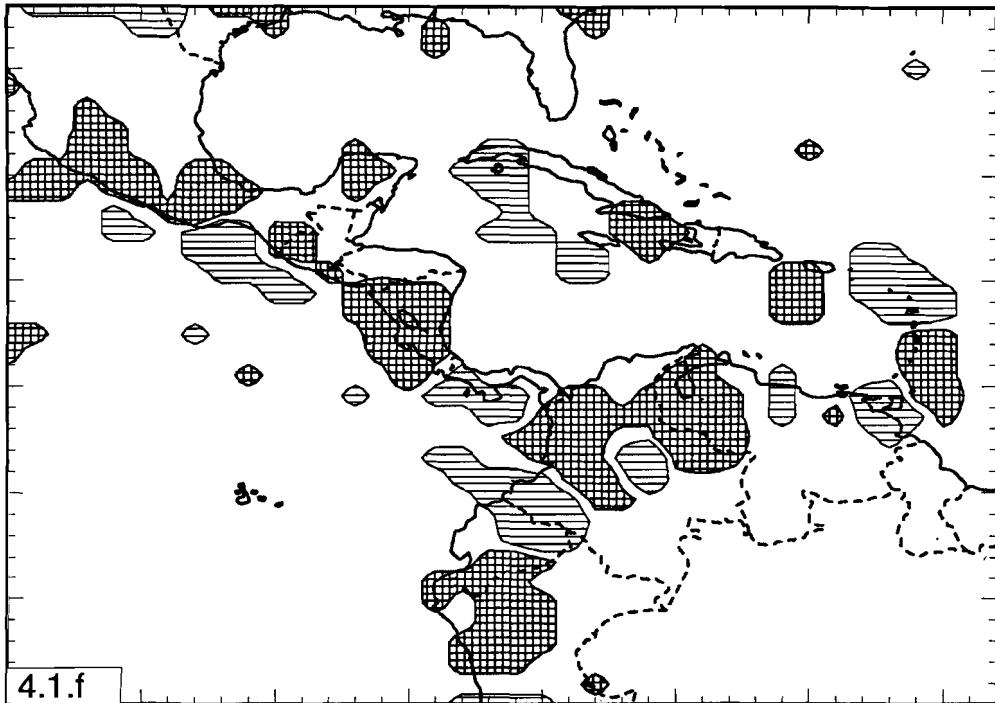




3D-Harmonic fit. Phases: P, PP and pP

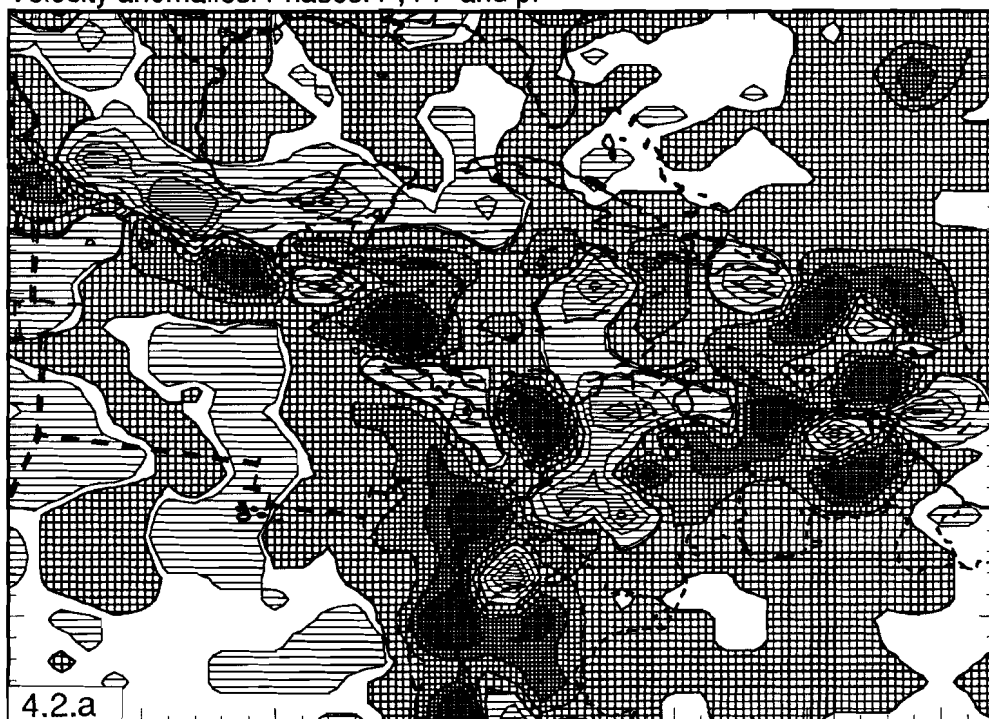


Permuted data: result after 15 iterations

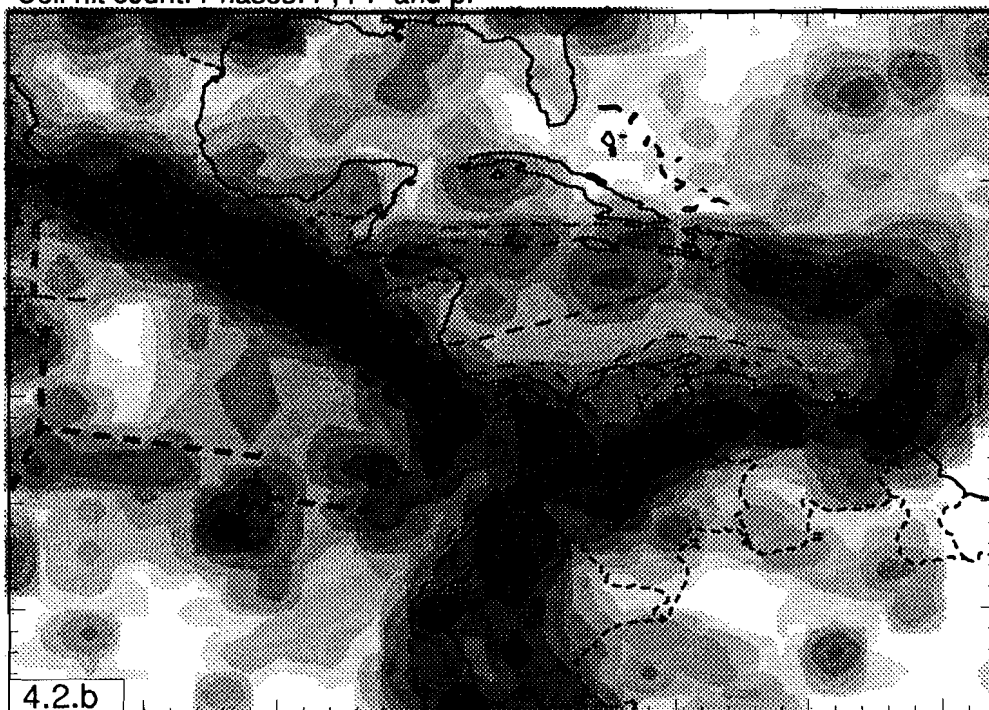




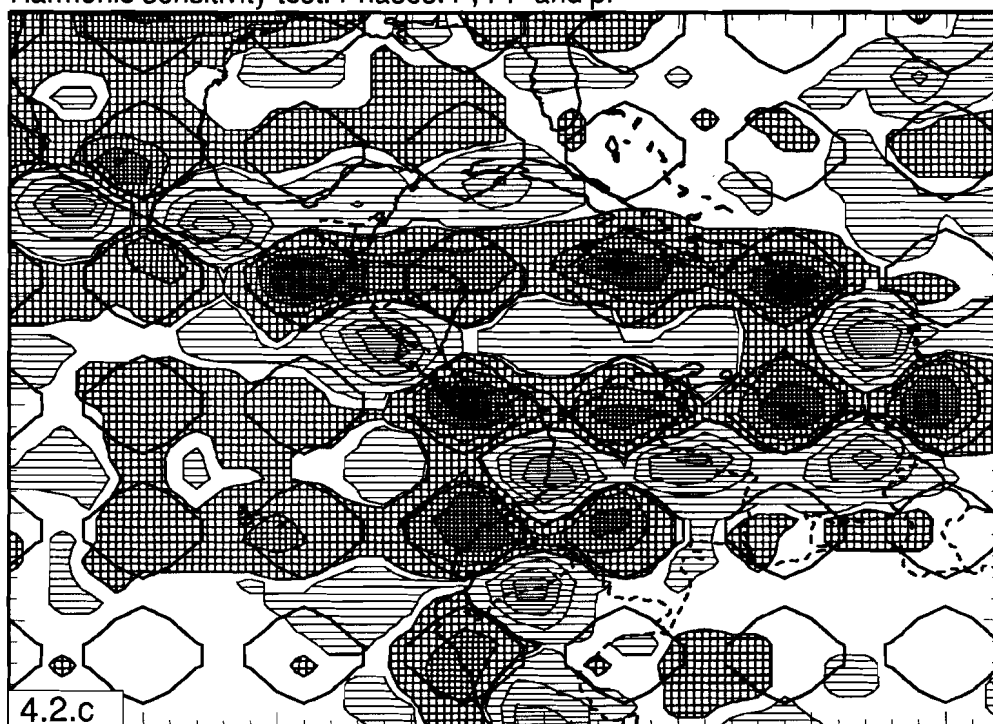
Velocity anomalies. Phases: P, PP and pP



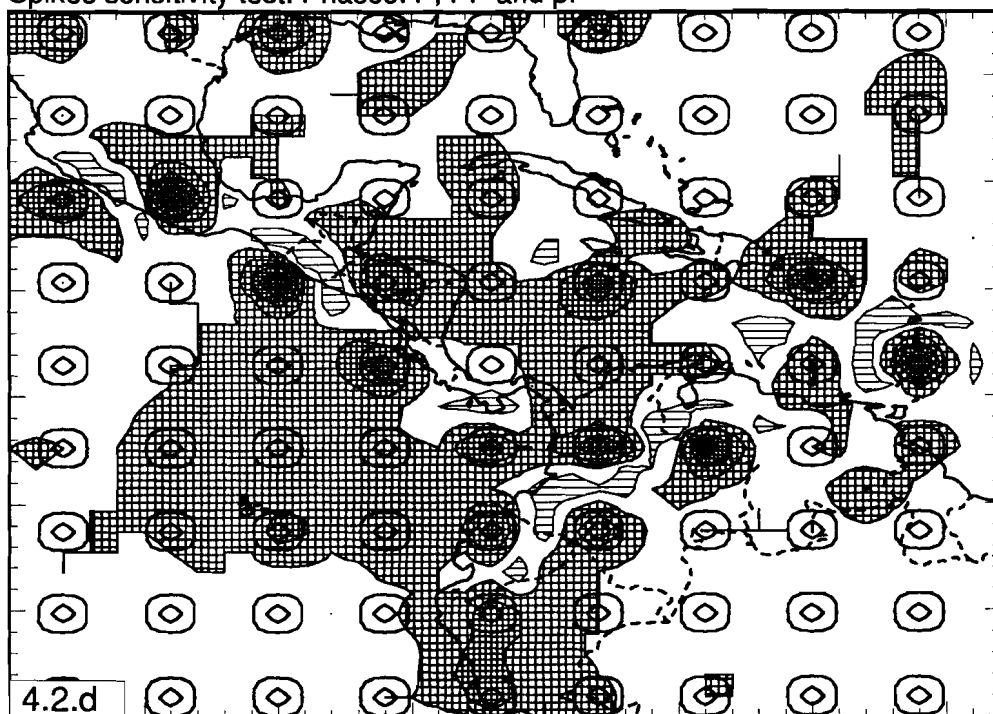
Cell hit count. Phases: P, PP and pP



Harmonic sensitivity test. Phases: P, PP and pP

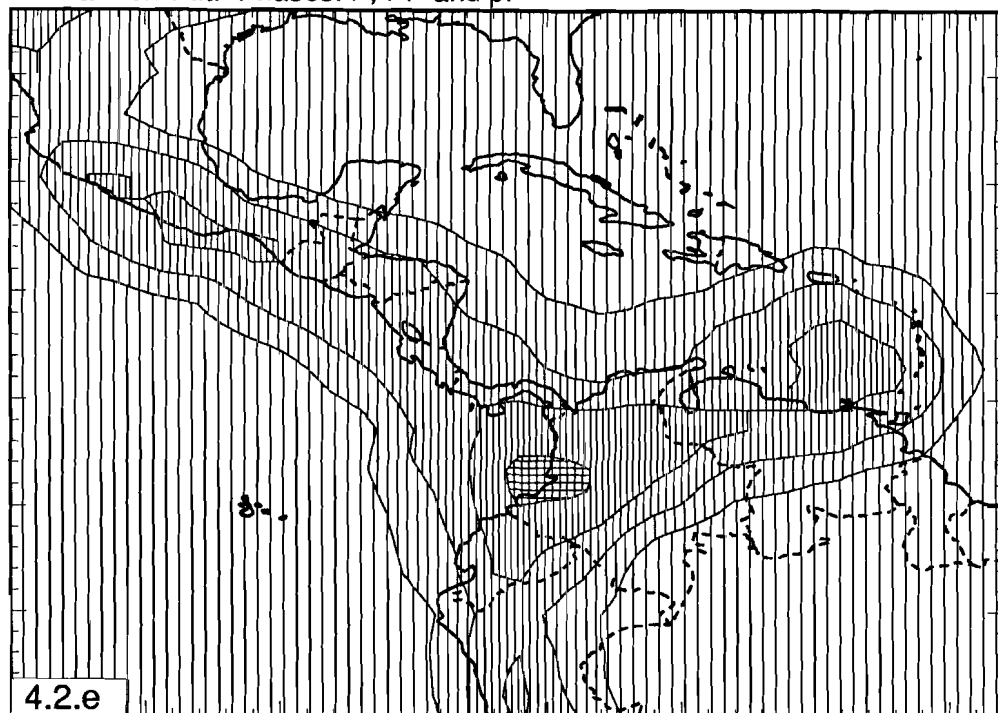


Spikes sensitivity test. Phases: P, PP and pP

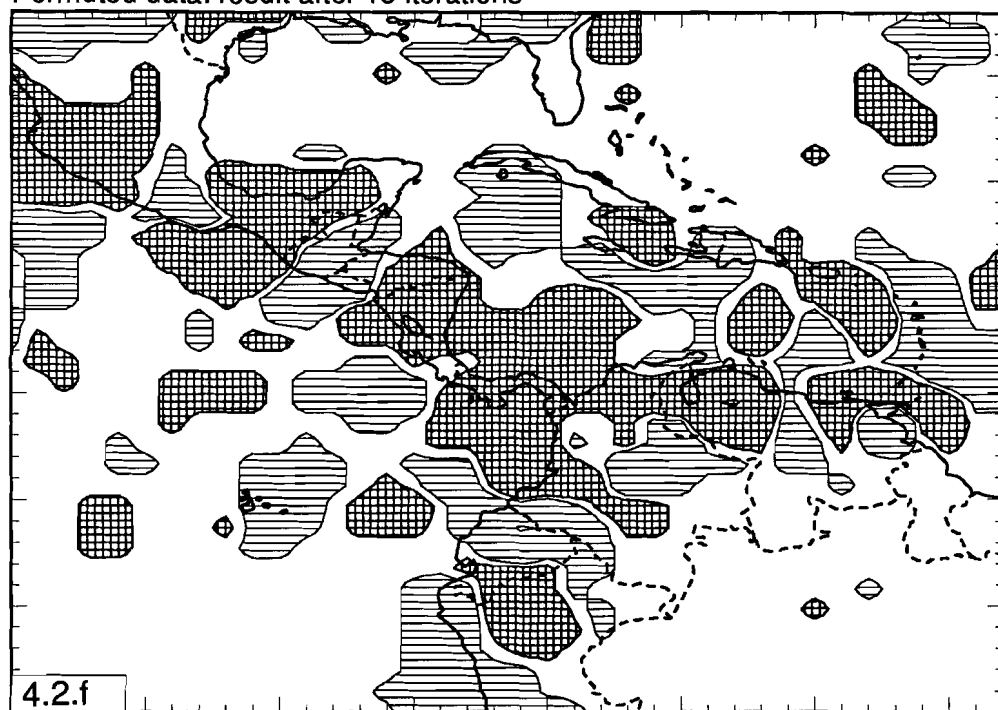




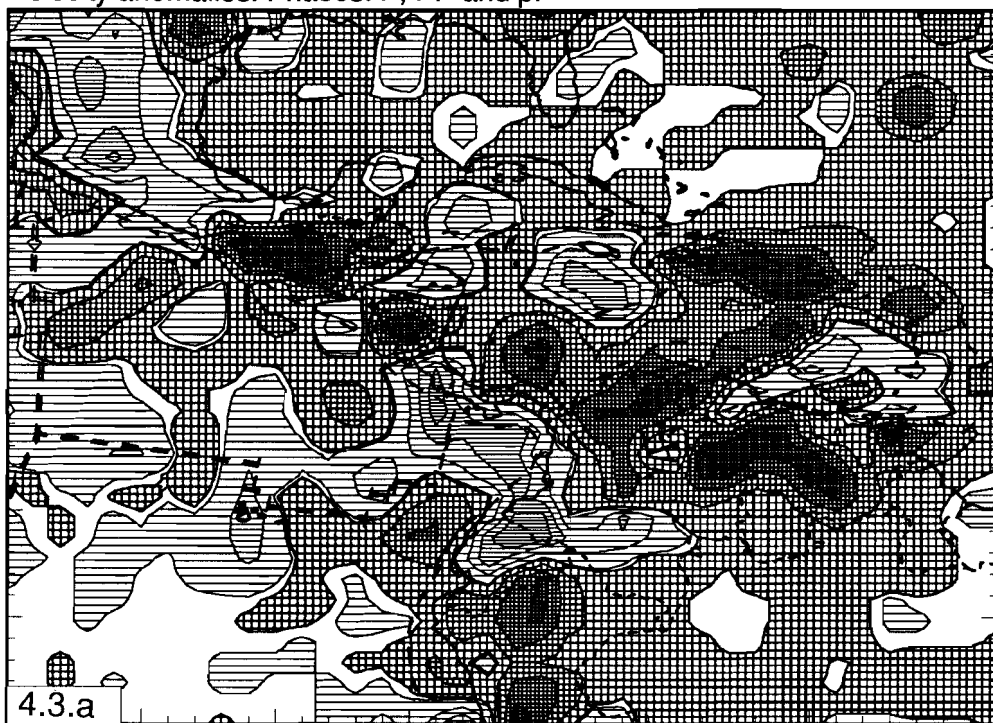
3D-Harmonic fit. Phases: P, PP and pP



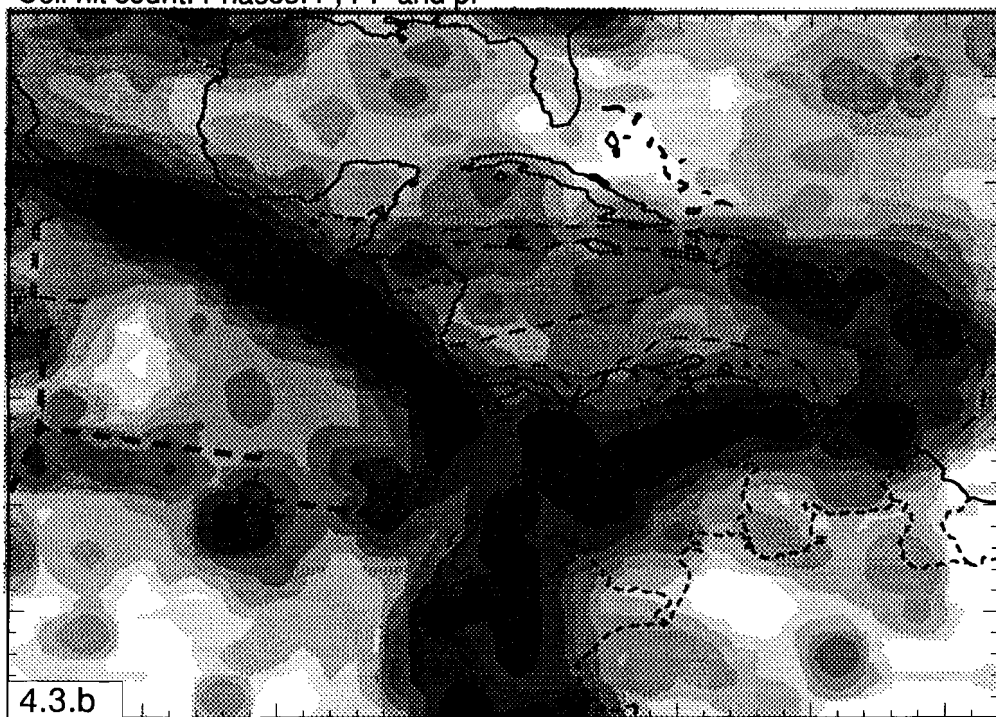
Permuted data: result after 15 iterations



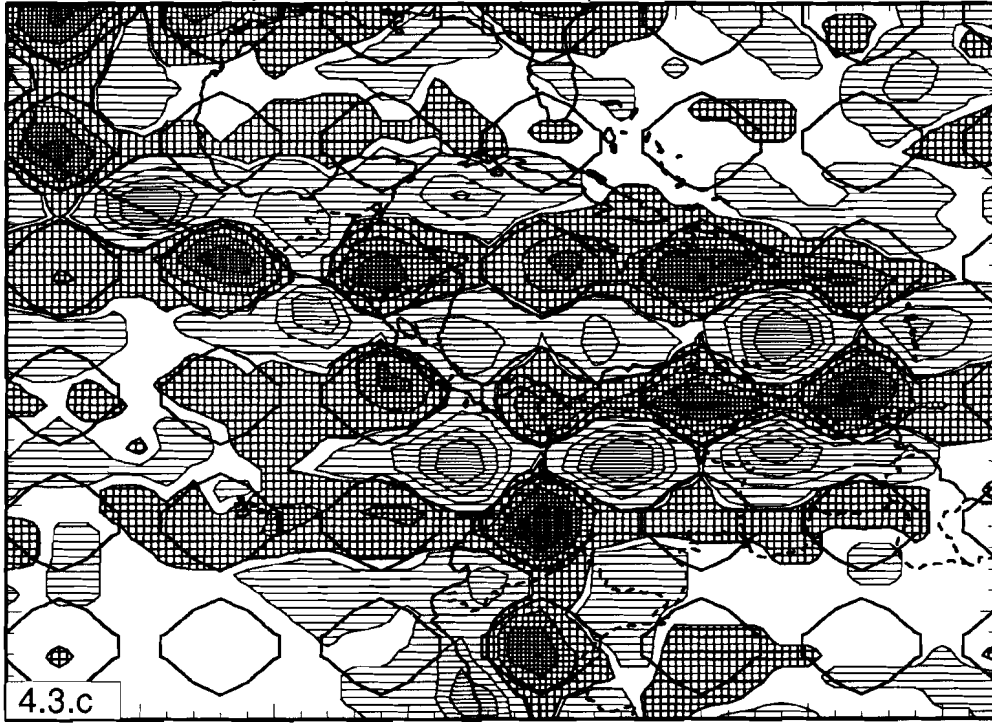
Velocity anomalies. Phases: P, PP and pP



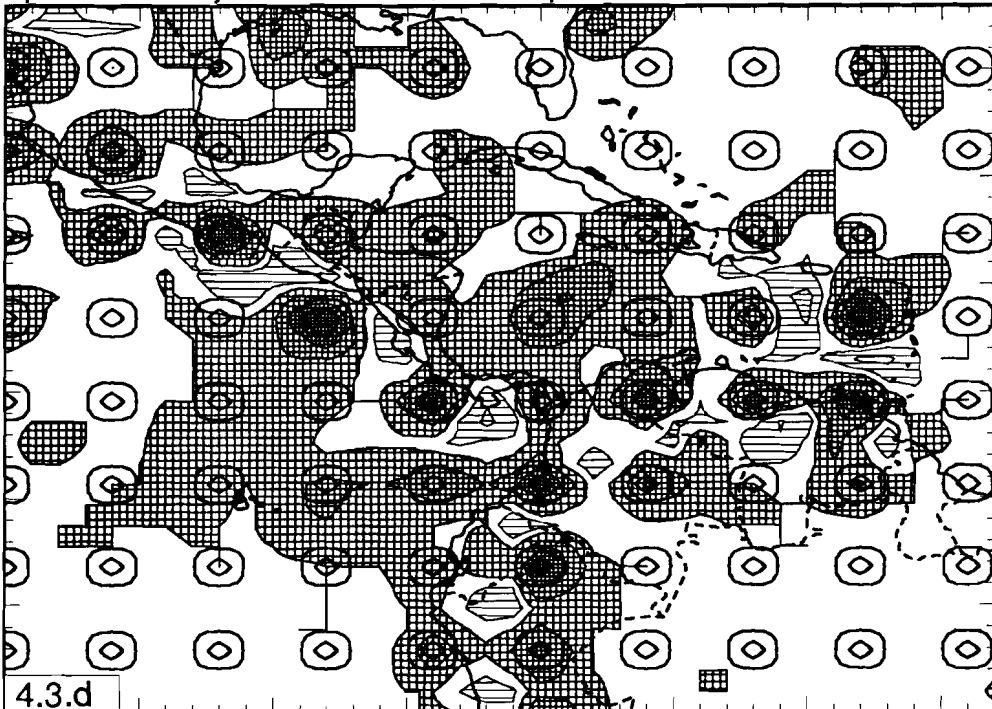
Cell hit count. Phases: P, PP and pP



Harmonic sensitivity test. Phases: P, PP and pP

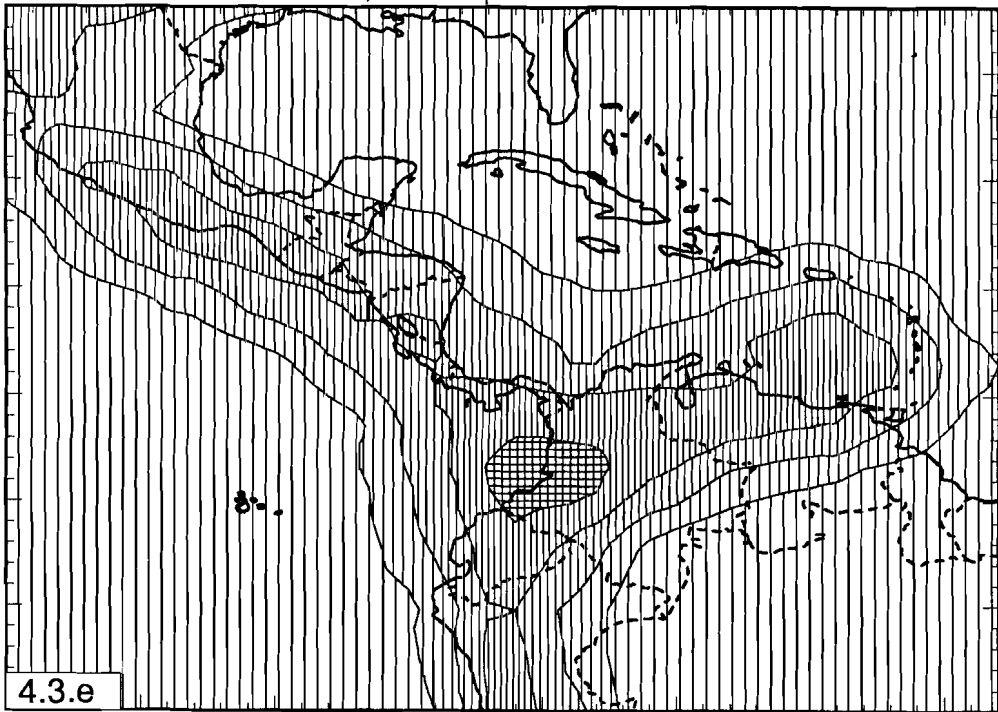


Spikes sensitivity test. Phases: P, PP and pP

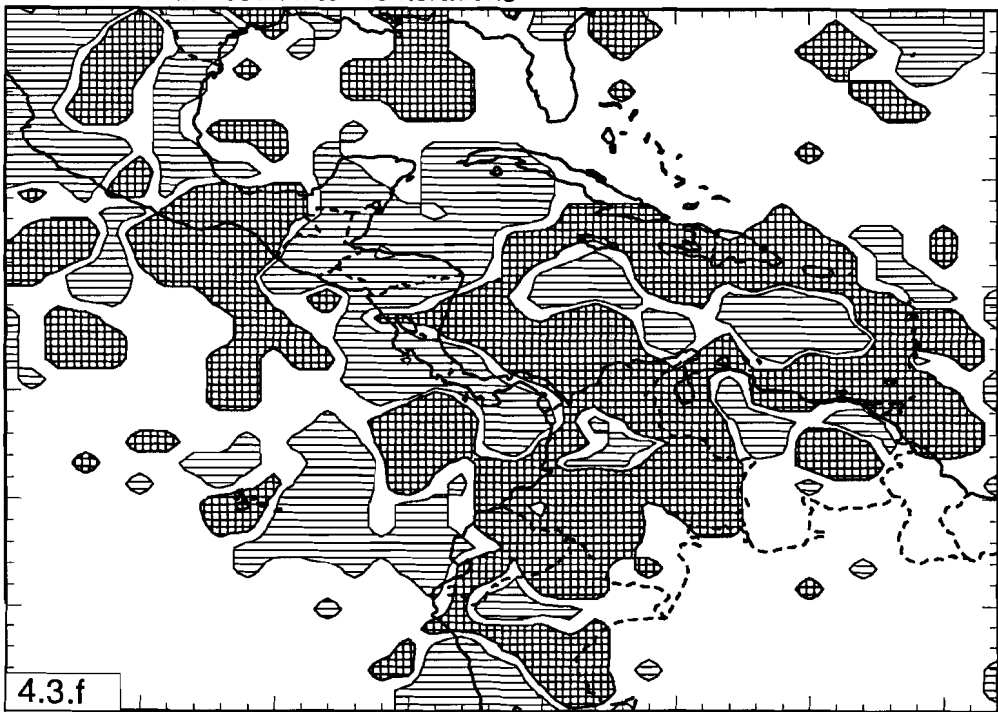




3D-Harmonic fit. Phases: P, PP and pP

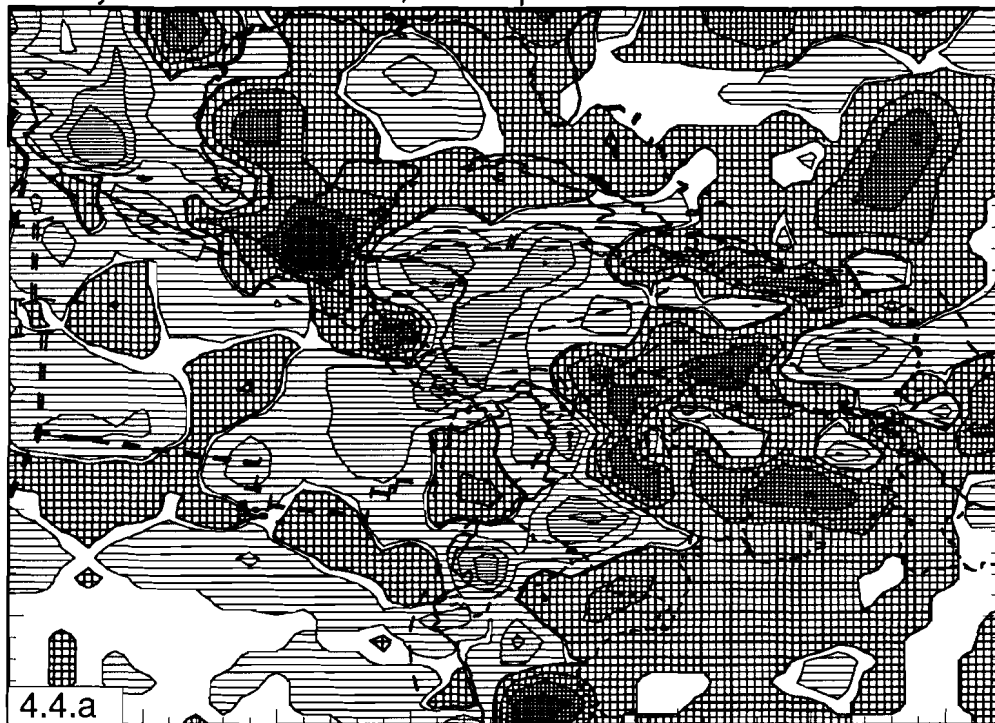


Permuted data: result after 15 iterations

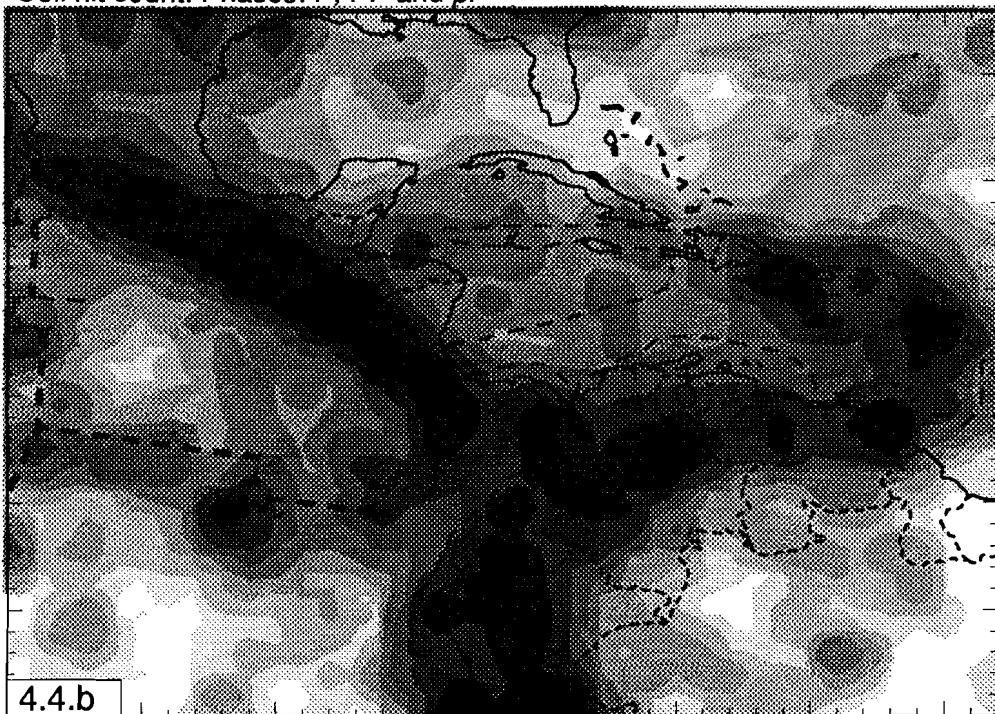




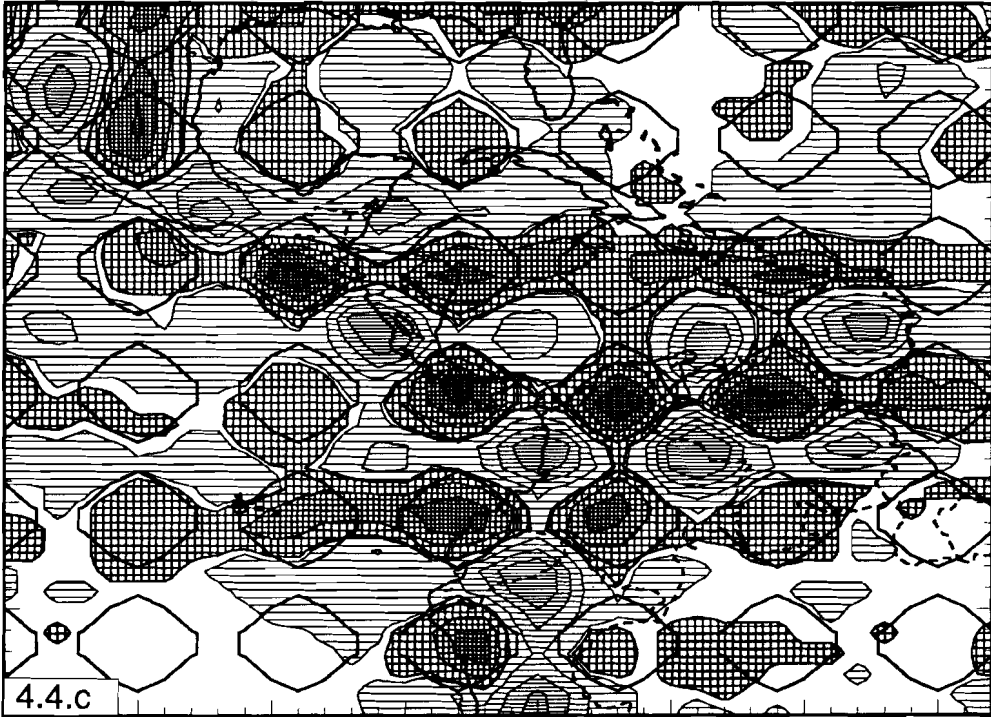
Velocity anomalies. Phases: P, PP and pP



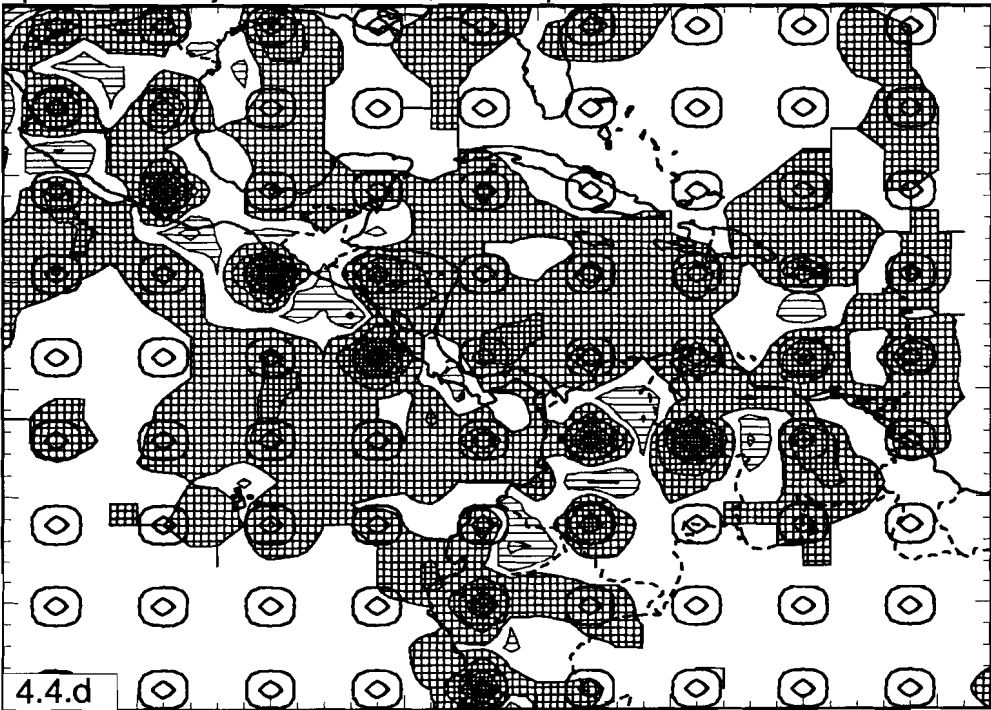
Cell hit count. Phases: P, PP and pP



Harmonic sensitivity test. Phases: P, PP and pP

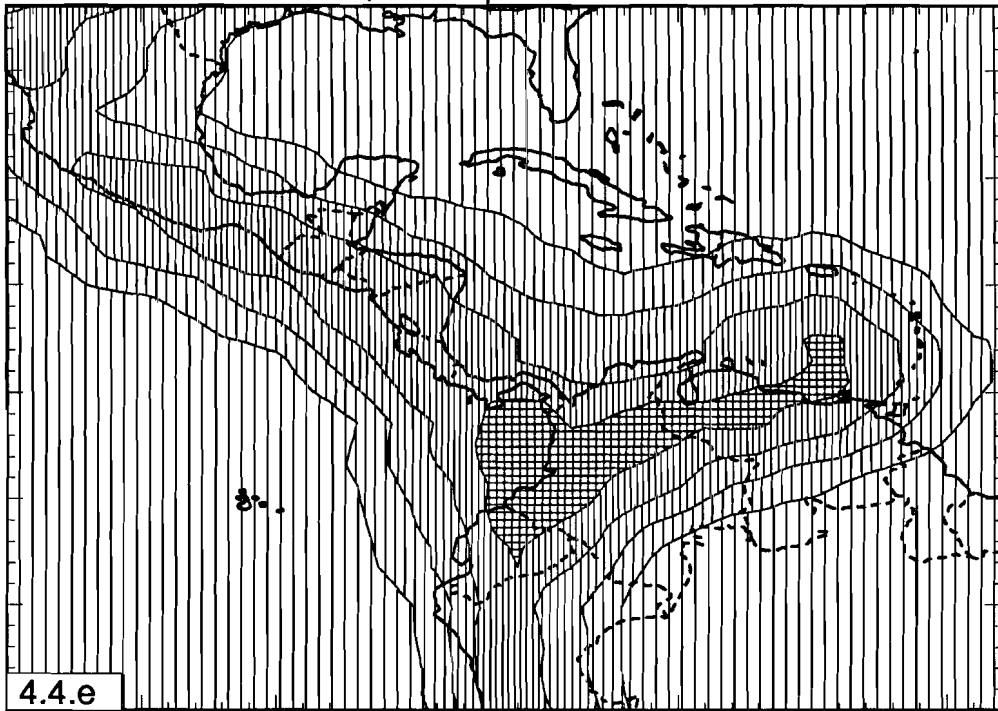


Spikes sensitivity test. Phases: P, PP and pP

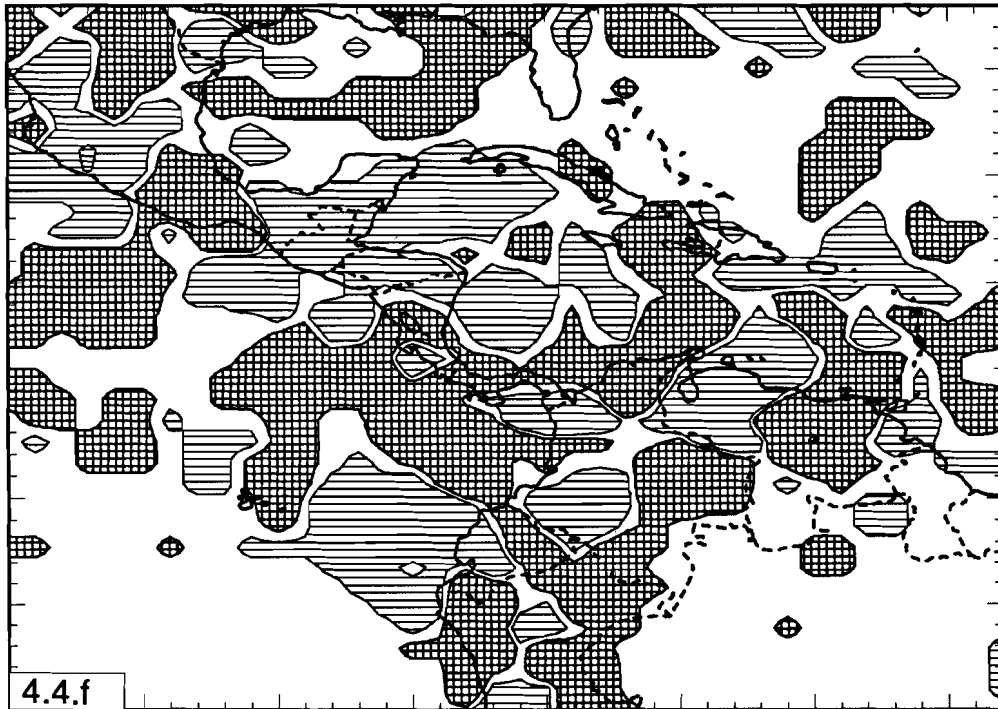




3D-Harmonic fit. Phases: P, PP and pP



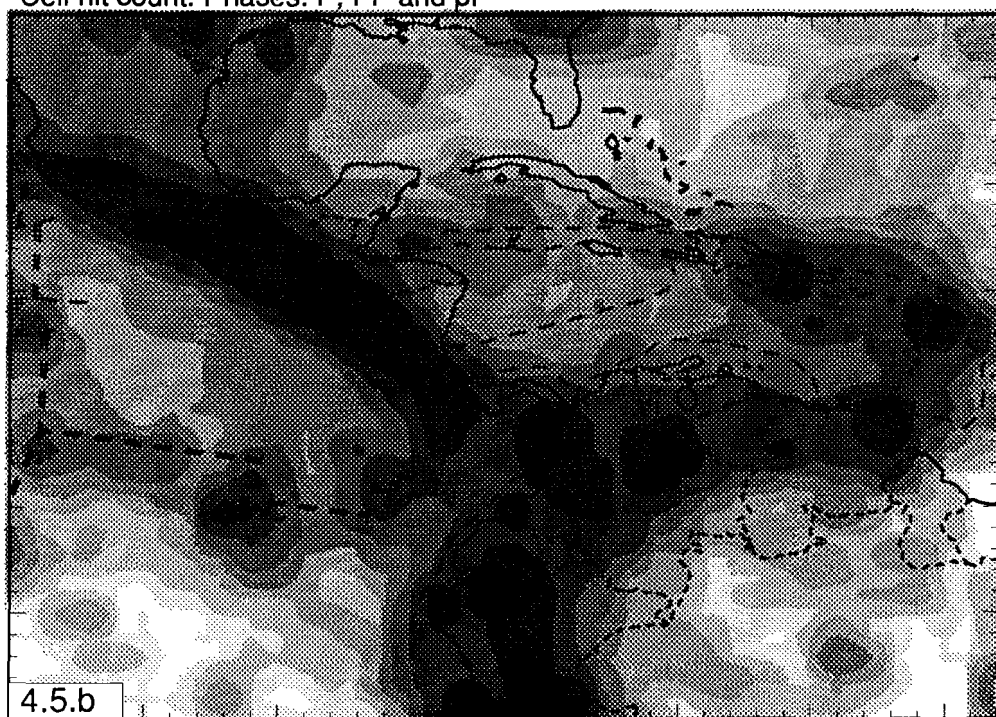
Permuted data: result after 15 iterations



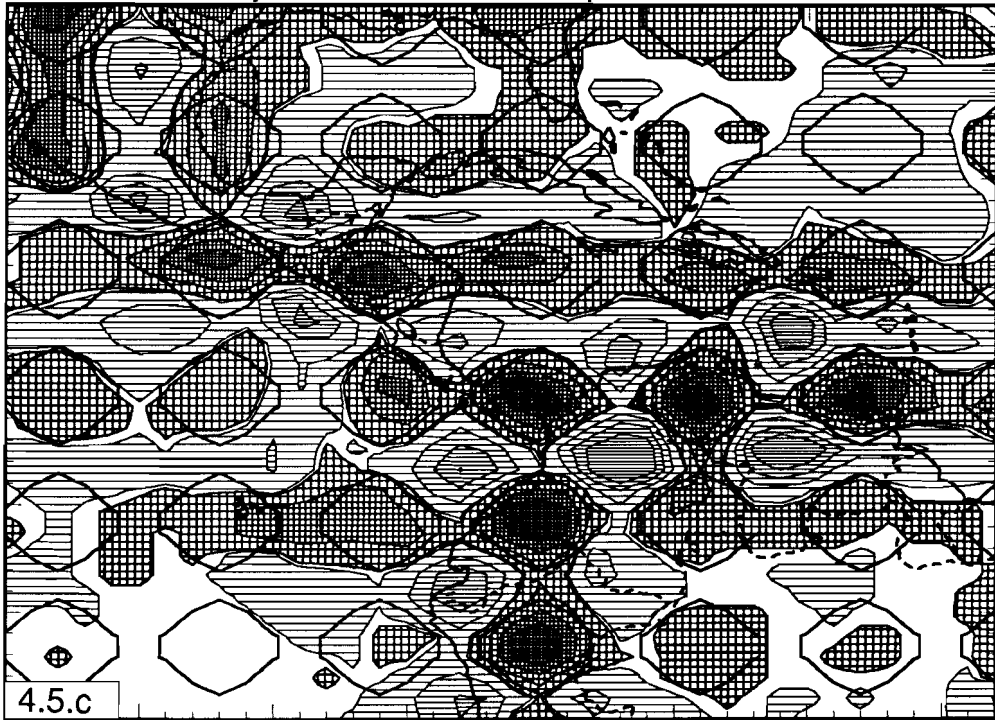
Velocity anomalies. Phases: P, PP and pP



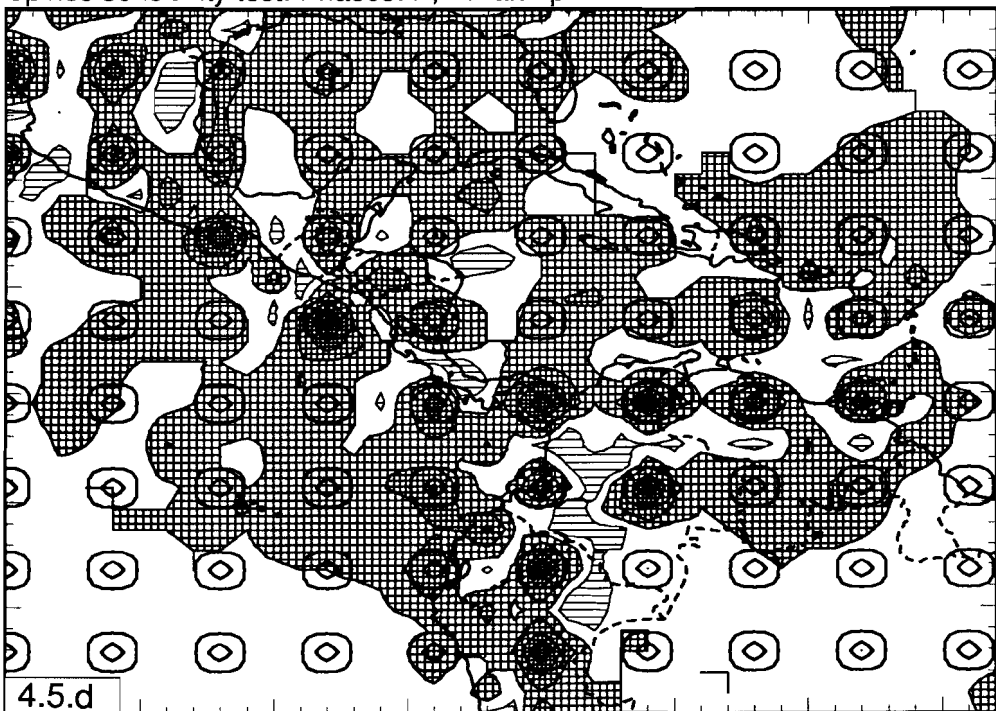
Cell hit count. Phases: P, PP and pP



Harmonic sensitivity test. Phases: P, PP and pP

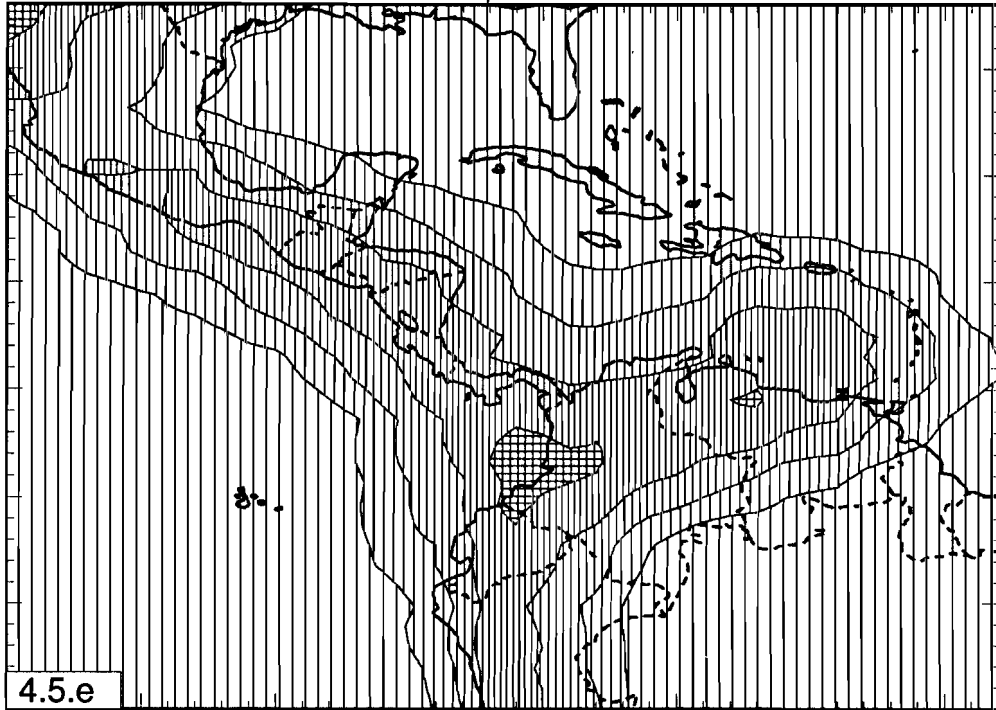


Spikes sensitivity test. Phases: P, PP and pP

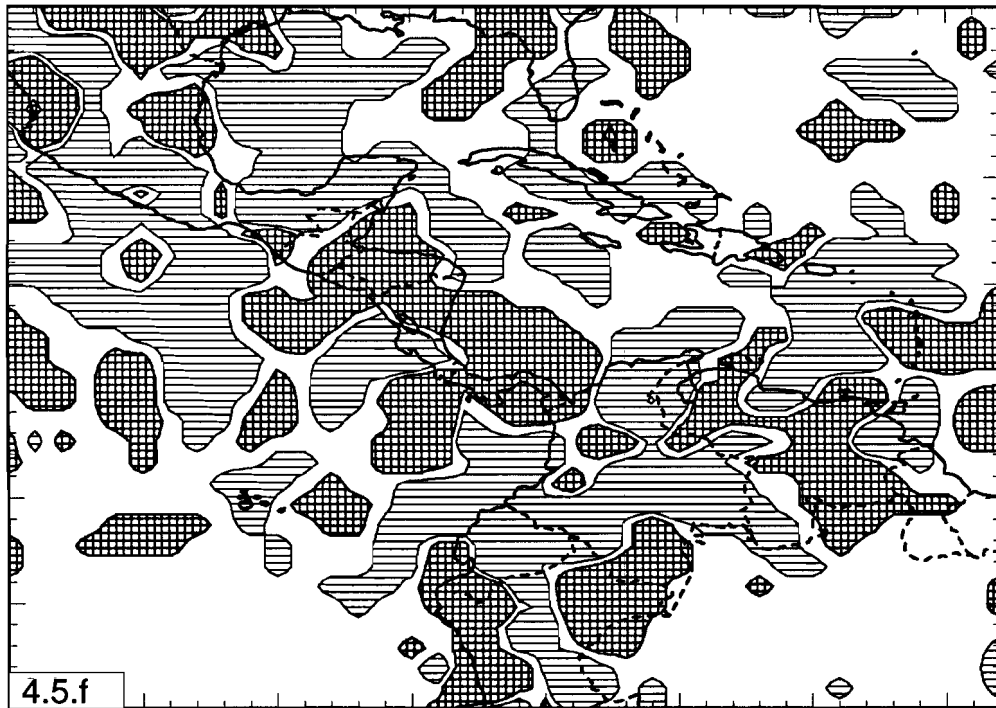




3D-Harmonic fit. Phases: P, PP and pP



Permuted data: result after 15 iterations

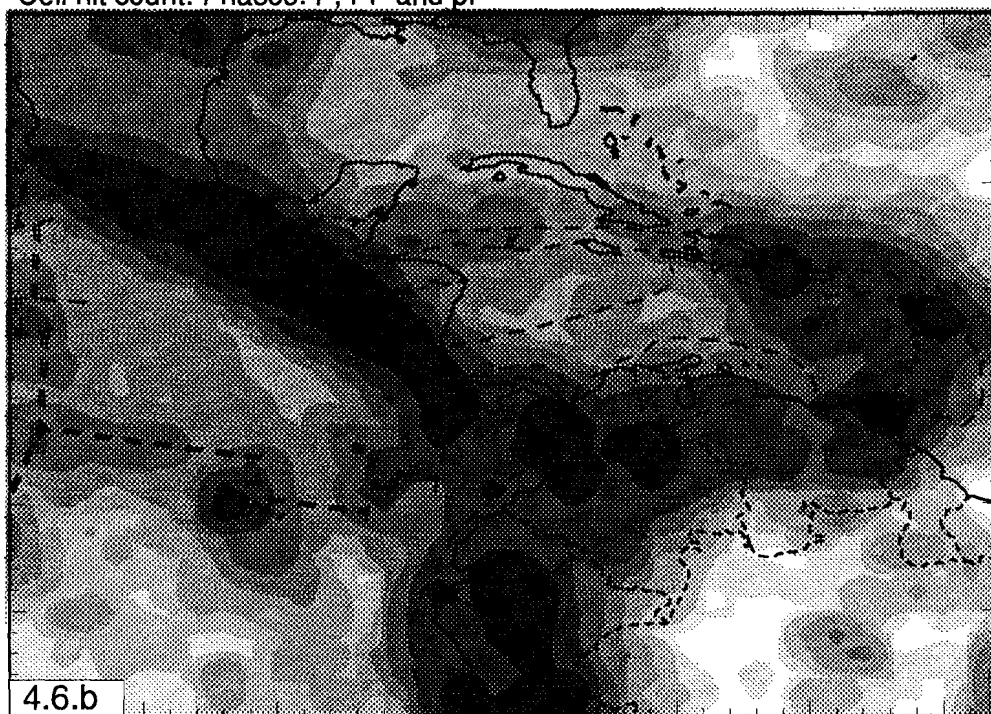




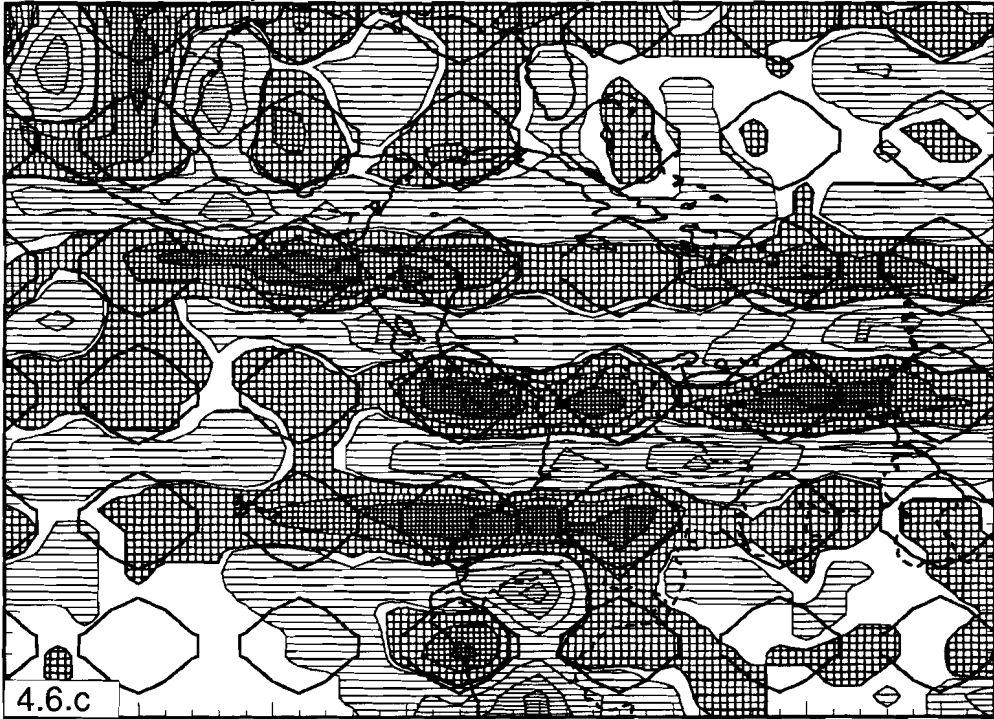
Velocity anomalies. Phases: P, PP and pP



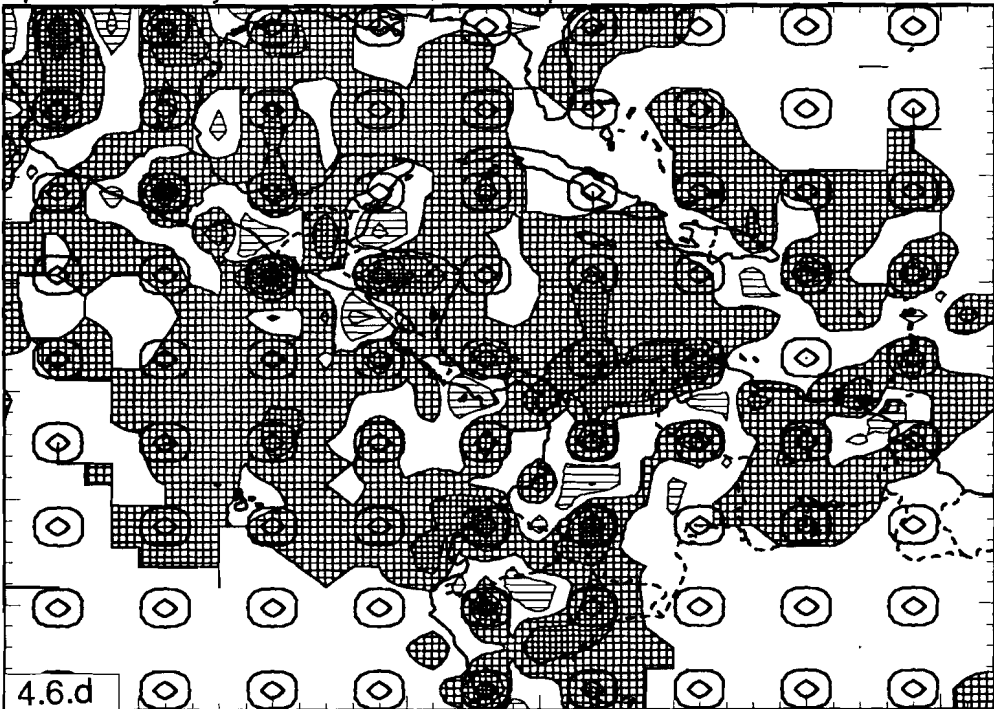
Cell hit count. Phases: P, PP and pP



Harmonic sensitivity test. Phases: P, PP and pP

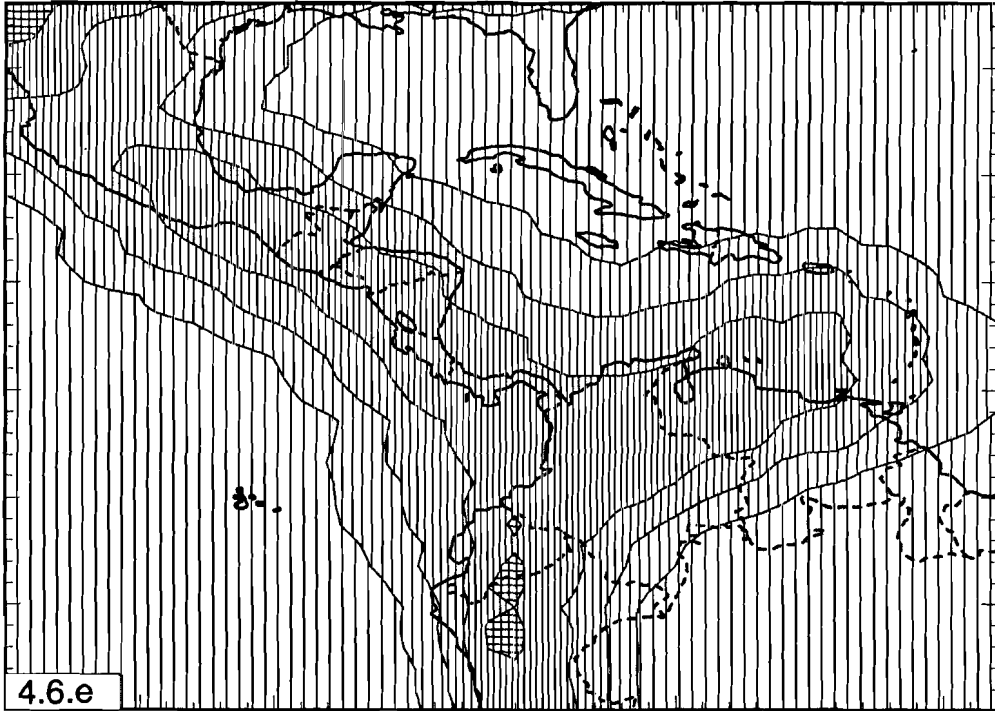


Spikes sensitivity test. Phases: P, PP and pP

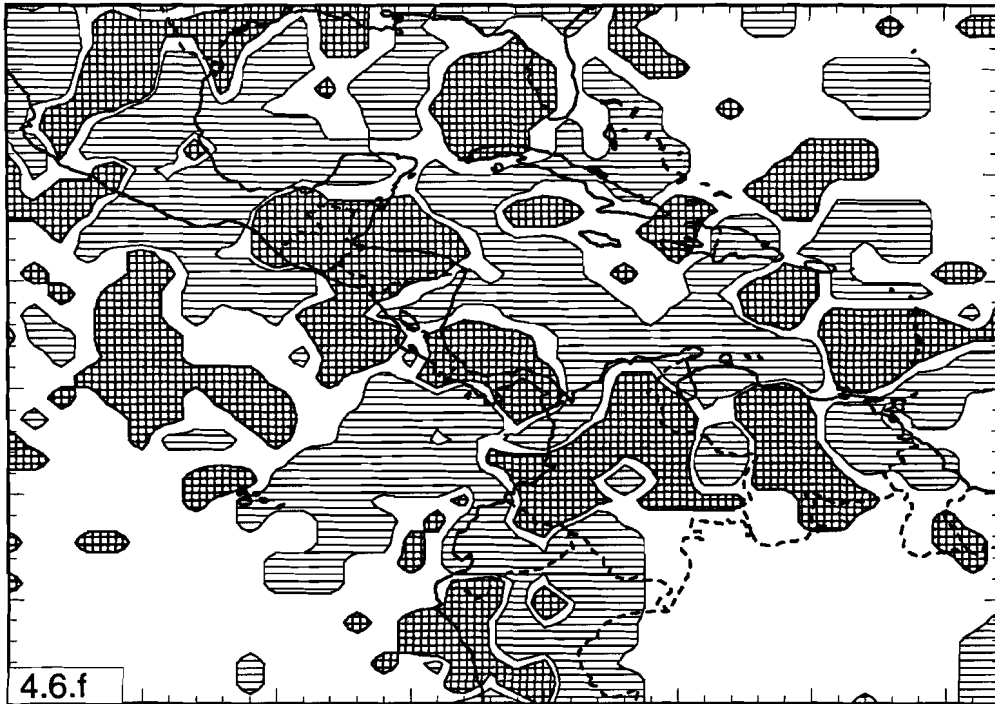




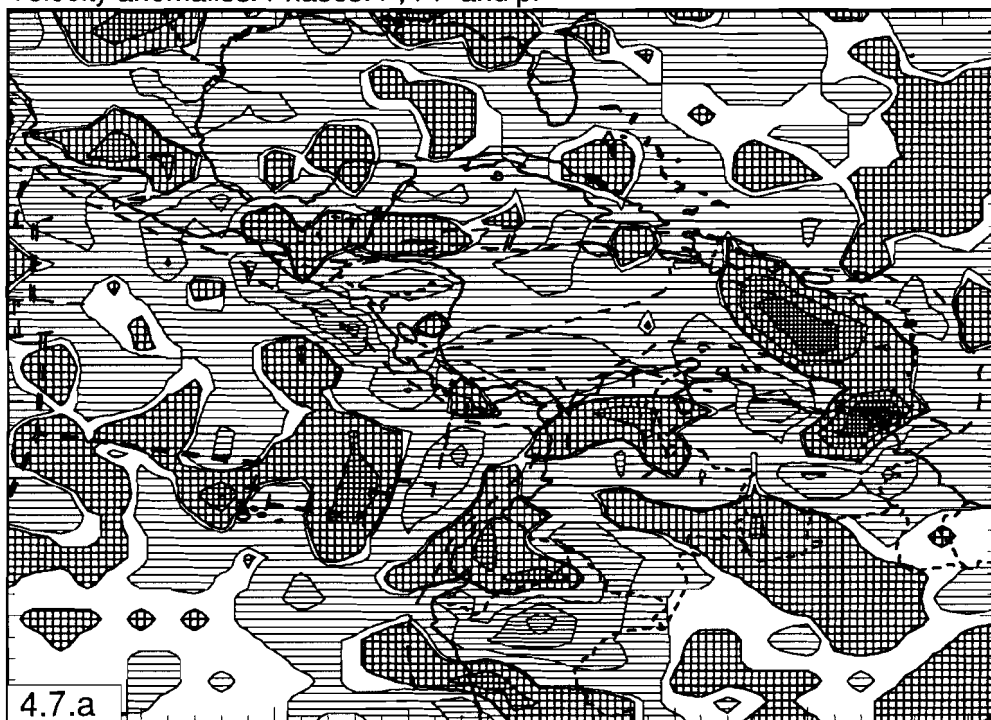
3D-Harmonic fit. Phases: P, PP and pP



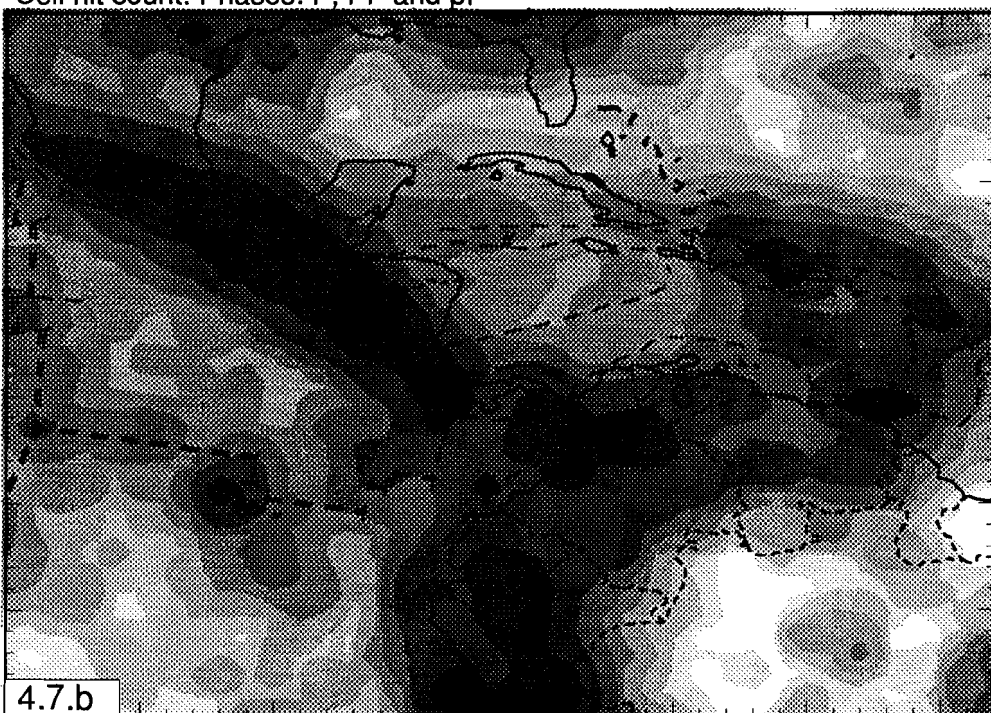
Permuted data: result after 15 iterations



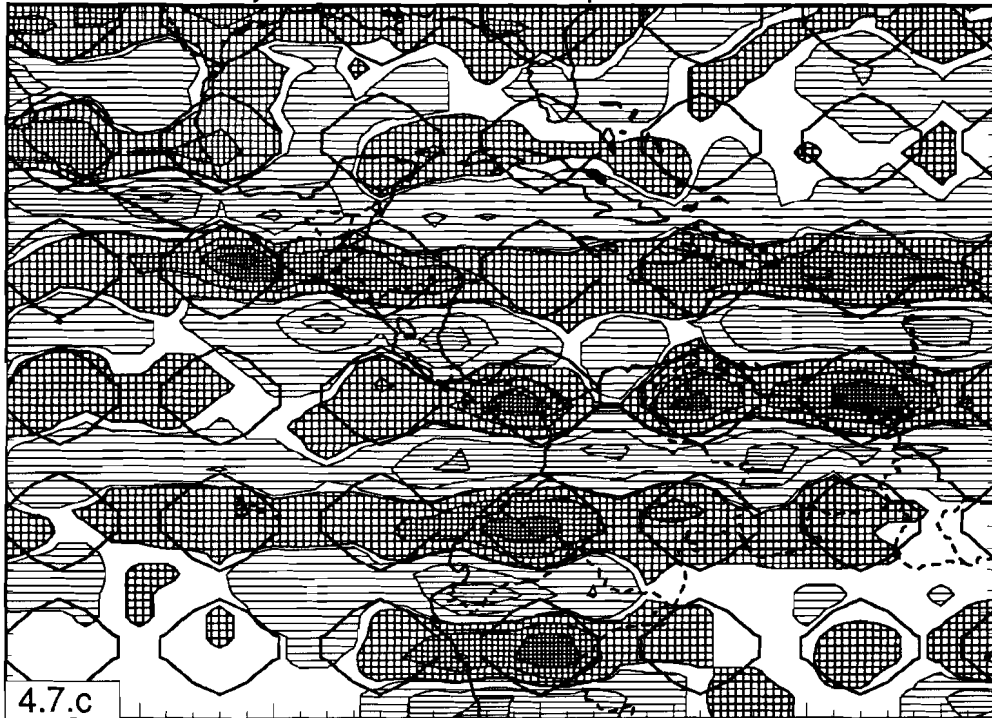
Velocity anomalies. Phases: P, PP and pP



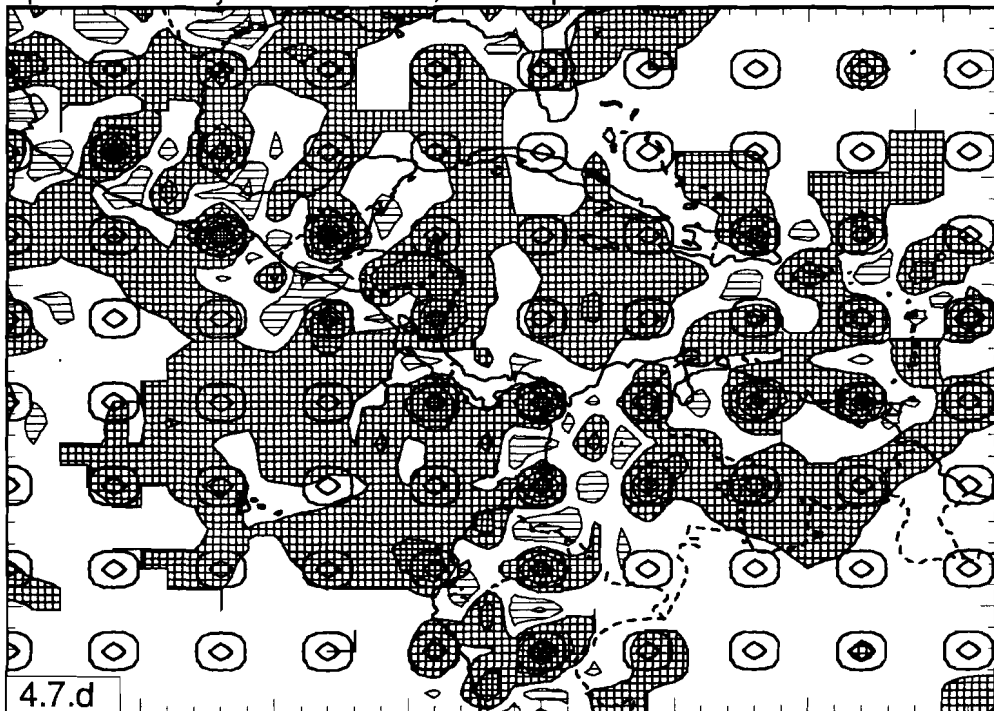
Cell hit count. Phases: P, PP and pP



Harmonic sensitivity test. Phases: P, PP and pP

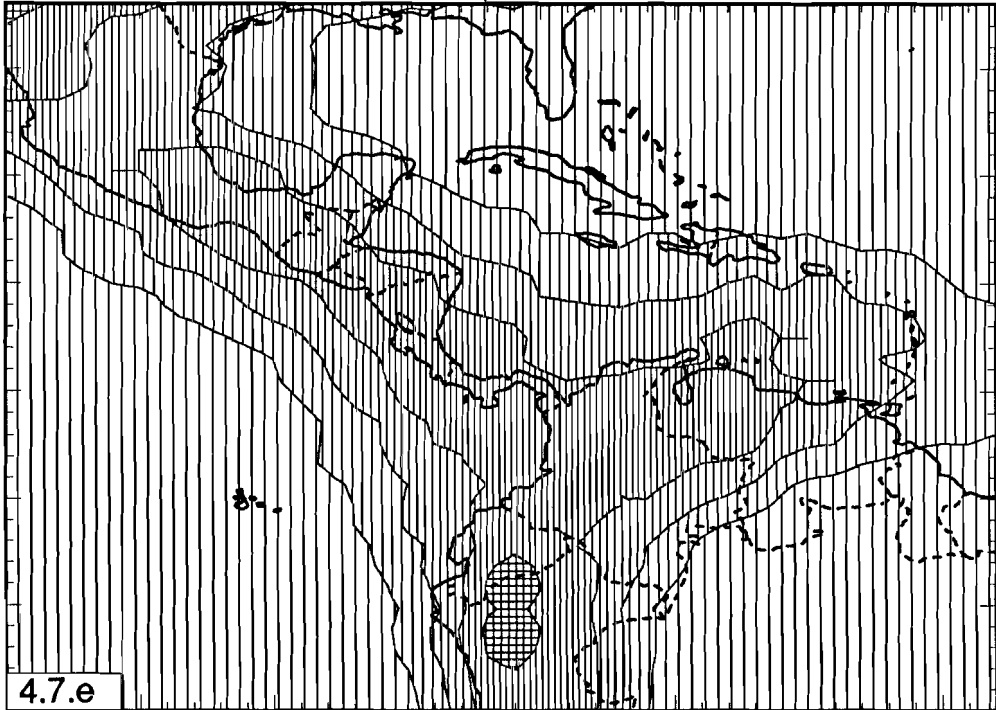


Spikes sensitivity test. Phases: P, PP and pP

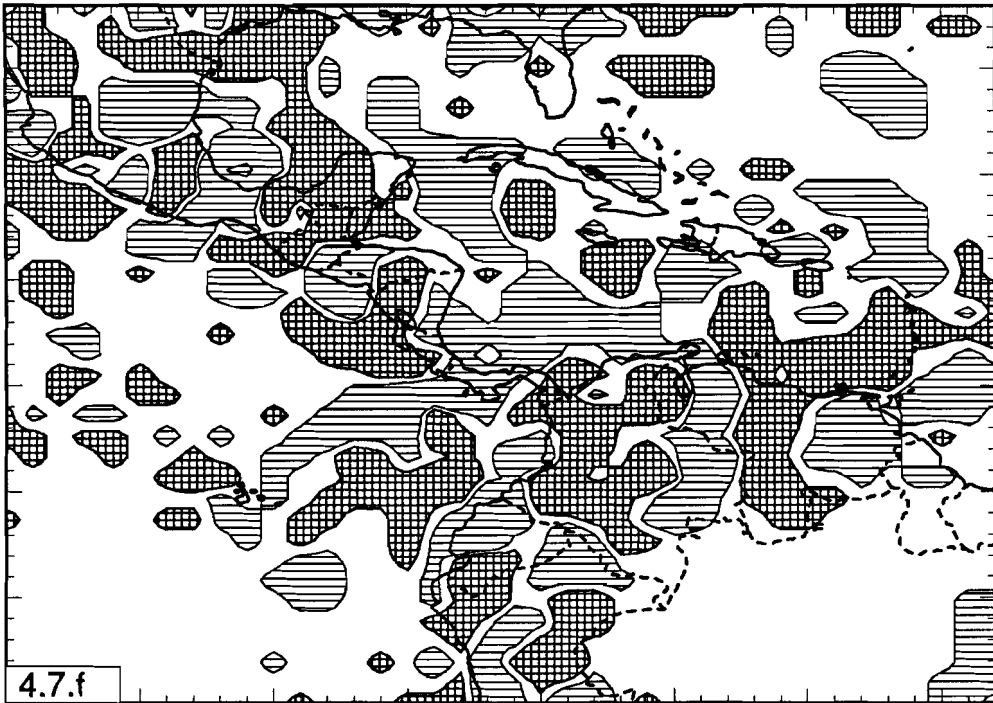




3D-Harmonic fit. Phases: P, PP and pP

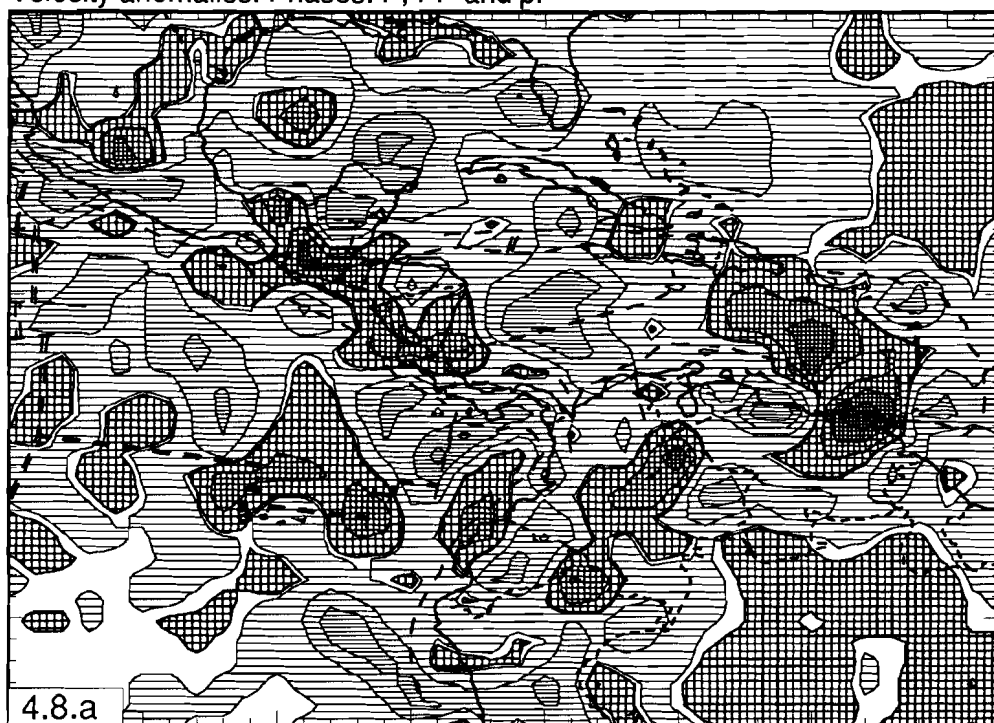


Permuted data: result after 15 iterations

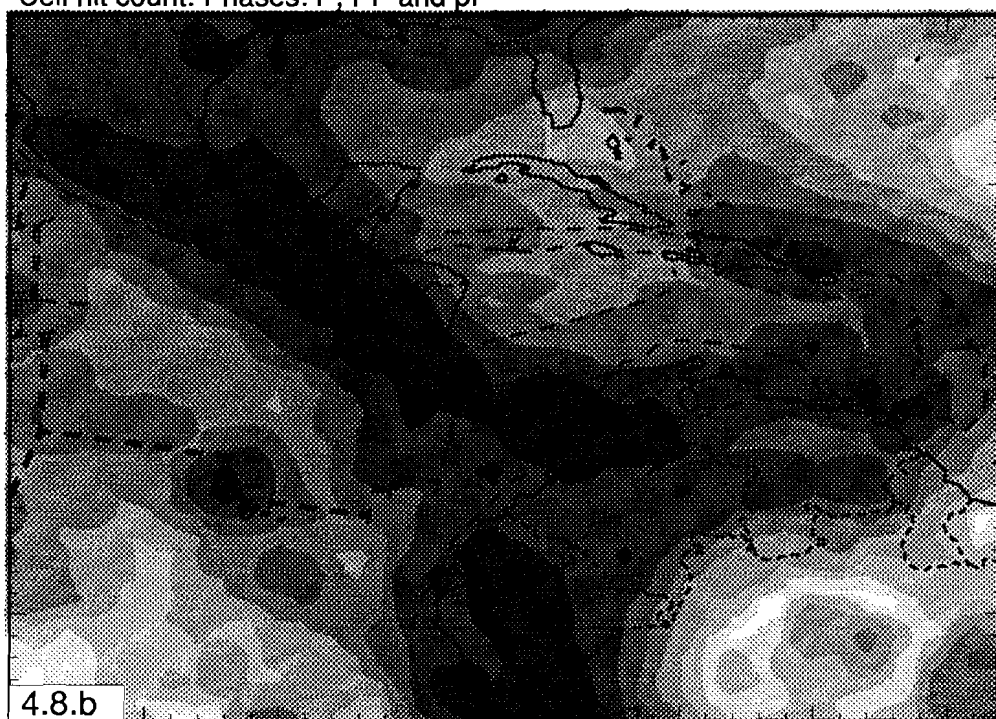




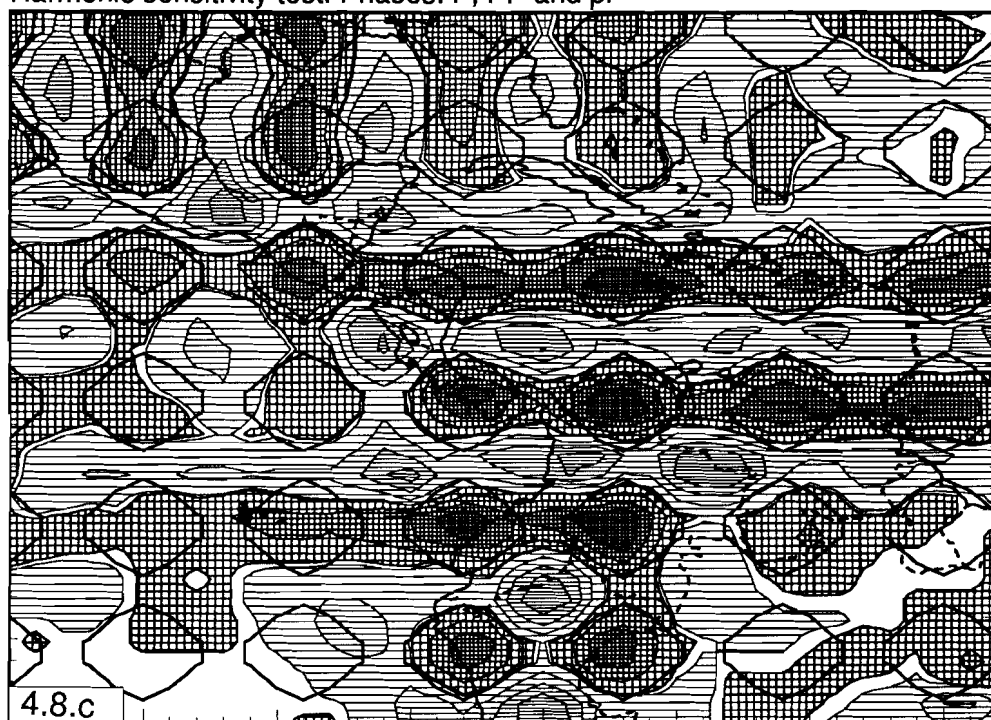
Velocity anomalies. Phases: P, PP and pP



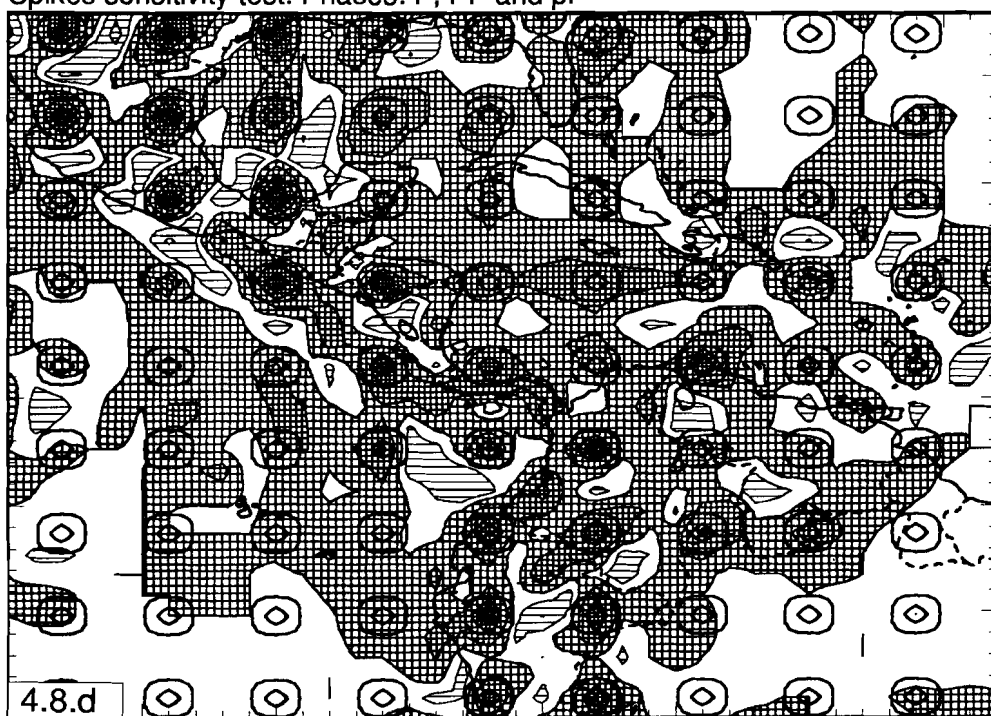
Cell hit count. Phases: P, PP and pP



Harmonic sensitivity test. Phases: P, PP and pP

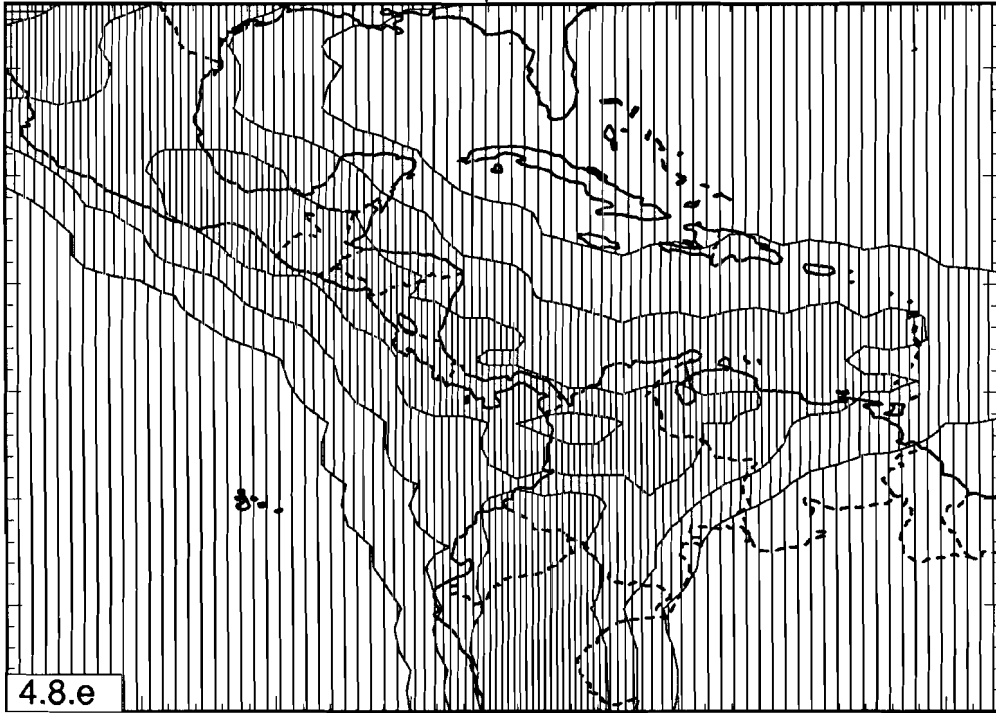


Spikes sensitivity test. Phases: P, PP and pP

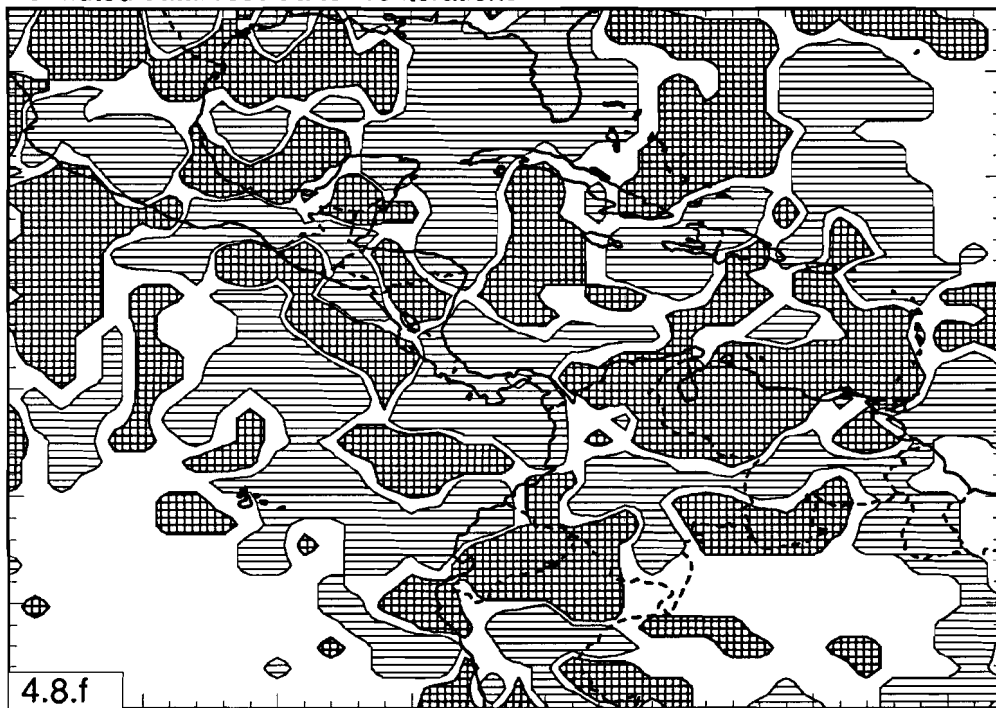




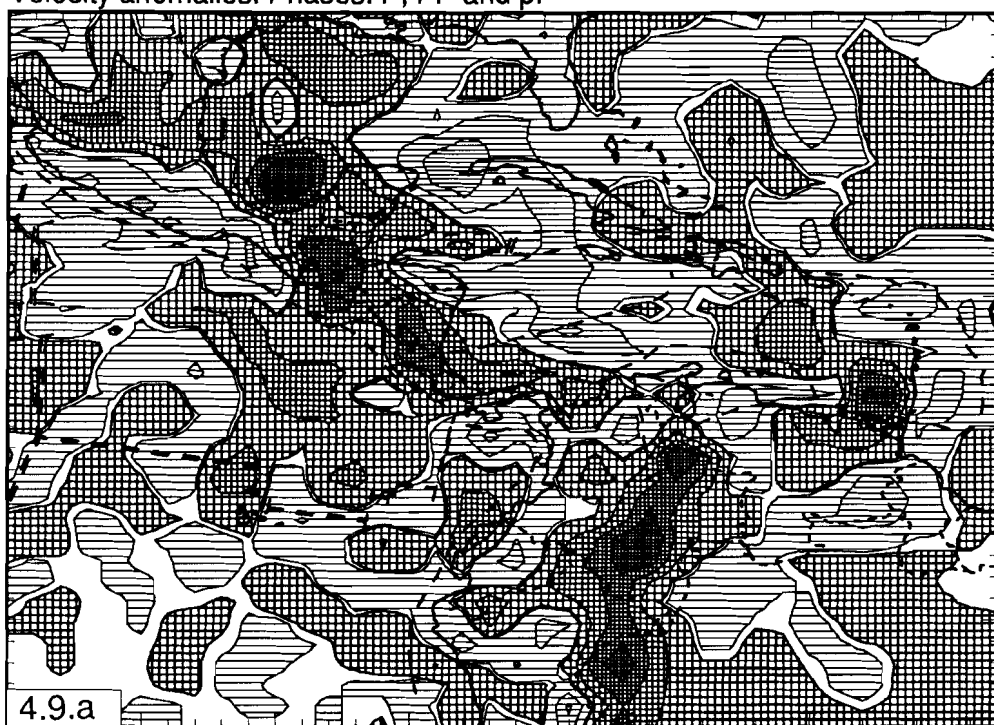
3D-Harmonic fit. Phases: P, PP and pP



Permuted data: result after 15 iterations



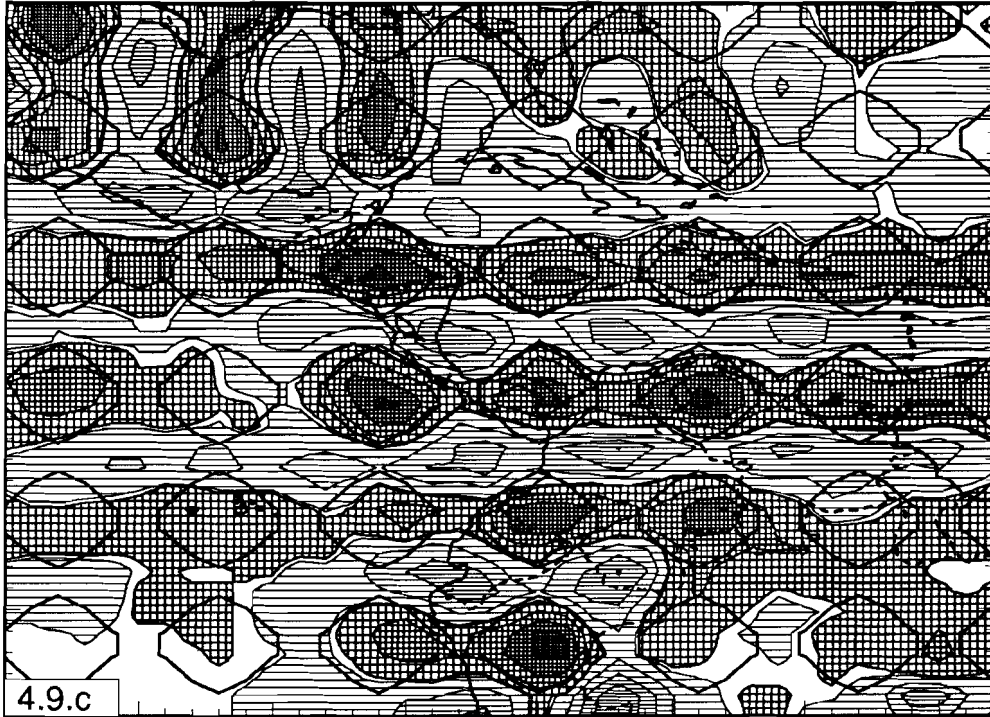
Velocity anomalies. Phases: P, PP and pP



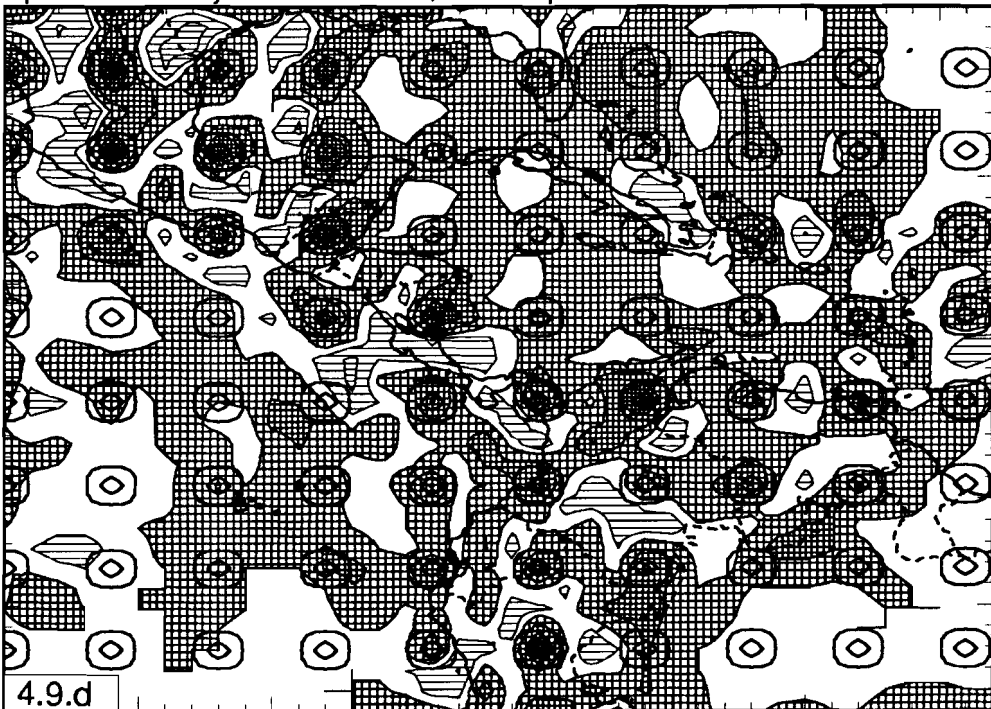
Cell hit count. Phases: P, PP and pP



Harmonic sensitivity test. Phases: P, PP and pP

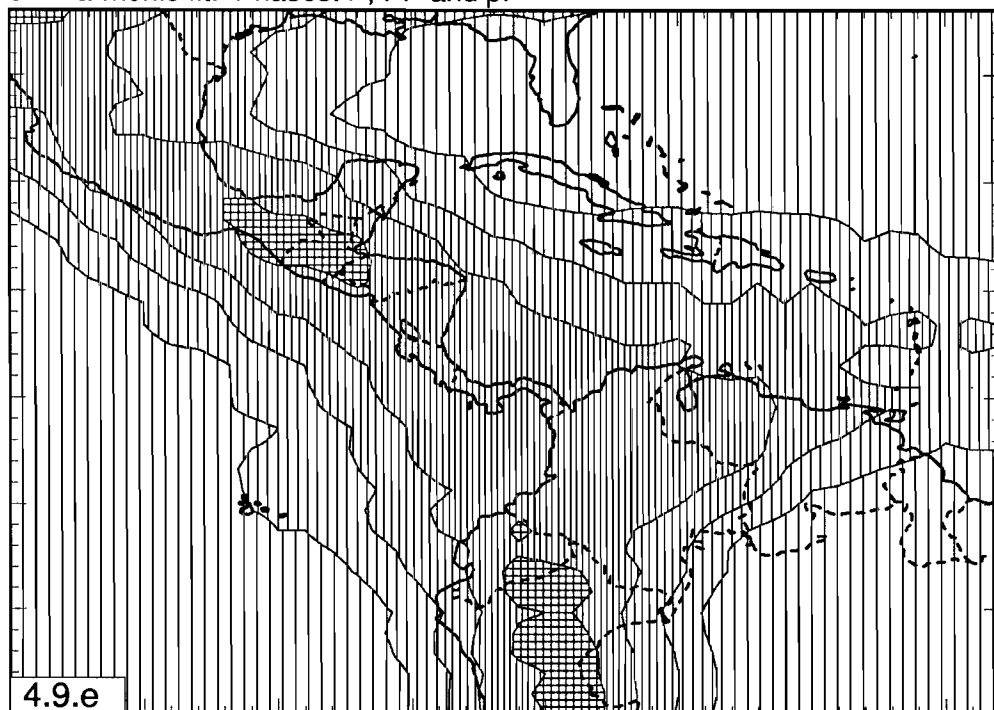


Spikes sensitivity test. Phases: P, PP and pP

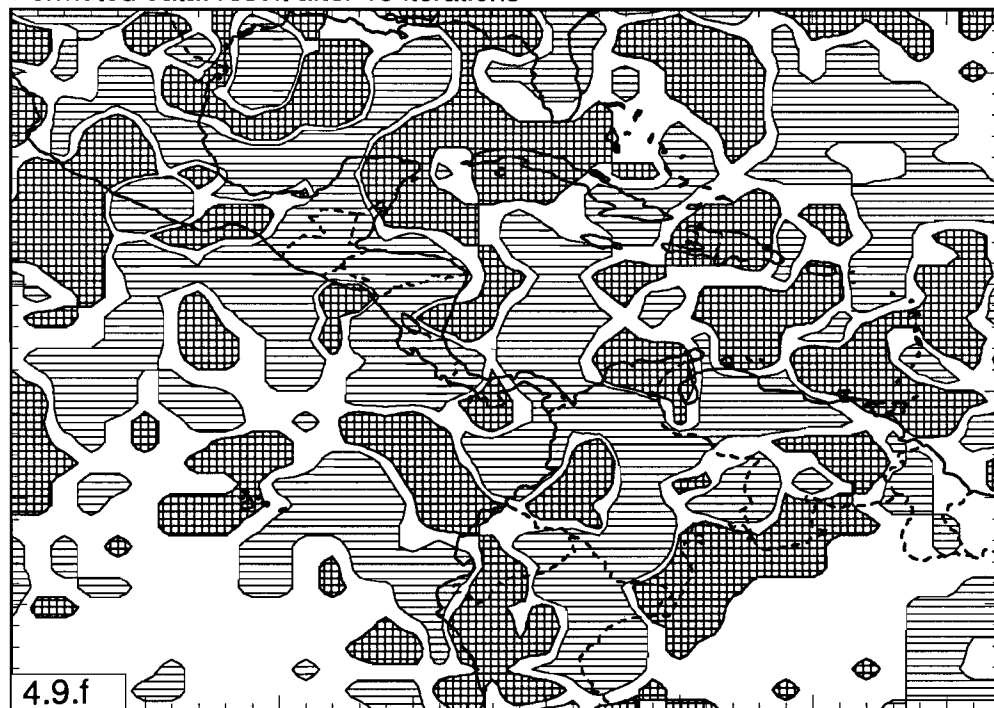




3D-Harmonic fit. Phases: P, PP and pP

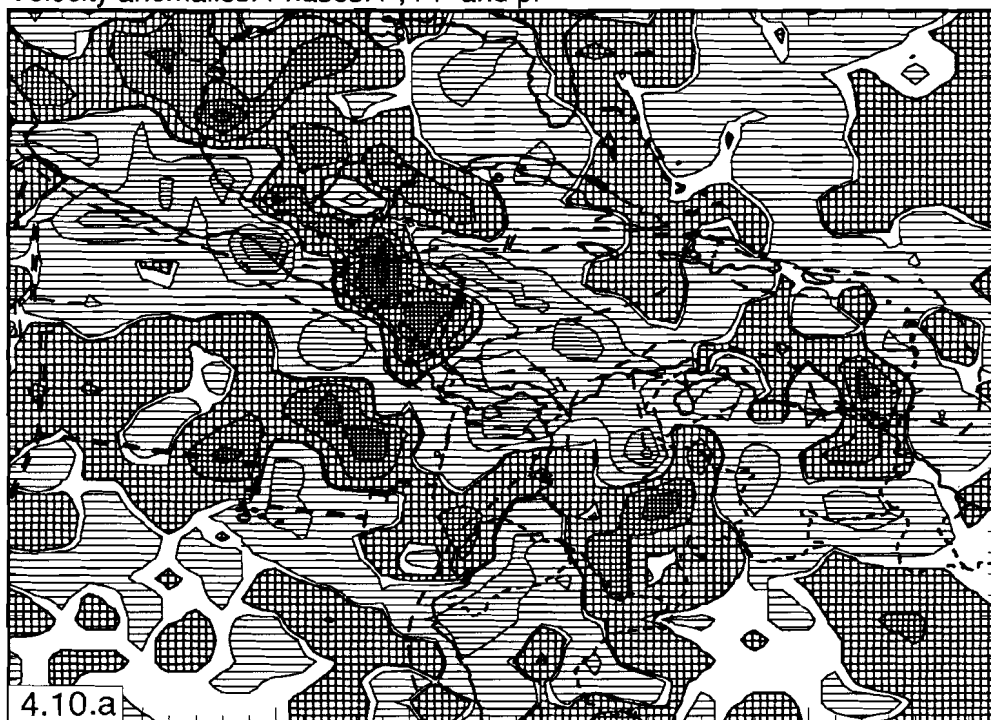


Permuted data: result after 15 iterations

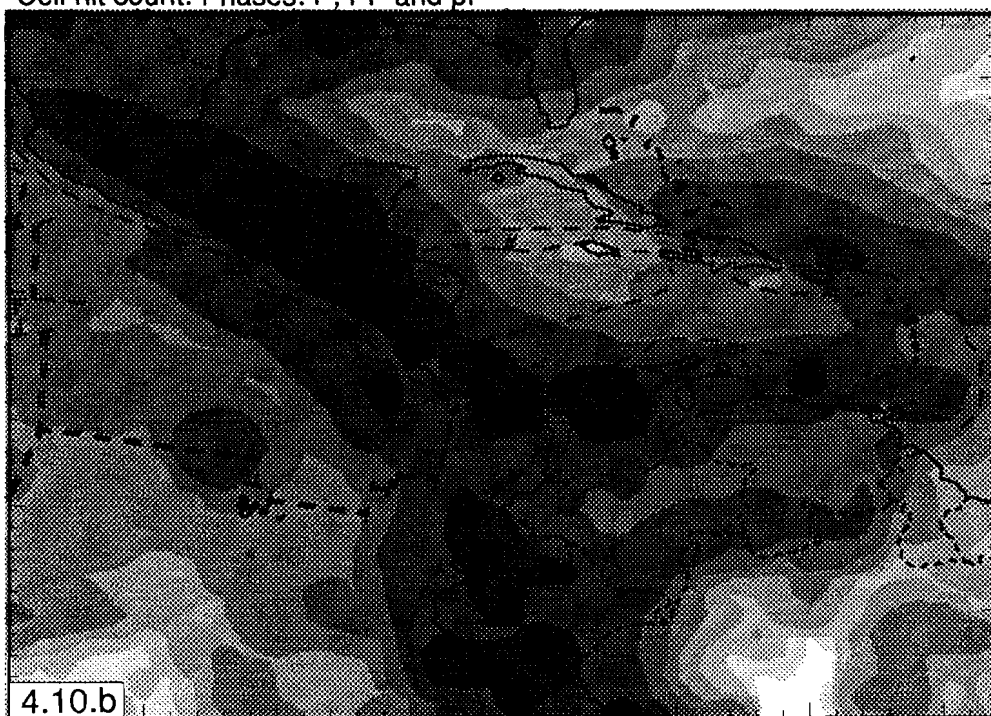




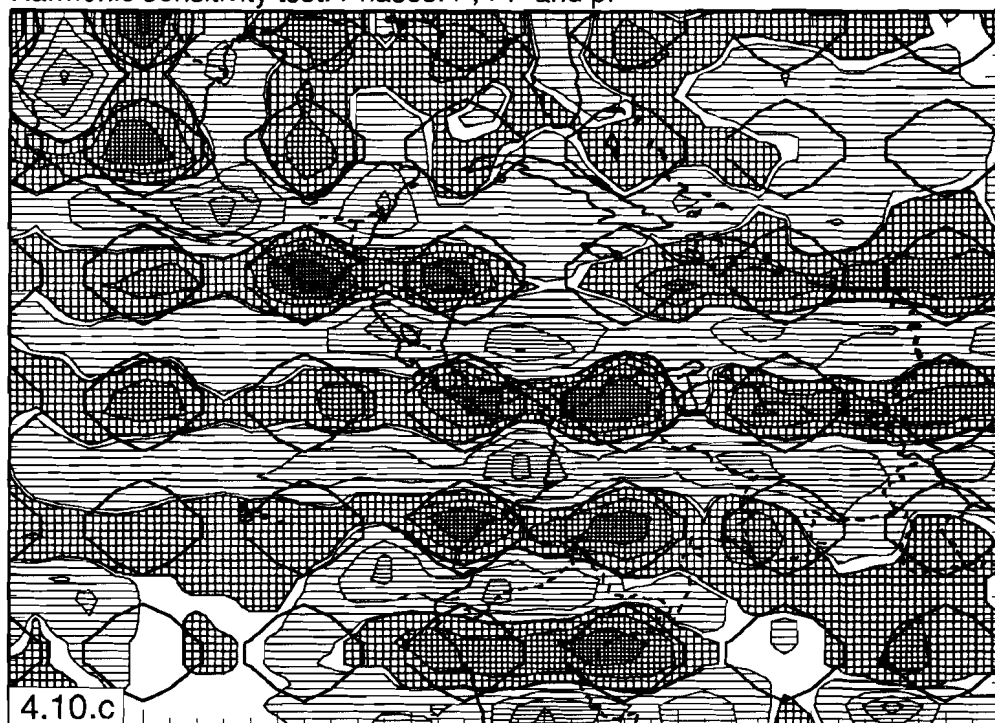
Velocity anomalies. Phases: P, PP and pP



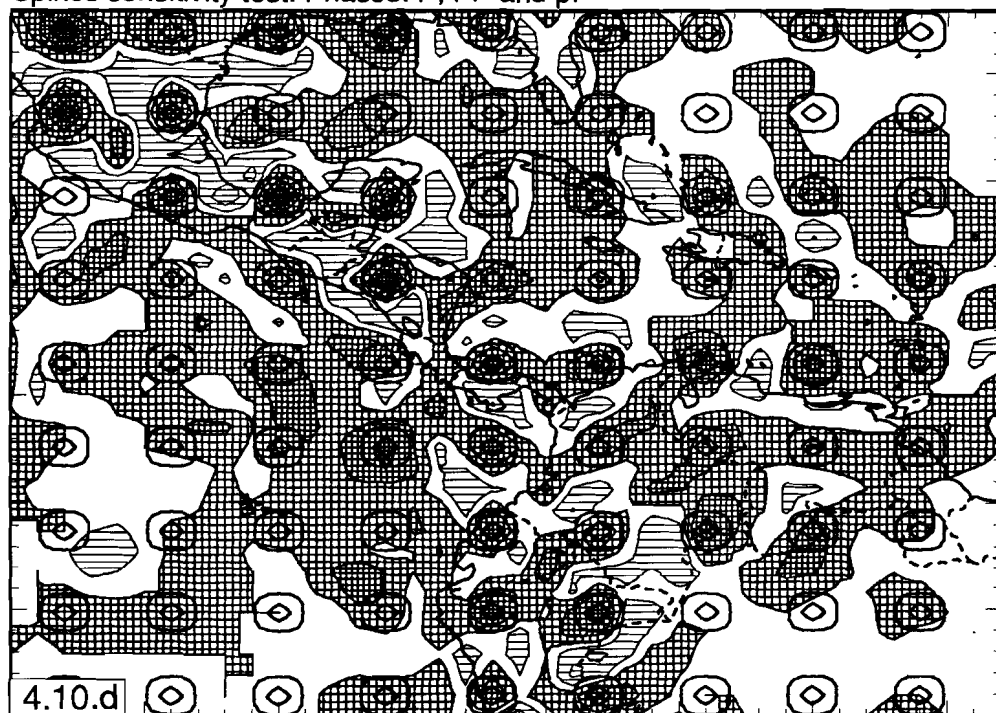
Cell hit count. Phases: P, PP and pP



Harmonic sensitivity test. Phases: P, PP and pP

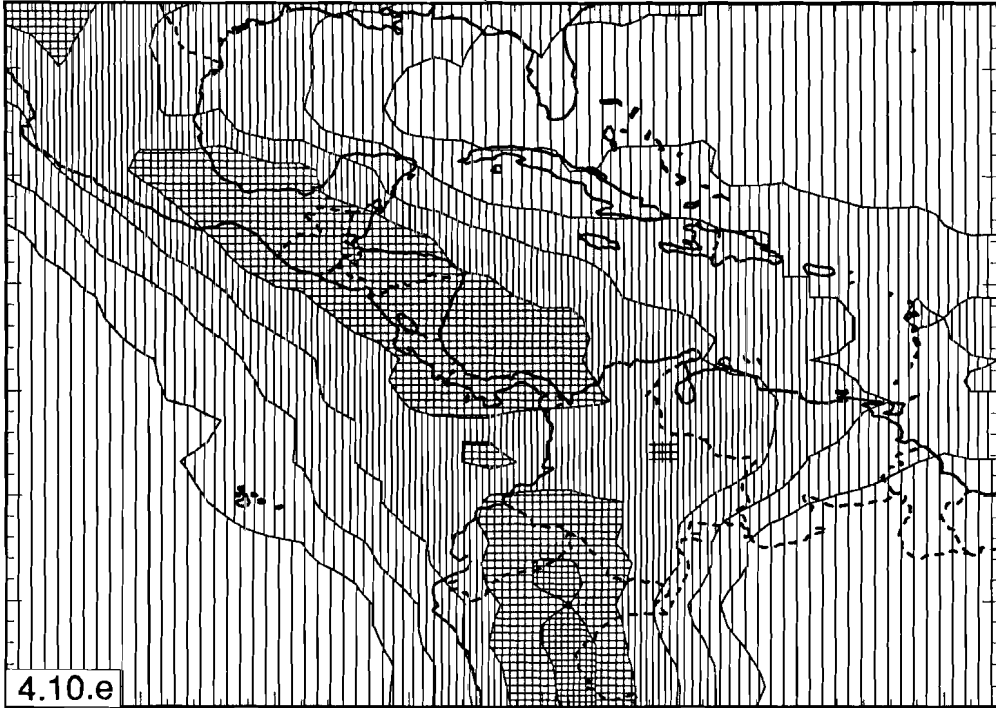


Spikes sensitivity test. Phases: P, PP and pP

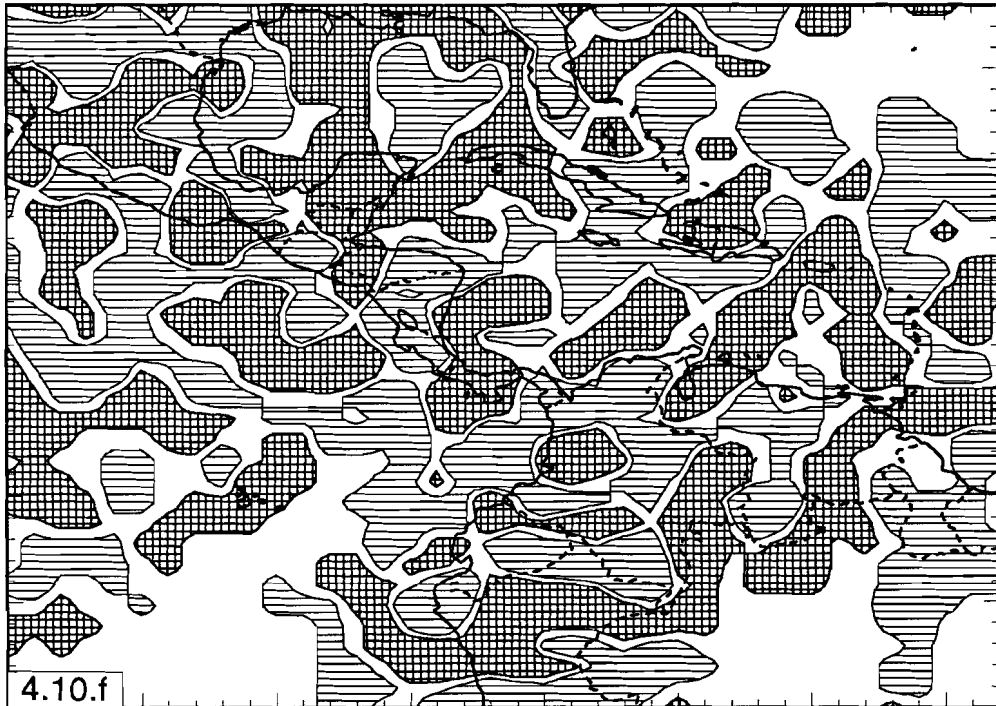




3D-Harmonic fit. Phases: P, PP and pP



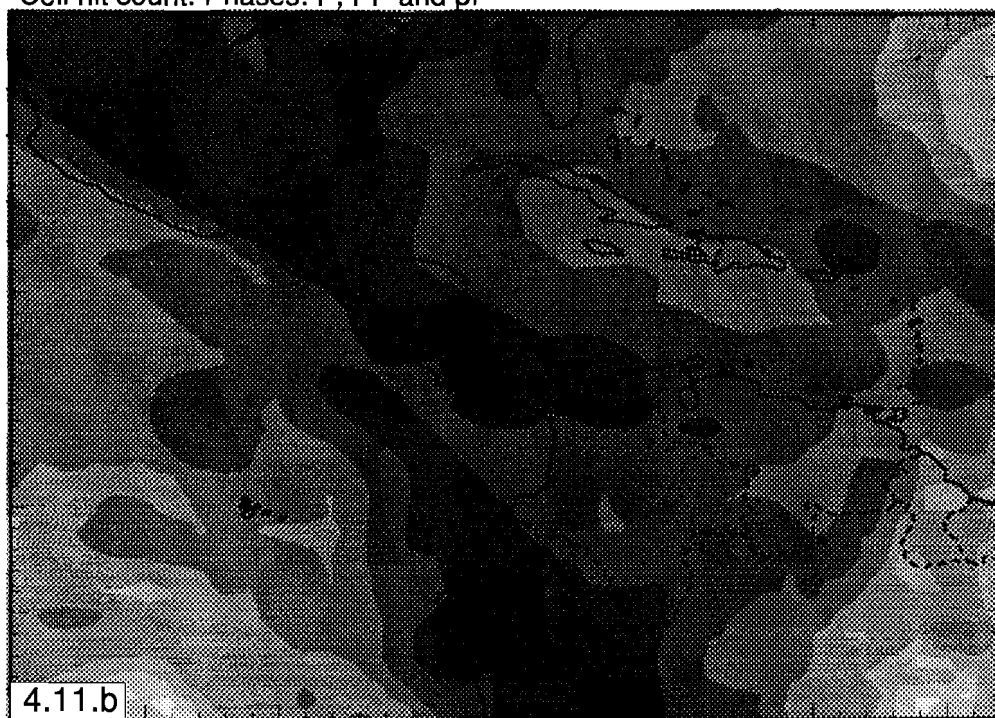
Permuted data: result after 15 iterations



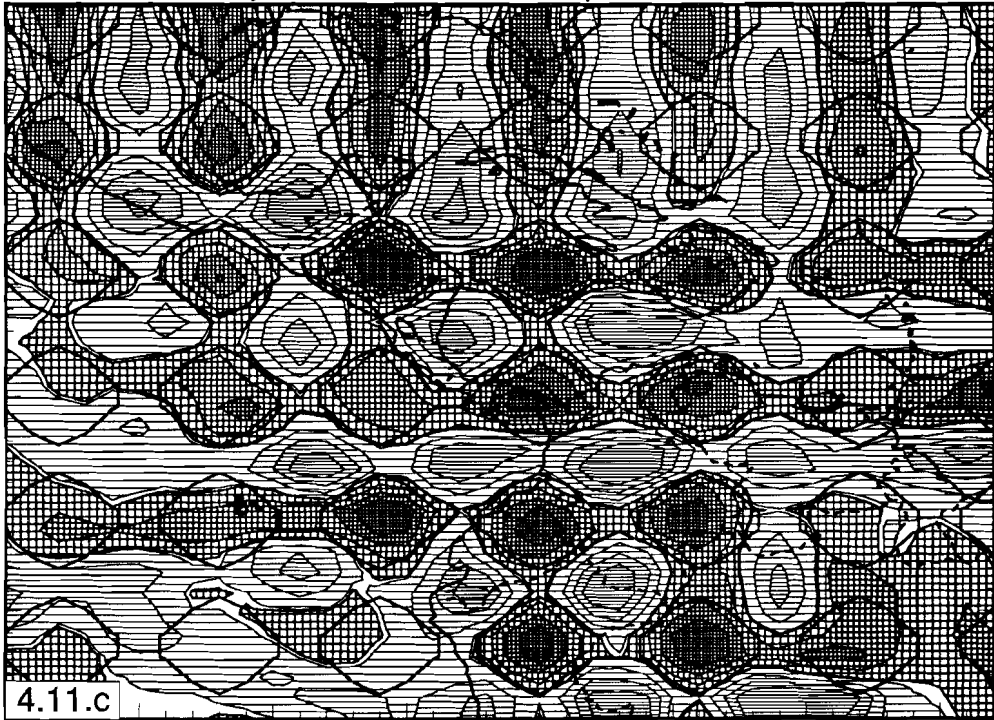
Velocity anomalies. Phases: P, PP and pP



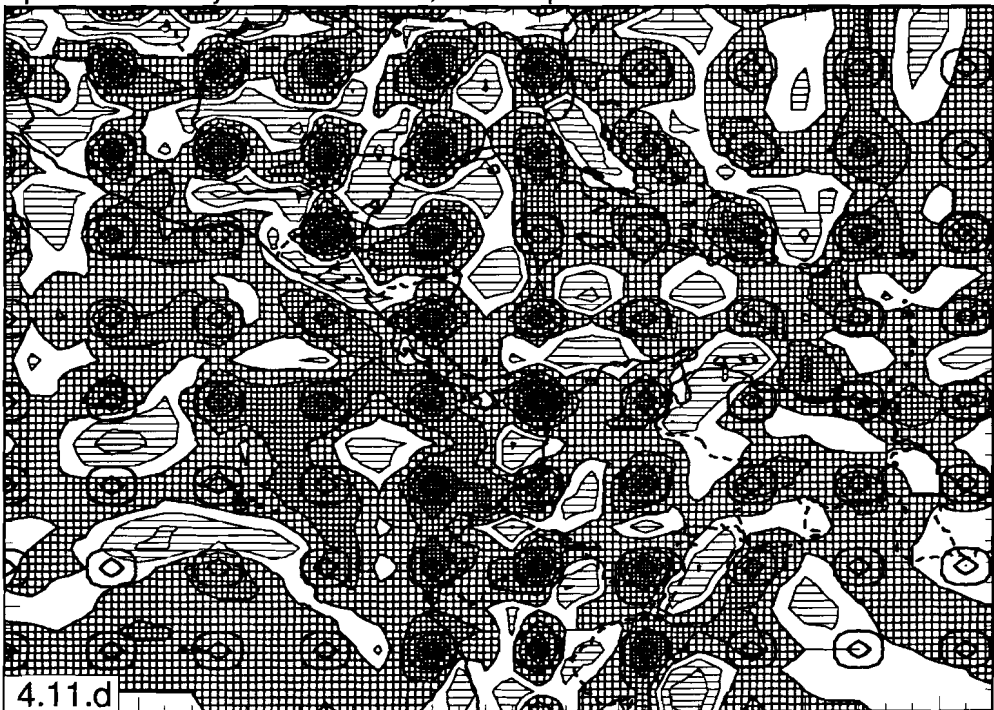
Cell hit count. Phases: P, PP and pP



Harmonic sensitivity test. Phases: P, PP and pP

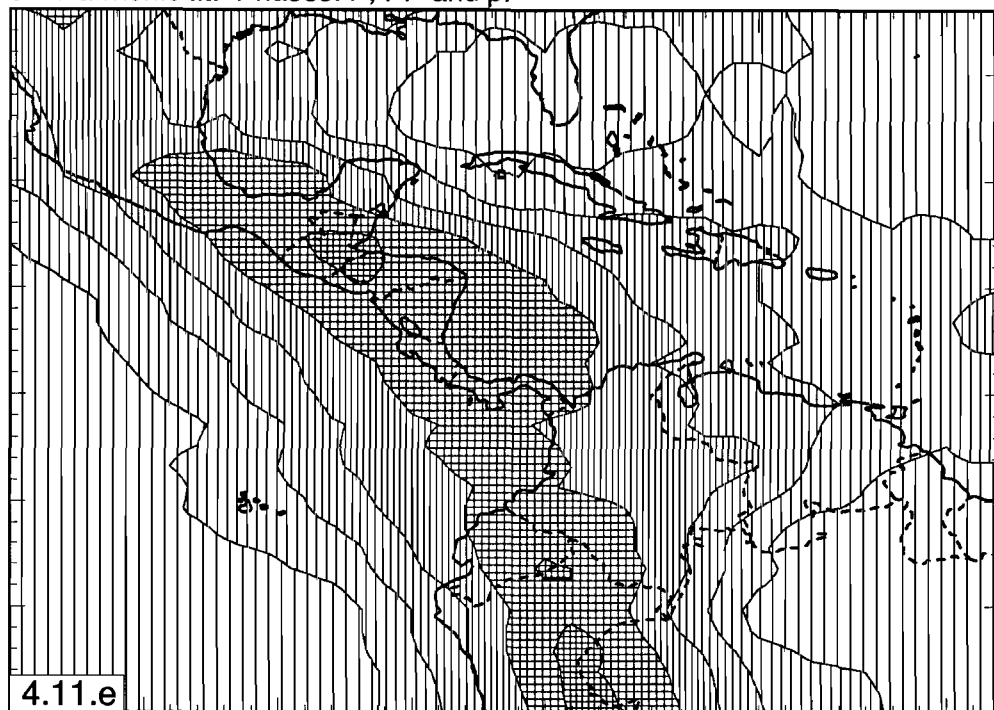


Spikes sensitivity test. Phases: P, PP and pP

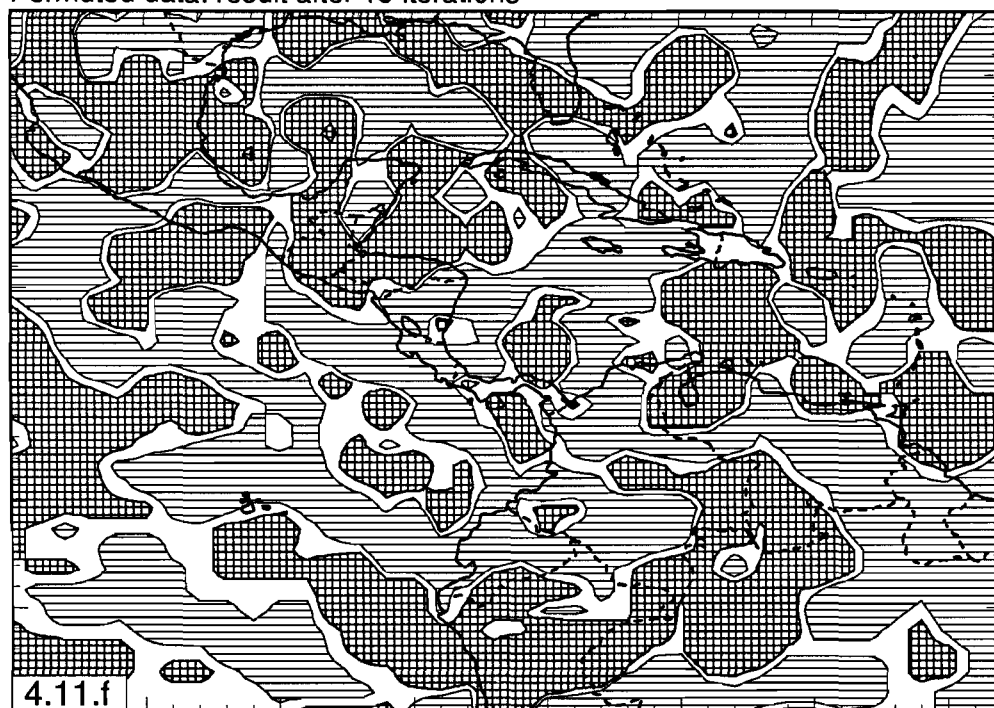




3D-Harmonic fit. Phases: P, PP and pP



Permuted data: result after 15 iterations

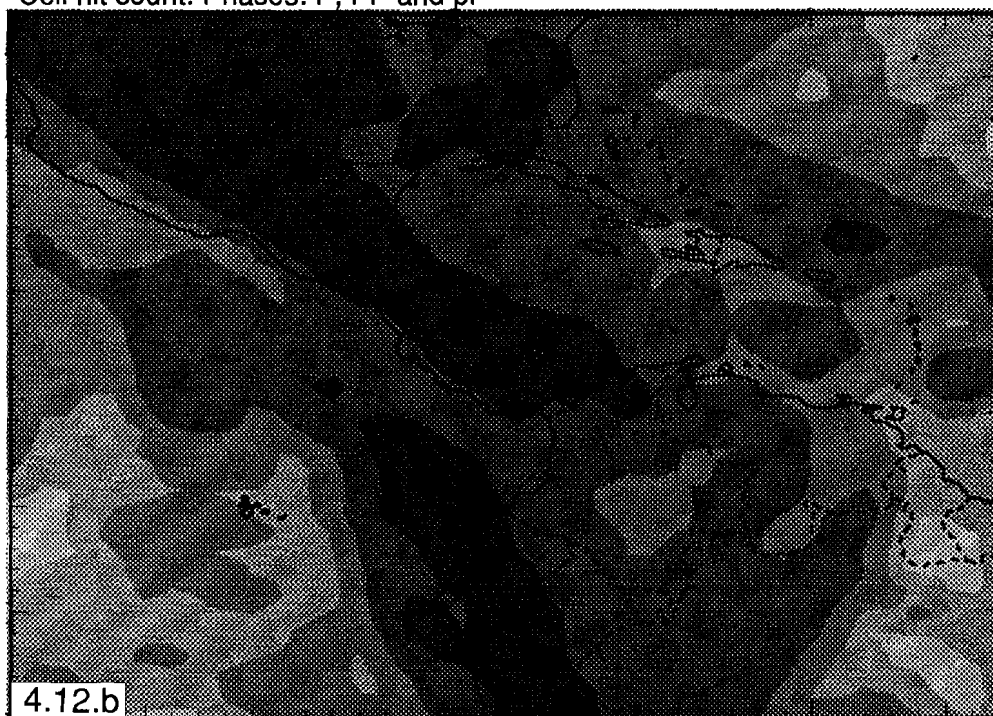




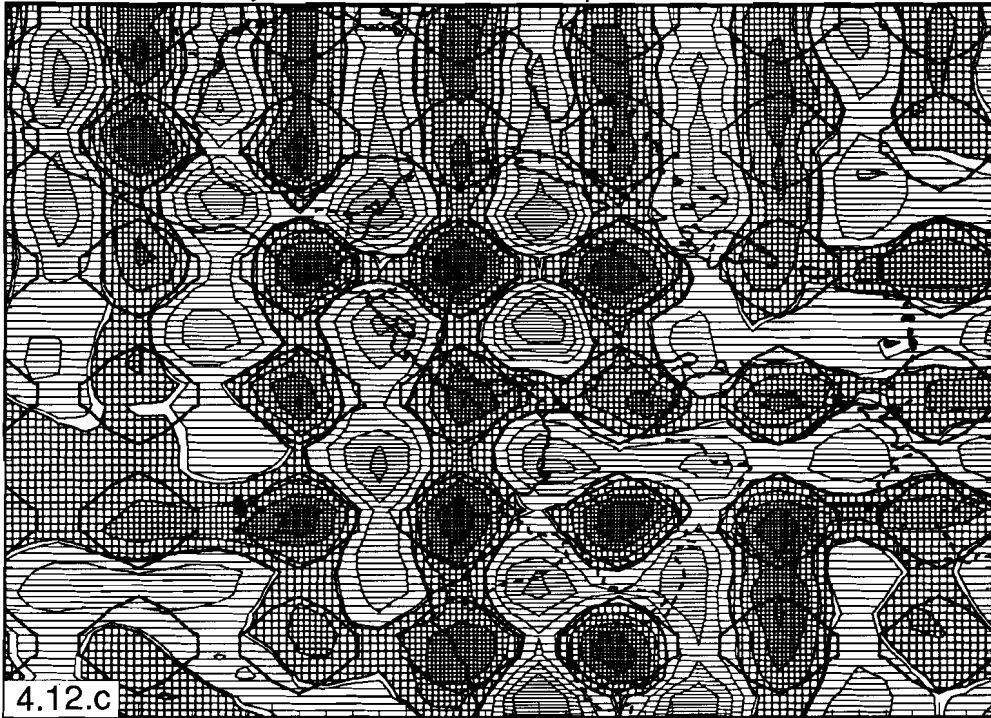
Velocity anomalies. Phases: P, PP and pP



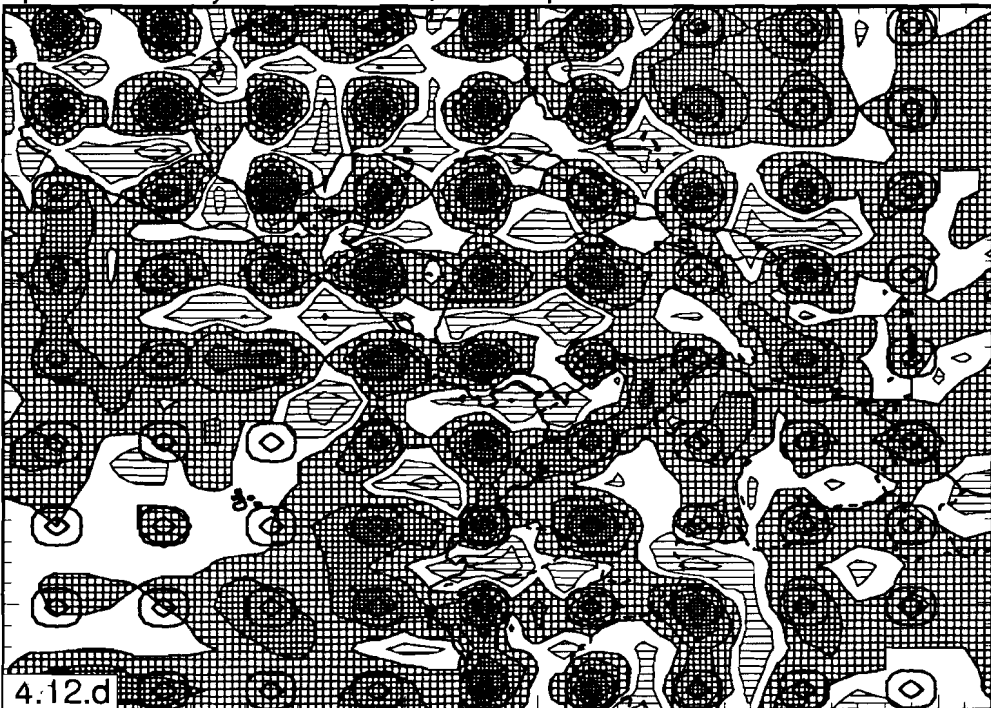
Cell hit count. Phases: P, PP and pP



Harmonic sensitivity test. Phases: P, PP and pP

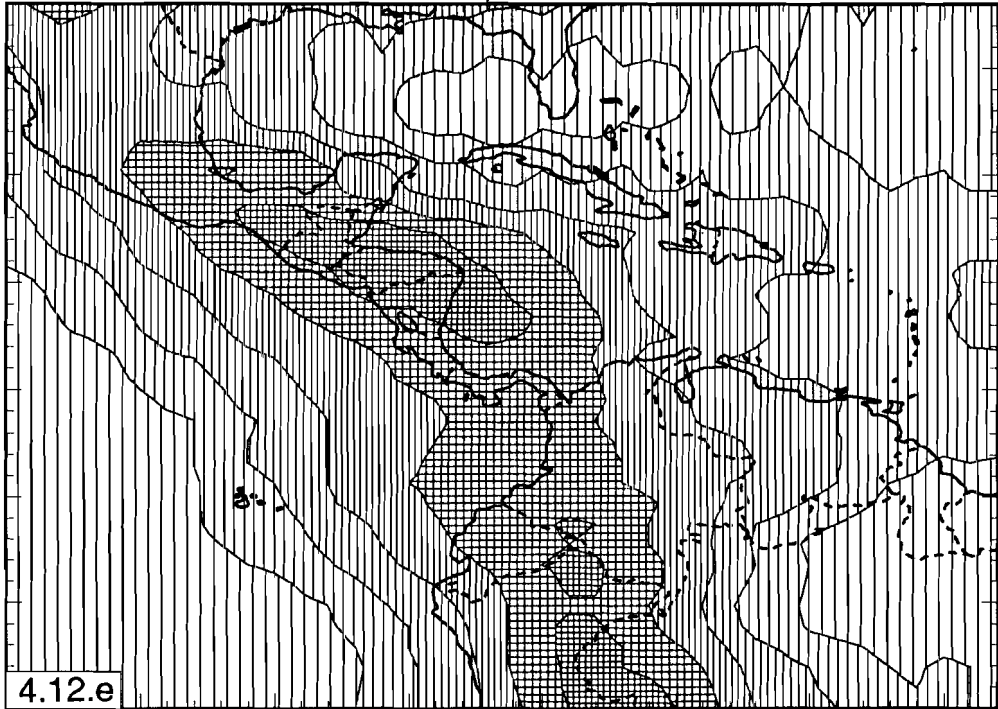


Spikes sensitivity test. Phases: P, PP and pP

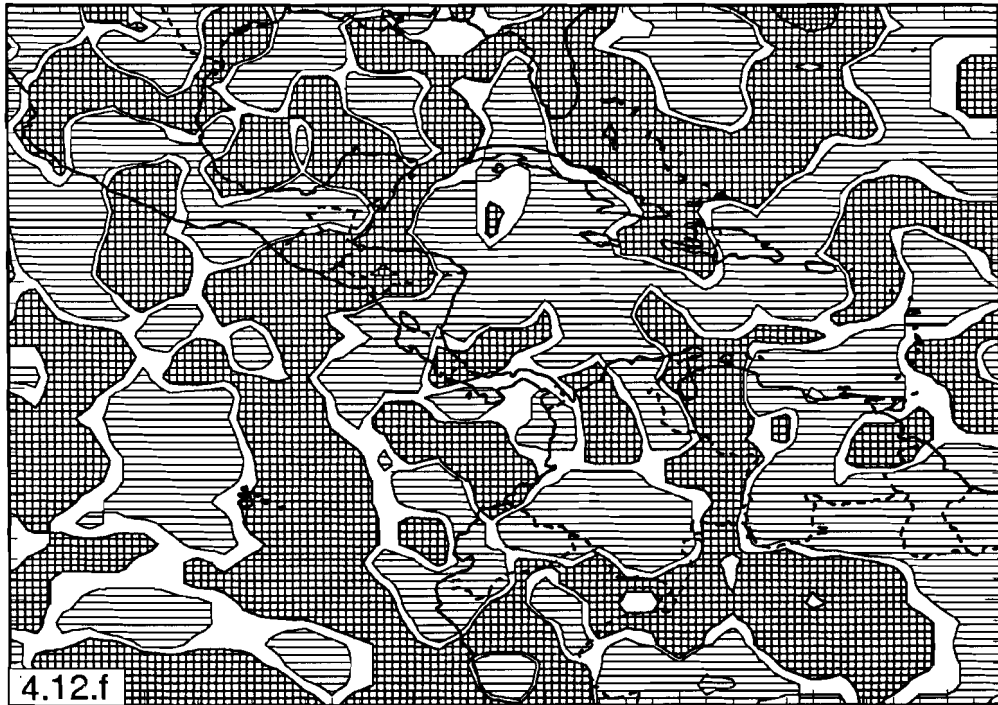




3D-Harmonic fit. Phases: P, PP and pP



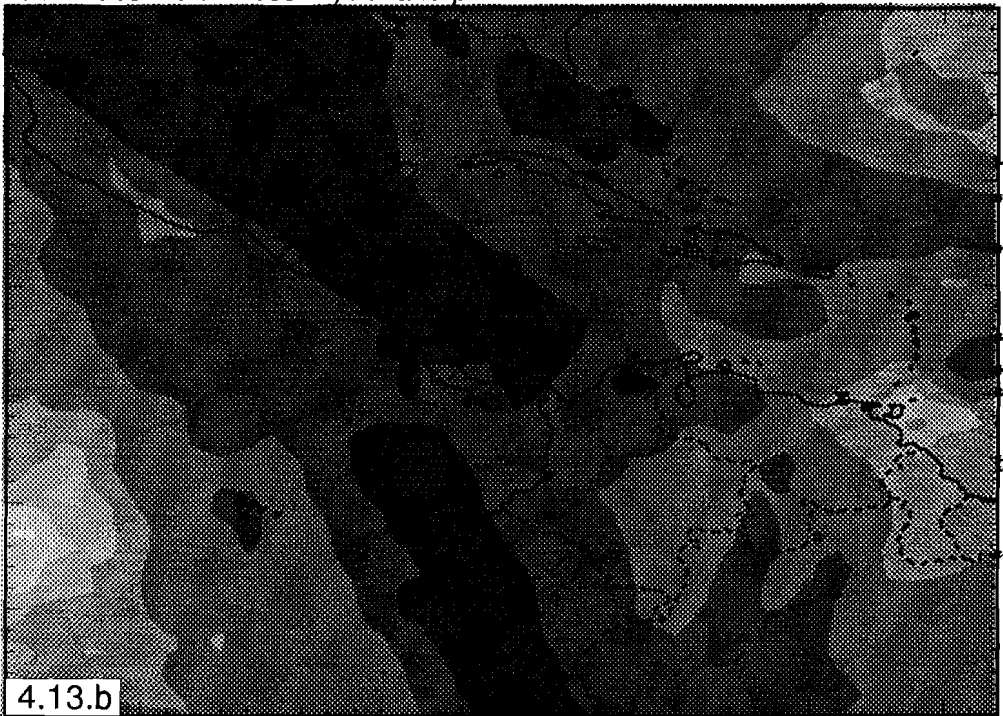
Permuted data: result after 15 iterations



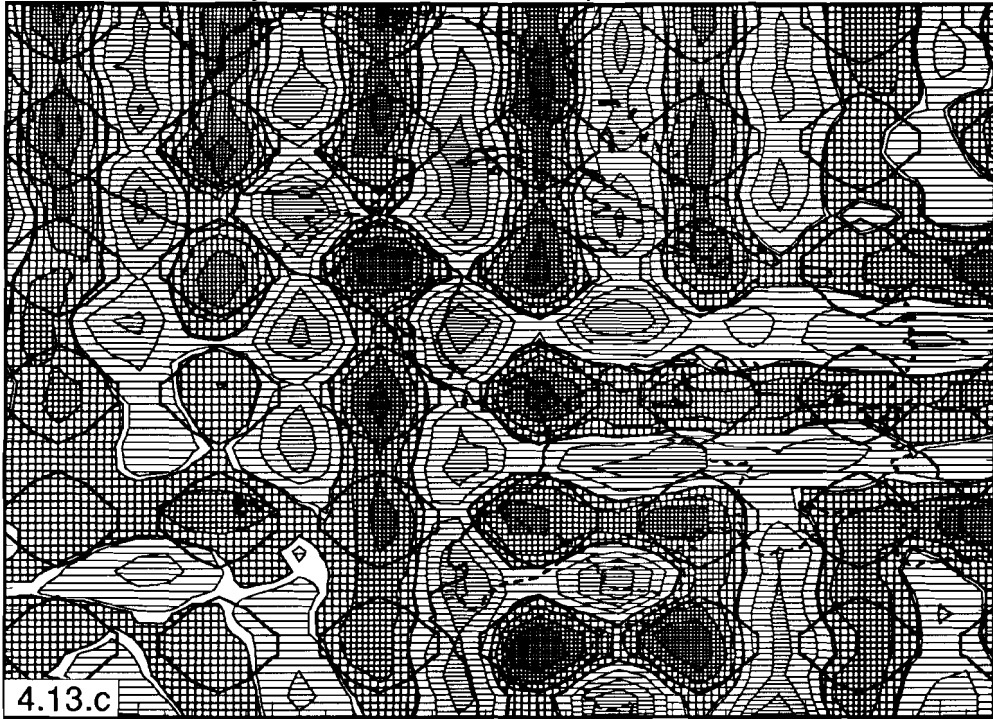
Velocity anomalies. Phases: P, PP and pP



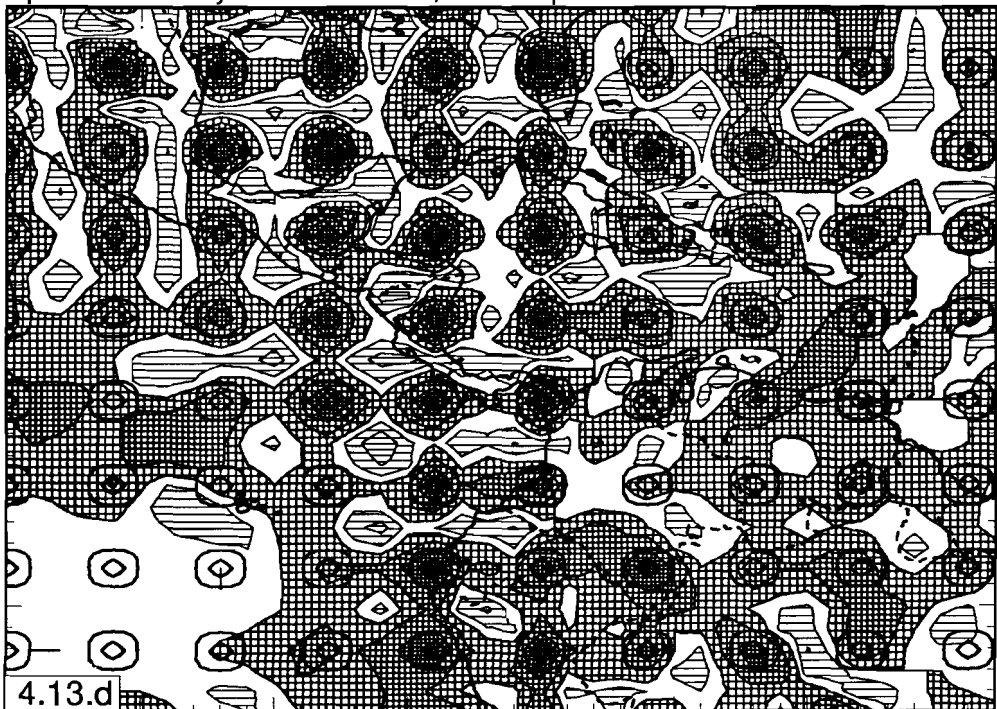
Cell hit count. Phases: P, PP and pP



Harmonic sensitivity test. Phases: P, PP and pP

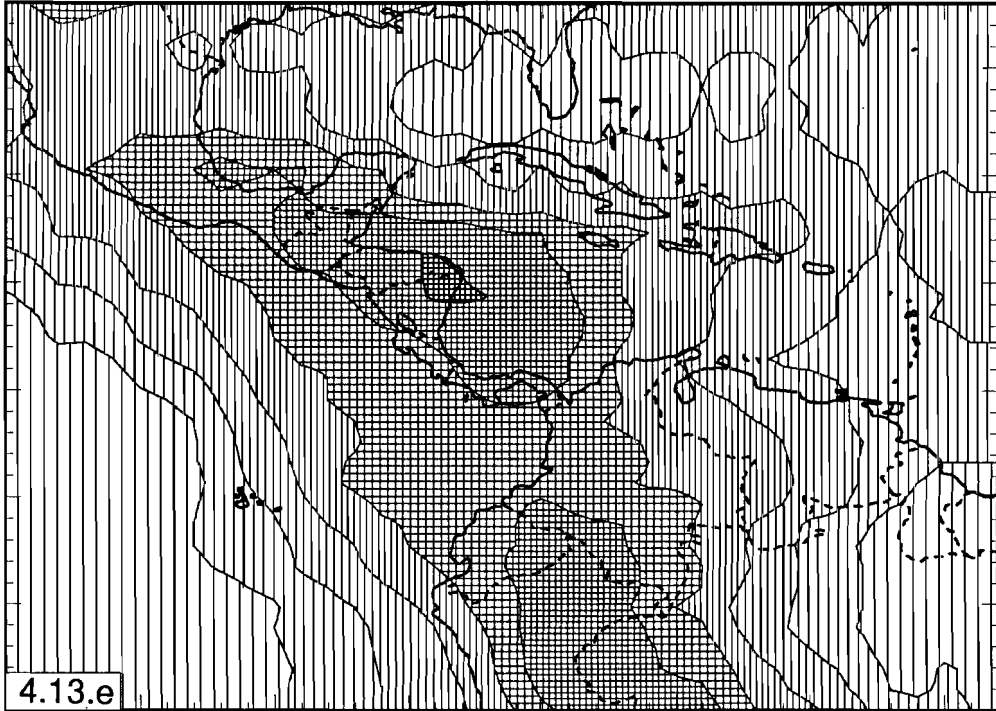


Spikes sensitivity test. Phases: P, PP and pP

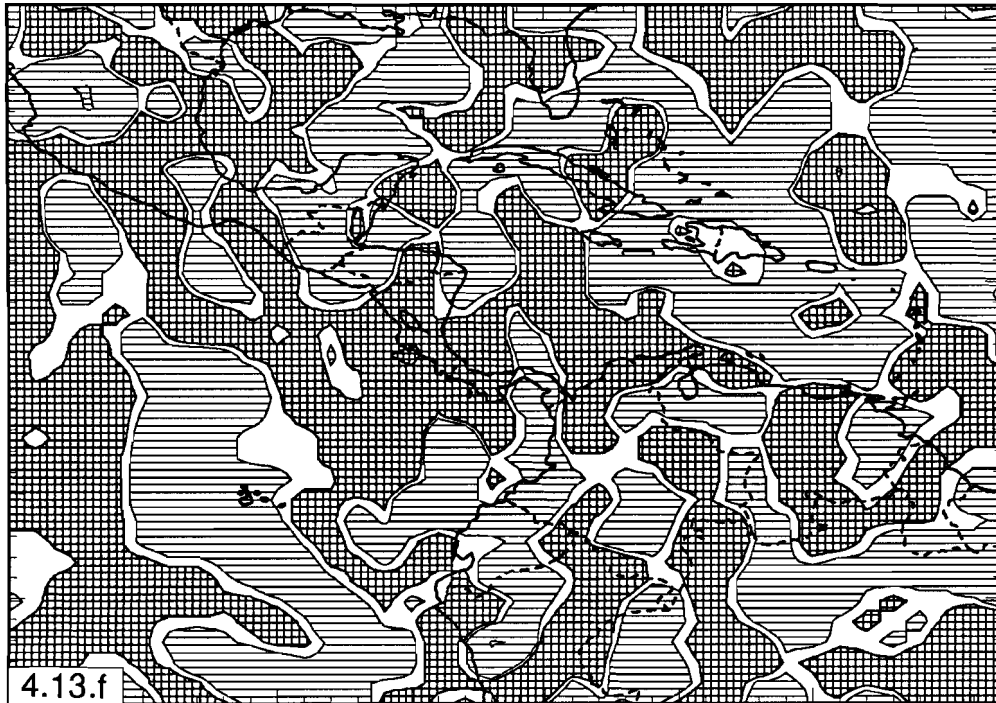




3D-Harmonic fit. Phases: P, PP and pP

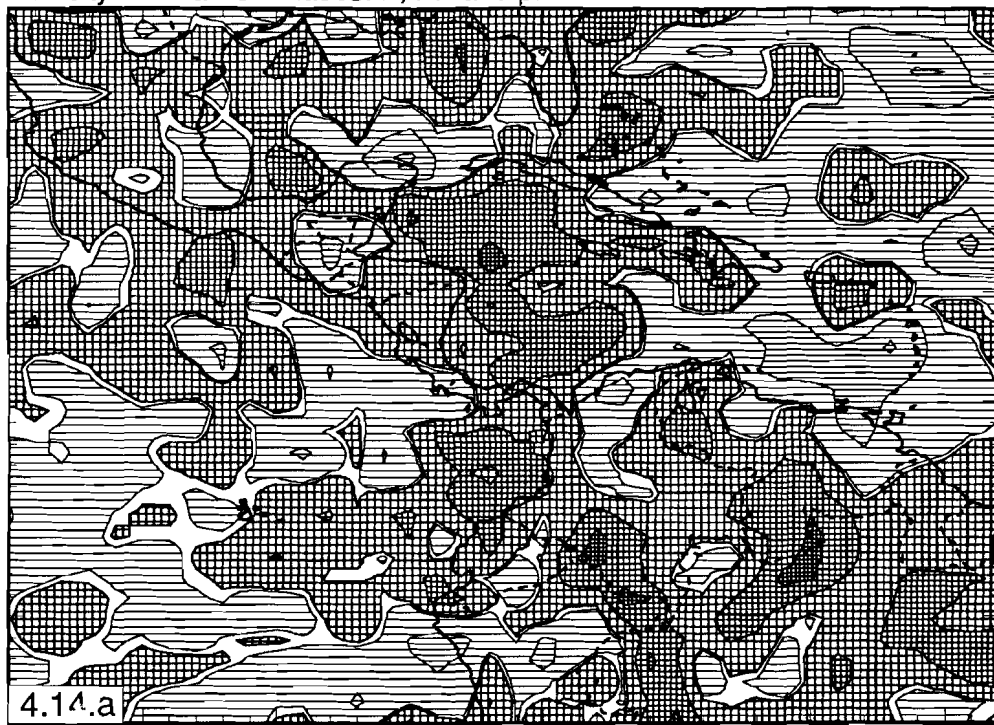


Permuted data: result after 15 iterations

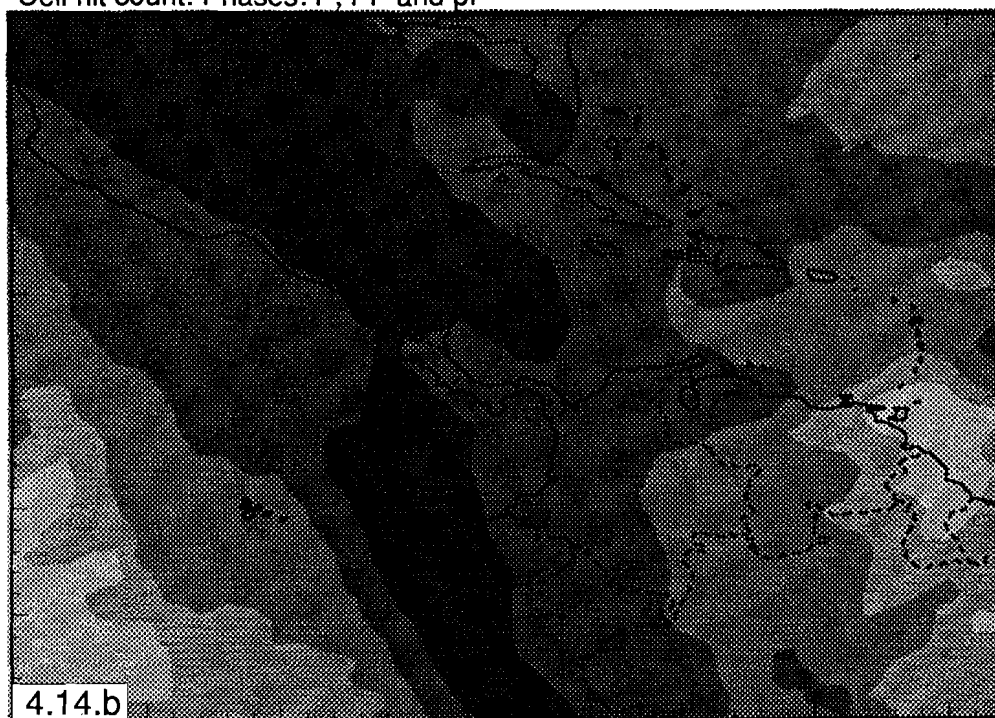




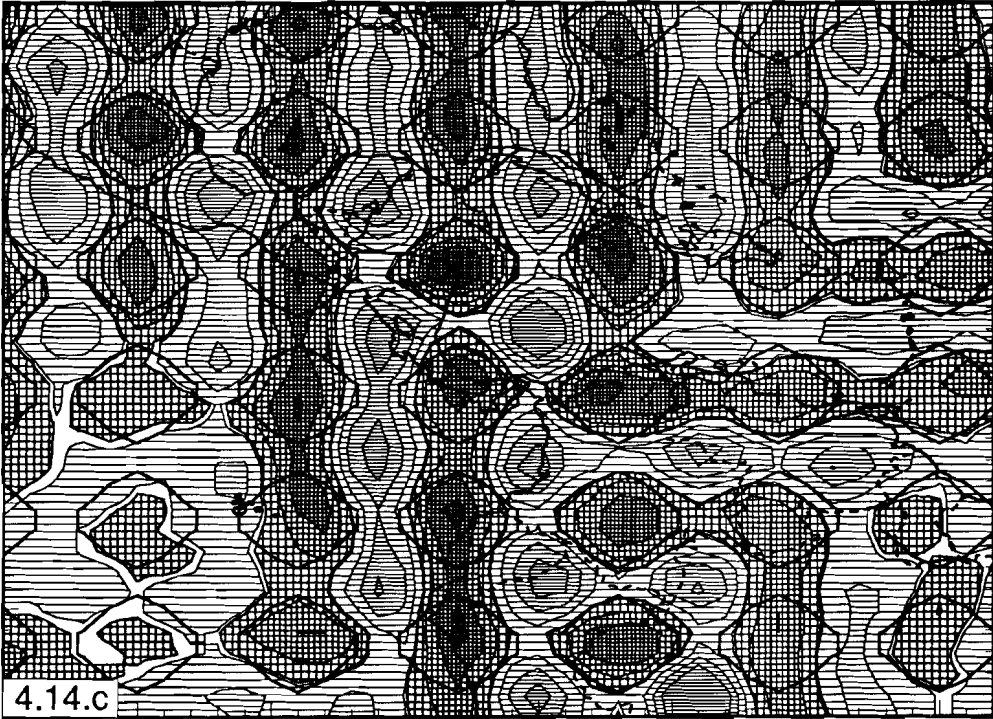
Velocity anomalies. Phases: P, PP and pP



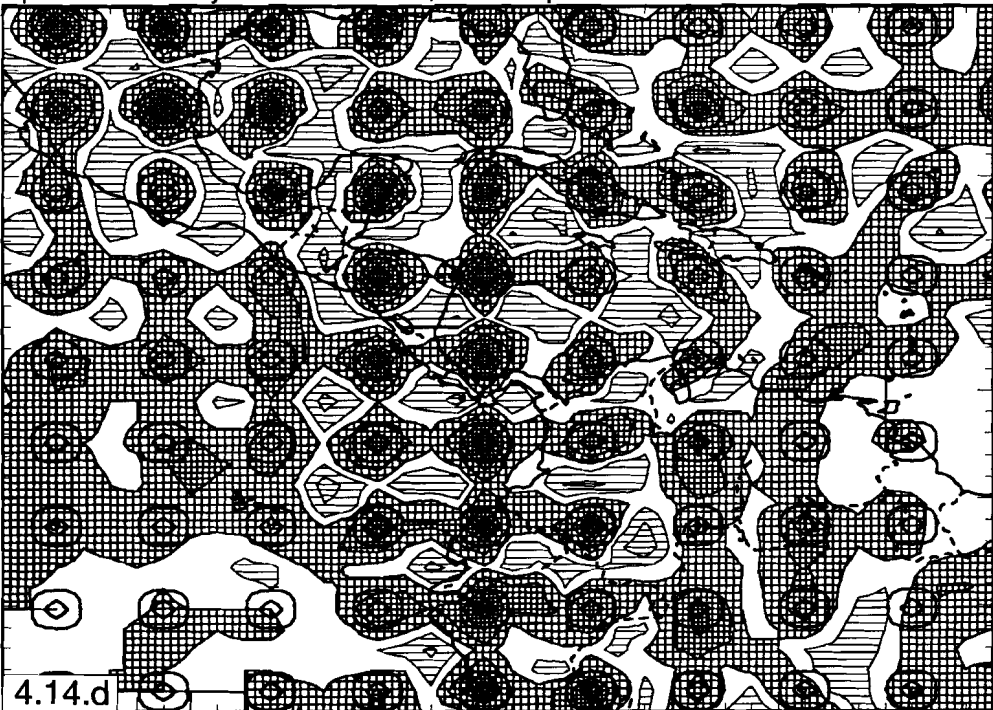
Cell hit count. Phases: P, PP and pP



Harmonic sensitivity test. Phases: P, PP and pP

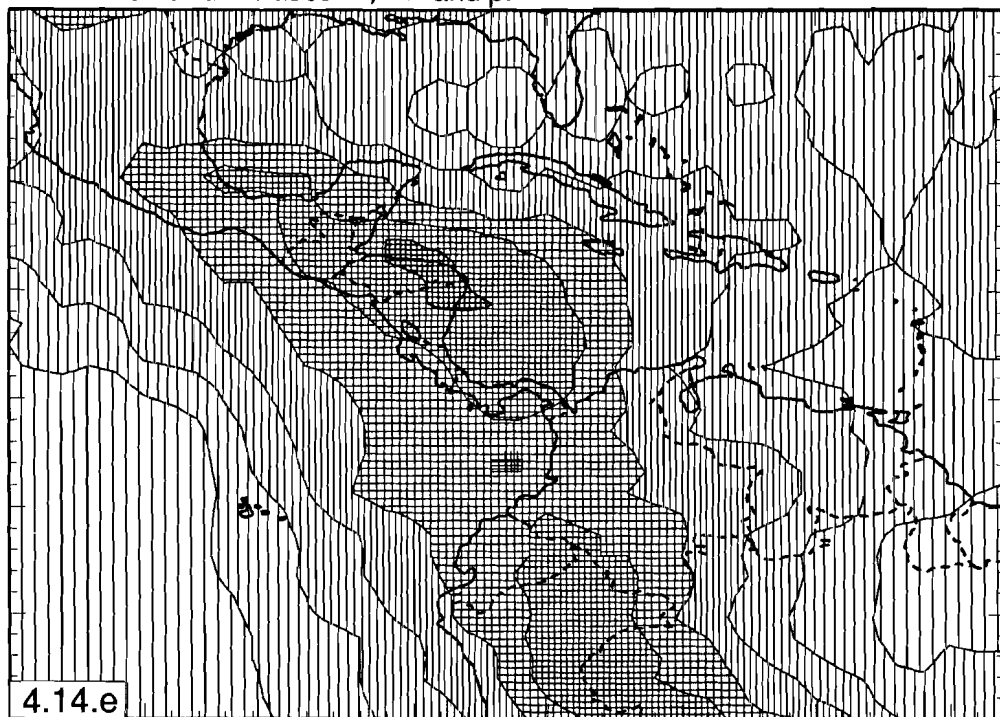


Spikes sensitivity test. Phases: P, PP and pP

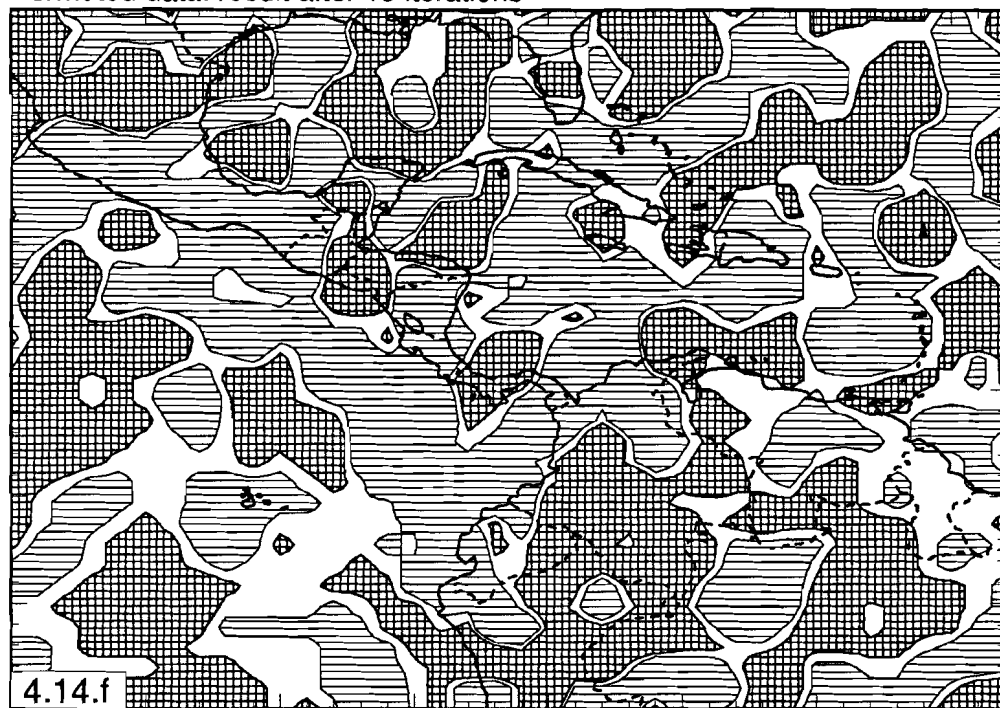




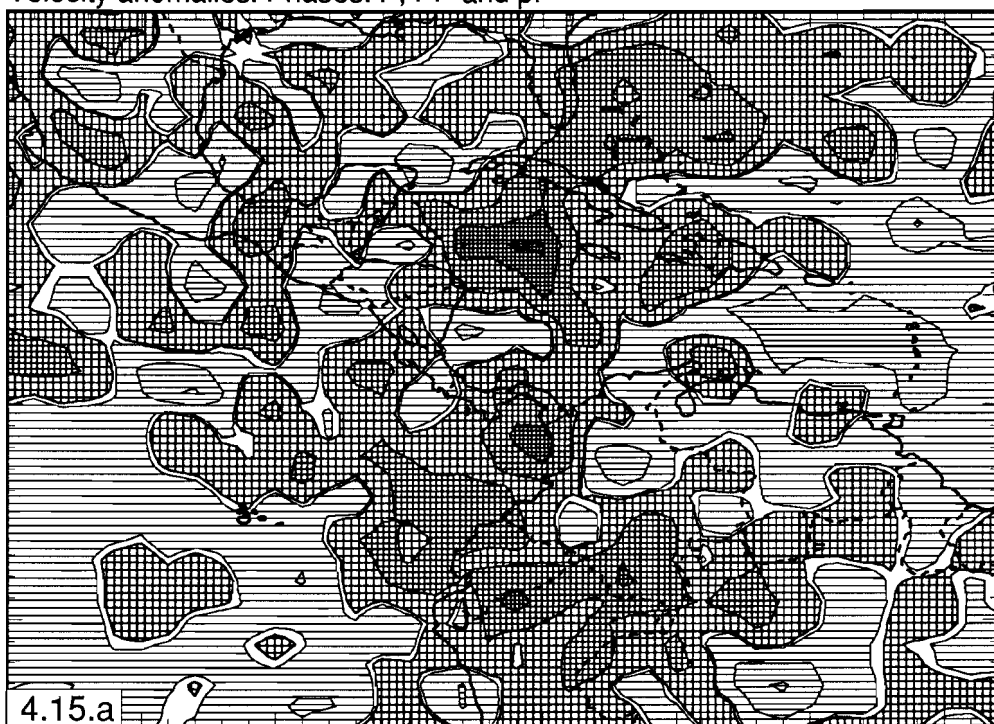
3D-Harmonic fit. Phases: P, PP and pP



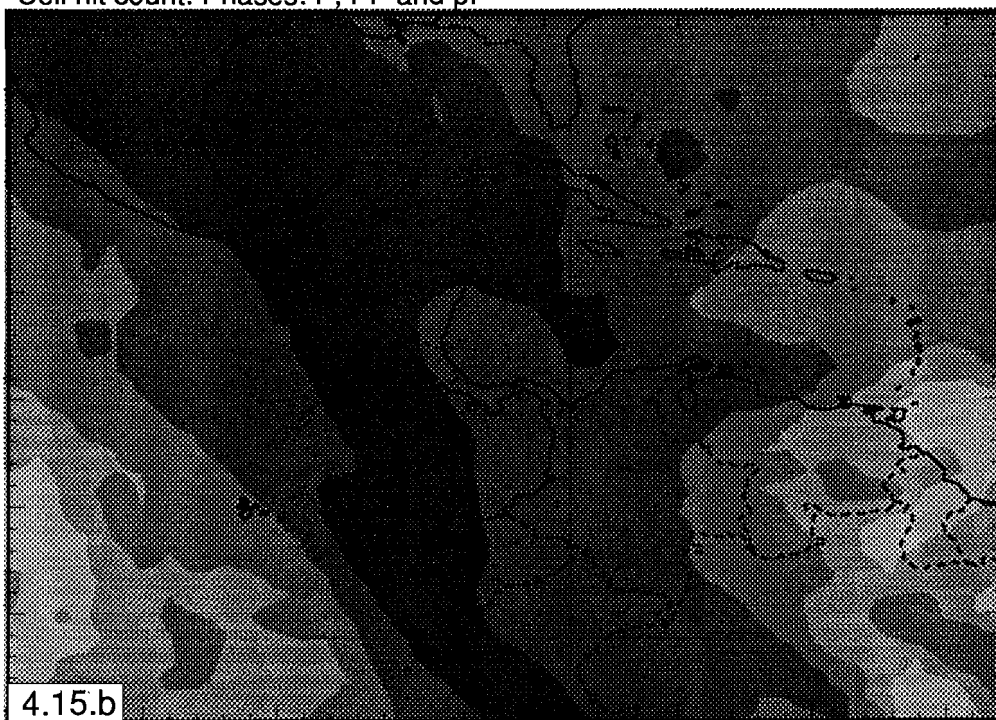
Permuted data: result after 15 iterations



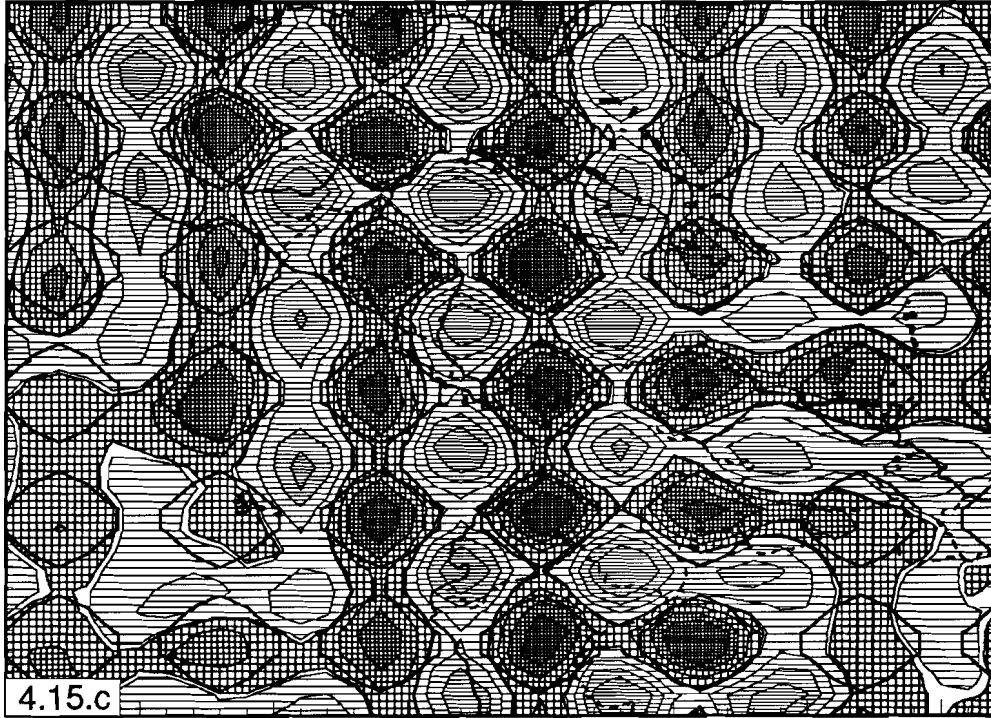
Velocity anomalies. Phases: P, PP and pP



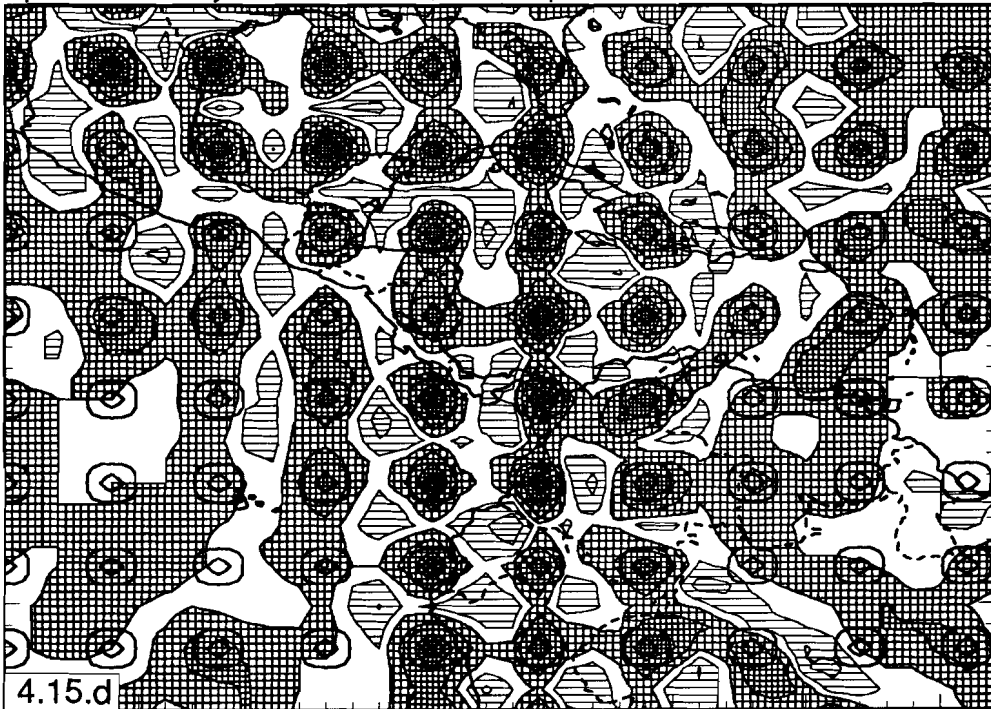
Cell hit count. Phases: P, PP and pP



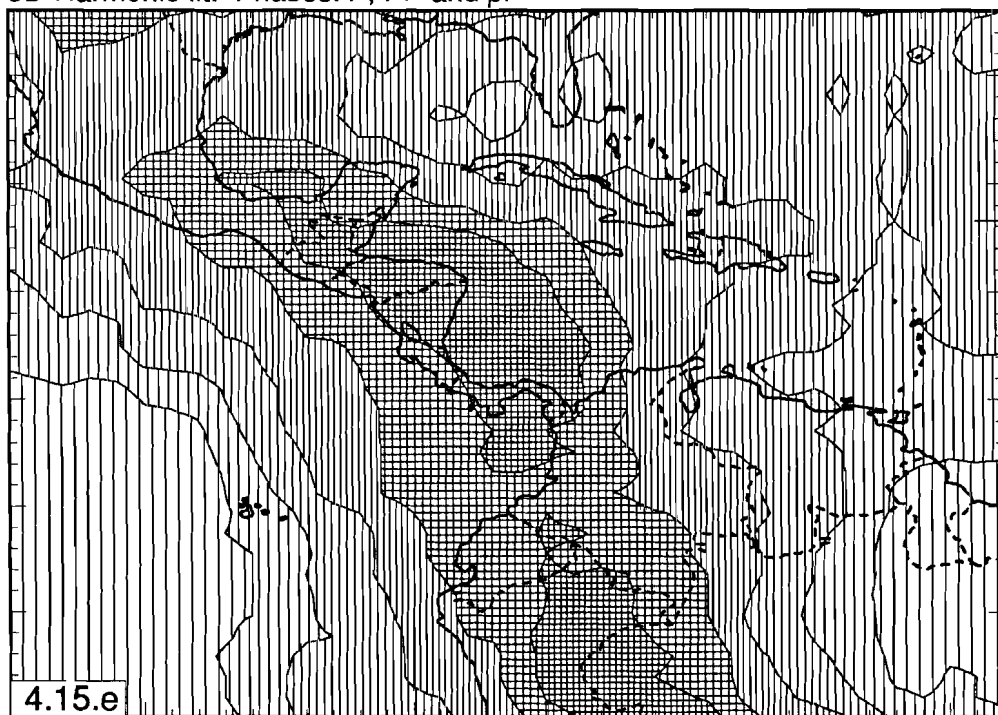
Harmonic sensitivity test. Phases: P, PP and pP



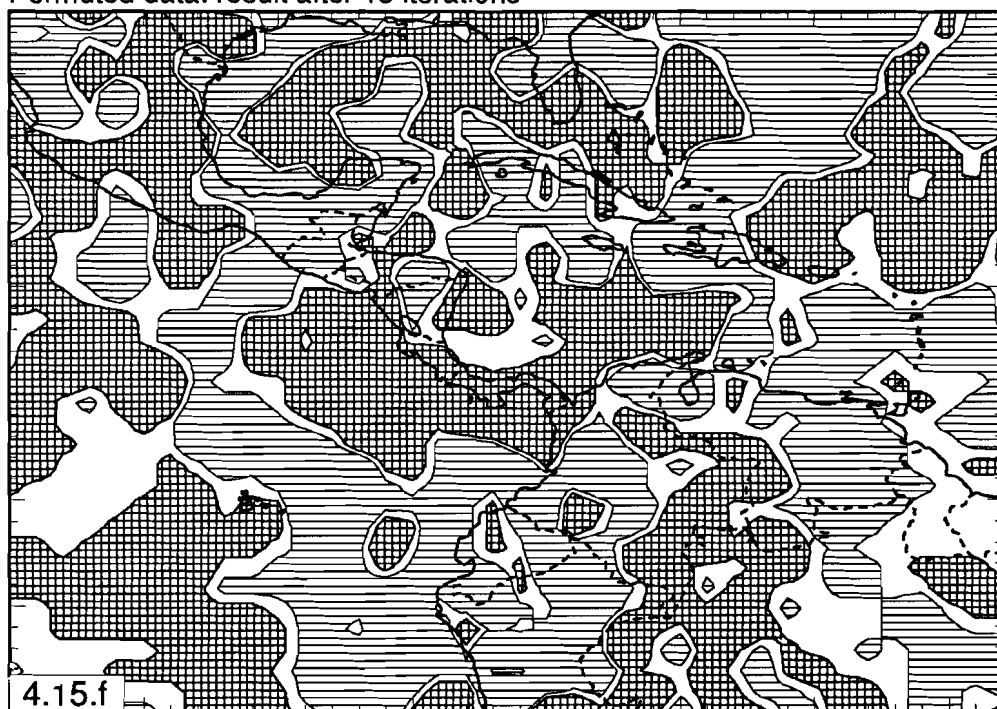
Spikes sensitivity test. Phases: P, PP and pP



3D-Harmonic fit. Phases: P, PP and pP



Permuted data: result after 15 iterations



## 5.4 Inversion results for the lower mantle

For the description of lower mantle structures, no reference is made to tectonical elements mapped at the surface.

### 5.4.1 Layers 11, 12 and 13: 660 - 1000 kilometer

The structure of the Earth's lower mantle is sampled by  $P$ ,  $PP$  and  $pP$  waves that are recorded at teleseismic distances, i.e., distances larger than approximately  $25^\circ$  for the  $P$  and  $pP$  phases, and larger than approximately  $50^\circ$  for the  $PP$  waves. The sampling of lower mantle structure is more homogeneous than that of structure in the upper mantle.

The comparison between the  $\mathbf{x}_{spike}$  images of layer 10, the deepest layer in the upper mantle, and the spike response in the lower mantle layers demonstrates a substantial improvement in the resolution of the input spikes. The spike response indicates good resolution of both the amplitude as well as the shape of small scale perturbations in mantle regions below the Gulf of Mexico, Middle America, the western part of the Caribbean Plate, and below the western part of South America. The quality of the spike response decreases with increasing depth in the lower mantle below the Lesser Antilles. The harmonic response and the harmonic model fit also support the observation that the resolution of lower mantle structures is substantially better than that of upper mantle anomalies. The resolution improved because of the more homogeneous sampling of structure by the  $P$ ,  $PP$ , and  $pP$  waves, and because Gaussian noise with a smaller standard deviation was added to model the smaller errors of the data of lower-mantle phases, as was discussed in section 3.6.4 and in Appendix 3A). The improved sampling can be inferred from the  $N_{hit}$  displays (Figures 5.4.[11-13]b).

At depths between 660 and 1000 km, I observe a high velocity feature below Middle America (Figures 5.4.[11,12]a). Examination of the Figures 5.4.[11-15]c,d, and e shows that the spatial resolution beneath Mexico and the central part of Middle America is good. The images of this lower-mantle high-velocity structure compare very well with the high velocity anomaly imaged in the deepest part of the upper mantle (Figure 5.4.10a). Just below the 660 km discontinuity, the imaged amplitude of the high velocity perturbation varies between +1.5 and +2.5%, relative to the reference model. With increasing depth, the amplitude reduces to +1.5% (layer 13, Figure 5.4.13a). The imaged peak-to-peak values, of the amplitudes of the fast and adjacent slow structures, decrease from 3 - 4% in layer 11 to 1.5 - 3% in layer 13. At upper mantle depths between 565 and 660 km (layer 10), the peak-to-peak value, below central Middle America, is of the order of 5 to 6%. Locally, the amplitudes of lower mantle structures are fairly well resolved, as can be concluded from the  $\mathbf{x}_{harmonic}$  and  $\mathbf{x}_{spike}$  displays. The harmonic fit gives an amplitude recovery of 60 - 80%, below Middle America, and slightly lower below western South America. Recall that the fit is smoothed laterally over 3 cells, and vertically over 1 cell.

Below the western part of South America high velocities are also present in mantle regions where resolution is good. I notice for this region some correlation between features in the displays of  $\mathbf{x}_{perm}$  and  $\mathbf{x}_{data}$  (e.g., Figures 5.4.11a and f), but the low-amplitude



anomalies in  $x_{perm}$  are neither continuous in lateral directions nor in depth. A correlation between  $x_{data}$  and  $x_{perm}$  does not exist at deeper levels (layers 12 and 13). Thus, whereas  $x_{perm}$  appears to vary randomly, features in  $x_{data}$  are continuous with depth and, consequently, can not merely be explained by artifacts of ray geometry in combination with the inversion algorithm. I conclude that the high velocity structure below western South America is realistic. Comparison of Figures 5.4.[8-13]a shows that this structure can be related to the upper mantle structure below western South America. At depths of 875 to 1000 km, in layer 13, the discussed high-velocity structures below Middle and South America become aligned and define an irregular, but continuous, structure, trending northwest to southeast (Figure 5.4.13a).

#### 5.4.2 Layers 14 and 15: 1000 - 1325 kilometer

Compared to the resolution in the previously discussed layers, the results of the sensitivity tests in this depth range indicate a further improvement of the resolution of lower mantle structures below the Gulf area, Middle America, the western Caribbean Plate, and below northwest South America.

In section 5.4.1, I described high velocity structures, which were laterally confined to narrow regions, in the lower mantle below the western part of the Caribbean Plate and below northwest South America. At depths below 1000 km, high velocity anomalies can also be observed in the lower mantle beneath these regions. The synthetic tests reveal good resolution. The morphology of the imaged structures, however, is much more irregular than in the lower mantle layers above 1000 km. In particular below South America, the perturbations in  $x_{perm}$  show similar characteristics as the anomalies in  $x_{data}$ , although  $x_{perm}$  structures are of much lower amplitude. No correlation between  $x_{perm}$  and  $x_{data}$  exists below Middle America and the western Caribbean.

I assume, that travel time residuals acquired along the ray paths outside the cell model are absorbed by station corrections. If this is not the case, structure sampled outside the cell model maps into the model. This can contaminate the solution in the lowermost layer(s). Mapping of lower mantle velocity anomalies below 1325 km into the lowermost layer of the cell model can explain the relatively high amplitudes (peak-to-peak values exceed 4%) of velocity anomalies below the western part of the Caribbean Plate (Figure 5.4.15a).

#### 5.4.3 Summary of results for lower mantle

Anomalously high  $P$  wave velocities are imaged below the Gulf of Mexico region and the western part of the Caribbean Plate, and below northwestern South America. These anomalies are continuous with depth. Below Middle America the amplitudes, as well as the shape, of the synthetic velocity models are well resolved. In general, there is no correlation between  $x_{data}$  and  $x_{perm}$ . Between 875 and 1000 km depth, the high velocities imaged below South America line-up with the anomalously high  $P$  wave velocities below the western Caribbean.

I observe a significant improvement of spatial resolution in the lower mantle with respect to the resolution of upper mantle structures. This improvement can be inferred

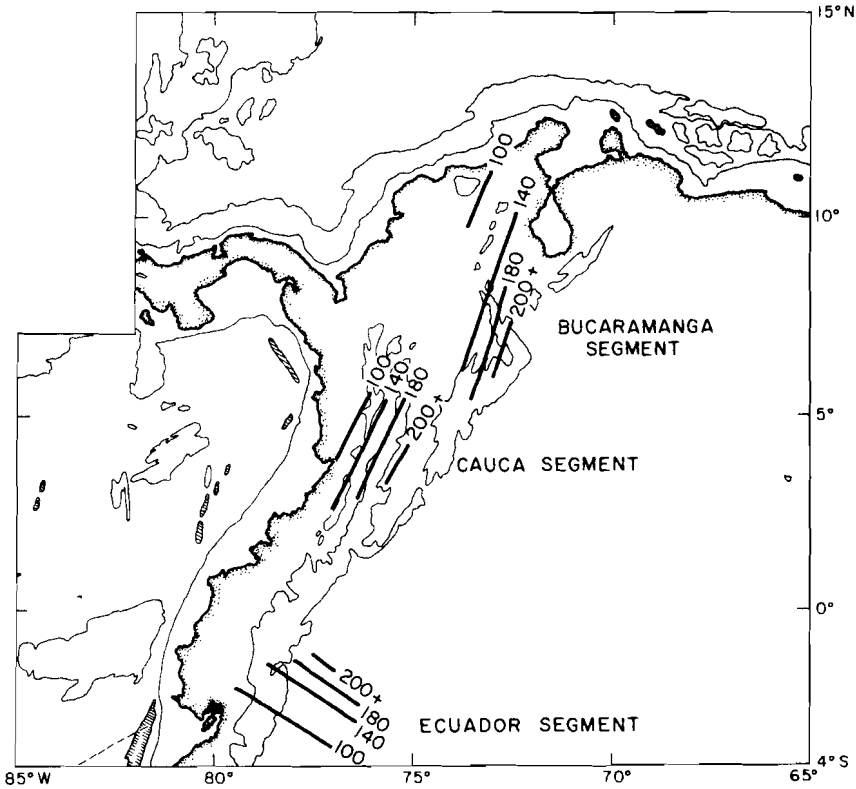
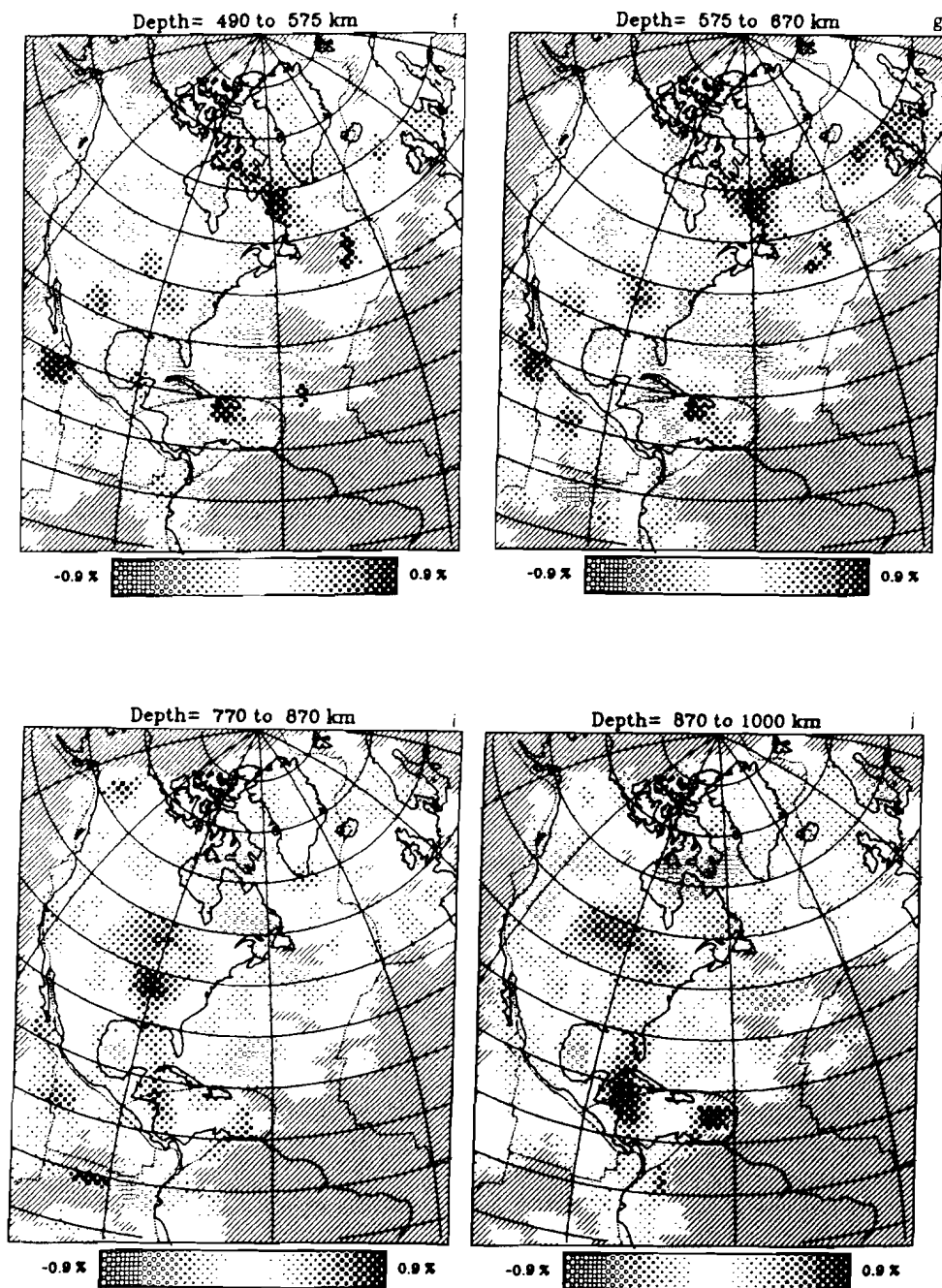


Figure 5.5. Contours of Wadati-Benioff zones below northwest South America, and identification of three segments of subducted lithosphere. After Pennington [1981].

from examination of the results of the synthetic tests (Figures 5.4.[11-15]c,d and e). The improved results of sensitivity tests can be explained as being due to the more homogeneous sampling by seismic waves of lower mantle structure (Figures 5.4.[11-15]b), and the lower standard deviation of the Gaussian distributed noise added to synthetic data of tele-seismic (lower mantle)  $P$  phases. In contrast to the better resolution, I notice somewhat higher amplitudes in the images obtained from the inversion of randomly permuted data than in the upper mantle layers. The morphology of features in  $x_{perm}$  is also comparable to the  $x_{data}$  images. In general, the inversion of randomly permuted delay-times results in random velocity perturbations which are only rarely continuous in horizontal directions or in depth. Nevertheless, their presence warns us to be cautious with the interpretation of the  $x_{data}$  images, and to be aware of artifacts.

### 5.5 Comparison with results of other investigations

Here, the results of my tomographic investigations of the velocity structure in the mantle below the Caribbean region are compared to results of other seismological investigations. In chapter 6, possible correlations with results of other investigations (seismicity, gravity,



*Figure 5.6.* Results of Grand [1987] for the shear velocity structure below North America. Note the images of high shear wave velocities in the upper mantle below the eastern Caribbean (a,b), and high velocities below Middle America and the western Caribbean at lower mantle depths (c,d).

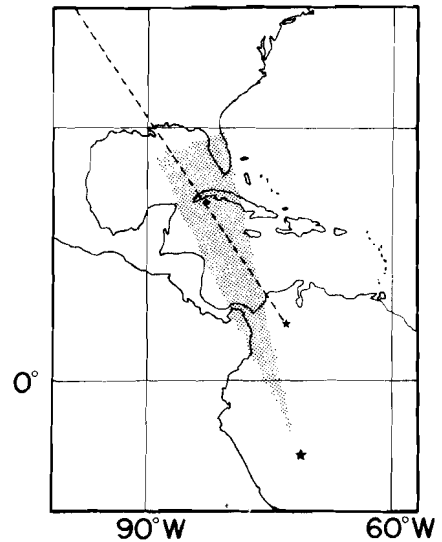
magnetic field) are discussed in more detail, and for smaller regions.

With regard to the large-scale velocity structure in the upper mantle, I can only compare my observations with the results of a tomographic analysis of the shear wave structure by Grand [1987]. In the discretization of the earth's interior, Grand used blocks of 500 x 500 km. He focussed on lower mantle images, and reports only little heterogeneity in the upper mantle. The shallow high velocities imaged in this study below the southern part of the Lesser Antilles and the northern part of South America compare well to Grand's results. The high velocity structures that are imaged below Middle America in the top 400 km of my model are not visible in Grand's results. In Figures 5.6a and 5.6b I copied Grand's results for two layers which cover a depth interval between 490 to 670 km. This depth range is comparable to the depths covered by layers 9 and 10 of the model used here. At these depths, Grand [1987] imaged high shear-wave velocities below the eastern part of the Caribbean: a northwest-to-southeast trending high-velocity structure from Hispaniola to northern Venezuela. The amplitudes of the high velocities, imaged in that mantle region, are of the order of 1% relative to his reference model. Comparison with Figures 5.4.[9,10]a shows that Grand's images of anomalously high shear velocities correlate very well with the variations of the  $P$  wave velocity that are imaged in the deeper part of the upper mantle below the eastern Caribbean, just west of the Lesser Antilles arc. The high velocity structure in Figures 5.4.[9,10] suggests a deviation of the  $P$  velocities of the order of 1.5 to 2.5% relative to reference model VCAR.

I observed anomalously high  $P$  velocities in the depth interval between 475 and 565 km below the western part of the Gulf of Mexico, Yucatan, and below the southern part of Middle America. High velocities are also suggested for  $S$  waves in Grand's image of this depth layer (Figure 5.6a). However, I observe also high velocities between 565 and 660 km below the western part of the Gulf area, whereas Grand reports  $S$  velocities lower than those of the reference model. Substantial low velocities of both  $P$  and  $S$  waves are imaged below the southeastern part of the Gulf of Mexico, western Cuba, and below the western Caribbean Plate. The high velocities imaged below Middle America, in the lowermost part of the upper mantle (Figures 5.4.[9,10]), are not present in Grand's images.

For the lower mantle, I can compare the results of this investigation with conclusions from other investigations [Jordan and Lynn, 1974; Lay, 1983; Grand, 1987; Vidale and Garcia-Gonzales, 1988]. From a study of  $ScS-S$  and  $PcP-P$  differential travel-time residuals, and absolute  $S$ -wave travel times, obtained from the registration of two South American earthquakes, Jordan and Lynn [1974] suggested the presence of velocity heterogeneities in the lower mantle below the Caribbean. They estimated the amplitude of this anomaly to be at least 1%, relative to the Jeffreys-Bullen model, both for  $P$  as for  $S$  velocities. Jordan and Lynn attributed this velocity anomaly to a thermal perturbation of the order of 200 – 300°C relative to the ambient mantle temperature. The approximate location of this feature is shown in Figure 5.7. The result of Jordan and Lynn [1974] was confirmed, and the lower mantle anomaly further constrained, by Lay [1983] who studied  $S$ ,  $ScS$ ,  $P$  and  $PcP$  differential travel-time residuals and relative amplitudes. Lay [1983] constrained the location of the anomalous structure, with velocities up to 2% faster than the

Figure 5.7. Location of high velocities (both  $P$  and  $S$ ) in the lower mantle below the western Caribbean [after Jordan and Lynn, 1974].



$S$ ,  $ScS$ ,  $P$  and  $PcP$  differential travel-time residuals and relative amplitudes. Lay [1983] constrained the location of the anomalous structure, with velocities up to 2% faster than the Jeffreys-Bullen model between 1000 and 1900 km in depth (Figure 5.8). Additional seismologic evidence for this high velocity structure below central Middle America and the western part of the Caribbean Plate was provided by the examination of body wave forms and amplitudes [Vidale and Garcia-Gonzalez, 1988].

In the tomographic images of the anomalous  $P$  velocities in the lower mantle below the Caribbean, I observe high velocities in a mantle region that correlates very well with the location inferred by Jordan and Lynn [1974]. A particularly good correlation exists between 660 and 1000 km. This correlation also holds for the two lowermost layers of the model (Figures 5.4.[14,15]a), although the images at those depths are more blurred.

The southward shift of the high velocity perturbations below the eastern Caribbean Plate, as discussed above, can also be discerned from the images of Grand [1987] between 575 and 770 km (Figures 5.6b,c). Similar correlations can be found between the  $P$  and  $S$  velocity structures below Cuba, and the central part of the Caribbean Plate, and below Middle America (Figure 5.6d). For northwestern South America, both investigations show high velocities in the lower mantle. The high velocity structures below Florida, Middle America, and below northwest South America correlate well at lower mantle depths (780-870 km). Important differences between the  $P$  and  $S$  velocity structures exist in the lower mantle below the eastern part of the Caribbean Plate. Between 770 km and 1300 km, Grand's images suggest substantial high shear-wave velocities, whereas no evidence for corresponding high  $P$ -wave velocities can be inferred from my study.

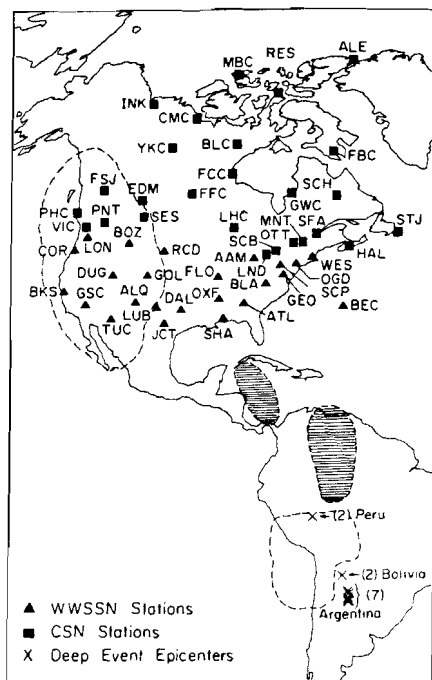


Figure 5.8. Horizontally hatched spots mark a fast region in the lower mantle regions below western Caribbean (depth range: 1000-1900 km) and a slow region below northern Brasil (depth range: 1700-2700 km) [after Lay, 1983].

## 5.6 Conclusions

In examining the results of my tomographic investigation, I reach the following conclusions with regard to the spatial resolution and the large-scale structures in the mantle below the Caribbean region:

- (1), the recovery of both the amplitudes and the morphology of the synthetic input models is good below Middle America and the northwestern part of South America, and reasonable in the upper mantle below the Lesser Antilles;
- (2), the spatial resolution is low at shallow depths beneath intraplate regions, along the boundary between the North American Plate and the Caribbean Plate near the Greater Antilles, and in the transition zone between the upper mantle discontinuities at 390 and 660 km;
- (3), a good correlation often exists between known geological and/or tectonical features and the imaged variations in  $P$  velocities, even in mantle regions where results of sensitivity tests designate the tomographic images as unreliable;
- (4), mantle regions below the convergent plate boundaries are characterized by  $P$ -wave velocities which are up to 3% higher than the velocities of the reference Earth model;
- (5), the observations of aspherical lower-mantle structures below Middle America are consistent with earlier publications;
- (6), the structures in the upper and lower mantle seem to be locally continuous, in particular below Middle America, which is suggestive for mass transport across the 660 km discontinuity.



## *Chapter 6*

# **Mantle structures below the convergent margins of Middle America, The Lesser Antilles, and northwestern South America**

## **6.1 Introduction**

In this chapter I discuss the morphology of the mantle structures below the margins of Middle America, the Lesser and Greater Antilles, and below the boundary between the Caribbean Plate and the northwestern part of the South American Plate. The knowledge about the morphology of subducted slabs can be used to obtain information about past plate motions, and to constrain kinematic plate reconstructions.

In chapter 4, I showed that according to recently published models [e.g., Ross and Scotese, 1988] subduction processes have been active in Middle America since the Early Cretaceous (140 Ma), and at least since the Paleocene (80 Ma) in the eastern Caribbean. With velocities of relative plate motions typical in the two regions, some thousands of kilometers of lithosphere of the Farallon and Cocos Plates must have been consumed at the Middle America trench, and some hundreds of kilometers of Atlantic lithosphere at the trench along the Lesser and Greater Antilles. In this chapter I investigate the morphology of the (remnants of) the lithosphere subducted below the Caribbean region, with the objective to find answers to the following questions: (1), Can evidence be obtained about the presence of subducted lithosphere that can be related to the mentioned subduction processes? (2), What happened to the presumably thousands of kilometers of subducted



lithosphere of the Farallon Plate? (3), What are the effects on the morphology of the Middle America subduction zone of the break-up of the Farallon Plate in the Cocos and Nazca Plates (25 Ma, [Wortel and Cloetingh, 1981])? (4), Does the morphology of the Lesser Antilles subduction zone indicate the presence of a plate boundary between the atlantic parts of the North and South American Plates? (5), Does a relation exist between the slab morphology and the differences in seismicity in the northern and southern part of the Lesser Antilles? (6), Can the nature and importance of the plate boundary between the Caribbean Plate and the northwestern part of the South American Plate be established? And more general, (7), Does the correlation between results from tomographic investigations and inferences about mantle structure from, e.g., seismicity studies provide additional information on the reliability of tomographic images?

An important source of information about mantle structures and about the tectonic reconstructions is the seismicity in the region. The study of focal mechanisms and the distribution of earthquake hypocenters provides crucial information about plate boundaries, the stress level in the tectonic units, the orientation of fault zones, the direction of relative plate motions, and about the geometry of the subduction-related seismic zones. For literature about the seismicity of the area I refer to a recent paper by Dewey and Suárez [1989]. They concisely review the seismicity in the entire Caribbean region, and extensively refer to previous investigations. With regard to the morphology of subduction zones, it is important to realize that the seismic zones - or Wadati-Benioff zones - only outline the seismogenic parts of the subducting slabs [Wortel, 1982]. Because the depths of earthquake hypocenters in the Caribbean region are restricted to the upper 250 km of the mantle, information about the morphology of, e.g., the subducted Farallon Plate can not be obtained from analyses of seismicity. In contrast to analyses of seismicity, seismic tomography provides us with a powerful tool to investigate aseismic parts of subducted slabs. Grand [1987], Spakman et al. [1988], and Zhou and Clayton [1988], presented images of slabs extending well below the seismic active parts of the subduction zones below North and Middle America, the Aegean region, and the northwestern Pacific.

With regard to the shallow mantle structures, the comparison between tomographic images and the detailed information about the seismogenic parts of subduction inferred from analyses of seismicity helps to interpret the tomographic images and provides additional estimates of the reliability of the images. In this chapter, I compare the geometry of the subduction-related seismic zones below Middle America and below the Greater and Lesser Antilles with the subduction zone morphology obtained from the tomographic inversion of  $P$ ,  $PP$ , and  $pP$  delay times. In a brief discussion about the tectonics of northwestern South America, I focus on the underplating of the southern part of the Caribbean Plate below the Maracaibo block and Venezuela [Kellogg and Bonini, 1982].

## 6.2 The Middle America subduction zone

Of importance for the tectonics of Central America is the subduction of the Farallon Plate from Middle Cretaceous (120 Ma) to Miocene (25 Ma) and, since the break-up of the

Farallon Plate in the Miocene, the subduction of the Cocos Plate. In the following sections, I first discuss the shallow structures in the mantle that can be associated with the subduction of the Cocos Plate. Subsequently, I address the deeper mantle structure in relation to the pre-Miocene subduction of the Farallon Plate.

### 6.2.1 Subduction of the Cocos Plate: a brief review of its complexity

Several phenomena cause the process of subduction of the Cocos Plate at the Middle America trench to be very complex. Firstly, subduction occurs below two different overriding plates, separated by an instable triple point. The relative motion between the North American Plate and Cocos Plate [e.g., Minster and Jordan, 1978] results in the overriding of the subduction zone north of the North America - Cocos - Caribbean triple point. Southward of this triple point, the Cocos Plate subducts beneath the slightly eastward moving Caribbean Plate [Minster and Jordan, 1978]. See Burbach et al., [1984], Ross and Scotese [1988], and Guzmán-Speziale et al. [1989] for further references about the plate tectonics of the region. The differences in constitution and motions, relative to the Cocos Plate, of the overriding plates may result in changes in the style of subduction (slab dip, coupling, amount of subducted sediments, seismicity) [e.g., Uyeda, 1982]. Secondly, due to the specific geometry of the Cocos Plate and the vicinity of the Pacific and Galapagos spreading systems, the age of oceanic lithosphere subduction below Middle America shows large variations along the Middle America trench. Differences in age of subducted lithosphere strongly influence the process of subduction and associated seismicity [Vlaar, 1975; Vlaar and Wortel, 1976; Wortel and Vlaar, 1988; Dewey and Suárez, 1989]. The collision of the East Pacific Rise with the North American Plate, and the incipient spreading at the Galapagos rift system in Early Miocene times, caused many plate reorganizations [e.g., Wortel and Cloetingh, 1981]. Thirdly, the subduction of bathymetric features at the Middle America trench, as the Cocos Ridge, the Tehuantepec Ridge, and the Orozco and Rivera Fracture Zones, influences the subduction process and the seismicity [e.g., Molnar and Sykes, 1969; Burbach et al., 1984; LeFevre and McNally, 1985; Wolters, 1986; Adamek et al, 1987].

The combination of these phenomena determines the morphology of the shallow part of the Middle America subduction zone. The study of the morphology of the subduction may shed light on the interaction and time relationships between the tectonic processes.

### 6.2.2 The shallow mantle structure: results of other investigations

It is generally acknowledged that the Middle America subduction zone consists of several segments. The degree of segmentation is, however, rather controversial amongst investigators and depends on the type of data used to investigate possible lateral discontinuities. A high level of segmentation of the Cocos Plate, subducted below Middle America, was proposed by Stoiber and Carr [1973]. These investigators recognized offsets in the volcanic chains and distinguished at least 12 segments in Middle America. Burbach et al. [1984], and Burbach and Frohlich [1986], argued that the relationship between the location of the active volcanic arc and the geometry of the subducting plate may be too

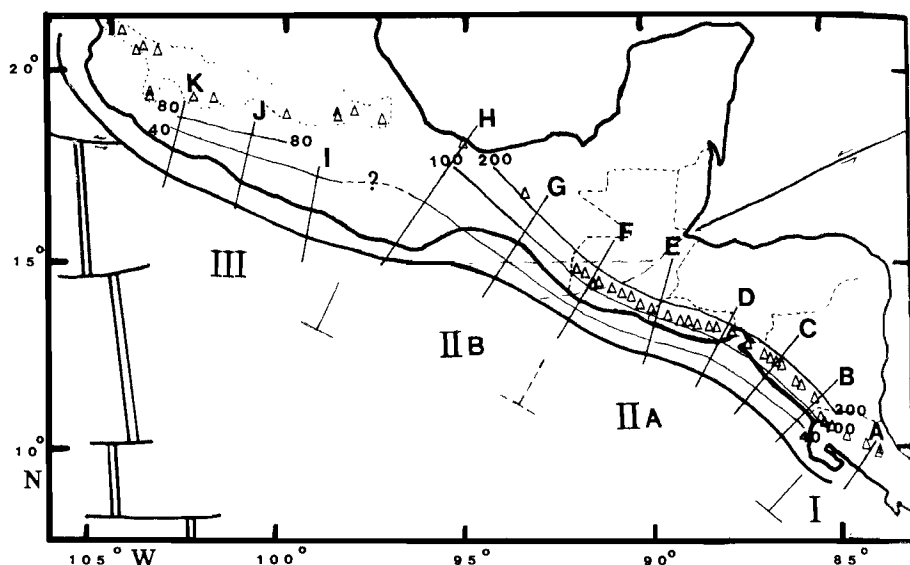


Figure 6.1. Segmentation, of the subducted Cocos Plate, based on seismicity. After Burbach et al. [1984].

complex to justify the segmentation proposed by Stoiber and Carr. Instead, they suggested a subdivision of the subducted part of the Cocos Plate into three segments, based on the distribution of mainly tele-seismically recorded earthquakes. The segmentation by Burbach et al. [1984] is presented in Figure 6.1. The first segment of the Cocos Plate, below Panama, and limited in the northwest near the Nicoya Peninsula, is characterized by the absence of a clear seismic zone below 70 km depth. This is interpreted as being indicative of ceased subduction due to presence of the buoyant Cocos Ridge [Burbach et al., 1984; Adamek et al, 1987]. Segment II of Burbach et al. [1984] extends from the Nicoya Peninsula (NP) to Orizaba (in Mexico), north of the intersection of the Middle America trench and the Tehuantepec Ridge (TeR) (Figure 6.1), and is marked by a well developed Wadati-Benioff zone down to 200-240 km depth. A possible boundary (separating segment IIa and IIb) is suggested by Burbach et al. [1984] below Guatemala (BB2, Figure 6.1). The northwestern limit of the poorly defined third seismic segment is formed by the intersection of the Middle America trench and the Rivera Fracture Zone (RFZ, Figure 6.2). Burbach et al. [1984] suggest that the transition from segment I to segment II is perhaps a tear in the subducted Cocos Plate, which may be induced by the subduction of the buoyant Cocos Ridge. No evidence is reported by Burbach et al. [1984] and Burbach and Frohlich [1986] for major tears associated with the subduction of the Tehuantepec Ridge and the Orozco and Rivera fracture zones. The subduction of these bathymetric features may, however, influence the dip of the subduction zone. Resolution in hypocenters of tele-seismically recorded events does not allow smaller-scale segmentation [Burbach et al., 1984]. Analyses of local network data provide high resolution images of

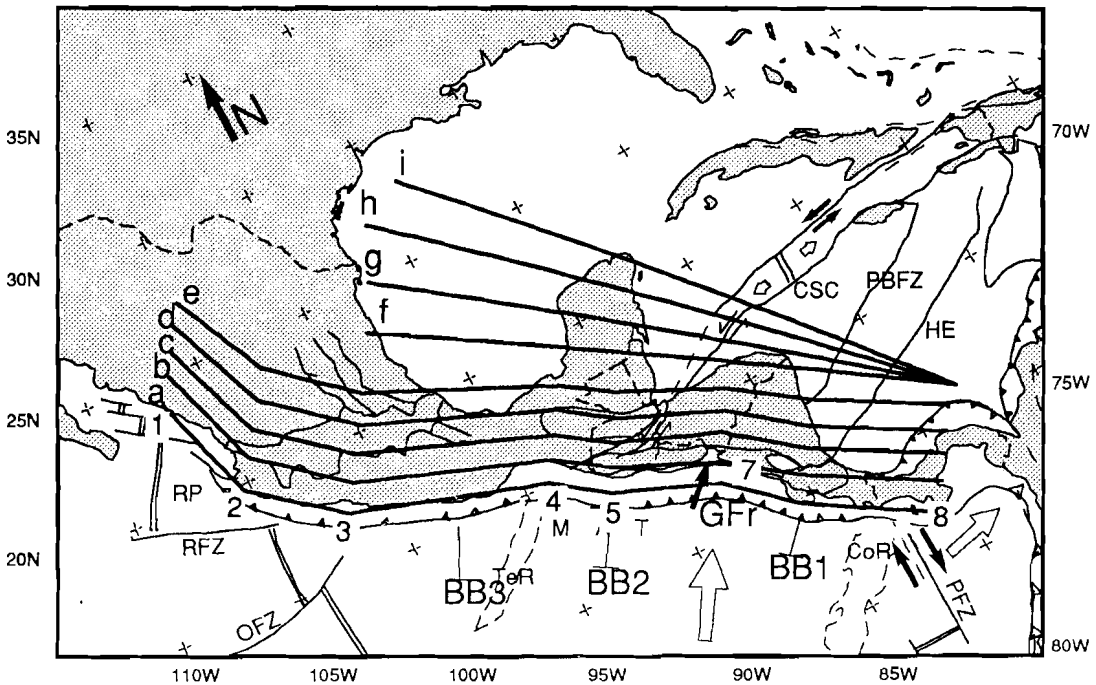


Figure 6.2. Geographic map of the Middle America region. BB 1, BB 2 and BB 3 are the boundaries of seismicity segment of the subducted Cocos Plate distinguished by Burbach et al. [1984]. A to I mark the lines of section discussed in the text and presented in Figure 6.3. RFZ Rivera fracture zone, RP Rivera Plate, TeR Tehuantepec ridge. For the remaining abbreviations see Figure 4.1 and Table 4.1.

Wadati-Benioff zones: these are important for the detailed investigation of the segment boundaries [e.g., Protti and McNally, 1989; Güendel and McNally, 1989]. In the remainder of this chapter, I refer to the segments defined by Burbach et al. [1984] with BB-I, BB-IIa, BB-IIb, and BB-III (Figure 6.1). Also from seismicity analysis, Wolters [1986] defined three or four segments in the subducting Cocos Plate, which are in general agreement with the segmentation of Burbach et al. [1984]. The division of the subducted Cocos Plate into three major segments is confirmed by the examination of magnetic anomalies derived from Magsat data [Counil and Achache, 1987]. Counil and Achache conclude that gaps in the magnetized layer of a subducted slab can be consistently associated with lateral discontinuities in the dip of the seismic zone, although the exact locations may be offset by some 150 km. As physical mechanisms for the magnetic gaps Counil and Achache [1987] propose either a locally increased temperature or a strain related demagnetization.

### 6.2.3 The shallow mantle structure: results of tomographic inversions

Both the high seismicity (analyzed by, e.g., Burbach et al. [1984] to delineate subduction zone segments) and the probable presence of upper-mantle temperature perturbations

related to the subduction of lithosphere are important ingredients for a successful tomographic survey. I present results of the tomographic inversions by means of vertical cross sections, both parallel and perpendicular to the Middle America trench.

The lines of intersection of the section planes and the earth's surface are given in Figure 6.2 (for the parallel sections) and 6.4 (for the perpendicular sections) with heavy solid lines. In all cross sections, the black dots mark the hypocenters of earthquakes used in the tomographic investigation. The hypocenters are plotted at locations which are computed from the original ISC locations by a relocation procedure during the tomographic inversion.

The sections 6.3[a-e] are discussed simultaneously from northwest to southeast. I only discuss the most relevant velocity structures. In Figures 6.3[a-i], mantle cross sections are shown to a depth of 937 km. In this text section, I focus on the upper 300 km of the cross sections because at these depths structures should be directly comparable to the inferences made from seismicity investigations [e.g., Burbach et al., 1984]. In section 6.2.4, I discuss the morphology of the Middle America subduction zone in the mantle below the seismic zones.

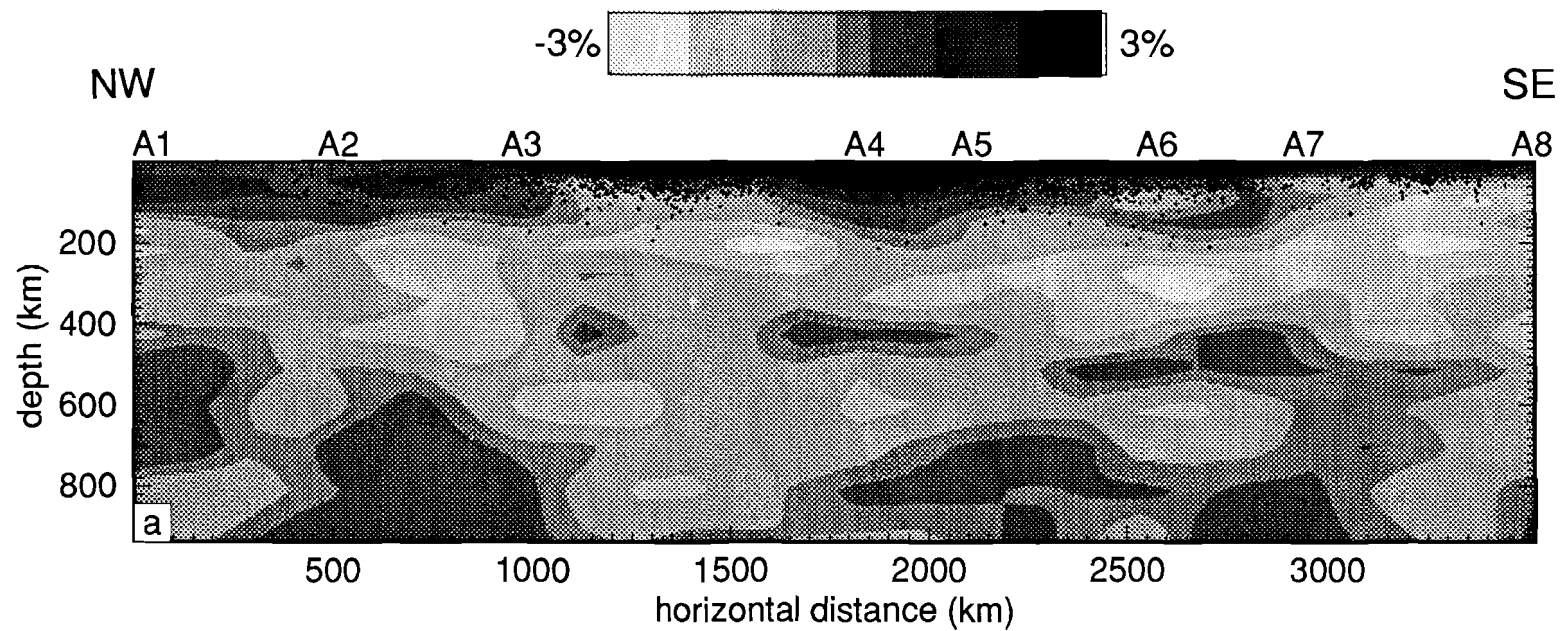
Estimates of resolution of Earth structure in terms of harmonic and spike responses and the harmonic fit (sections 5.2.3, 5.2.4 and 5.2.5) can be obtained from Figure 5.4c,d and 5.4e. In general, the resolution of mantle structures is rather good in the elongated region along the Middle America trench, but drops rapidly with increasing lateral distance both to the northeast and to the southwest.

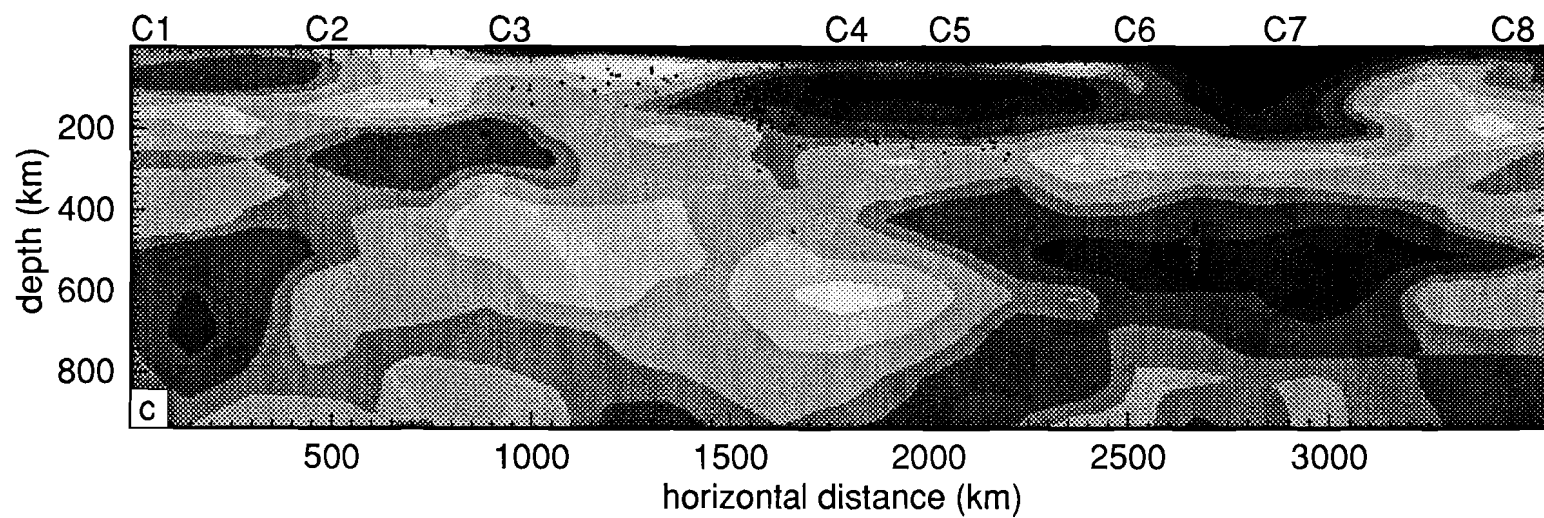
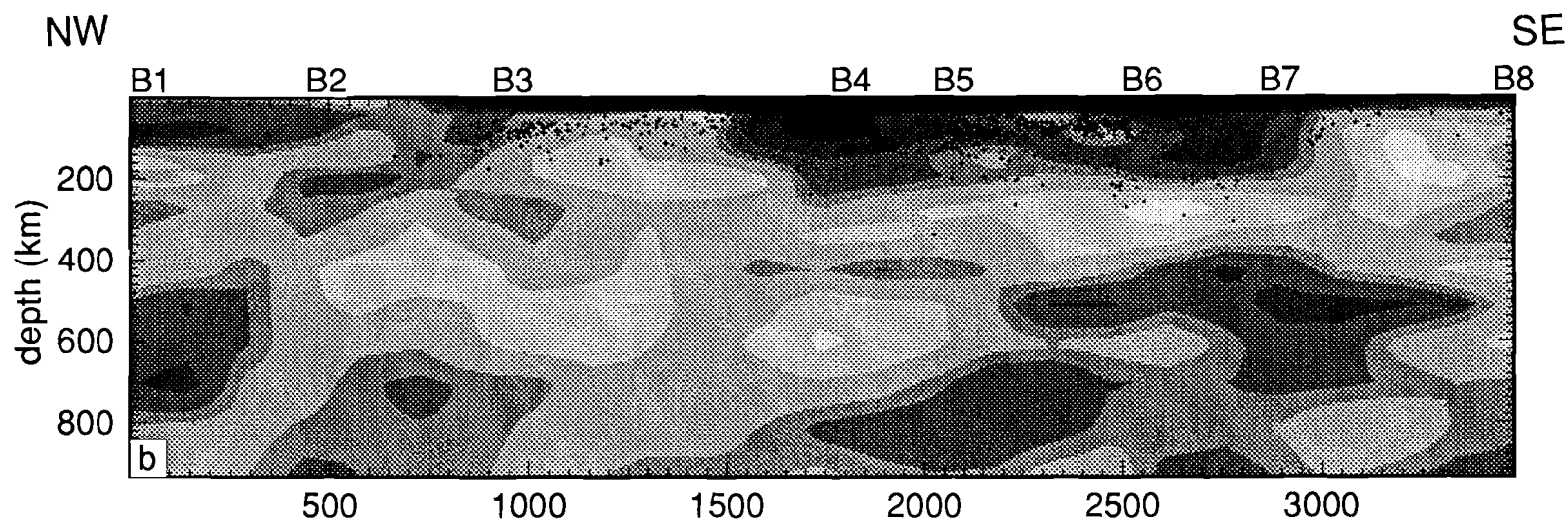
Two additional remarks should be made about the presentation of the cross sections. The horizontal distances given below the x-axes of the plots should formally be given in degrees. The figures in kilometers actually represent the distance along-strike at the earth's surface. Secondly, one should be careful to directly infer the dip of given velocity features from the vertical cross sections parallel to the MAT. The strikes of cross sections are lined up along the trench, but are not necessarily parallel to the strike of the subduction zone [Burbach et al., 1984]. Consequently, the apparent, and not the true, dips are visible in the vertical cross sections.

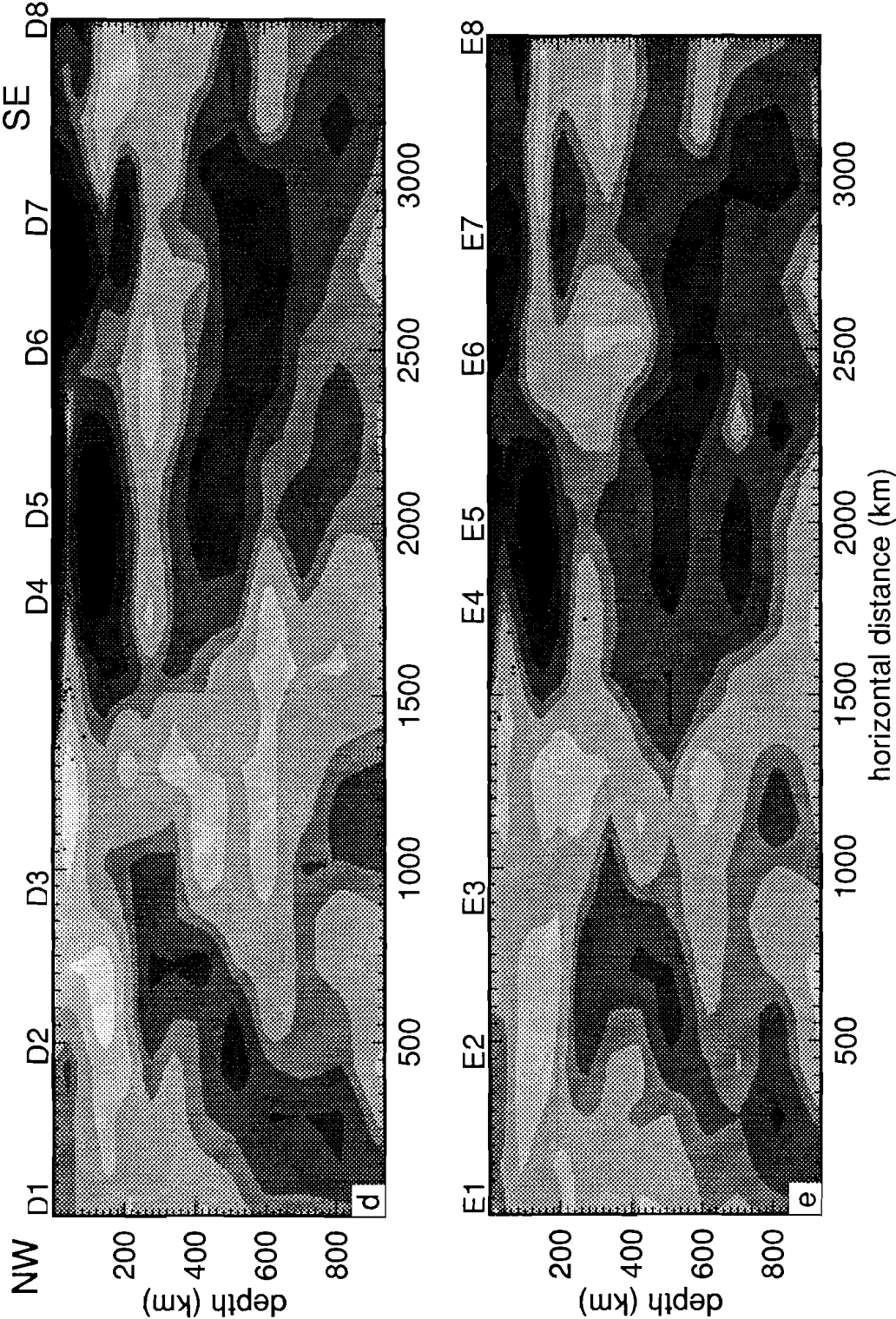
#### *Mantle cross sections parallel to the Middle America trench*

In Figure 6.2, the lines of section are given of the cross sections parallel to the Middle America Trench (MAT). The cross sections are shown in Figure 6.3[a-i]. In the upper-mantle velocity structure above 200 km, a sharp velocity contrast is visible in section 6.5a, below A3. High velocities extend downward to about 150 km northwest of A3, whereas to the southeast a transition occurs to lower velocities between depths of 100 to 150 km. Also in sections 6.5b,c,d and 6.5e, a transition is discernible from high velocities, to the northwest, to low velocities, to the southeast of section point 3. With increasing distance to the MAT, the depth, at which this lateral variation occurs, increases to about 400 km in section 6.3e (below E3). In section 6.3a, the location of this lateral velocity contrast coincides with the intersection of the Orozco Fracture Zone (OFZ) and the MAT (Figure 6.2). In section 6.3b (just southeast of B2), and, in particular, in sections 6.3c and 6.3d (between section points C2 and C3, and D2 and D4), velocities up to 3% lower than the

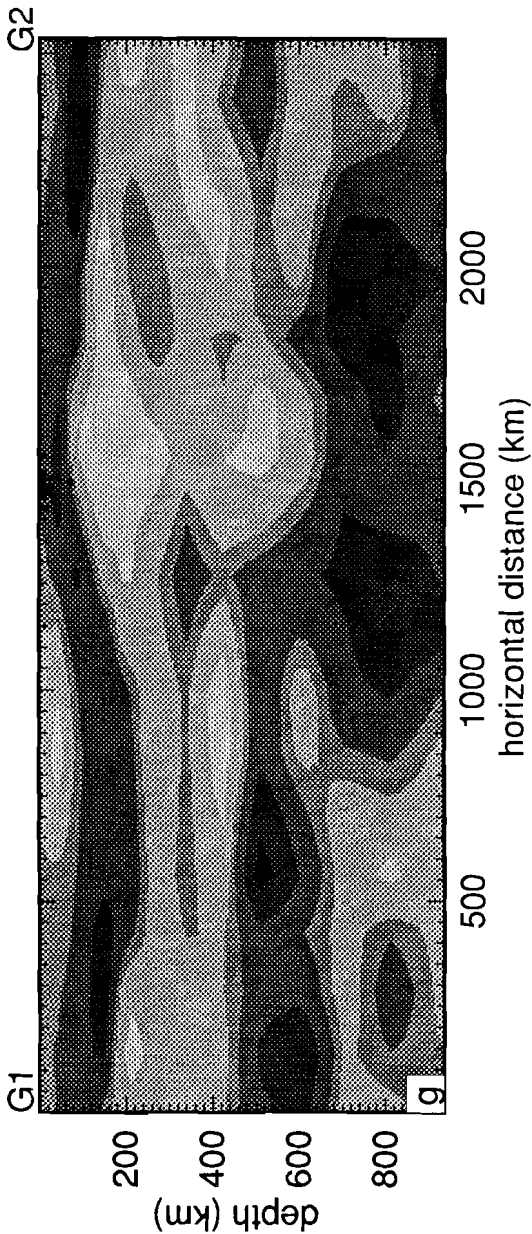
Figure 6.3. Vertical mantle cross sections down to approximately 950 km depth along section lines a, b, c, d, e, f, g, h, and i depicted in Figure 6.2. The sections are discussed in section 6.2.3.

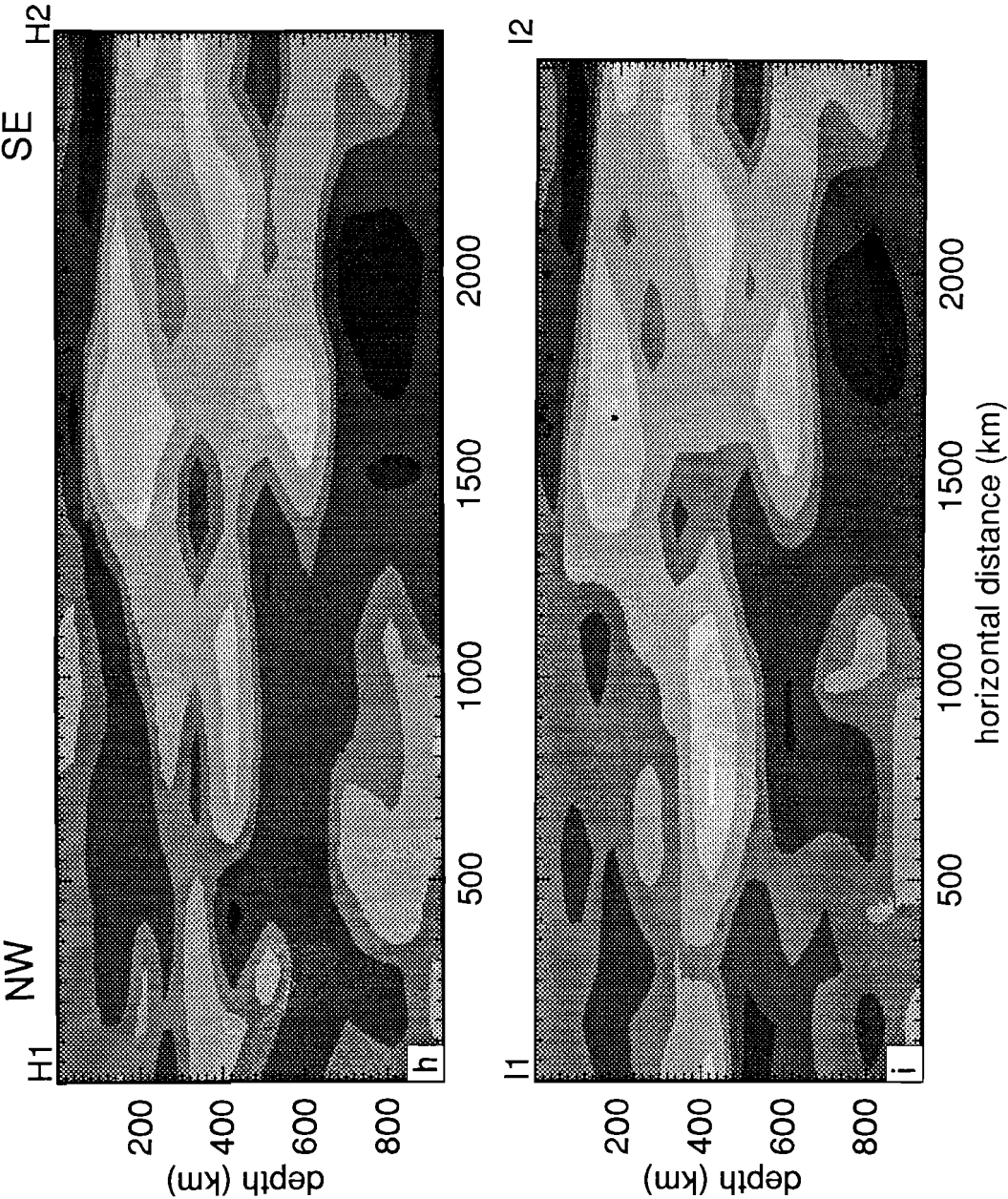










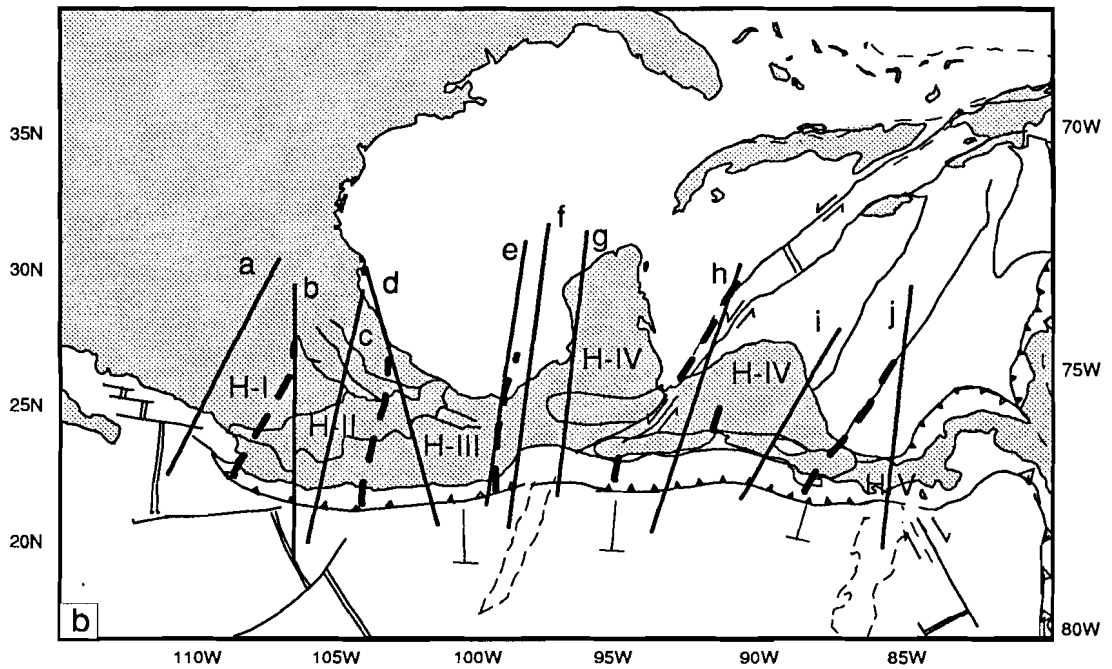
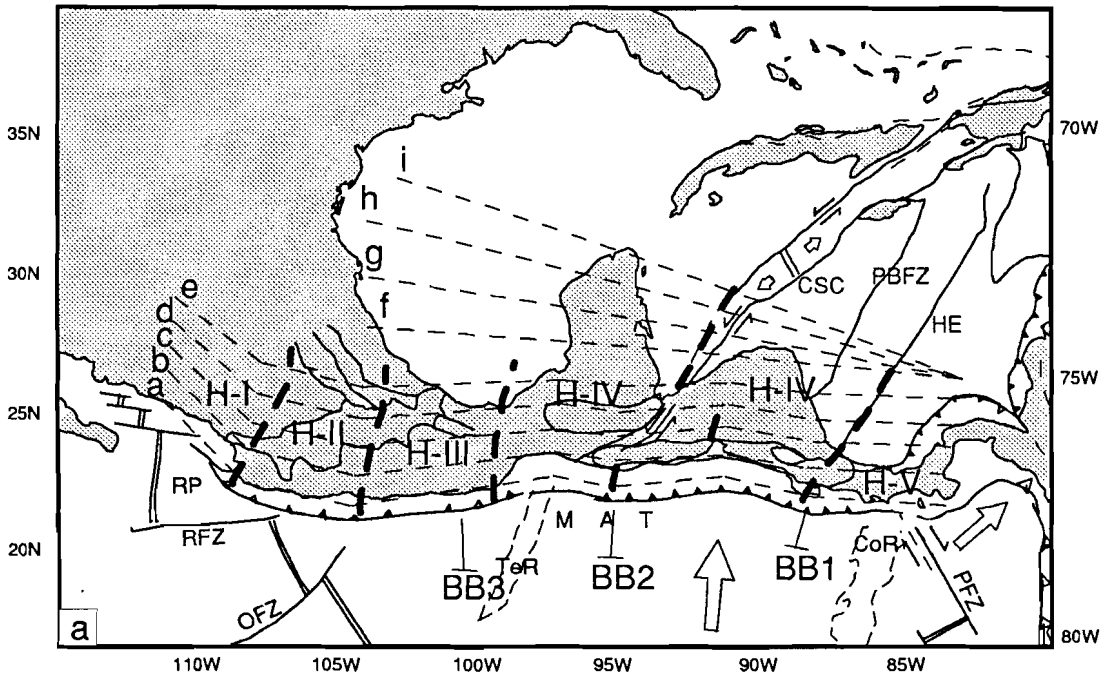


reference velocities are visible below the Trans Mexican Volcanic Belt (TMVB). In all cross sections of Figure 6.3, the mantle region southeast of the TMVB, between point 3 and halfway between 3 and 4, is characterized by high velocities at shallow depth, and low velocities down to 200 km. This situation changes dramatically between section points 3 and 4, where to the south east the depth extent of the shallow high velocities increases rapidly, and even more with increasing distance from the MAT (hence, from section 6.3a to 6.3e). In sections 6.3b, 6.3c, and 6.3d, this lateral contrast in  $P$  velocities coincides with the increased depth of seismicity. Burbach et al., [1984] used this spatial variation in seismicity to define the boundary between their seismicity segments III and IIb (Figure 6.1). Close to the MAT, the contrast in seismicity is not discernible (Figure 6.3a). With increasing horizontal distance to the MAT, the boundary is visible at greater depths. In section 6.3d and 6.3e, the low velocities northwest of the boundary are separated from the high velocities to the southeast at depths of 400-700 km. The division of the subducted Cocos Plate in small segments as proposed by Stoiber and Carr [1973] cannot be verified in detail by these tomographic images, because, the cell size used to discretize the mantle volume under study does not allow a description of features on such a small scale.

Southeast of the lateral variations in the imaged  $P$  velocities and the seismicity between section points 3 and 4 (Figures 6.3[a-c]), the first significant lateral contrast in the  $P$  velocity structure occurs near point A7 (Figure 6.3a), in the vicinity of the Nicoya Peninsula (NP in Figure 6.2). Thus, from the velocity structure no evidence can be obtained for the interaction between the MAT and the Tehuantepec Ridge, which occurs near section point 4 in Figure 6.3[b-e]. Between the previously described segment boundary below the Isthmus of Tehuantepec and the lateral velocity contrast near the Nicoya Peninsula, high velocities prevail down to 180 km (section 6.3a) and 240 km (section 6.3e). I remark that the deep earthquakes ( $> 200$  km) below southern Middle America are probably mislocated [personal communication, M. Protti, UCSC, 1989; and J. Dewey, USGS, 1990]. The southeastern terminus of this segment migrates from just northwest of point 7 in section 6.3a to halfway point 7 and 8 in sections 6.3d,e. The trace at the Earth's surface of this sharp lateral velocity contrast is marked in Figure 6.4. This contrast in  $P$  velocity structure coincides with the boundary between seismic segment BB-I and BB-IIa.

Within this segment, the high velocities are restricted to shallower depths between section points A5 and A6 in Figure 6.3a. Between B5 and B6 in Figure 6.3b the decreased vertical distance to the shallow low velocities is also visible. With distance from the trench the image of this "low velocity gap" shifts towards the southeast.

*Figure 6.4.* (a) Locations of segment boundaries distinguished after analysis of the mantle cross sections parallel to the MAT (heavy dashed lines). Heavy solid line mark the locations of mantle cross sections approximately perpendicular to the MAT, that are displayed in Figure 6.5. (b) Boundaries and segments as distinguished by Burbach et al [1984] and as inferred from this study.



As a consequence, the lateral extent of the high velocity structure northwest of the boundary coinciding with BB3 (Figure 6.1), increases towards the east. This is also outlined in Figure 6.4. In the sections A and B the northwestern terminus of this "low velocity gap" coincides very well with boundary between segments II-A and II-B, defined by Burbach et al. [1984]. However, this segment boundary inferred from the tomographic images is not as persistent with increasing horizontal distances from the trench as the boundary BB2 between BB-IIb and BB-III. Instead, at larger distances to the MAT, the trace of the feature observed in the tomographic sections matches very well with the boundary between the El Salvador and Nicaragua volcanic segments distinguished by Stoiber and Carr [1973]. In sections 6.3a and 6.3b (below point 5) the images suggest that the segment boundary influences the aspherical structures at much larger depths (500 km). At even larger horizontal distances to the MAT, the suggested boundary strikes parallel to the northern plate boundary zone.

Southeast of the Nicoya Peninsula (seismicity segment BB-I), the upper-mantle *P* velocity structure is characterized by a shallow high-velocity layer (upper 33 km), below which low velocities prevail. In sections B and C, the velocities in this depth range are up to 3% lower than the reference velocities for that depth interval. The location of these low velocities mark the site where the Cocos Ridge collides with the MAT.

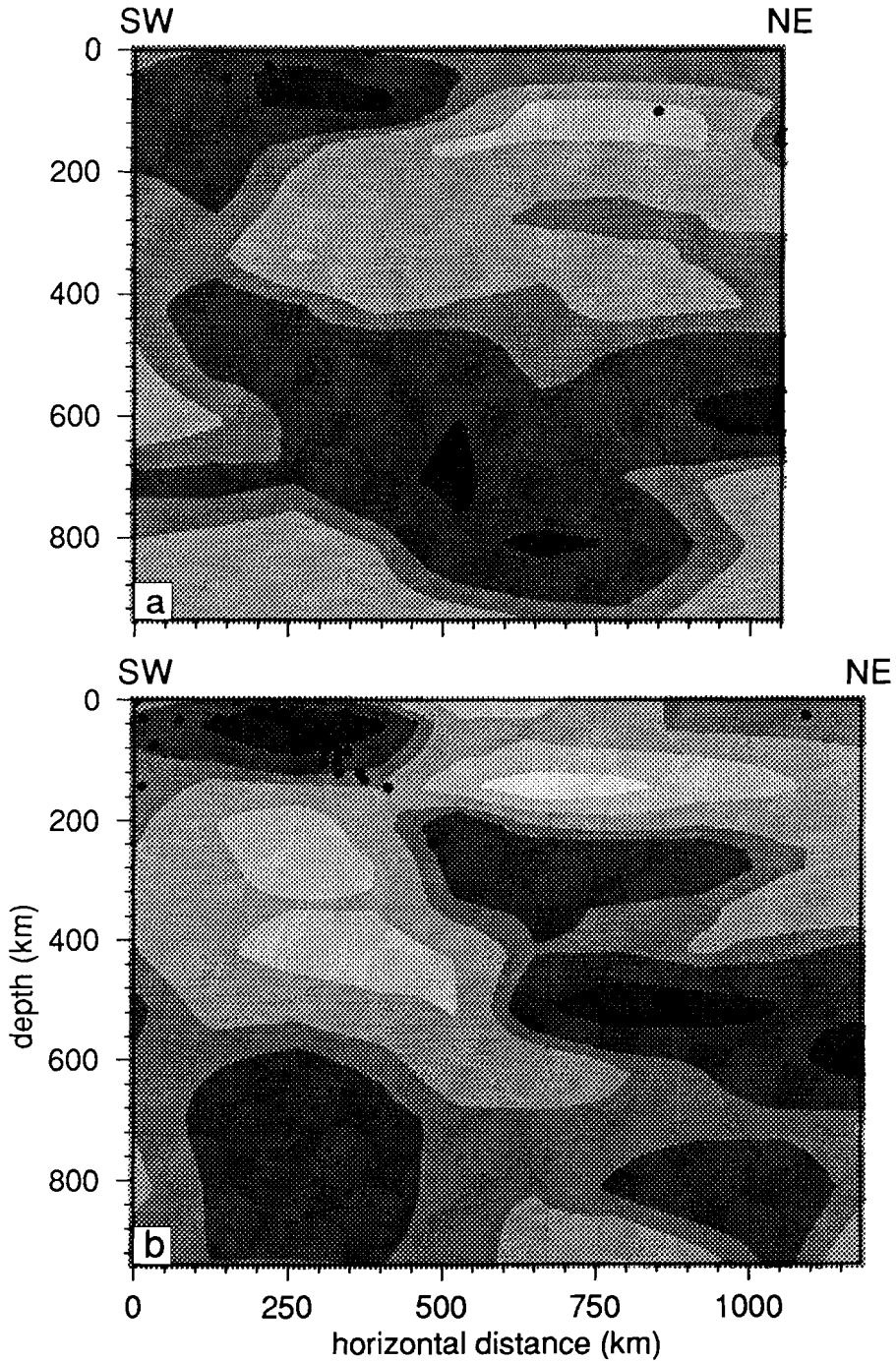
Further east, in the mantle sections 6.3[f-i], no shallow-depth features can be observed that can be directly correlated to the subduction of the Cocos Plate below Middle America. An exception may be the lens-shaped high velocity feature at 250 km depth and near 2000 km horizontal distance in section F (see also the cross section of Figure 6.5j). In the upper 300 km of sections 6.3[f-i], the lateral transition can be observed of the Caribbean Plate to the North American Plate below the Gulf of Mexico.] In sections 6.3f,g, the intersection with the Northern Plate Boundary Zone (NPBZ) is marked by shallow seismicity near 1500 km horizontal distance. North and south of the NPBZ the imaged structures differ considerably. Below the Caribbean Plate, south of the NPBZ, a shallow high velocity layer is visible down to 100 to 130 km. Towards the north, however, these high velocities dip below the Gulf of Mexico, with increasing depths to ca. 200 km just east of Mexico, and to ca. 350 km in the central part of the Gulf of Mexico.

In Figures 6.4a and 6.4b the traces at the Earth's surface are given of the velocity contrasts that are observed in the sections parallel to the MAT. The segments distinguished in Figure 6.4b are hereafter referred to as H-I to H-V.

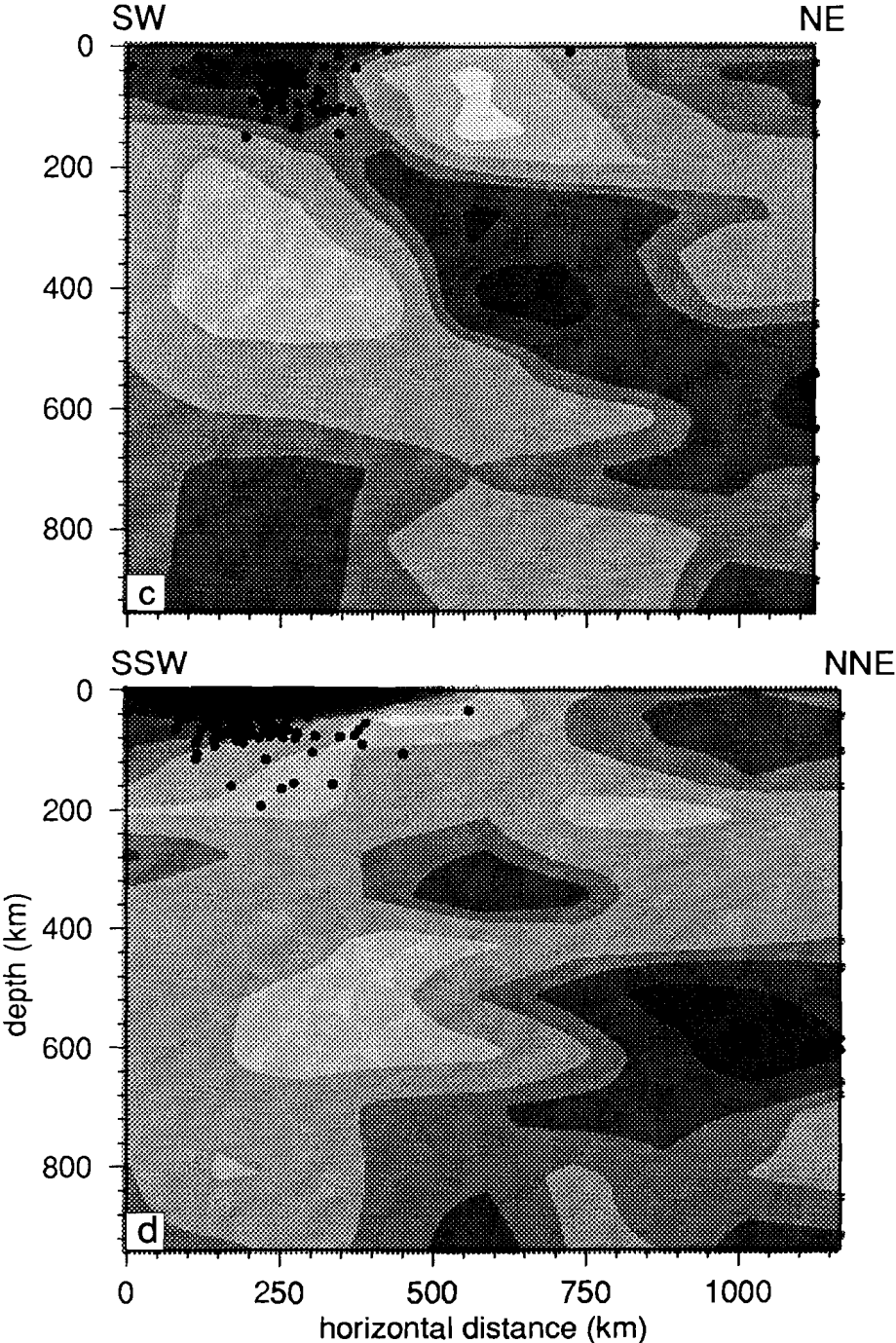
#### *Mantle sections across the Middle America trench*

In Figure 6.5, I present mantle cross-sections computed approximately perpendicular to the MAT, and which are characteristic for the aspherical structure below the distinct segments of the subducted Cocos Plate.

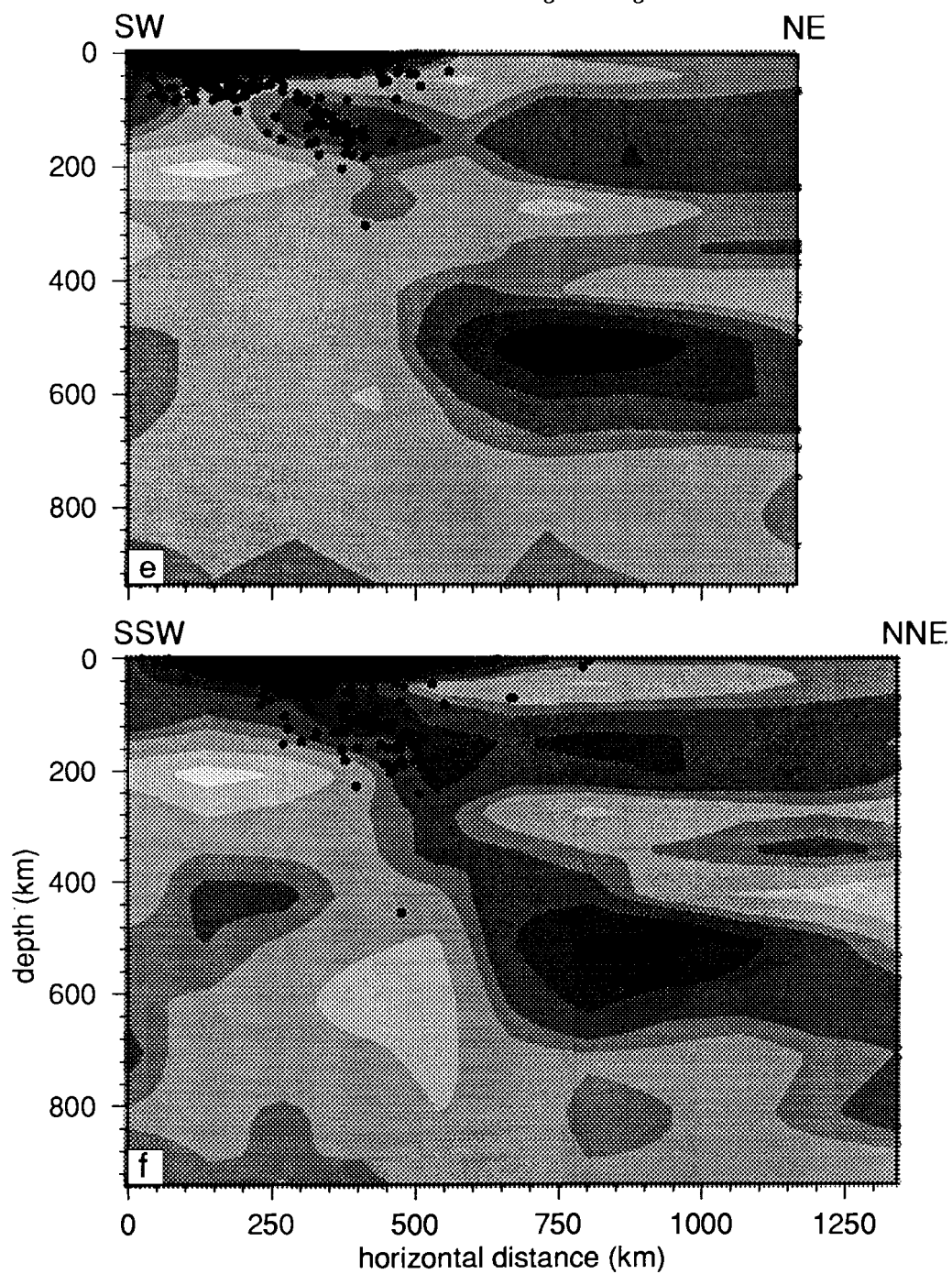
Figure 6.5a shows a cross section through the mantle *P*-velocity structure below segment H-I. In this image, neither a well developed Wadati-Benioff is present, nor does the image of the mantle structure indicate the subduction of oceanic lithosphere attached to the Cocos Plate. The high velocities below 400 km are discussed in text section 6.2.4.



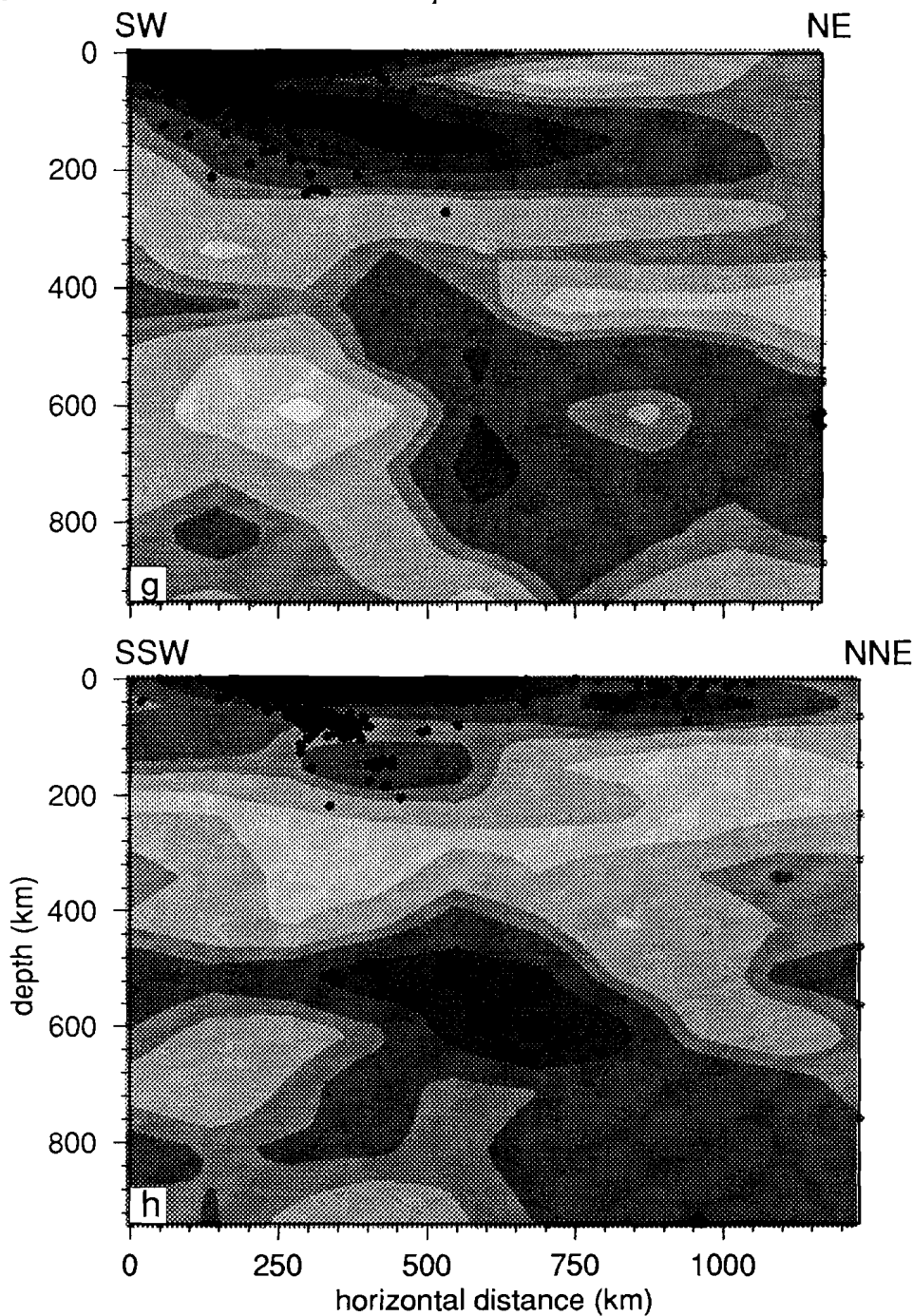
*Figure 6.5.* Mantle cross sections 6.5a to 6.5j approximately perpendicular to the Middle America trench. The locations of the sections are given in Figure 6.4. For discussion see section 6.2.3.

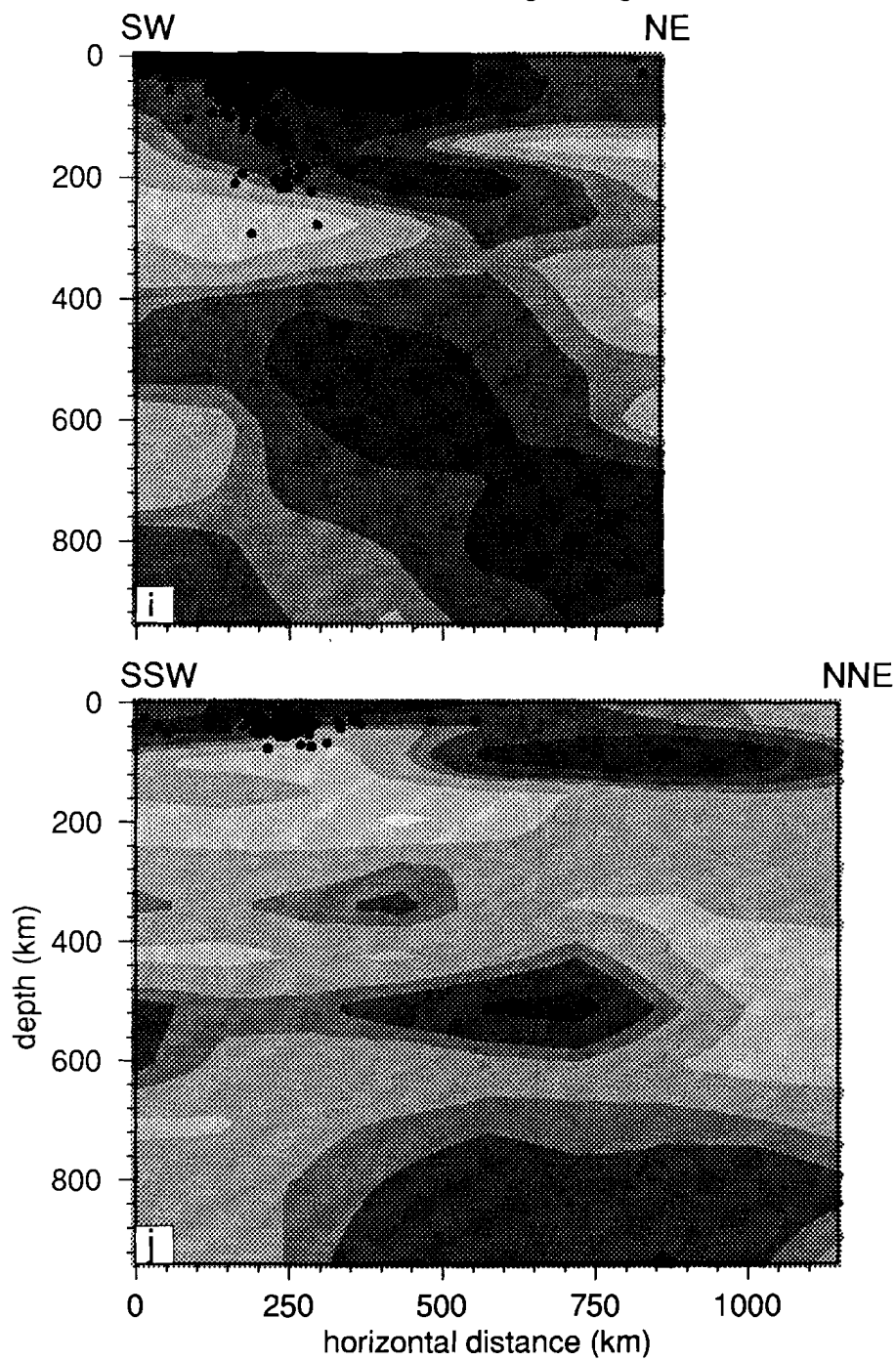












The aspherical structure in the mantle below segment H-II is represented by Figures 6.5b and 6.5c. In both sections a seismic zone is visible. Section 6.5c can be directly compared to section K of Burbach et al. [1984]. This cross section shows a rather continuous structure characterized by anomalously high  $P$  velocities. The anomaly can be continued below the Wadati-Benioff zone. I interpret the structure in section 6.5b as the gradual transition from 6.5a to 6.5c. Both in section 6.5b and in 6.5c, the Trans Mexican Volcanic Belt (TMVB) is marked by pronounced low velocities.

Segment H-III, corresponding to Burbach's BB-III, is characterized by the absence of a well developed Wadati-Benioff zone, and the absence of a "slab-like" high velocity structure near the seismicity (section 6.5d). This indicates that no down going lithosphere (of the Cocos Plate) is present below this segment. Section 6.5d represents the shallow mantle structure just southeast of the intersection of the Orozco Fracture Zone (OFZ) with the MAT.

Further southeast, across the Isthmus of Tehuantepec, the morphology of the mantle structure, and the relationship between structure and seismicity, changes significantly. This change marks the location of the boundary between segments H-III and H-IV. Both in Figure 6.5e and in 6.5f the seismicity outlines the shallow part of the imaged aspherical structures. Across boundary between H-III and H-IV, the dip of the seismic zone increases and the deep mantle structure becomes apparently continuous with the shallow structure (Figure 6.5f). The interpretation of the velocity structure shown in section 6.5f is difficult because of the ambiguous relationships between the high velocity features near the Wadati-Benioff zone, the structure of the deeper mantle, and the presence of a sub-horizontal structure with high velocities which is associated with the Gulf of Mexico region. A solution of this problem can be obtained from the examination of the spatial resolution in the images.

Examination of the variation of the harmonic fit with depth (Figures 5.4.[4-7]e) reveals that the spatial resolution of structures below the plate boundary zone near the Isthmus of Tehuantepec is good. In contrast, both towards the northeast and towards the southwest the harmonic fit rapidly drops with increasing horizontal distance to this zone, and the structures below the Gulf of Mexico are poorly resolved. From this observation, I conclude that the images of aspherical structure below central Mexico are more reliable than the images of the structure below the Gulf area. In the cross sections 6.5e and 6.5g, which are adjacent to 6.5f, I interpret the structure in the upper 200 km which is characterized by high  $P$  velocities, as the image of subducted lithosphere of the Cocos Plate. Towards the northeast the transition to the high velocities below the Gulf area is not well resolved, and an estimate of the length of the sub-horizontal subduction zone can not be given. In the sections 6.5e and 6.5g, the aspherical structure which is visible at larger depths is clearly separated from the shallow structures. This deeper structure will be discussed further in the text section 6.2.4. Both in the horizontal cross-sections of Figure 5.4.6a, and in the vertical cross-sections of Figure 6.3d, it can be observed that only in a small mantle region the continuation is suggested between the deep structure and the shallow structures. The resolution of such small a detail should be questioned. Similar to the interpretation of the

shallow structures in Figures 6.5e,g, I interpret the structure in the upper 200 or 250 km as the image of the subducted Cocos Plate. The lateral extent of the shallow subduction zone can not be established because of lack of resolution. The vertical distance to the high velocity anomaly below 300 km is apparently smaller in Figure 6.5f than in the images 6.5e,g of adjacent mantle regions, and a possible slab detachment is not resolved.

To the southeast, in sections 6.5h,i the seismic zone still outlines a shallow high-velocity feature. In Figure 6.5i, it is shown that a slab-like high-velocity structure in the shallow mantle below the southeasternmost part of segment H-IV can be continued well beyond the seismic zone. The aseismic part of this velocity structure has a smaller dip than the seismic part of the structure. The image of the aspherical mantle structure below the Lake of Managua (Figure 6.5i) also suggests that shallow part (< 300 km) is detached from the high velocity structure at larger depths (> 400 km).

Figure 6.5j shows the structure which is typical for the mantle below segment H-V (the tomographic equivalent of Burbach's seismicity segment BB-I). The cross section is characterized by the absence of a well developed seismic zone and there are no indications for subduction from the imaged pattern of seismic velocities.

#### 6.2.4 Tomographic images of the deep mantle structure below Middle America

The analyses of seismicity do not indicate aspherical mantle structures deeper than approximately 250 km below Middle America. However, in almost all cross-sections presented in Figures 6.3 and 6.5 anomalously high *P* velocities are imaged below 250 km. These velocities mark an east-to-northeast dipping aseismic structure below Middle America, which can be continued to lower mantle depths. This was also concluded from Figure 2.6 in chapter 2, in which I showed an almost continuous structure between 300 km and the bottom of the model at a depth of over 1300 km. I remark that the spatial resolution in the depth range between 300 and 600 km is poor as compared to the resolution at lower mantle depths. Consequently, the interpretation of structures in the transition zone to the lower mantle are necessarily tentative.

The vertical cross-sections of Figure 6.5 and, in particular, the horizontal sections of the Figures 5.4[5-10]a and the vertical sections of Figure 6.3, show that the structure between 250 and 390 km is laterally very heterogeneous and discontinuous. However, with increasing depth below 390 km the structure becomes laterally more continuous over larger distances, as can be observed in, e.g., Figures 6.3d and f. The Figures 6.3c,d,e show that between 250 and 390 km the aspherical mantle consists of two separated aseismic structures. The structure northwest of the section point 3 in sections 6.3[b-e] has a steep apparent dip to the northwest. Southeast of the boundary between H-III and H-IV, an aseismic structure dips to the southeast with a small apparent dip. The observation that with increasing lateral distance from central Mexico the vertical distance increases between the shallow high-velocity structures (discussed in section 6.2.3) and the aseismic structure in the deeper mantle, is confirmed by the images of Figure 6.5. As mentioned above, the vertical separation between shallow and deep structures is probably not resolved in Figure 6.5f.

With increasing depth and distance to the MAT, the lateral distance between the two structures decreases (Figures 6.3c,d,e) and below the western part of the Caribbean Plate the anomalies merge into a laterally continuous structure (Figures 6.3[f-i]). As I discussed in chapter 4, this structure can be continued into the lower mantle where it is located in the mantle region where also Jordan and Lynn [1974], Lay [1983], Grand [1987] and Vidale and Garcia-Gonzalez [1988] found evidence for anomalously fast body-wave propagation.

#### 6.2.5 Summary and discussion of mantle $P$ -velocity structure below Middle America

A general conclusion concerns the diagnostic value of sensitivity tests to estimate the spatial resolution in tomographic images. In chapter 4 it was concluded that for the upper three layers the spatial resolution was not very good. In particular, the inversion method failed to recover the input spikes at shallow depth levels. In addition, the harmonic fit nowhere exceeds 50% below Middle America (Figure 5.4e). In spite of this apparently disappointing resolution, the results of this tomographic investigation compare very well with other studies and, which is more important, with surface tectonic and geologic features. This is very encouraging. With respect to the assessment of reliability of the tomographic images I remark that in particular the spike sensitivity tests have a limited diagnostic value. Perhaps the recovery of the sign of the input anomalies, in images resulting from the harmonic sensitivity test, may be a sufficient condition to judge the results as reliable.

From the examination of the tomographic images of the anomalous  $P$  velocities in the shallow mantle below Middle America, the Middle America subduction zone can be divided in five distinct segments. This segmentation of the convergent boundary is consistent with independent investigations of volcanic chain offsets [Stoiber and Carr, 1973], geometry of the seismic zones [Burbach et al., 1984; LeFevre and McNally, 1985; Burbach and Frohlich, 1986; Wolters, 1986; Dewey and Suárez, 1989], and of the magnetization of the subducted slab [Counil and Achache, 1987]. However, in most cross sections presented in this chapter, it is evident that the source locations of the earthquakes only outline the upper part of the structures that can be associated with remnants of the subducted Cocos Plate.

The lateral variations in seismic  $P$  velocities at shallow depths reflect the complex processes related to post-Miocene subduction of the Cocos Plate, and except for the boundary between segment H-III and H-IV (or BB-IIb and BB-III) all boundaries can be directly related to large-scale tectonic features: The boundary between H-I and H-II coincides with the northwestern terminus of the MAT; the transition from H-II to H-III occurs near the intersection of the Orozco fracture zone with the Middle America trench; the trace of the boundary between H-IV and H-V is remarkably coincident with the surface expression of the Hess Escarpment (HE in Figure 6.2). The transition between H-III and H-IV (and BB-III and BB-IIb) is more difficult to be correlated to tectonic features. The boundary occurs just north of the intersection of the Tehuantepec Ridge and the trench. Its location at the Middle America trench coincides with the site of the incipient motions along the Polochic fault zone in the Pliocene [Burkart, 1983]. This suggests that the boundary

between H-III and H-IV marks the transition between subduction north of the North America-Cocos-Caribbean triple junction to subduction below the southern part of Middle America south of the triple point. Guzmán Speziale et al. [1989] report marked differences in tectonic features on either side of the Isthmus of Tehuantepec, which would not be consistent with structure which is only restricted to the subducted plate. I postulate that the lateral structures within segment H-IV that I described in text section 6.2.2 result from the post-Miocene left-lateral motion along the Polochic-Motagua fault zone of the Chortis block relative to central Mexico and Yucatan.

The arrival at the Middle America trench of young oceanic lithosphere of the Cocos Plate near the East Pacific Rise and near the Galapagos spreading centre probably caused the cessation of subduction below northern Mexico and below Panama respectively [Wortel and Cloetingh, 1981]. Indeed, the segments H-I and H-V, which I distinguished in the present study, are characterized by the absence of velocity variations that are indicative of down going subduction at shallow depths. With respect to the latter segment, I remark that the shallow mantle below the site where the bathymetric Cocos Ridge collides with the MAT is marked by low velocities. In sections 5.4.2 and 5.4.3 I showed that also low velocities prevail in the shallow mantle below the site of collision of the Carnegie Ridge with the Colombia trench near Ecuador (sections 5.4.2 and 5.4.3 [also Wolters, 1986]). In surface wave investigations the Cocos Ridge also emerges as a pronounced low velocity feature [M. Woods, personal communication, 1987].

With regard to the structure below 250 km, I conclude that the aseismic structure described in 6.2.4 is the image of the Farallon Plate subducted below Middle America. Consistent with the discovery of Jordan and Lynn [1974], the tomographic images presented here indicate the presence of anomalous *P* velocities in the lower mantle below the Middle America subduction zone. The cross sections show that the upper-mantle velocity anomalies, imaged below 250 km, are continuous with the lower mantle anomalies. I stress that the continuity of imaged velocities does not necessarily mean that also the physical structure is continuous into the lower mantle. Moreover, the spatial resolution in the transition zone between the upper mantle discontinuities does not allow such a conclusion based on tomographic results only. However, I argue that in the past geologic history of this region several thousands of kilometers of (old) oceanic lithosphere of the Farallon Plate were consumed at the pre-Miocene Middle America trench. I tentatively assume that in the past history of the Caribbean region not enough space has been available in the upper mantle region between the Middle America and the Lesser and Greater Antilles subduction zones for the accumulation of the amount of lithosphere subducted below Middle America. By these arguments and with the given tomographic images, the disappearance of remnants of the subducted Farallon Plate into the lower mantle is more likely than a restriction of the subduction process to the upper mantle, unless complex interactions with the Antilles subduction zones are taken into account.

The relationship between the shallow structure of the subducted Cocos Plate and the deeper structure can be explained tentatively by Neogene relative plate motions between the southern and northern part of Middle America and by the break-up of the Farallon Plate

in the Miocene. In Early-Neogene times ( $\approx 35$  Ma) large parts of present-day central Mexico had been devoid of the effects of subduction of the Farallon Plate because of the Mesozoic and Paleogene position of the Chortis block (chapter 4). Since the Late Eocene - Early Oligocene, the left lateral motion continued of the Chortis block relative to present-day central Mexico and Yucatan. This process caused an increasing length of the MAT along the present-day Isthmus of Tehuantepec to be exposed to subduction of increasingly younger lithosphere of the Farallon Plate. After the break-up of the Farallon Plate into the Cocos and Nazca Plates in the Early Miocene (20-25 Ma) [Wortel and Cloetingh, 1981], the relatively young lithosphere of the Cocos Plate subducted below Middle America. In northern Mexico (the northern terminus of the MAT) and near Panama, the cessation of down going subduction due to the collision with very young oceanic lithosphere, may have triggered a detachment between the locally buoyant Cocos Plate and the subducted Farallon Plate. With progressing time, the zone of detachment may have migrated towards more central parts of the MAT [R. Wortel, personal communication, 1990]. This hypothetical scenario can explain the absence of remnants of the Farallon Plate in the upper 400 km below the Isthmus of Tehuantepec and the varying vertical distances between the shallow mantle structure associated with the subduction of the Cocos Plate and the deeper anomalies related to the Farallon Plate. Both the resolvability of possible slab detachments and details of the suggested tectonic processes are subjects of future research. Similar to the method described by Spakman et al. [1989], I suggest to investigate the resolvability of slab detachments by the use of realistic synthetic velocity models as input of sensitivity tests. These input models should then simulate a detached subduction zone.

### 6.3 Subduction of Atlantic lithosphere below the Greater and Lesser Antilles

#### 6.3.1 Seismotectonic setting: other investigations

Several plate-kinematical parameters and tectonophysical phenomena related to the process of subduction of the oceanic lithosphere of the Atlantic Plates below the eastern Caribbean are fundamentally different from the subduction of the Cocos Plate below the western Caribbean.

In a previous section, 6.2.1, I discussed the complexities of tectonics of the Middle America region. These are summarized here. The Cocos Plate subducts below two different overriding plates. The relative velocities between the plates involved are relatively high ( $O(6 \text{ cm/yr})$ ). The age of the lithospheric plate that presently subducts at the Middle America trench varies laterally, but is generally low. The combination of this high convergence rate and the rather young lithosphere cause the subduction to be strongly *coupled*. Subduction of buoyant bathymetric features (e.g., the Cocos Ridge) influences the subduction process. Because of the interaction of active spreading systems with the Middle America trench subduction ceased in northern Mexico and near Panama, and many plate reorganizations occurred since the Miocene (see section 6.2 for references and more details).

In the east, the Caribbean Plate overrides the Atlantic lithosphere which is probably divided in the North American and the South American Plates. Hereafter, the North

American Plate and the South American Plate are referred to as the Atlantic Plates. The location of the boundary between the two subducted plates is unclear [Jordan, 1975; Minster and Jordan, 1978; Stein et al., 1982; Sykes et al., 1982; Roest, 1987; Stein et al., 1988; Harper, 1990]. Compared to the subduction below Middle America, a more important difference is the high age of the lithosphere subducted at the Lesser Antilles trench ( $O(80 - 100\text{ Ma})$ ), and the low rate of convergence between the Caribbean Plate and the Atlantic Plates ( $< 2\text{ cm/yr}$ ). Along the strike of the Lesser Antilles Trench (LAT) the variation of lithospheric age of the Atlantic Plate is small [e.g. Molnar and Sykes, 1969; Minster and Jordan, 1978; Stein et al., 1982; Sykes et al., 1982; McCann and Sykes, 1984]. These factors cause the subduction in the Antilles region to be primarily *decoupled*, and a substantial part of slip to occur aseismically [Ruff and Kanamori, 1980]. This decoupling may be enhanced by the subduction of thick sedimentary wedges in the southern part of the LAT, and counteracted by the attempted subduction of (aseismic) bathymetric features on the Atlantic Plates [McCann and Sykes, 1984]. The presence or the absence of bathymetric features influence the subduction process in, and the seismic potential of, the eastern Caribbean [Stein et al., 1982; McCann and Sykes, 1984]. The nature of the subduction of the bathymetric structures on the Atlantic Plate, e.g., whether or not the Baracuda ridge is buoyant, and the effects on seismicity is still debated [Stein et al., 1986; McCann and Sykes, 1986]. Although a substantial amount of slip in subduction zones occurs aseismically, sharply defined Wadati-Benioff zones are reported, particularly below the northeasternmost Caribbean [Stein et al., 1982; McCann and Sykes, 1984]. Consequently, the geometry of the down-going seismogenic zone is fairly well known below the northern Lesser Antilles, and below the eastern Greater Antilles [e.g., figure 3 of Stein et al., 1982; figures 7-9 of McCann and Sykes, 1984]. From south to north a shoaling of the seismic zone is can be inferred from the cited figures. Proceeding towards the southern Lesser Antilles, the seismicity changes considerably [Tomblin, 1975; Dorel, 1981]. The deepest seismicity occurs in the central part of the Lesser Antilles arc (near  $15^\circ\text{N}$ ) [Dorel, 1981]. The southern Lesser Antilles is characterized by substantially lower seismicity [Stein et al., 1982]. Causal relationships between this lower seismicity and the subduction of bathymetric ridges, the presence of plate boundaries, and lubrication by high fluid pressures in the thick sediment wedge of the Orinoco fan, have been proposed by many authors (references in Stein et al. [1982], and McCann and Sykes [1984]).

In contrast to the Neogene plate reorganizations in the Farallon/Cocos realm, the relative motion of plates surrounding the eastern Caribbean have been nearly constant since Eocene times. Dating of volcanic rocks revealed that subduction below the present Lesser Antilles arc may be as old as the Middle Eocene and can perhaps be traced back to Late Jurassic times in outcrops on the Desirade islands and in samples dredged from the Aves Ridge (presumably a remnant arc) [Masclé et al., 1986; Bouysse, 1988]. I remark that although subduction processes may have been active since the Late-Jurassic (Figure 4.2), the subduction of Proto-Caribbean lithosphere in Mesozoic and Paleocene times [Ross and Scotese, 1988] did probably not result in down going subduction zones. Rather, underplating and lithospheric doubling [Vlaar, 1983] may have occurred due to the low age



of the Proto Caribbean lithosphere (< 45 Ma, Figure 4.2), which partly explains the highly heterogeneous crustal structure of the present Caribbean Plate [Burke et al., 1978]. Down going subduction below the Caribbean Plate could have been triggered in the Late-Paleocene when relatively old Atlantic lithosphere was encountered.

In chapter 4, I showed that substantially more Atlantic lithosphere has disappeared in the mantle below the present Caribbean Plate than suggested by the length of the seismogenic zones. The major part of the relicts of disappeared lithosphere can not be investigated by seismicity studies. Here, I present results of the tomographic inversion of  $P$ ,  $PP$  and  $pP$  delay times. Images are shown of the aspherical structures in the Earth's (upper) mantle below the Caribbean region that can be related tentatively to surface tectonic processes, but which extend far below the deepest seismicity.

### 6.3.2 Spatial resolution in tomographic images of mantle below the eastern Caribbean

Unfortunately, the spatial resolution in the tomographic images in the mantle region below the northeastern Caribbean Plate is low. This had to be concluded in chapter 4 after analyses of the results of the sensitivity tests as presented in the Figures 5.4c,d,e. The resolution is significantly higher in tomographic images of the mantle structures below the Southern Plate Boundary Zone (SPBZ) and the southeastern part of the Caribbean Plate. In a previous section of this chapter (section 6.2.5), I argued that even in areas with unsatisfying response to synthetic input models, the possible correlation between features in the tomographic images and results of independent investigations suggests that the images can be meaningful. However, the overall resolution is lower than in the mantle regions below Middle America, and the results presented in this section necessarily have a preliminary character and discussions and conclusions should be considered tentative. Probably, the size of the cells of the imposed cell model (Figure 1.6) is too small for the adequate parameterization of Earth structure below the eastern Caribbean. I assume that large-scale velocity structures, of the order of several cells, are reasonably well resolved. Therefore, I discuss structures at a larger scale than in the previous discussion of the Middle America subduction zone (section 6.2).

### 6.3.3 The aspherical mantle structure below the eastern part of the Caribbean Plate

In Figure 6.6, the lines of section are given of the mantle cross sections presented in Figures 6.7 and 6.8 and discussed in this text section. Figure 6.7 illustrates the mantle structure in north-to-south cross sections. In Figure 6.8, sections are presented more perpendicular to the trench or the strikes of the seismic zones.

In Figure 6.7a, neither the seismicity nor the imaged velocity anomalies indicate the down going of lithosphere below the Northern Plate Boundary Zone (NPBZ). This section is located west of the intersection of the Beate ridge (BeR in Figure 4.1) and the Hess Escarpment (HE) with the NPBZ, and west of the western terminus of the Muertos trench (MT). The structures visible below the Southern Plate Boundary Zone (SPBZ), near the Maracaibo Block (MB in Figure 4.1), are discussed below (section 6.4). To the east, along

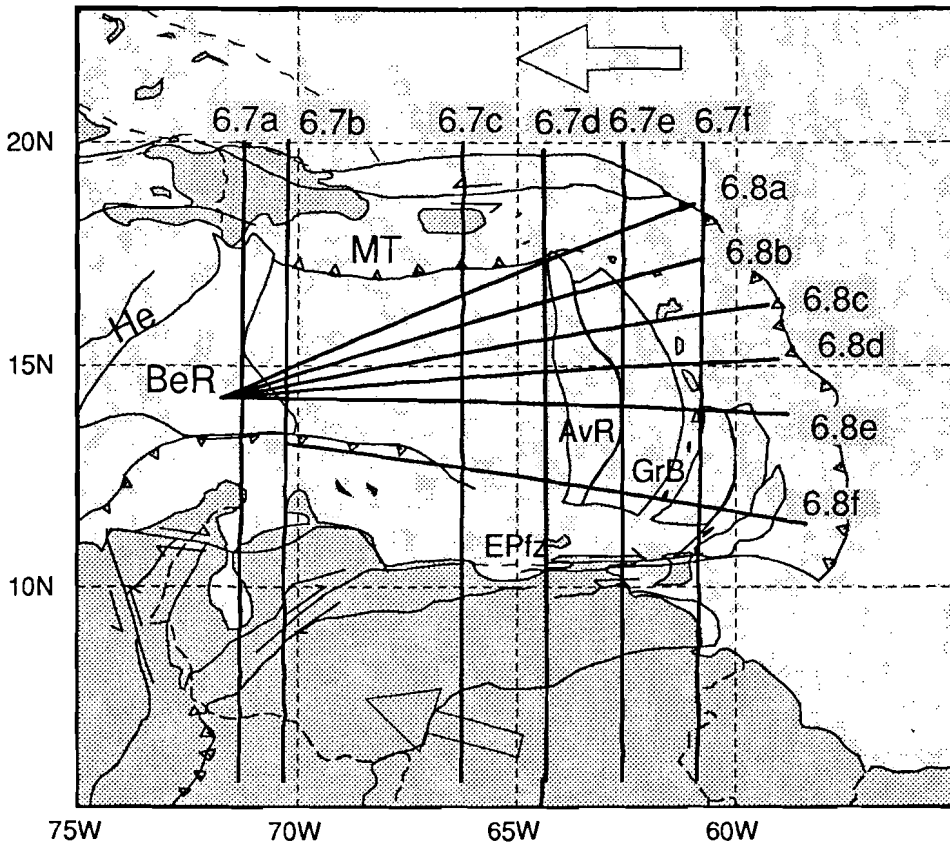
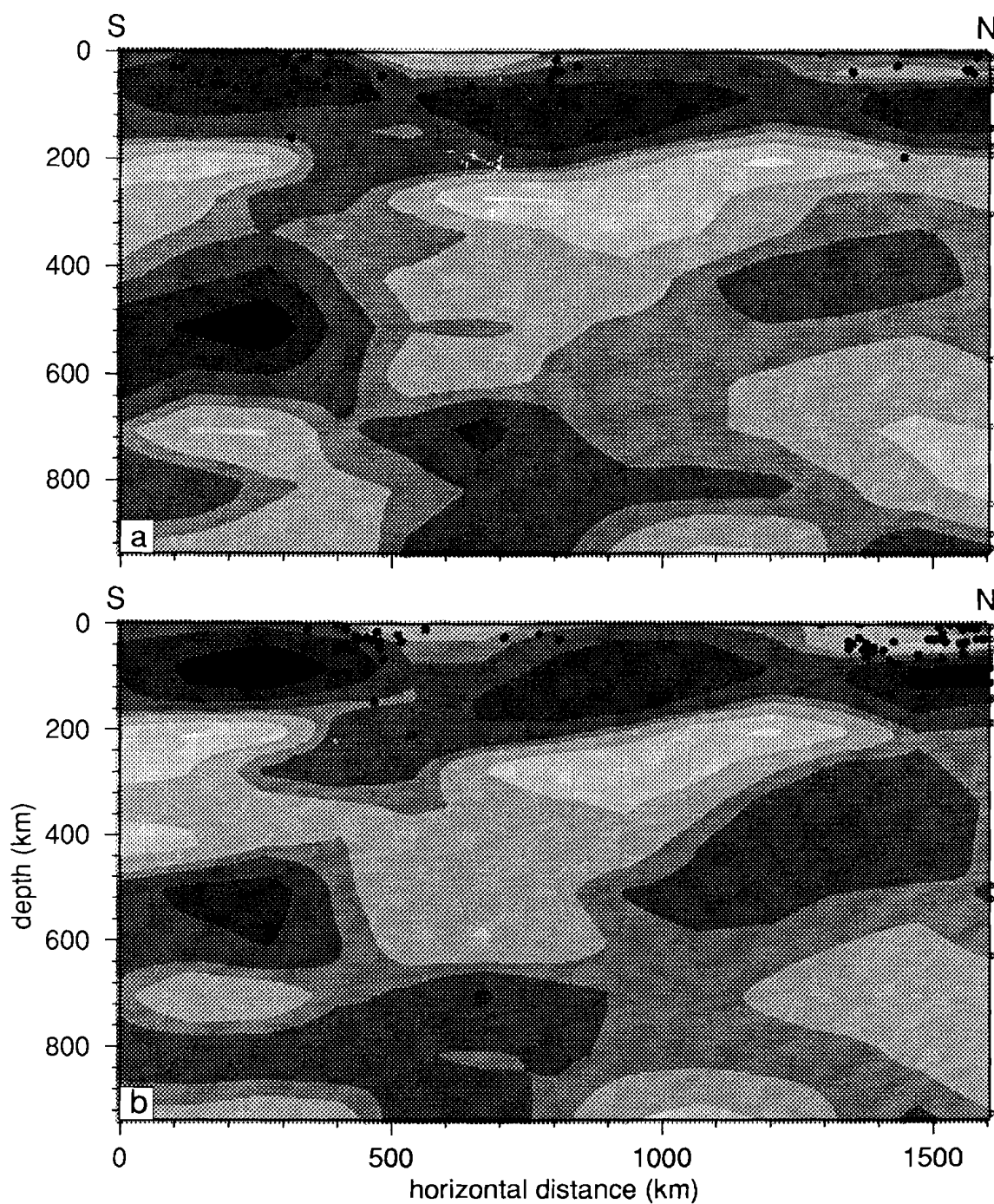


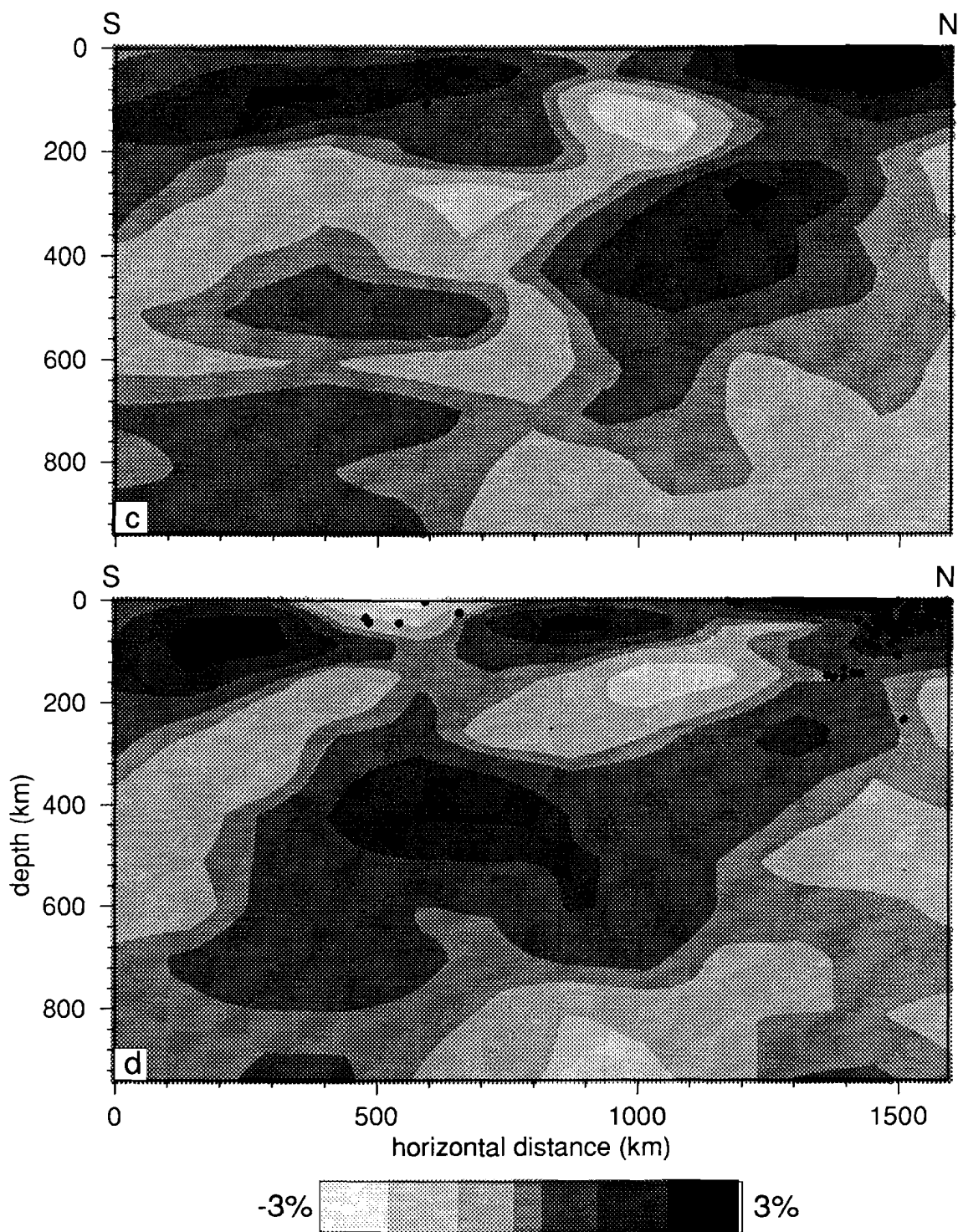
Figure 6.6. Geographic map of the eastern Caribbean showing the strikes of the sections discussed in section 6.3 of the text.

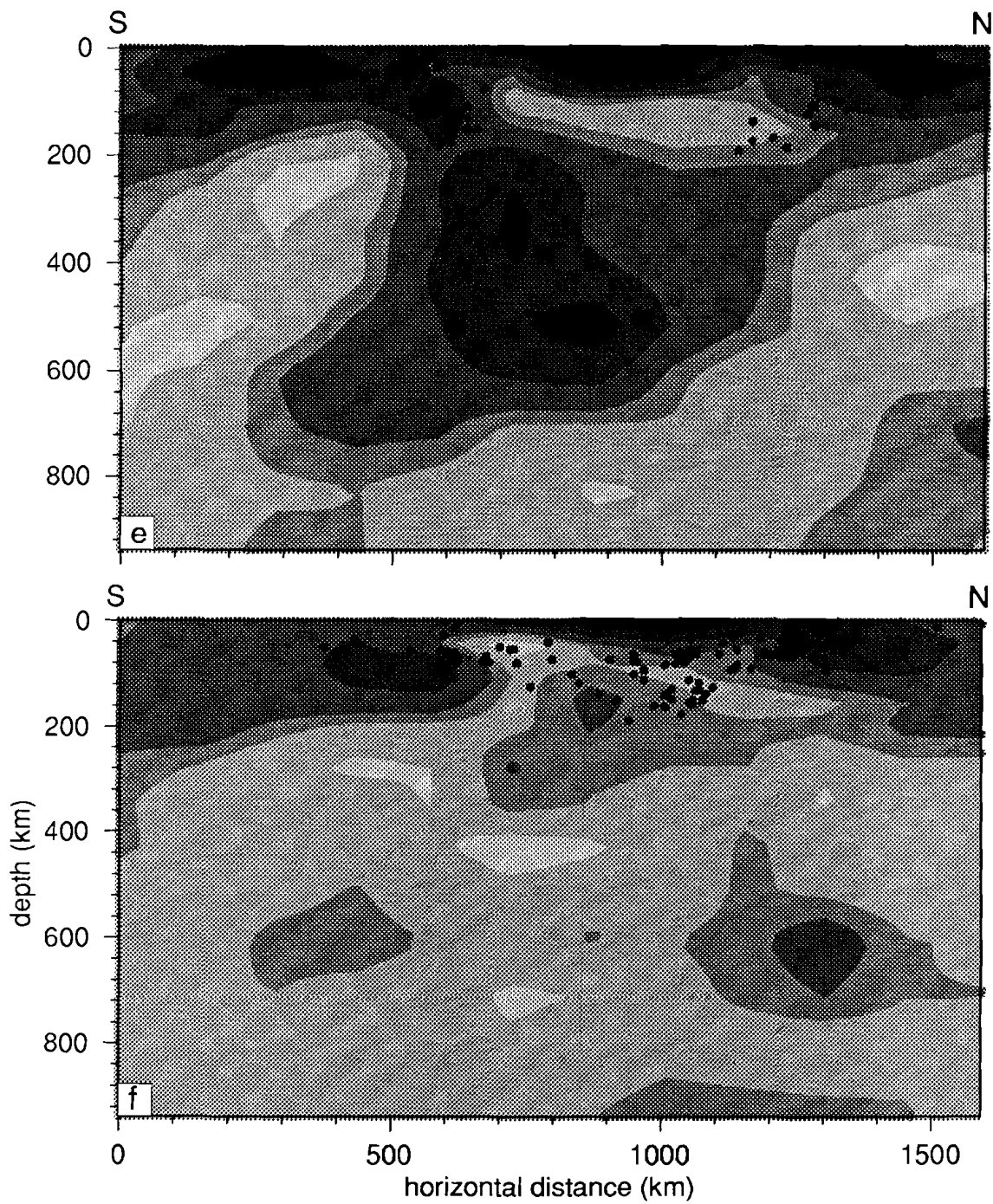
the 70°W meridian, an elongated high velocity structure is visible below western Hispaniola (Dominican Republic), and below the northeastern Caribbean Plate (section B in Figure 6.7). No subduction or underplating of lithosphere is suggested by the locations of earthquake hypocenters used in the tomographic investigation. The shallow structure below both the NPBZ and the SPBZ is characterized by low velocities, whereas in the central part of the Caribbean Plate high velocities prevail.

Towards the east, the south-dipping high-velocity structure below the Greater Antilles (Puerto Rico) becomes continuous to the shallow high velocities near a poorly developed seismic zone (Figure 6.7c).



*Figure 6.7.* North to south sections to a depth of 950 km illustrating mantle velocity structures below the eastern Caribbean. The locations of sections 6.7a to 6.7f are marked on Figure 6.6.





The image of the high velocity structure that extends to depths of ca. 400-500 km is restricted to the mantle region north of the 13<sup>th</sup> parallel. It is shown below, that the high velocity structures below 400 km and south of ca. 12° N are continuous to the shallow structures in the east, which are associated with subduction below the southern Lesser Antilles. Also in Figure 6.7d low velocities are visible at shallow depths below the SPBZ (El Pilar fault zone, EPfz in Figure 6.6). An apparently continuous high velocity anomaly below the NPBZ dips towards the south. The decrease of the dip of this feature relative to the dip in section 6.7c may be caused by a decreased angle between the line of section of Figure 6.7d and the strike of the subduction zone. The upper ca. 180 km of this high velocity structure is outlined by the Wadati-Benioff zone. At larger depths in the upper mantle, the structure becomes continuous with the high velocities below the southeastern part of the Caribbean, where pronounced high velocities occur south of 15° N. No relationship between the deep structure between 9° N and 12° N, and the shallow structures below the SPBZ (El Pilar fault zone) can be revealed from this image. Also the image presented in Figure 6.7e suggests the predominance of high velocities in the upper mantle south of the 15<sup>th</sup> parallel. The image of the high velocity anomaly is continuous to the shallow high velocities, and to the zone of high seismicity below the Araya-Paria peninsula in northern Venezuela.

The aspherical structure of the upper mantle below the Greater and Lesser Antilles can be further illustrated by sections approximately perpendicular to the island arcs (Figure 6.8). Figure 6.8a shows a section east of Puerto Rico, northwest of the bend in the island arc. This section is computed approximately perpendicular to the contours of constant depth to the seismic zone that are published by McCann and Sykes [1984, their figure 9]. The maximum seismicity occurs at a depth of 150 km. The upper 150 km of the mantle in the central part of the Caribbean Plate is marked by high velocities. In the discussion below, I address the lateral structure of the small low velocity anomaly which is visible in the depth range between 50 and 150 km, and bounded by the shallow high velocities in the central Caribbean, and the inclined high velocity anomaly in the east. As is demonstrated below, this low velocity feature becomes more pronounced towards the south. The inclined velocity anomaly (velocity perturbation > +2%) can be continued to a depth of approximately 550 km. Towards the southeast, in the northeast to southwest striking section of Figure 6.8b, essentially the same features can be observed. I only mention the apparent widening of the low velocity region as compared to the situation north of this section (section 6.8a). Also the depth extent of the low velocity region increases to the south. The low velocity anomaly is located below the northern part of the Grenada basin (GrB, in Figure 6.6).

Section 6.8c intersects the northern Lesser Antilles north of the 15<sup>th</sup> parallel. I focus attention on an apparent transitional change in the morphology of the slab-like velocity anomaly from north to south. Compared to the previous sections of Figures 6.8a and 6.8b, in Figure 6.8c: (1), the seismic zone is slightly steeper and extends to larger depths; (2), the correlation between seismic zone and high velocities is lost, and focii are located in low velocity structures; and (3), the image of the deep high-velocity anomaly suggests a larger

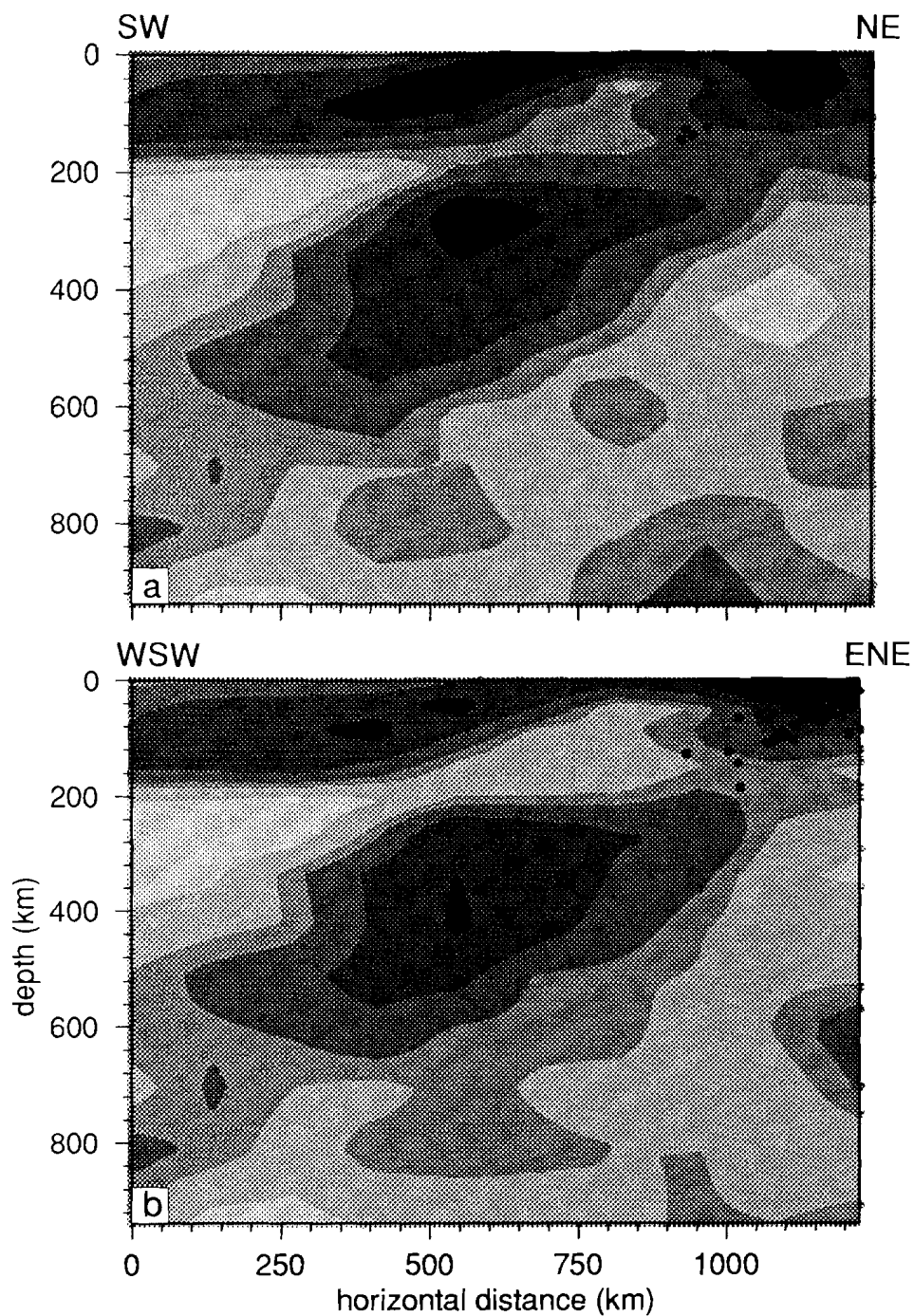
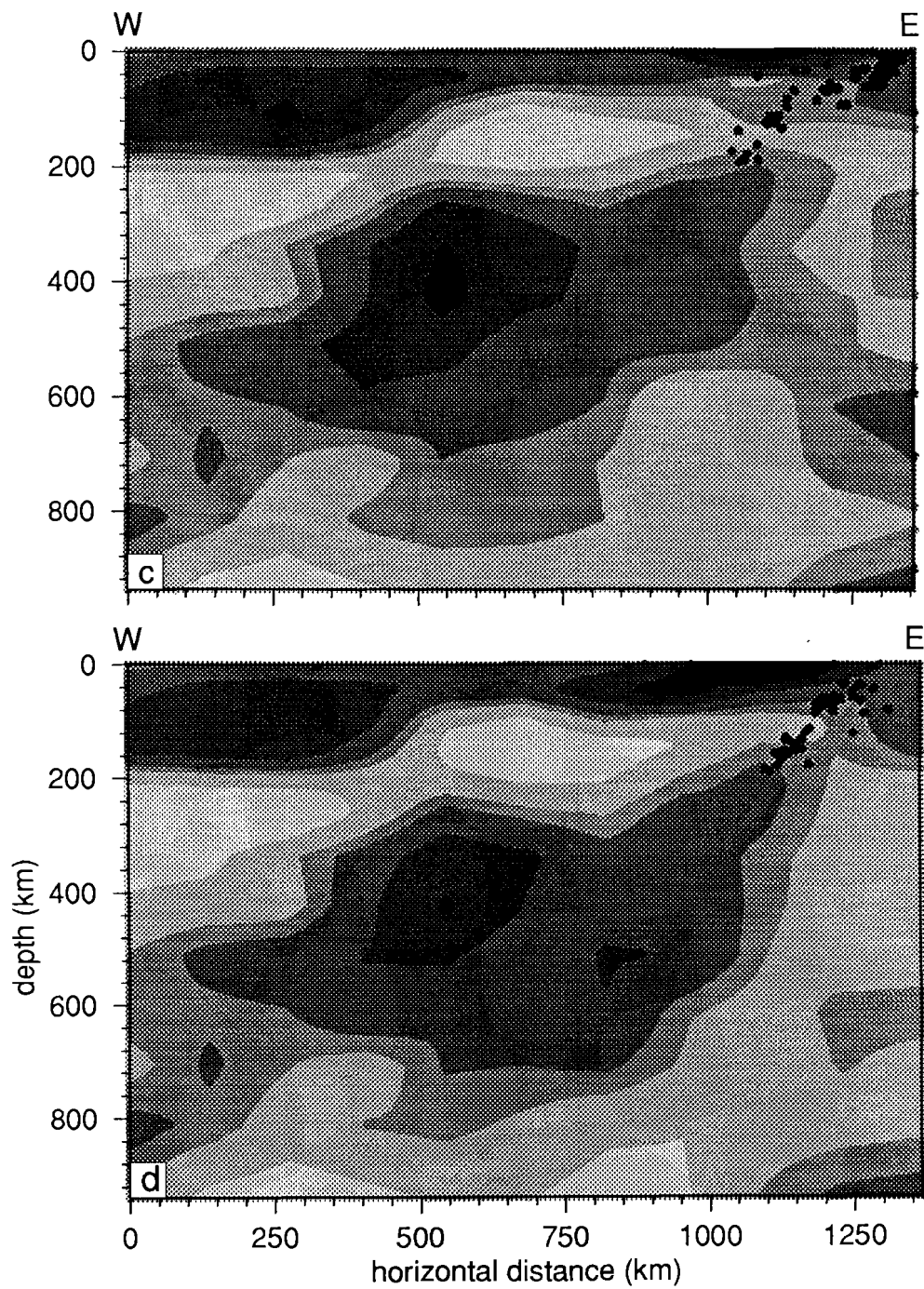
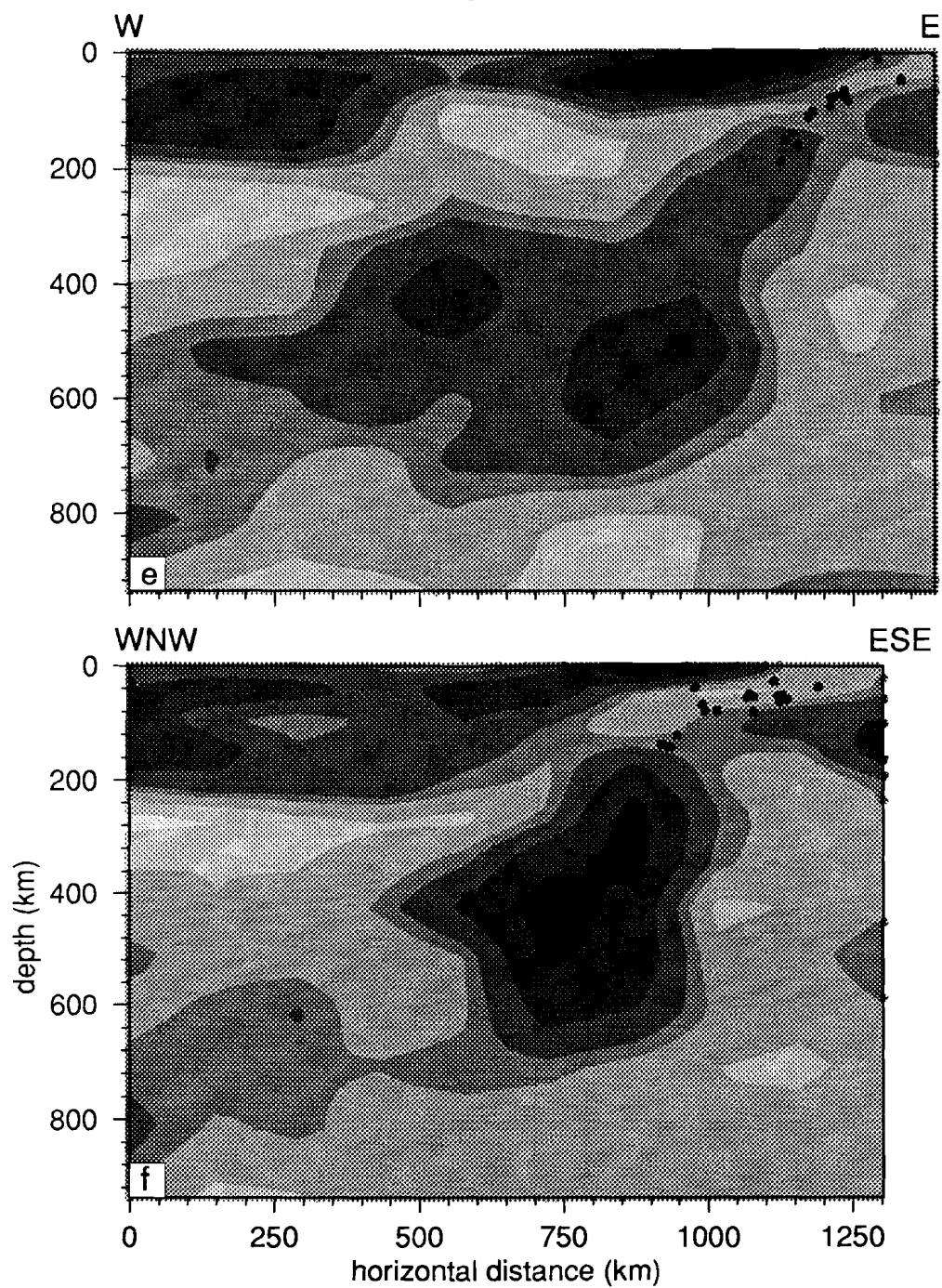


Figure 6.8. Cross sections 6.8a to 6.8f approximately perpendicular to the Greater and Lesser Antilles arcs. Note the change in slab morphology across ca. 15° N.









dip immediately below the seismic zone. With regard to (2) I remark that earthquakes of the seismic zone are located in the elastic part of the subducted lithosphere, which is commonly marked by lower temperatures and higher seismic velocities than the ambient mantle. The occurrence of many earthquakes in regions with anomalously low  $P$  wave velocities is not expected and not yet understood. The observation indicates either shortcomings of the imaging technique, or of our (or my) perception of the relation between temperature, seismic velocity, and rheology. Crossing the 15<sup>th</sup> parallel, the north-to-south lateral change in morphology of the velocity anomaly becomes more pronounced (section 6.8e). No significant increase in depth of the feature is observed. Section 6.5f shows the morphology of the high velocity structure near 12° N.

The imaged structures in Figures 6.8b and 6.8f can be considered characteristic for the mantle below the northern Lesser Antilles and below the southern part of the Lesser Antilles respectively. The difference between the imaged structures in these cross sections illustrates the lateral change in slab morphology across the 15° N parallel.

#### 6.3.4 Discussion of tomographic images and some tectonic implications

In chapter 5 I showed that the resolution of small-scale structures is worse than below Middle America. In the sensitivity tests with short harmonics the sign of the input anomalies is generally well resolved, in contrast to the amplitudes of the perturbations. Although the cross section lack, in particular, vertical resolution, I assume that large-scale structures of the order of several hundreds of kilometers are sufficiently well resolved to allow tentative interpretations. As a working hypothesis, I interpret the inclined slab-like velocity anomalies in the Figures 6.7 and 6.8 as transections through the blurred image of the Atlantic lithosphere subducted below the eastern Caribbean. I remark the poor resolution of the amplitudes of the imaged anomalies does not allow the discrimination from the presented results between images of active subduction zones and images of remnants of past subduction. The tomographic images of the aspherical variations of  $P$  velocities below the eastern Caribbean reveal that:

- (1) high  $P$  wave velocities are visible well below the seismic zones of the Greater and Lesser Antilles subduction zones.
- (2) lateral changes occur in the morphology of subducted lithosphere below the Greater Antilles near the intersection of the Muertos trench, the Beate Ridge, and the Hess Escarpment.
- (3) the morphology of the lithosphere of the Atlantic Plates subducted below the Lesser Antilles changes significantly across the 15° N parallel.
- (4) the anomalously high  $P$  wave velocities imaged in the deeper part of the upper mantle below the Southern Plate Boundary Zone can be continued to the site where shallow high velocity anomalies, and seismicity, mark the subduction of the Atlantic part of the South American Plate below the southern Lesser Antilles.

With regard to (1), I remark that the continuation of subducted lithosphere to depths of 500-600 km agrees with an initiation of down going subduction in the Eocene (45 Ma) combined with velocities of convergence of the order of 0 to 2 cm/yr.

The lateral change in the aspherical structure below the Greater Antilles occurs near the Dominican Republic. East of the Dominican Republic high  $P$  velocities are imaged in the mantle below the Northern Plate Boundary. West of the intersection between the Northern Plate Boundary and the imaginary northeastern continuation of the Hess Escarpment, no evidence can be obtained from the seismicity or from the imaged structure for (past) subduction. With respect to the Hess Escarpment, I recall that the tomographic images of the Middle America subduction zone suggest the coincidence of the boundary between the segments H-IV and H-V and the Hess Escarpment (Figure 5.4, and text section 6.2.5). The velocity structures below both the Greater Antilles arc and below the southern Middle America arc are cut-off to large depths by an imaginary vertical plane that strikes approximately along the Hess Escarpment. These observations support the hypothesis, that the Hess Escarpment is the trace of an arc-arc transform fault [e.g., Sykes and McCann, 1984; Ross and Scotese, 1988]. Although apparently no evidence exists for present-day activity along the Hess Escarpment, also relatively recent processes, e.g., the Miocene-to-present subduction of the Cocos Plate north of the Nicoya Peninsula, seem to be influenced by the location of the Hess Escarpment. These observations indicate that the Hess Escarpment is the surface expression of a tectonic phenomenon that has been important for the neotectonics of the Caribbean Plate. Its role in the Neogene history of the region is, however, not well understood.

The second lateral change in the morphology of the down going velocity anomaly which is discernible from the tomographic images occurs below the central Lesser Antilles, approximately across the 15<sup>th</sup> parallel. Below the northern Lesser Antilles the high velocity feature has a significant shallower dip than below the southern Lesser Antilles. The images suggest a transitional change over a distance of several hundreds of kilometers. In the images, a slow region is visible at shallow depths below the back-arc area of the Lesser Antilles subductions zone. In the northern part of the Lesser Antilles, this structure is less well developed than in the southern part of the arc, where the back-arc region is marked by the Grenada Basin (GrB, in Figure 6.6). The axis of this low velocity anomaly is located along 65° W. If the hypothesis is correct that the down going high velocity structure represents the blurred image of the subduction zone below the Lesser Antilles, I postulate that the significant steeper slab dip below the southern Lesser Antilles is the result of the retrograde motion of the subducted old lithosphere of the Atlantic Plate. This "roll back" process can be related to the Paleocene back-arc opening of the Grenada Basin in the southeastern Caribbean [Bouysse, 1988]. The arcuate morphology of the continuous high-velocity structures below the northern Lesser Antilles and below the eastern Greater Antilles may be less favourable for withdrawal of the subducted old lithosphere. The in-slab stresses that result from the difference in retrograde motion of the subduction zone below the northern and southern Lesser Antilles, may be laterally released in a sub-vertical zone of weakness near 15°N. I suggest that the discussed change in slab morphology

across  $15^{\circ}\text{N}$  marks the transition from the atlantic part of the North American Plate to the atlantic part of the South American Plate. The scenario of a more efficient "roll back" of the subducted slab below the southern Lesser Antilles, laterally decoupled near  $15^{\circ}\text{N}$  from the slab below the northern Lesser Antilles, and the resulting steeper subduction in the south, explains the higher degree of decoupling between the overriding Caribbean Plate and the Atlantic Plate. Together with the high fluid pressures related to the subduction of the thick sedimentary wedge of the Orinoco delta this explains the substantially higher ratio of aseismic subduction in the southern Lesser Antilles.

I conclude that the oceanic part of the South American Plate subducts below the southern Lesser Antilles. This tectonic setting suggests a tear between the atlantic part of the South American Plate and the continental part of the Plate. This tear would then be located at the southern limit of the Lesser Antilles, near the Araya-Paria Peninsula in northern Venezuela (Figure 6.6). In this context, the southern part of the imaged structure in section 6.7e is relevant, because it shows relation between the high seismicity at shallow depths below the Araya-Paria Peninsula and the down going slab north of it. Sykes and Molnar [1969] reported at least two focal mechanisms of earthquakes located below the eastern part of Araya-Paria (Figure 6.7e), that indicate tear-faulting (mechanisms no. 118 (32 km focal depth) and no. 119 (74 km) [Sykes and Molnar, 1969]). On the other hand, however, many investigators agree on a small convergent component in the relative motions of the South American Plate and the Caribbean Plate [e.g., Ladd, 1976; Minster and Jordan, 1978; Kellogg and Bonini, 1982; Pindell et al, 1988]. Convincing evidence for at least local convergence between the Caribbean and the South American Plates, is provided by images of the underplating of the Caribbean Plate below the South American Plate. I discussed this evidence in the next section (6.4).

If the atlantic part of the South American Plate subducts below the Caribbean Plate, and if the relative motion between the Caribbean and continental South American Plate has a (small) convergent component, then what happens to the atlantic South American Plate in the deeper mantle? Insight in this geometrical problem can be obtained from the examination of the north-to-south sections across the SPBZ as presented in Figure 6.7. West of section 6.7c, the high velocities associated with subducted lithosphere of the atlantic part of the South American Plate is visible at depths of 500-600 km, near a southern limit at  $7^{\circ}\text{N}$ . In section 6.7d, east of 6.7c, the subducted South American Plate is visible at 400 km and  $9^{\circ}\text{N}$ , and in 6.7e, the southern limit of the high velocities at 300 km depth is near  $11^{\circ}\text{N}$ . The southward migration of the high velocity structure, with increasing distance from the Lesser Antilles trench and hence with increasing depth, was also observed in chapter 5 (sections 5.4.4 and 5.4.5). The discussed observations suggest the overriding by the continental South American Plate over the deep parts of the subducted oceanic South American Plate. This is indicative of a northward component in the relative motion of the South American Plate in the mantle reference frame.

In this setting, the atlantic part of the South American Plate that is subducted below the Araya-Paria Peninsula can exert slab-pull forces on the hinge area in northeastern Venezuela, which can cause the down warping of continental crust below the easternmost

Venezuela basin. This scenario provides an explanation for the pronounced lows in the gravity maps (free-air and Bouguer) of Bowin [1976]. See also discussions of Bonini [1978] and Vierbuchen [1984]. The free-air gravity low in northeastern Venezuela is amongst the largest negative free-air anomalies on earth where topography is above sea level [Bowin, 1976].

#### 6.4 Evidence for underthrusting of the Caribbean below South America

The exact location of the boundary between the Caribbean Plate and the South American Plate, and the style of deformation along this plate contact, are still major problems in the understanding of Caribbean tectonics. Instead of one single well-defined plate boundary, deformation occurs in a diffuse Plate Boundary Zone (PBZ) [Mann and Burke, 1984]. A thorough discussion of the tectonics of this region is beyond the scope of this thesis. Here, I focus on the nature of the contact between the South American Plate and the Caribbean Plate along the Curacao Trench (Figure 6.9c).

Whereas strike slip predominates in the eastern part of the southern PBZ and compression along the Colombia-Peru trench in the west, transpression predominates in northwestern South America. According to Ladd [1976], Pindell and Dewey [1982], and Pindell et al. [1988], the relative motion between the North and South American Plates has been convergent since the Late Eocene (anomaly 21) and the Early Oligocene. Evidence for a Cenozoic transpressional strain regime in the southwestern Caribbean and for the underplating of the Caribbean Plate below South America has been reported from geological studies [for references Bonini et al., 1984; Eva et al., 1989], from analyses of seismicity [Molnar and Sykes, 1969; Dewey, 1972; Pennington, 1981; Kellogg and Bonini, 1982], and from gravity anomalies [Bowin, 1976; Kellogg and Bonini, 1982].

In this section, I provide additional evidence for the underplating/subduction of the Caribbean Plate beneath the Maracaibo Block (MB, in Figure 6.9) in northwest South America from the analysis of the aspherical variations of  $P$  wave velocities. In Figure 6.9a, I present a north-to-south vertical section across the southern Caribbean Deformed Belt (SCDB, Figure 4.1), the Oca and Bocono fault zones, and the eastern part of the Maracaibo block. The most striking feature in this tomographic image is the inclined velocity anomaly below the northernmost South American Plate. This structure dips approximately  $10^\circ$  to  $15^\circ$  towards the south and is continuous to the high velocities below the Caribbean Plate in the north. The high velocities of this structure are imaged to a depth of about 280 km, at a distance of approximately 700 km south of the Curacao trench. The shallow structures below the eastern part of the Maracaibo block, bounded by the Oca fault in the north and the Bocono fault in the south east, are marked by slightly lower velocities than the reference model ( $< 1\%$ ). Towards the south, there is a transition to substantially higher velocities across the Bocono fault zone. These higher velocities may be related to the Precambrian Guyana Craton. The velocity structure perpendicular to this north-to-south cross-section, at  $10^\circ$  N, is presented in Figures 6.9b. Figure 6.9b shows the lateral extent of the high velocity structure below the Maracaibo block, and the change in velocity structure across approximately  $71^\circ$  W. The high velocities associated with the slab-like

structure of Figure 6.9a are restricted to below the Maracaibo block. In contrast to the rather undisturbed down going velocity structure in the east (Figure 6.9a), no evidence for a down going structure below western Venezuela and northeastern Colombia can be obtained from the images. Examination of sections across the Curacao Trench show that undisturbed underplating is indicated by the images only east of the intersection of the Beate Ridge (BeR, Figure 4.1) with the trench. This may be indicative of complications due to attempted oblique underplating of the Beate Ridge. The latitude of the "leading edge" of the slab-like structure near 8° N approximately coincides with the southernmost point of the Caribbean Plate, at the surface, near southeast Panama and northwest Colombia (longitude -77° W).

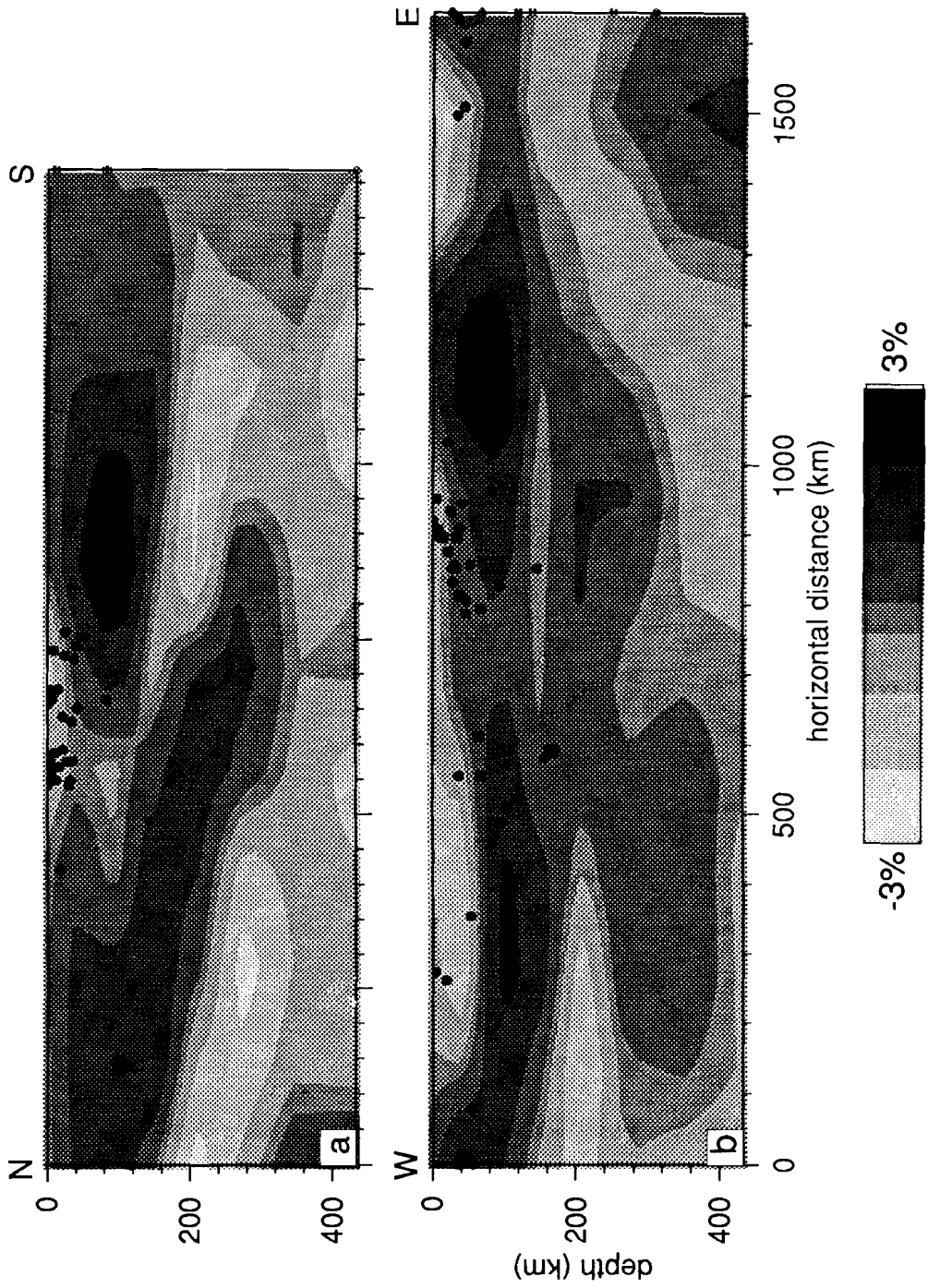
From Figures 5.4[1-5]c,e, it can be concluded that the quality of the harmonic response is good for the discussed upper mantle region. For the cross section in Figure 6.9a the harmonic fit, is given in Figure 6.10. This figure reveals rather good resolution in the upper mantle region in the central part of the image presented in Figure 6.9a. The tomographic images presented in Figures 6.9 and 6.10 provide evidence for the underplating of the Caribbean Plate below the northern part of the South America Plate to a depth of 280 km and as far south as 8° N.

In this particular region, the seismicity is restricted to the northwest South America intraplate realm, near the dextral Oca and Bocono fault zones [e.g., Dewey, 1972]. In the cross sections shown (Figure 6.9) the structure is aseismic, in contrast to observation of a down-going seismic zone further west [Pennington, 1981; Kellogg and Bonini, 1982], see also Figure 4.5. The velocity structure either suggests that underplating of the Caribbean Plate occurs aseismically, or that in the present-day tectonics no motion between the Caribbean Plate and the South America Plate occurs along this plate contact.

The structure presented in Figure 6.9 is highly suggestive for (past) subduction of the Caribbean Plate towards the south or southeast, and thus for convergence between the Caribbean Plate and the South American Plate. However, I argue that no convergent component is necessary in the relative motions between the Caribbean and South American Plates to produce the discussed structures. I advocate an alternative interpretation that is based on the approximate coincidence between the latitude of the southernmost part of the high velocity structure, in Figure 6.9a, and the latitude of the southernmost part of the Caribbean Plate, at (-77° W, 8° N). This coincidence indicates that the Caribbean Plate did not move significantly towards the south with respect to the South American Plate. In this interpretation, the structure imaged in Figure 6.9a is the result of an eastward motion of the Caribbean Plate relative to South America, contemporaneous with - or followed by - northward movement of the Andean and, in particular, the Maracaibo Blocks.

## 6.5 Conclusions

In this chapter, I discussed the aspherical variations of  $P$  wave velocities, determined by the tomographic inversion of  $P$ ,  $PP$ , and  $pP$  delay times, in the mantle below the convergent boundaries in the Caribbean region. Wherever relevant, I compared the results of the tomography with inferences about mantle structure from other investigations, e.g., of



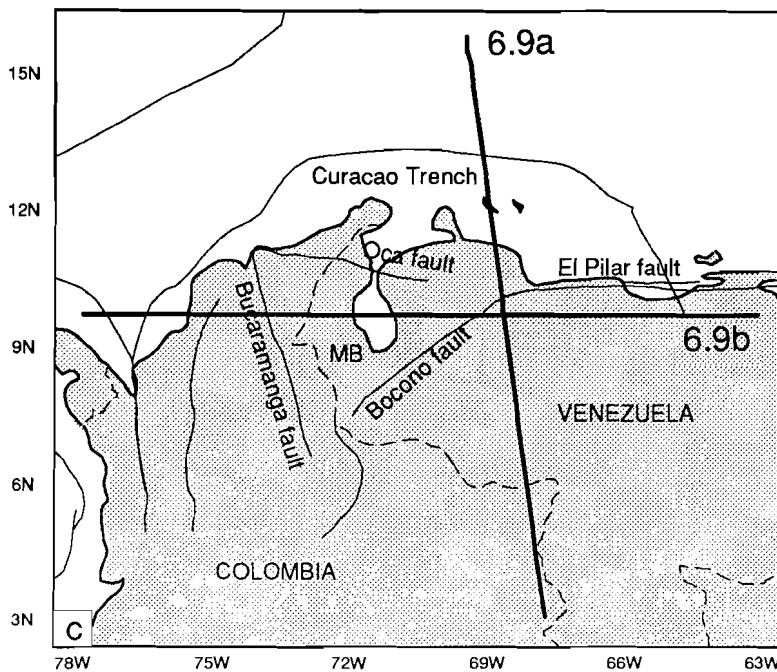


**Figure 6.9.** Upper mantle cross sections illustrating the underthrusting of the southernmost Caribbean Plate below northern South America. (a) North-south section through the eastern part of the maracaibo block. (b) East-west section through the Maracaibo block. (c) Geographic map of northwest South America and the lines of section of Figures 6.9a and 6.9b.

seismicity.

In particular in Middle America, shallow velocity anomalies that are visible in the tomographic images correlate very well with specific distribution of seismicity, and with surface tectonic and geologic features. This encouraging agreement also holds for parts of the tomographic solution where results of sensitivity tests predict low resolution of small scale anomalies. This indicates that the relation between synthetic experiment and the "true earth" is not at all trivial, which may restrict the value of, in particular, the spike sensitivity test as a diagnostic tool to assess the reliability of the solution.

From central Mexico to Panama, differences in velocity structure along the Middle America trench (to a depth of about 300 km) correlate well with the segmentation of the subducted Cocos Plate based on seismicity [e.g., Burbach et al., 1984] and on magnetic anomalies [Counil and Achache, 1987]. Five distinct segments are derived from the tomographic images. In segments H-II (central Mexico, near Trans Mexican Volcanic Belt) and H-IV (from south Mexico to the Nicoya Peninsula near the southwestward continuation of the Hess Escarpment) the imaged structures are indicative of low-angle subduction of the Cocos Plate. The aspherical structures imaged in the mantle below



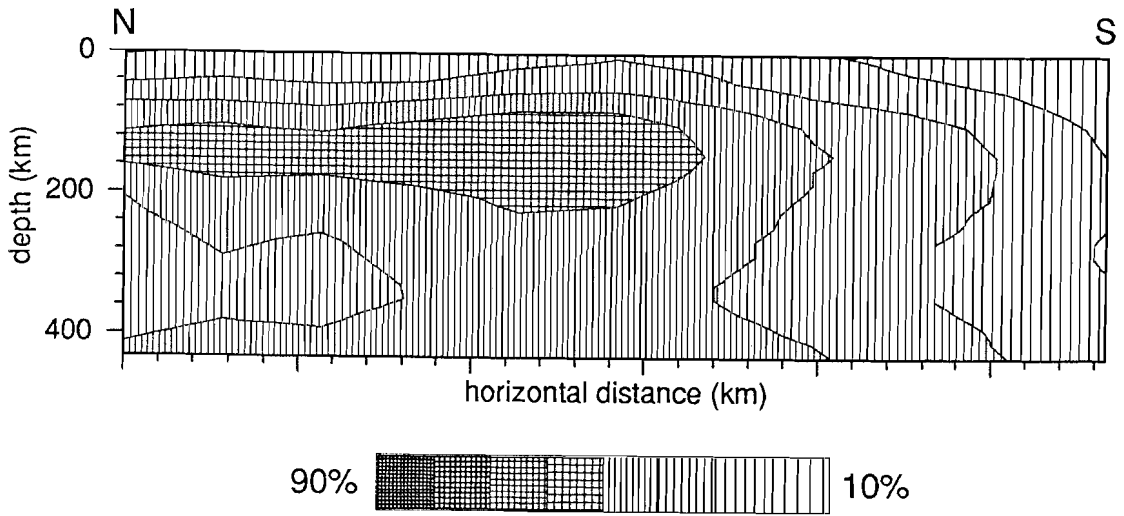


Figure 6.10. Harmonic model fit for the mantle cross section presented in Figure 6.9a.

segment H-I (northern Mexico), segment H-III (the Isthmus of Tehuantepec), and segment H-V (Panama), do not indicate the down going of the Cocos Plate, at the Middle America trench. For segments H-I and H-V this can be explained by the cessation of subduction after the arrival at the trench of young oceanic lithosphere near the East Pacific Rise and the Galapagos spreading centre (or Cocos-Nazca spreading centre). A possible explanation for the absence of subducted lithosphere below the Isthmus of Tehuantepec is the continuing left lateral motion of the Chortis block (southern Middle America) relative to central Mexico and Yucatan (northern Middle America). As a result of this motion, the trench segment along the Isthmus has been exposed only recently to (attempted) subduction of young lithosphere of the Cocos Plate.

I interpret the large-scale velocity anomalies at depths larger than 300 km as the blurred image of the northeast to east dipping remnants of the subducted Farallon Plate. The velocity anomaly associated to the subducted Farallon Plate is continuous across the 660 km discontinuity and is also visible in the lower mantle. I postulate the penetration into the lower mantle below the western part of the Caribbean Plate of the subducted Farallon Plate.

Below the eastern Caribbean an arcuate velocity anomaly is imaged that is interpreted tentatively as the image of the remnants of subducted Atlantic lithosphere. Subduction-related high-velocity slabs are imaged to depths of 500 to 600 km. A lateral change in slab morphology is observed across the  $15^{\text{th}}$  N parallel. South of  $15^{\circ}$  N the dip of the velocity anomaly is significantly larger than the dip of the structure north of the  $15^{\text{th}}$  parallel. I interpret the imaged lateral change in the morphology of the Lesser Antilles as the transition from the North American to the South American Plate near  $15^{\circ}$  N. South of the hypothetical plate boundary, the retrograde motion of the subducted (old) lithosphere of the

atlantic part of the South American Plate has been more efficient than that of the subducted North American Plate north of 15°N. This difference in the subduction process causes the southern part of the Lesser Antilles subduction zone to be more decoupled, which explains the higher ratio of aseismic slip. Also the occurrence of substantially more back-arc spreading in the southern part of the arc, which resulted in the Grenada Basin, can be explained by this scenario.

Tomographic images provide evidence for the (past) underplating of the southern Caribbean Plate below a micro plate formed by the Maracaibo Block in northwest South America. The presented image of the underplated Caribbean lithosphere below parts of the South American Plate is suggestive of convergence between the Caribbean Plate and the South American Plate. However, I advocate an alternative interpretation. The southernmost part of the Caribbean Plate below the Maracaibo Block does not extent further south than the southernmost part of the Caribbean Plate at the surface near Panama, which suggests that the Caribbean Plate did not move significantly to the south with respect to the South American Plate. A right-lateral strike slip motion of the Caribbean Plate relative to the large South American Plate, contemporaneous with - or followed by - a northward displacement of the Maracaibo Block micro plate explains the presented images. The discussed structure provides evidence that the contact between the Caribbean Plate and the South American Plate along the Curacao Trench is important in the Neogene tectonic history of the southern plate boundary zone in northwest South America.

Apart from the local convergence due to the displacements of micro plates in the northwestern part of South America, no convergence between the Caribbean Plate and the South American Plate is suggested from the tomographic images. However, the presence below the northernmost continental South American Plate of high velocity structures associated with subducted lithosphere of the atlantic South American Plate is indicative of a small northward component of South American Plate movement in the mantle reference frame.

## References

- Adamek, S., F. Tajima and D. A. Wiens, Seismic rupture associated with subduction of the Cocos Ridge, *Tectonics*, 6, 6, 757-774, 1987.
- Bonini, W. E., Anomalous crust in the eastern Venezuela basin and the bouguer gravity anomaly field of northern Venezuela and Caribbean borderland, *Geol. Mijnb.*, 57(2), 117-122, 1978.
- Bonini, W. E., R. B. Hargraves, and R. Shagam, *The Caribbean-South American plate boundary and regional tectonics*, Geol. Soc. Am. Memoir, 162, 421 pp., 1984.
- Bourgois, J., J. F. Toussaint, H. Gonzalez, J. Azema, B. Calle, A. Desmet, L. A. Murcia, A. P. Acevedo, E. Parra, and J. Tournon, geological; history of the Cretaceous ophiolitic complexes of northwestern South America (Colombian Andes), *Tectonophysics*, 143, 307-327, 1988.
- Bouysse, P., Opening of the Grenada back-arc basin and evolution of the Caribbean Plate during the Mesozoic and early Paleogene, *Tectonophysics*, 149, 121-143, 1988.
- Bowin, C., The Caribbean: gravity field and plate tectonics, *Geol. Soc. Am. Spec. Paper*, 169, pp. 39, 1976.
- Buchbinder, G. G., On PP and SS reflection point anomalies, *Can. J. Earth Sci.*, 19, 434-437, 1982.
- Burbach, G. V., C. Frohlich, W. D. Pennington, and T. Matumoto, Seismicity and tectonics of the subducted Cocos Plate, *J. Geophys. Res.*, 89, B9, 7719-7735, 1984.
- Burbach, G. V., and C. Frohlich, Intermediate and deep seismicity and lateral structure of subducted lithosphere in the circum-Pacific region, *J. geophys. Res.*, 24, 4, 833-874, 1986.
- Burdick L.J., A comparison of the upper mantle structure beneath North America and Europe. *J. Geophys. Res.*,
- Burkart, B., Neogene North American-Caribbean plate boundary across northern Central America: offset along the Polochic fault, *Tectonophysics*, 99, 251-270, 1983.
- Burke, K., P. J. Fox, and A. M. C. Sengör, Buoyant ocean floor and the evolution of the Caribbean, *J. Geophys. Res.*, 83, 3949-3954, 1978.
- Case, J. E., and T. L. Holcombe, Geologic-tectonic map of the Caribbean region: U. S. Geological Survey Miscellaneous Investigations Map I-1100, scale 1:2,500,000, 1980.
- Case, J. E., T. L. Holcombe, and R. G. Martin, Map of geologic provinces in the Caribbean Region, in: *The Caribbean-South American plate boundary and regional tectonics*, edited by W. E. Bonini, R. B. Hargraves and R. Shagam, pp 1-30, Geol. Soc. Am. Memoir, 162, Boulder, CO, 1984.
- Choy, G. L., and P. G. Richards, Pulse distortion and Hilbert transformation in multiply reflected and refracted body waves, *Bull. Seism. Soc. Am.*, 65, 1, 55-70, 1975.
- Counil, J. I., and J. Achache, Magnetization gaps associated with tearing in the Central America subduction zone, *Geophys. Res. Lett.*, 14, 11, 1115-1118, 1987.
- Counil, J. L., J. Achache, and A. Galdeano, Long-wavelength magnetic anomalies in the Caribbean: plate boundaries and allochthonous continental blocks, *J. Geophys. Res.*, 94, B6, 7419-7431, 1989.
- Darragh, R. B., Mapping of upper mantle structure from differential (PP -P) travel time residuals, *Phys. Earth Planet. Inter.*, 41, 6-17, 1985.
- Dewey, J. W., Seismicity and tectonics of western Venezuela, *Bull. Seismol. Soc. Am.*, 62, 1711-1751, 1972.

- Dewey, J. W., and S. T. Algermissen, Seismicity of the Middle America arc-trenchsystem near Managua, *Bull. Seismol. Soc. Am.*, **64**, 1033-1048, 1974.
- Dewey, J. W., and G. Suárez, Seismicity of Middle America, in: *J. E. Case and G. deno (eds), The Geology of North America, H, The Caribbean Region. (DNAG)*, Geol. Soc. Am., Boulder (CO), in press.
- Dorbath, C., and L. Dorbath, Travel time residuals of *PP* waves reflected under the central Atlantic Ocean, *Phys. Earth Planet. Inter.*, **25**, 121-128, 1981.
- Dorel, J., Seismicity and seismic gaps in the Lesser Antilles arc and earthquake hazards in Guadeloupe, *Geophys. J. R. Astr. Soc.*, **67**, 679-696, 1981.
- Dziewonski, A. M., Mapping the lower mantle: determination of lateral heterogeneity in P velocity up to degree and order 6, *J. geophys. Res.*, **89**, 5929-5952, 1984.
- Dziewonski, A. M., A. L. Hales, and E. R. Lapwood, Parametrically simple earth models consistent with geophysical data, *Phys. Earth Plan. Int.*, **10**, 12-48, 1975.
- Dziewonski, A. M., and F. Gilbert, The effect of small, aspherical perturbations on travel times and a re-examination of the corrections for ellipticity, *Geophys. J. R. astr. Soc.*, **44**, 7-17, 1976.
- Dziewonski, A. M., B. H. Hager and R. O'Connell, Large-scale heterogeneities in the lower mantle, *J. Geophys. Res.*, **82**, 239-255, 1977.
- Dziewonski, A. M., and D. L. Anderson, Travel times and station corrections for *P* waves at teleseismic distances, *J. Geophys. Res.*, **88**, 3295-3314, 1983.
- Engdahl, E. R., and D. Gubbins, Simultaneous travel time inversion for earthquake location and subduction zone structure in the Central Aleutian Islands, *J. Geophys. Res.*, **92**, B13, 13,855-13,862, 1987.
- Engdahl, E. R., and S. Billington, Focal depth determination of central aleutian earthquakes, *Bull. Seism. Soc. Am.*, **76**, 1, 77-93, 1986.
- Engdahl, E. R., and R. Kind, Interpretation of broad-band seismograms from central Aleutian earthquakes, *Ann. Geophys.*, **4**, B, 233-240, 1986.
- Eva A. N., K. Burke, P. Mann, G. Wadge, Four-phase tectonostratigraphic development of the southern Caribbean, *Mar. Petrol. Geol.*, **6**, 9-21, 1989.
- Fisher, K. M. T., T. H. Jordan, and K. C. Creager, Seismic constraints on the morphology of deep slabs, *J. Geophys. Res.*, **93**, B, 4773-4783, 1988.
- Forsyth, D. W., Determinations of focal depths of earthquakes associated with the bending of oceanic plates at trenches, *Phys. Earth Planet. Inter.*, **28**, 141-160, 1982.
- Fukao, Y., Upper mantle P structure on the ocean side of the Japan-Kurile Arc, *Geophys. J. R. astr. Soc.*, **50**, 621-642, 1977.
- Girardin, N., Travel time residuals of *PP* waves reflected under oceanic and continental platform regions, *Phys. Earth Planet. Inter.*, **23**, 199-206, 1980.
- Grand, S. P., Tomographic inversion for shear velocity beneath the North American Plate, *J. Geophys. Res.*, **92**, B13, 14,065-14,090, 1987.
- Gudmundsson, O., J. H. Davies and R. Clayton, Stochastic analysis of global travel time data: mantle heterogeneity and random errors in the ISC data, (*submitted to*) *Geophys. J. Int.*, 1989.
- Güendel, F. and K. McNally, High resolution image of the Benioff zone and mechanisms of large earthquakes near the southern terminus of the Middle America trench: Costa Rica and southern

- Nicaragua, C. A. (abstract) *EOS Trans. AGU*, 70, 43, 1210, 1989.
- Guzmán-Speziale, M., W. D. Pennington and T. Matumoto, The triple junction of the North America, Cocos and Caribbean Plates: seismicity and tectonics, *Tectonics*, 8, 5, 981-998, 1989.
- Harper, J. F., Plate dynamics: Caribbean map corrections and hotspot push, *Geophys. J. Int.*, 100, 423-433, 1990.
- Hill, D. P., Phase shift and pulse distortion in body waves due to internal caustics, *Bull. Seism. Soc. Am.*, 64, 1733-1742, 1974.
- Hirahara, K., A large-scale three-dimensional seismic structure under the Japan islands and the Sea of Japan, *J. Phys. Earth*, 28, 221-241, 1977.
- Hirahara, K., Three-dimensional seismic structure beneath southwest Japan: The subducting Philippine Sea Plate, *Tectonophysics*, 79, 1-44, 1981.
- Hirahara, K., and T. Mikumo, Three-dimensional seismic structure of subducting lithospheric plates under the Japan islands, *Phys. Earth Planet. Inter.*, 21, 109-119, 1980.
- Holcombe, T. L., and G. F. Sharman, Post-Miocene Cayman Trough evolution: a speculative model, *Geology*, 11, 714-717, 1983.
- Humphreys, E. D., and R. Clayton, Adaption of the tomographic method of inversion to seismic travel time problems, (submitted to) *J. Geophys. Res.*, 1990.
- Jeffreys, H., and K. E. Bullen, Seismological Tables, *British Association for the Advancement of Science, London*, 1940.
- Jeffreys, H., and E. R. Lapwood, The reflection of a pulse within a sphere, *Proc. Roy. Soc. London, Ser. A*, 241, 455-479, 1957.
- Jordan, T. H., The present-day motions of the Caribbean Plate, *J. Geophys. Res.*, 80, 4433-4439, 1975.
- Jordan, T. H., and W. S. Lynn, A velocity anomaly in the lower mantle, *J. Geophys. Res.*, 79, 2679-2685, 1974.
- Kellogg, J. N., and W. E. Bonini, Subduction of the Caribbean Plate and basement uplifts in the overriding South American Plate, *Tectonics*, 1, 251-276, 1982.
- King, D. W., R. A. W. Haddon and E. S. Husebye, Precursors to PP, *Phys. Earth Planet. Inter.*, 10, 103-127, 1975.
- Ladd, J. W., Relative motion of South America with respect to North America and Caribbean tectonics, *Geol. Soc. Am. Bull.*, 87, 969-976, 1976.
- Lay, T., Localized velocity anomalies in the lower mantle, *Geophys. J. R. Astron. Soc.*, 72, 483-516, 1983.
- LeFevre, L. V., and K. C. McNally, Stress distribution and subduction of aseismic ridges in the Middle America subduction zone, *J. Geophys. Res.*, 90, B6, 4495-4510, 1985.
- Mann, P., and Burke, K., Neotectonics of the Caribbean. *Rev. Geophys. Space Phys.*, 22, no.4, 309-362, 1984.
- Mann, P., G. Draper, and K. Burke, Neotectonics of a strike slip restraining bend system, Jamaica, *Soc. Econ. Paleontol. Min.*, 211-226, 1985.
- Martin, C. F., Mapa tectónico: norte de América del Sur, publication of *República de Venezuela, Ministerio de energía y minas*, scale 1:2,500,000, 1978.
- Mascle, A., B. Biju-Duval, P. de Clarens, and H. Munsch, Growth of accretionary prisms: tectonic processes from Caribbean examples, in: *The origin of arcs*, edited by F. C. Wezel, 375-400, Elsevier

- Science Publishers, Amsterdam, 1986.
- McCann, W. R., and L. R. Sykes, Subduction of aseismic ridges beneath the Caribbean Plate: implications for the tectonics and seismic potential of the northeastern Caribbean, *J. Geophys. Res.*, **89**, 4493-4519, 1984.
- McCann, W. R., and L. R. Sykes, Reply, *J. Geophys. Res.*, **91**, 787-791, 1986.
- Minster, J. B., and T. H. Jordan, Present-day plate motions, *J. Geophys. Res.*, **83**, 5331-5354, 1978.
- Molnar, P., and L. R. Sykes, Tectonics of the Caribbean and Middle American Regions from focal mechanisms and seismicity, *Geol. Soc. Am. Bull.*, **80**, 1639-1684, 1969.
- Nolet, G., Solving or resolving inadequate and noisy tomographic systems, *J. Comp. Phys.*, **61**, 463-482, 1985.
- Nolet, G., Seismic wave propagation and seismic tomography, in: *Seismic Tomography*, (ed.) G. Nolet, Reidel Publishing Company, Dordrecht 1-23, 1987.
- Nolet, G., Seismic Tomography, 386 pp., Reidel Publishing Company, Dordrecht, 1987.
- Paige, C. C., and M. A. Saunders, LSQR: an algorithm for sparse linear equations and sparse least squares, *ACM Trans. Math. Soft.*, **8**, 43-71 and 195-209, 1982.
- Pemington, W. D., Subduction of the eastern Panama basin and seismotectonics of northwestern South America, *J. Geophys. Res.*, **86**, 10753-10770, 1981.
- Pindell, J., and J. F. Dewey, Permo-Triassic reconstruction of western Pangea and the evolution of the Gulf of Mexico/Caribbean Region, *Tectonics*, **1**, 179-177, 1982.
- Pindell, J. L., S. C. Cande, W. C. Pitman III, D. B. Rowley, J. F. Dewey, J. Labrecque and W. Haxby, A plate-kinematic framework for models of Caribbean evolution, *Tectonophysics*, **155**, 121-138, 1988.
- Protti, J. M., and K. McNally, Stress geometries within the subducted Cocos Plate near the southern terminus of the Middle America trench beneath Costa Rica, C. A., (abstract) *EOS Trans. AGU*, **70**, 43, 1210, 1989.
- Roest, W., Seafloor spreading pattern of the north Atlantic between 10° and 40° N, *Ph.D. thesis University of Utrecht*, 1987.
- Ross, M. I., and C. R. Scotese, A hierarchical tectonic model of the Gulf of Mexico and Caribbean region, *Tectonophysics*, **155**, 139-168, 1988.
- Rosencrantz, E., and J. G. and Sclater, Depth and age of the Cayman Trough, *Earth Planet. Sci. Lett.*, **79**, 133-144, 1986.
- Ruff, L., and H. Kanamori, Seismicity and the subduction process, *Phys. Earth Planet. Inter.*, **23**, 240-252, 1980.
- Schenk, T., G. Mueller and W. Bruestle, Long-period precursors to *pP* from deep-focus earthquakes: the Moho underside reflection *pMP*, *Geophys. J. Int.*, **98**, 317-327, 1989.
- Spakman, W., Upper mantle delay time tomography with an application to the collision zone of the Eurasian, African and Arabian Plates, *Ph.D. thesis University of Utrecht*, 1988.
- Spakman, W., and G. Nolet, Imaging algorithms, accuracy and resolution in delay time tomography, in *Mathematical Geophysics: a survey of recent developments in seismology and geodynamics*, edited by N.J. Vlaar et al., Reidel, Dordrecht, 155-188, 1988.
- Spakman, W., M. J. R. Wortel and N. J. Vlaar, The Hellenic subduction zone: a tomographic image and its geodynamical implications, *Geophys. Res. Lett.*, **15**, 1 60-63, 1988.
- Spakman, W., S. Stein, R. van der Hilst and R. Wortel, Resolution experiments for NW Pacific

- subduction zone tomography, *Geophys. Res. Lett.*, *16*, 1097-1101, 1989.
- Stein, S., J. Engeln, D. Wiens, K. Fujita and R. Speed, Subduction seismicity and tectonics in the Lesser Antilles Arc, *J. Geophys. Res.*, *87*, 8642-8664, 1982.
- Stein, S., J. Engeln, D. Wiens, R. Speed and K. Fujita, Slow subduction of old lithosphere in the Lesser Antilles, *Tectonophysics*, 139-148, 1983.
- Stein, S., D. A. Wiens, J. F. Engeln, and K. Fujita, Comments on: "Subduction of aseismic ridges beneath the Caribbean Plate: implications for the tectonics and seismic potential of the northeastern Caribbean" by W. R. McCann and L. R. Sykes, *J. Geophys. Res.*, *91*, 784-786, 1986.
- Stein, S., C. DeMets, R. G. Gordon, J. Brodholt, D. Argus, J. F. Engeln, P. Lundgrun, C. Stein, D. A. Wiens, and D. F. Woods, A test of alternative Caribbean Plate relative motion models, *J. Geophys. Res.*, *93*, 3041-3050, 1988.
- Stewart, I. C. F., Travel time residuals of *PP* waves reflected under atlantic Canada, *Bull. Seism. Soc. Am.*, *66*, 4, 1203-1219, 1976.
- Stoiber, R. E., and M. J. and Carr, Quaternary volcanic and tectonic segmentation of Central America, *Bull. Volcanol.*, *37*, 304-325, 1973.
- Sykes, L. R., and M. Ewing, The seismicity of the Caribbean Region, *J. Geophys. Res.*, *70*, 5065-5074, 1965.
- Sykes, L. R., W. R. McCann and A. L. Kafka, Motion of Caribbean Plate during the last 7 million years and implications for earlier Cenozoic movements, *J. Geophys. Res.*, *87*, 10656-10676, 1982.
- Tomblin, J. F., The Lesser Antilles and Aves Ridge, in: *The ocean basins and margins, vol. 3, The Gulf of Mexico and the Caribbean*, edited by A. E. M. Naim and F. G. Stehli, 467-500, Plenum, New York, 1975.
- Uyeda, S., Subduction zones: and introduction to comparative subductology, *Tectonophysics*, *81*, 133-159, 1982.
- Van der Hilst, R. D., A 3-D image of large scale structures in the mantle below the Caribbean region, *Annales Geophysicae, EGS abstract*, *38*, 1989.
- Van der Hilst, R. D., and W. Spakman, A Tomographic image of the Lesser Antilles subduction zone, (*abstract*) *EOS Trans. AGU*, 1987.
- Van der Hilst, R. D., and W. Spakman, Importance of the reference model in linearized tomography and images of subduction below the Caribbean Plate, *Geophys. Res. Lett.*, *16*, 1093-1096, 1989.
- Van der Hilst, R. D., and E. R. Engdahl, On the use of *pP* and *PP* in delay time tomography, (*abstract*) *EOS Trans. AGU*, *70*, 1228, 1989.
- Van der Hilst, R. D., and E. R. Engdahl, On the use of *pP* and *PP* in delay time tomography, (*submitted to Geophys. J. Int.*), 1990a.
- Van der Hilst, R. D., and E. R. Engdahl, Relocation of ISC hypocenters and 3D mantle structure below Japan from inversion of *P*, *pP*, and *PP* data, (*abstract for AGU N.W. Pacific meeting, Aug. 1990*) *EOS Trans. AGU*, 1990b.
- Van der Sluis, A., and H. A. van der Vorst, Numerical solution of large, sparse linear algebraic systems arising from tomographic problems, in: ..., 49-84, 1987.
- Vidale, J. E., and D. Garcia-Gonzalez, Seismic observation of a high-velocity slab 1200-1600 km in depth, *Geophys. Res. Lett.*, *15*, 4, 369-372, 1988.
- Vierbuchen, R. C., The geology of the El Pilar fault zone and adjacent areas in northeastern Venezuela,

- in: *The Caribbean-South American plate boundary and regional tectonics*, edited by W. E. Bonini, R. B. Hargraves and R. Shagam, pp 1-30, Geol. Soc. Am. Memoir, 162, Boulder, CO, 1984.
- Vlaar N. J., The driving mechanism of plate tectonics: a qualitative approach, in: *progress in Geodynamics*, G. J. Borradaile, A. R. Ritsema, H. E. Rondeel, and O. J. Simon (eds), North holland, Amsterdam, pp. 234-245, 1975.
- Vlaar, N. J., and M. J. R. Wortel, Lithospheric aging, instability and subduction, *Tectonophysics*, 32, 331-351, 1976.
- Wielandt, E., On the validity of the ray approximation for interpreting delay times, in: *Seismic Tomography*, (ed.) G. Nolet, Reidel Publishing Company, Dordrecht 85-98, 1987.
- Wiens, D. A., Effects of near source bathymetry on teleseismic *P* waveforms, *Geophys. Res. Lett.*, 14, 761-764, 1987.
- Wiens, D. A., Bathymetric effects on body waveforms from shallow subduction zone earthquakes and application to seismic processes in the Kurile trench, *J. Geophys. Res.*, 94, 2955-2972, 1989.
- Wolters, B., Seismicity and tectonics of southern Central America and adjacent regions with special attention to the surroundings of Panama, *Tectonophysics*, 128, 21-46, 1986.
- Woodward, R., and G. Masters (1987), Using long period differential times to study global aspherical structure, (abstract) *EOS Trans. AGU*, 68, 44, 1376, 1987.
- Woodward, R., Structure of the Earth's upper mantle from long-period seismic data, f Ph.D. Thesis University of California, San Diego, U. S. A., 1989.
- Wortel, M. J. R., seismicity and rheology of subducted slabs, *Nature*, 296, 553-556, 1982.
- Wortel, M. J. R., and S. A. P. L. Cloetingh, On the origin of the Cocos-Nazca spreading center, *Geology*, 9, 425-430, 1981.
- Wortel, M. J. R., and S. A. P. L. Cloetingh, A mechanism for fragmentation of oceanic plates, *Am. Assoc. Petrol. Geol. Memoir*, 34, 793-801, 1983.
- Wortel, M. J. R., and N. J. Vlaar, Age-dependent subduction of oceanic lithosphere beneath western South America, *Phys. Earth Planet. Int.*, 17, 201-208, 1978.
- Wortel, M. J. R., and N. J. Vlaar, Subduction zone seismicity and the thermo-mechanical evolution of downgoing lithosphere, *Pageoph*, 128, 3/4, 625-659, 1988.
- Wright, C., Array studies of seismic waves arriving between *P* and *PP* in the distance range 90° to 115°, *Bull. Seism. Soc. Am.*, 62, 3, 385-400, 1972.
- Yoshii, T., A detailed cross-section of the deep seismic zone beneath northeastern Honshu, Japan, *Tectonophysics*, 55, 349-360, 1979.
- Zhou, H. W., and R. Clayton, Mantle velocities from *PP* waves, *EOS (abstr)*, 66, 46, 975, 1985.
- Zhou, H. W., How well can we resolve the deep seismic slab with seismic tomography?, *Geophys. Res. Lett.*, 15, 12, 1425-1428, 1988.
- Zhou, H. W., and R. Clayton, *P* and *S* wave travel-time inversions for subducting slab under the island arcs of the Northwest Pacific, *submitted to J. Geophys. Res.*, 1990.
- Zhou, H. W., Travel time tomographic studies of structures around subducted lithospheric slabs, *Ph.D. Thesis, California Inst. of Technol.*, 1989.
- Zielhuis, A., W. Spakman, and G. Nolet, A reference model for tomographic imaging of the upper mantle shear velocity structure beneath Europe, in: *Digital seismology and modelling of the lithosphere*, edited by: Cassinis, R., G. Panza, and G. Nolet, 333-340, Plenum, London, 1989.



## Summary and conclusions

I address in this thesis two principal topics. Firstly, in chapters 2 and 3 I discuss improvements on the method of  $P$  delay-time tomography which were necessary to obtain reliable tomographic images of the mantle structure below the Caribbean region. These improvements include the reduction of reference model artifacts and the incorporation of seismic waves other than the direct  $P$  wave. Although inspired by complications specific for the Caribbean region, these improvements are directly applicable to other seismic tomographic studies with body waves. Secondly, I present and discuss new tomographic images of the aspherical mantle structure below the Caribbean region in chapters 5 and 6. I investigate the structure of the upper mantle and of the lower mantle to a depth of approximately 1300 km, and relate it to tectonic phenomena that have been important for the tectonic evolution of the Caribbean region.

### *Reduction of reference model artifacts*

An important aspect in seismic delay-time tomography is the choice of a one-dimensional reference model of seismic velocities relative to which the tomographic problem is linearized. Ray paths which are computed in the reference models that are commonly used in global seismology, like the Jeffreys-Bullen model or the PREM model, do not differ significantly for the lower mantle. However, in the upper mantle the distances between the actual ray paths and the reference-model ray paths can be of the order of 100 km, due to the presence or the absence of a Low Velocity Zone and/or seismic discontinuities. These differences are of the order of the spatial dimensions of the cell sizes that are typically used in regional tomographic studies. I demonstrate that the use of different one-dimensional reference models in seismic delay-time tomography can result in significantly dissimilar images of the aspherical upper-mantle structure, which can give rise to non-unique and even contradicting interpretations. The cognizance of possible artifacts in the tomographic images due to the use of inappropriate reference models is very important in interpreting these images. This applies in particular to the investigations of the morphology of subduction zones across the boundary between upper and lower mantle.

ISC delay-time data, which are computed with travel time tables computed from the global Jeffreys-Bullen model, are used to derive a regional reference model. This model better represents the average spherically symmetric Earth's mantle below the Caribbean. In contrast to the global Jeffreys-Bullen model, the new reference model for the Caribbean mantle, referred to as VCAR, depicts seismic discontinuities in the upper mantle. These discontinuities occur at two depths: 390 and 660 km. Near these discontinuities, significant differences occur in the tomographic images computed either with the Jeffreys-Bullen or the VCAR model. The tomographic images computed relative to the VCAR model show less reference model artifacts than those referenced to the Jeffreys Bullen model.

### *Incorporation of $PP$ and $pP$ phases in the tomographic method*

A second problem encountered in recent investigations of the aspherical mantle structure with seismic body-wave tomography is that shallow structures beneath intraplate areas remain often unresolved because they are not adequately sampled by direct  $P$  waves. This is a serious complication in the case of the Caribbean region because both the epicenters of earthquakes and the locations of seismological stations occur in relatively narrow zones along the plate boundaries. The shallow structures below intraplate regions can be sampled more adequately by later arriving compressional waves which are reflected at the Earth's surface in such a region, like the  $PP$  and the  $pP$  waves. In chapter 3, I review the complications involved in the use of routinely acquired  $PP$  and  $pP$  data, and I investigate various sources of errors typical for these phases. The data of the different seismic phases used in the investigation are weighted with their variances. Incorporation of  $PP$  and  $pP$  waves in seismic tomographic studies improves the quality of the images because: (1), these waves sample Earth's structure not ordinarily sampled by direct  $P$  waves; (2), these waves add rays that are oblique to rays of direct waves; of special importance where the latter sample mantle structure in selected directions; and (3),  $pP$  data constrain the earthquake focal depths better. The incorporation of  $PP$  and  $pP$  phases in tomographic methods is straightforward and is preferable to the direct analyses of  $pP-P$  and  $PP-P$  differential travel-time residuals because it requires fewer assumptions and avoids doubtful approximations. The spatial resolution of the tomographic images improves significantly by the incorporation of  $PP$  and  $pP$  data. I show that there are important differences between images computed with the combination of  $P$ ,  $PP$ , and  $pP$  data and images determined by the inversion of  $P$  data only.

The benefits of incorporating  $PP$  and  $pP$  data for the Caribbean region are relatively small. Firstly, because the number of  $pP$  and in particular  $PP$  data is very small compared to the number of  $P$  data; secondly, because of the relatively large reading errors in  $PP$  and  $pP$  data; thirdly, because the difference in ray geometry between the  $pP$  waves and the direct  $P$  waves is small due to lack of seismicity at greater depths; and fourthly, because of the inconsistency between the ISC delay times of phases other than the direct  $P$  phase and the ISC source parameters.

### *The spatial resolution in the tomographic images*

I present the images of aspherical mantle structure below the Caribbean region in chapters 5 and 6. These images are obtained by the tomographic inversion of  $P$ ,  $PP$ , and  $pP$  travel-time residuals that are computed relative to reference model VCAR.

In the shallow part of the upper mantle the spatial resolution is good below the plate boundary zones where seismicity is high. Shallow structures are poorly resolved beneath intraplate regions which are characterized by low seismicity and the absence of seismological stations. However, a good correlation often exists between the imaged variations in seismic velocities and the inferences about aspherical structure from the seismicity of the region, even in regions where sensitivity tests suggest poor resolution. I therefore conclude that the results of sensitivity tests are not necessarily unequivocal in assessing the reliability of

shallow structures in the tomographic images.

Spatial resolution is poor in the depth range between 300 and 660 km. This is caused by the relatively low number of rays that have turning points immediately above the discontinuities and by the higher noise level in the data from waves that turn in the mentioned depth range. For the major part of the model, the resolution of lower mantle structure is very good. The interpretations of the relationship between upper and lower mantle structures have to be considered tentative because of the poor resolution in the transition zone between the upper mantle discontinuities, as mentioned above.

#### *The Middle America subduction zone*

Slab-like structures which are characterized by anomalously high *P*-wave velocities are imaged in the mantle below Middle America. The aspherical variations in seismic velocities extend well below the seismic zones associated with the Middle America subduction zone, and can be continued into the lower mantle where they coincide with the anomalous structure that was discovered in the early seventies by seismologists who analysed differential travel times of direct waves and waves reflected at the core-mantle boundary. Recently published tectonic models of the evolution of the Caribbean region indicate the subduction of thousands of kilometers of lithosphere of the Farallon and Cocos Plates below Middle America (chapter 4). Probably not enough space has been available to accommodate this amount of subducted lithosphere between the Middle America and the Antilles subduction zones. The tomographic images of the Middle America subduction zone show continuity of velocity anomalies across the 660 km seismic discontinuity, which strongly suggests the penetration of the subducted Farallon Plate into the lower mantle below the Caribbean region.

The Neogene plate reorganizations occurred in the Middle America realm. For example the left lateral motion of the southern part of Middle America (Chortis) relative to the northern part (central Mexico and Yucatan), and the break-up of the Farallon Plate followed by the collision of the East Pacific Rise and the Galapagos Spreading centre with the Middle America trench. These tectonic events explain in part the morphology of the upper 400 km of the Middle America subduction zone.

#### *The Lesser Antilles subduction zone and the North-South American Plate Boundary*

The Lesser Antilles subduction zone is imaged well below the seismic zones to a depth of 600 km. This depth correlates with the initiation of down going subduction in Eocene times (ca. 45 Ma) and convergence velocities of the order of 0-2 cm/yr between the Caribbean and the Atlantic Plates. The morphology of the Lesser Antilles subduction zone changes significantly across the 15°N parallel. South of approximately 15°N the image of the subducted atlantic plate dips steeper, and can be continued to greater depths than north of the 15<sup>th</sup> parallel. The differences in slab morphology along the Lesser Antilles subduction zone are interpreted by a more efficient retrograde motion of the old (*O*(100 Ma)) atlantic lithosphere that is subducted at the southern part of the Lesser Antilles trench. The imaged change in the morphology of the Lesser Antilles subduction zone is indicative of the

transition from the North American Plate to the South American Plate near the  $15^{\circ}$  N parallel. The "roll back" of the subducted atlantic part of the South American Plate explains the higher degree of tectonic *decoupling* of the southern part of the Lesser Antilles subduction zone and thus the significant decrease in subduction related seismicity towards the south. It also supports the hypothesis that the Grenada basin is a back-arc extension basin that opened in east-to-west direction.

#### *The Caribbean - South American Plate boundary*

Tomographic images also provide evidence for underplating at the Curacao trench of the Caribbean Plate below the Maracaibo Block, a micro plate in northwest South America. Although this underplating is not reflected in the seismicity of the region, the images suggest that the contact formed by the Curacao trench plays or has played an important role in the relative motion between the Caribbean Plate and the South American Plate. The tomographic images do not indicate a significant convergence between the Caribbean Plate and the entire South American Plate. I conclude that the principal motion between these plates is a right-lateral strike slip, and that the local underplating of the Caribbean is caused by the northward motion of the Maracaibo micro plate.

## Samenvatting (Summary in dutch)

Het inwendige van de aarde kan eenvoudig worden voorgesteld door een bol bestaande uit diverse lagen: de aardkorst, de aardmantel, en de aardkern. Hoewel op zeer grote schaal stabiel, op kleinere schaal is deze opbouw aan veranderingen onderhevig. Er vinden bewegingen plaats tussen verschillende delen van de aardkorst, die weer in belangrijke mate bepalend zijn - of bepaald worden - voor bewegingen in de dieper gelegen aardmantel. Deze bewegingen (tektonische processen) zijn de oorzaak van bijvoorbeeld aardbevingen and vulkaanuitbarstingen. Voor gebieden op aarde die regelmatig door deze verwoestende natuurfenomenen worden getroffen is het van groot belang dat we hun oorzaak, de tektonische processen, goed begrijpen. Op een complexe manier kunnen deze processen zowel oorzaak en gevolg zijn van (a-sferische) structuren in het inwendige van de aarde die afwijken van boven genoemde bolsymmetrische (sferische) gelaagdheid. Het onderzoek dat in dit proefschrift is beschreven heeft tot doel de structuren in de aarde onder het Caraibische gebied te bepalen en ze te relateren aan de tektonische processen die de vele aardbevingen en vulkaanuitbarstingen in dit gebied veroorzaken. Hierbij wordt gebruik gemaakt van een seismisch tomografische methode. Een belangrijk onderdeel van deze studie betreft enkele verbeteringen van de tomografische methode.

Met behulp van seismische tomografie kan worden bepaald hoe de werkelijke aarde afwijkt van een eenvoudig aardmodel dat gekenmerkt wordt door een bolsymmetrische opbouw. Dit model, waarmee de echte aarde wordt vergeleken, is het zogenaamde referentie model. In de hier toegepaste methode van seismische tomografie onderzoeken we de snelheid waarmee seismische golven, die ontstaan bij een aardbeving, zich door de aarde voortplanten. Hiervoor vergelijken we de tijdsduur tussen het plaatvinden van de beving en het moment waarop de golven bij een seismologisch station aankomen, met de reistijd die wordt berekend in het referentie model. Het eventuele verschil tussen deze geobserveerde en berekende tijden geeft informatie over mogelijke verschillen tussen de werkelijke aarde en het referentie model. De in kaart gebrachte verschillen vormen de tomografische beelden.

Er zijn verschillende referentie modellen bekend die een gemiddelde structuur van de hele aarde beschrijven. Het hier beschreven onderzoek laat echter zien dat deze modellen niet geschikt hoeven te zijn voor toepassing op kleinere schaal. In tegendeel: de interpretatie van de tomografische beelden is afhankelijk van het referentie model dat als uitgangspunt voor de berekeningen wordt gekozen. Er wordt besproken hoe de tomografische methode kan worden aangepast zodat storende effecten van een mogelijk verkeerd gekozen referentie model kan worden verminderd. De besproken aanpassing is ook direkt toepasbaar op geografische gebieden anders dan het hier onderzochte Caraibische gebied.

In de medische tomografie heeft men een vrijwel volledige controle over de opstelling van bronnen en ontvangers en dus over de manier waarop het te onderzoeken lichaamsdeel wordt belicht. Bovendien kan men experimenten overdoen om betere resultaten te bereiken. In de grootschalige seismische tomografie bestaan deze mogelijkheden niet: we zijn afhankelijk van de natuur voor de lokaties van bronnen (aardbevingen) en voor de plaatsing

van ontvangers (seismologische stations) zijn we afhankelijk van de verdeling tussen land en water.. Tot nu toe is in de hier toegepaste vorm van seismische tomografie voornamelijk gebruik gemaakt van de golf die direkt van de aardbevingshaard naar het ontvangende station gaat. Het tijdstip waarop deze golf bij een ontvangend station aankomt is meestal nauwkeurig te bepalen. Van deze direkte golf zijn veel reistijdgegevens beschikbaar via internationale data centra. Een groot nadeel is, dat in grote gebieden op aarde geen seismologische stations staan (b.v. in oceanische gebieden) en dat de direkte golf geen informatie geeft over ondiepe strukturen onder deze gebieden. Informatie over deze strukturen kan wel worden verkregen als we golven gebruiken die eerst aan het aardoppervlak reflektoren en vervolgens in een station geregistreerd worden. Hoe meer golven van dit type in elke registratie van een aardbeving kunnen worden geïdentificeerd, des te meer informatie kan worden verkregen over gebieden in de onderzochte aardmantel die niet voldoende worden "belicht" door de direkte golven. In dit proefschrift is aangetoond dat het gebruik van de aan het aard oppervlak gereflekteerde golven samen met de direkte golven een beter resultaat geeft, dan de toepassing van direkte golven alleen. Ook dit resultaat is zeer van belang voor het tomografisch onderzoek van andere delen van de aarde.

Met de verbeterde tomografische methode is de aarde onder het Caraibische gebied onderzocht tot op een diepte van ongeveer 1300 kilometer. Grootschalige variaties in de voortplantingssnelheid van seismische golven zijn aangetoond in de aardmantel dieper dan 670 kilometer: de grens(laag) tussen de zogenaamde boven-mantel en de onder-mantel. Dit resultaat bevestigt eerder gepubliceerde waarnemingen. Van groot belang is dat in dit onderzoek de relatie is aangetoond tussen deze diepe snelheidsvariaties en de strukturen in de ondiepere boven-mantel. De tomografische beelden wijzen sterk op de continuïteit van strukturen aan weerszijden van de grens op 670 kilometer diepte. Hoewel dit met behulp van tomografische beelden nooit bewezen kan worden, suggereert deze continuïteit dat grootschalig materiaal transport in de aardmantel niet gescheiden plaatsvindt in de boven- en onder-mantel, maar dat in elk geval plaatselijk bewegingen mogelijk zijn in de gehele mantel.

Ook met betrekking tot de regionale tektoniek (de bewegingen tussen de verschillende delen van de aarkorst) en de geologische geschiedenis van het Caraibische gebied zijn de resultaten die zijn besproken in dit proefschrift van belang. Met behulp van tomografie is onderzocht hoe de oceanische korst onder de Atlantische Oceaan langzaam onder de Caraibische Plaat verdwijnt (subduceert). De vorm van het gesubduceerde materiaal duidt sterk op de aanwezigheid van een plaatgrens tussen de Noord en Zuid Amerikaanse Platen vlakbij de 15°N breedtegraad. Met de tomografische beelden van de subductie zone onder de eilanden boog van de Kleine Antillen kan ook het tektonische proces dat leidt tot aardbevingen in het oostelijke deel van het Caraibische gebied beter begrepen worden. Ook in Midden Amerika bestaat een duidelijke relatie tussen seismiteit en de gevonden variaties in seismische snelheden. De strukturen in de tomografische beelden van de bovenste 400 kilometer onder Midden Amerika bevatten veel informatie over de tektonische geschiedenis van de afgelopen 25 miljoen jaar. In dit proefschrift is ook aangetoond dat het zuidelijke deel van de Caraibische Plaat onder het noordelijke deel van de Zuid Amerikaanse Plaat schuift.

## Dankbetuiging (Acknowledgements)

Van deze gelegenheid wil ik gebruik maken iedereen te bedanken die heeft bijgedragen aan mijn onderzoek en aan de totstandkoming van dit proefschrift.

In de eerste plaats dank ik mijn promotor professor N. J. Vlaar. Hij heeft mij de mogelijkheid gegeven dit onderzoek uit te voeren. De vrijheid die hij mij daarbij heeft gegeven heb ik zeer gewaardeerd. Veel dank ben ik verschuldigd aan mijn co-promotor Wim Spakman. Zonder de begeleiding van en samenwerking met Wim zou het uitvoeren van dit onderzoek moeilijker en zeker minder leuk zijn geweest. Zijn grondige kennis van de seismische tomografie is voor mij een grote steun geweest. Professor Rinus Wortel is vanaf het begin nauw betrokken geweest bij mijn onderzoeksproject. Diskussies met hem over tektonische problemen waren voor mij zeer leerzaam, en ik wil hem bedanken voor de interesse die hij altijd in mijn werk heeft gehad. De gesprekken met professor Guust Nolet waren voor mij erg motiverend. Zijn ideeën en suggesties hebben een belangrijke invloed gehad op de uiteindelijke invulling van mijn onderzoek.

Guust was also closely involved with the organization of my visits to the U.S. Geological Survey (USGS) in Golden, Colorado. I like to thank everybody at the USGS for their hospitality and for the wonderful times they have given me during my stays in Golden. In particular, I thank Bob Engdahl. He gave me the opportunity to visit the USGS twice. His attitude towards science and his enormous experience in seismology have been very stimulating for me. Because of his sense of humor, his reviews of my sometimes awkward english were not embarrassing but pleasant and very instructive.

With regard to this thesis I also want to thank professor Guust Nolet, professor Rinus Wortel, professor Bernard de Jong, Hanneke Paulssen, and Wim Spakman for critically reviewing (parts of) the manuscript.

Met name wil ik ook mijn kollega's Hanneke Paulssen, Alet Zielhuis, Bernard Dost, Roel Snieder bedanken voor de zeer vriendschappelijke samenwerking. Ook in drukke tijden bleken zij altijd wel bereid mij ergens mee te helpen. Samen hebben we veel plezier gehad. Zonder Alet's hulp bij het druk-klaar maken van dit proefschrift zou mijn slechte gewoonte alles op het laatste moment te doen zeker zijn afgestraft.

Veel dank ben ik verschuldigd aan een aantal mensen die niet direkt bij mijn onderzoek betrokken zijn geweest, maar zonder wier hulp mijn werk moeilijker en zeker tijdrovender zou zijn geweest. Ik dank de medewerkers van het Accademische Computer Centrum Utrecht, met name Frits von der Linden, voor de medewerking die ik heb ondervonden in de afgelopen jaren waarin ik veel gebruik heb gemaakt van de faciliteiten van dit rekencentrum. Bert van Corler en Jaap Hollenberg hebben menig probleem voor mij opgelost toen ik gebruik maakte van de superkomputer van het SARA in Amsterdam. Via Ko van Gend heb ik steeds gemakkelijk over de op het KNMI aanwezige gegevens kunnen beschikken. Ik heb veel profijt gehad van het vakmanschap van Hans Schiet. Door zijn inzet heb ik steeds snel kunnen beschikken over dia's, foto's en copy-proofs voor verschillende presentatie doeleinden.

Mijn ouders ben ik veel dank verschuldigd. Zij hebben mij tijdens mijn studie en mijn onderzoek altijd gesteund en gestimuleerd.

Tot slot wil ik iedereen bedanken die interesse hebben getoond voor mijn werk en die een bijdrage hebben geleverd aan de fantastische tijd die ik in Utrecht heb doorgebracht.

Part of this reseach was funded by the Netherlands Organization for the Advancement of Pure Research (NWO). NATO financially supported my visits to the USGS in Colorado (grant 0910/87). SURF (NFS) supported computations on the C205 supercomputer of the SARA in Amsterdam. I greatly appreciated that I was permitted access to the computer facilities of the Orfeus Data Center (ODC) in Utrecht.



## **Curriculum Vitae**

12-01-1961	Born in Oostzaan, The Netherlands.
1973 - 1979	VWO-B, Christelijk Streek Lyceum te Ede, The Netherlands.
08-03-1982	Kandidaatsexamen G4 (Geology with physics and mathematics).
30-06-1986	Doctoraal examen Geophysics (cum laude).
24-11-1986	Doctoraal examen Structural Geology (cum laude).
1986 - present	Research assistant at the Department of Theoretical Geophysics, University of Utrecht, The Netherlands.